# Measurement and simulation of half-integer Shapiro steps in graphene-based SQUIDs

Max Frederick Taylor, MPhys(Hons)

A thesis submitted for the degree of *Doctor of Philosophy*

Department of Physics

Lancaster University

February, 2025

# Abstract


Title: Measurement and simulation of half-integer Shapiro steps in graphene based SQUIDs
Author: Max Frederick Taylor

Graphene-based superconducting quantum interference devices (SQUIDs) were measured in a current-biased regime with and without irradiation by a microwave (MW) signal. The charge carrier concentration in graphene can be varied with electrostatic gating, tuning the transparencies of the Josephson junctions (JJs) in the SQUIDs. The junctions in these devices are fabricated with graphene encapsulated in hexagonal boron nitride where the NbTi superconducting electrodes make highly transparent one-dimensional contacts with the graphene. They are expected to facilitate ballistic transport of charge carriers, implying a non-sinusoidal current-phase relation (CPR) similarly to superconductor-normal metal-superconductor (SNS) JJs. A characteristic feature of the non-sinusoidal CPR is the appearance of half-integer Shapiro steps when the CPR is highly skewed. Half-integer Shapiro steps should also be visible when an amount of magnetic flux equal to a half-integer multiple of the magnetic flux quantum is present in the SQUID loop. This sets this investigation apart from other work, which are focused on individual graphene-based JJs. As superconducting circuits become more complex, it will be important to understand the behaviour of circuit components beyond single junctions.

These phenomena were explored both with the graphene SQUIDs and with a numerical simulation of the resistively and capacitively shunted junction (RCSJ) model. The simulation used a skewed CPR which could be varied based on the transparency of the JJs, applicable to ballistic SNS junctions.

Simulation results confirmed the expected behaviours of devices with a skewed CPR and is a promising avenue for exploring further fractional Shapiro steps. The experimental measurements of the graphene SQUIDs found half-integer Shapiro steps, giving evidence of a ballistic tuneable CPR in these graphene-based devices and establishing a precedent for further investigation.

# Contents

# List of Figures

# List of Tables

# Acknowledgements

Firstly, I would like to thank my supervisors Dr M.D. Thompson and Professor J.R. Prance for their expert guidance throughout my PhD. In particular, thanks to Dr Thompson for his support while I have been writing up under unideal circumstances.

Secondly, I would like to thank my friends, family and colleagues their support and camaraderie, in particular DT, ED, EF, EG, FB, GR, JP, JT, and PC.

Additional recognition of roles and contributions are given below.

## Supervisors

Dr Michael D. Thompson

Professor Jonathan R. Prance

## Contributions

Daan Wielens - Advice regarding high-frequency measurements in an Oxford Instruments Triton dilution refrigerator.

Graphene NOWNANO CDT - Funding for the PhD studentship.

Jonathan Prance - The base code of the SQUID simulation.

Joshua Chawner - The start of building the RF wiring stick.

Lancaster University HEC - Access to high-end computing resources to run the simulations.

Michael Thompson - Training with regard to operation of the dry dilution refrigerator.

Moshe Ben Shalom - Fabrication of the 'Double SQUID'.

Patrick Steger - Training with regard to bending and stripping coaxial wires, and attaching crimp connectors.

Wendong Wang - Fabrication of the 'Big SQUID'.

# Declaration

I declare that this thesis is my own work which has not been submitted in substantially the same form for the award of a higher degree elsewhere.

Approximate word count: 40,000 words.

# Nomenclature

**2DM** two-dimensional material. 1, 6–9, 14, 23, 37

**ac** alternating current. vi, 4, 10, 17, 18, 32, 43, 45, 47, 51, 60–62, 69, 72, 74, 78, 85, 89, 91, 92, 95, 138, 139

**BW** bandwidth. 64

**CPR** current-phase relation. i, v, viii, 10, 17, 18, 25–30, 36, 37, 40–44, 48, 49, 58, 65, 66, 68–75, 79, 106, 110–113, 118, 122, 128–130, 138, 139, 141, 145

**CVD** chemical vapour deposition. 6, 9, 24

**dc** direct current. v, viii, 10, 11, 17, 18, 25, 30, 33, 60–63, 67, 75, 77, 84, 89, 91–93, 95, 105, 116, 117, 119, 120, 124–128, 131, 134

**EBL** electron beam lithography. 81

**GJJ** Graphene Josephson junction. 9, 17, 19, 22–25, 28, 29, 35, 36, 39, 103, 130, 137

**hBN** hexagonal boron nitride. 7, 9, 19, 20, 23, 24, 43, 81, 83, 103, 138

**HEC** high-end computing (cluster). xi, 59, 164

**HOPG** highly-oriented pyrolytic graphite. 7, 14

**IV** current-voltage (characteristic). vi–viii, 35, 40, 41, 59, 66, 69, 70, 74, 79, 84, 89, 91, 93, 95, 96, 98, 100, 104, 105, 119, 122, 130, 131

**JJ** Josephson junction. i, v, vi, 1, 4, 5, 9, 10, 16, 17, 19, 23, 25, 27–30, 32, 33, 35–38, 40–43, 47–49, 63, 69, 74, 86, 89, 96, 98, 103, 139

**JTL** Josephson transmission line. 5

**LI** lock-in (amplifier). 89

**MW** microwave. i

**P-IV** power-current-voltage (characteristic). 131, 133, 134, 137, 140

**PID** proportional-integral-derivative (controller). 89

**PSD** power spectral density. 64

**RCSJ** resistively and capacitively shunted junction. i, vi, ix, x, 10, 30, 45, 47, 48, 55, 58, 59, 63, 65, 70, 74, 78, 79, 139, 165

**RF** radio frequency. v–ix, xi, 9, 30, 41, 45, 60, 62, 65, 66, 69–72, 74–77, 80, 84–86, 89, 90, 93–95, 113–115, 118–121, 123–126, 128–131, 135, 136, 138, 145, 161

**RIE** reactive ion etching. 81

**rms** root-mean-square. 64, 91

**SFQ** single flux quantum. 4, 5, 9, 35, 36

**SFS** superconductor-ferromagnet-superconductor (Josephson junction). 37

**SGS** superconductor-graphene-superconductor (Josephson junction). 23, 81, 82, 101

**SIS** superconductor-insulator-superconductor (Josephson junction). v, 17–20, 35

**SLUG** superconducting low-inductance undulatory galvanometer. 30

**SMA** subminiature version A. 86

**SNS** superconductor-normal (metal)-superconductor (Josephson junction). i, 1, 9, 17, 19–22, 25, 26, 35, 42, 47, 103

**SQUID** superconducting quantum interference device. i, v–xi, 1, 9–12, 28–38, 40, 41, 43–45, 48–53, 55, 57–60, 62–73, 75, 78–84, 86, 87, 89, 91–96, 98–118, 121–133, 135–140, 146–160, 162

**TMD** transition metal dichalcogenide. 6, 7

**vdW** van der Waals. 7–9

References to equations are sorted by chapter and number in parenthesis. (chapter.number)
References to figures, tables, and chapters/sections are sorted by chapter and number without brackets. chapter.number
Citations to literature are presented as numbers in order of first appearance in square brackets. [number]

# Chapter 1

# Introduction to superconductors, two-dimensional materials, and their hybrid devices

This thesis explores the properties and behaviour of superconducting quantum interference devices (SQUIDs) which use the two-dimensional material (2DM) graphene as the weak link in their superconductor-normal metal-superconductor (SNS) type Josephson junctions (JJs). These devices are at an intersection between two fields of condensed matter physics: superconductivity and two-dimensional materials. This introductory chapter will contain mostly qualitative discussions of each field pertaining to the history, key impacts, and motivations for future direction of research. The last section of this chapter will describe the structure of the thesis.

## Contents

## 1.1 Superconductivity

Superconductivity is an example of quantum phenomena being observable on a macroscopic scale. Fundamentally, superconductivity is a phase of matter in which the electrical resistance is zero, and any magnetic fields are expelled from the material. In this section the history of the field will be briefly discussed, but as this is widely available[1, 2] more focus will be placed on the motivation behind current superconductivity research and in particular superconducting devices.

### 1.1.1 History and motivations

The zero resistance property of superconductors was first observed by Kamerlingh Onnes in mercury in 1911 when he was performing experiments with liquid helium[3]. A sharp transition from finite to zero resistance was observed when the mercury was cooled below 4.2 K. The temperature at which a superconductor undergoes this phase change is called the critical temperature $T_c$. Onnes' experiments were initially about liquefying helium[4] and then performing experiments with it, including testing the effects on electrical resistance in metals. The discovery of zero resistance mercury at low temperature gave an additional reason for developments to be made into low-temperature refrigeration systems and experimental apparatus.

The second identifying characteristic of superconductors was then observed by Walther Meissner and Robert Oschsenfeld in 1933. The perfect diamagnetism exhibited by the superconductors in their work set superconductors apart from what would otherwise just be 'perfect' conductors[5]. If a perfect conductor has an external magnetic field applied to it, and is then subsequently cooled down below $T_c$ to zero resistance, the magnetic field would not be affected. On the other hand, if the same is done to a superconductor, the field is expelled from inside the superconductor as shown in figure 1.1. This happens due to screening currents generated close to the surface of the superconductor which produce an opposing magnetic field. However, if the applied field is strong, above the critical field strength $H_c$, the screening currents are not able to prevent the magnetic field from entering the superconductor and destroying the superconductivity. In type-I superconductors (usually pure metals such as aluminium and tin), the critical field is represents a transition point between the superconducting and resistive phases. However, in type-II superconductors (often compounds of niobium) there is a mixed state between the lower $H_{c1}$ and upper $H_{c2}$ critical fields, with the lower limit marking the transition between the superconducting and mixed states, and the upper limit marking the transition between the mixed and resistive states. The mixed state has some magnetic penetration, such that there are both superconducting and resistive regions in the material. Type-II superconductors tend to have higher critical fields than type-I, making them useful for applications such as superconducting magnets.

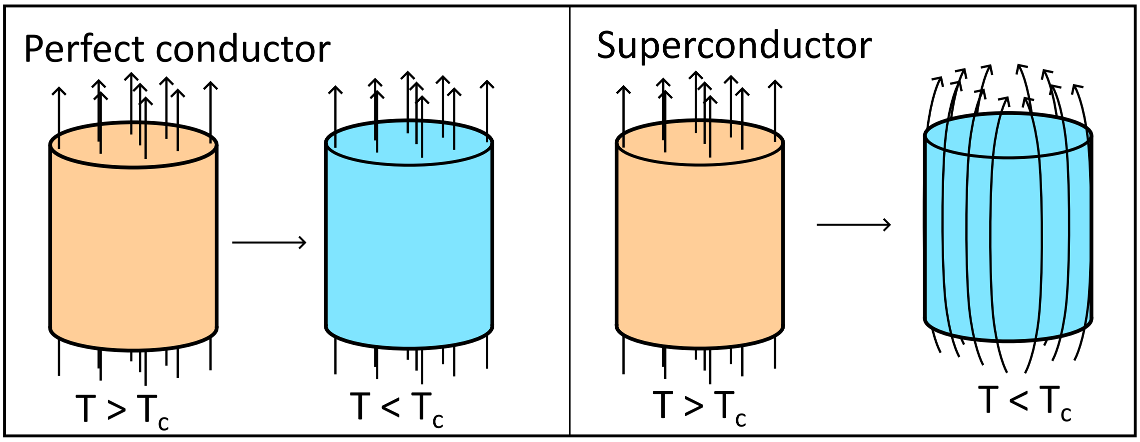


Figure 1.1: An illustration of the Meissner effect. The arrows represent an externally applied magnetic field. Comparing a perfect conductor and a superconductor in a uniform magnetic field outside of the zero-resistance phase (orange, $T > T_c$), the field is usually able to penetrate the material completely. When cooled below the critical temperature (blue, $T < T_c$), in a perfect conductor, just becoming zero-resistance has no effect on the field, whereas the superconductor expels the field.

With the two characteristics together it was clear that there was a new class of material worth studying, and refrigeration technology was already being developed which could be applied to this area of research. The immediate implication of zero resistance materials is that they would eliminate Joule heating, a significant source of inefficiency in the transfer of electrical current. Joule heating is a process in which electrical energy is converted to heat energy as charge carriers collide with and scatter off the atoms in a material. The amount of power dissipated in the material $P$ depends linearly on the resistance of the material $R$ and quadratically on the current being passed through it $I$, such that $P = I^2R$. This is why low resistance metals like copper, gold and platinum are commonly used in present day electronic devices, but superconducting materials in their place would make passive losses negligible. This would be especially significant for facilities like data centres and supercomputers which have huge quantities of electronic circuitry. Currently, the heat generated by electronics means that these facilities must include cooling for the electronics so that they continue to function, leading to an even greater financial and environmental cost. One approach to this problem is to try and recover the waste heat to use elsewhere[6], but superconductors could greatly reduce the amount of waste heat produced. Although superconductors would not completely eliminate energy losses due to operating requirements often taking them out of their superconducting state, they would still make a huge impact, especially for power transmission and distribution. The main challenge for superconductors is that they typically need extreme environmental conditions of low temperature or high pressure to support supercurrent. There are additional challenges around scaling infrastructure to support those conditions. In the ideal case, a material would be discovered that is superconducting under ambient conditions: room temperature and atmospheric pressure. The search for high-temperature superconductors is a significant ongoing research question because of the technological implications of an ambient temperature and pressure superconductor. However, low temperature superconductors can already access other applications in electronic devices which are distinct from what is possible in non-superconducting electronics due to their quantum mechanical properties. These often take advantage of the low-temperature requirement, which at present is well enabled by ultra low temperature cooling equipment. Given that cooling is already needed in these intensive computing facilities, another approach is to lean into that requirement and develop cryogenic electronics to integrate into large scale computing, replacing the energy-inefficient components one part at a time, such as with superconducting memory circuits[7].

### 1.1.2 Refrigeration and superconducting devices

While the zero resistance property is the main draw to high-temperature superconductor research, superconductors can also be used in quantum circuits, and this work is firmly based on low-temperature superconductors. Making low temperature sample environments more accessible is an activity increasingly taken on by industry which should help accelerate progress in developments of superconducting technologies. Commercial dilution refrigerators available today can regularly reach temperatures below 10 mK. This is more than enough for a lot of superconducting devices, as well as those devices that are not superconducting but possess qualities that nevertheless require low temperatures[8], or that are used in conjunction with superconducting devices. Dilution refrigerators are usually built to accommodate complex electronics setups because of the types of devices being tested.

Going further than this into sub-1 mK temperatures is usually done using nuclear adiabatic demagnetisation[9], which is rarely used because it requires a dedicated cooling stage with consideration of magnetic field and electronics beyond that which is normally required in typical wet or dry dilution refrigerators[10]. Ongoing work includes techniques for applying nuclear adiabatic demagnetisation on-chip to assist with getting quantum devices into the microkelvin regime with less investment into the experimental setup than previously required[11].

Regarding superconducting devices, there was a paradigm shift in 1962 originating from Brian Josephson's theoretical predictions of supercurrent passing through thin barriers inside superconductors[12]. The 'Josephson effects' make the phase of the superconducting wavefunctions into a quantity that could be measured and manipulated, allowing for new ideas in electronics to be explored with the 'Josephson junction' (JJ) as the base circuit element. Superconducting device technologies are some of the main candidates for enabling large-scale quantum computing[13] and dark matter detection using Josephson travelling wave parametric amplifiers[14]. They have the intrinsic benefit of very low thermal noise at low temperatures, so weak signals are more likely to be visible above the noise floor, and electronic states are longer-lived.

Another development for superconducting electronics was the design of a full digital computing logic basis using overdamped JJs called single flux quantum (SFQ) logic[15]. The underlying principle is that it uses the presence or absence of SFQ pulses to represent 1s and 0s respectively. SFQ pulses are generated by a JJ undergoing a full $2\pi$ phase change (or 'phase slip') in the resistive state before returning to the superconducting state. While briefly in the resistive state, the JJ has a finite voltage generated across it by the ac Josephson effect. Having undergone a $2\pi$ phase slip, the area under the produced voltage curve is quantised to the magnetic flux quantum $\Phi_0 = 2.07$ mV ps. Josephson junctions can undergo a phase slip in a time on the order of ps, not only making this technology extremely fast but also giving it potential for integration with optical circuits[16, 17]. SFQ circuits are also a candidate for superconducting qubit control circuits, in part because they would operate in the local cryogenic environment and reduce the wiring requirement from room temperature[18–22].

Operating SFQ circuits requires that SFQ pulses are reproduced at different stages. These events occur at individual JJs. If a JJ is biased just beneath its critical current, a short pulse (such as another SFQ pulse) incident on the JJ provides enough extra current to cause it to be briefly biased above its critical current, causing it to generate a new SFQ pulse. Pulses can be transported to other parts of a circuit in this way using a Josephson transmission line (JTL), a simple structure which can have multiple stages, each stage using one JJ as shown in figure 1.2. As the pulse area is quantised to $\Phi_0$, the quicker the phase rotation happens, the higher the amplitude of the SFQ pulse. This can allow a JTL to provide amplification by increasing the critical current of subsequent JJs along the circuit. As an SFQ pulse can be generated in an amount of time on the order of ps, this corresponds to peak voltages on the order of mV, due to the quantisation to the magnetic flux quantum. These qualities further place SFQ logic as having strong potential as part of superconducting technologies as the applications increase in scale and become more widely applied.

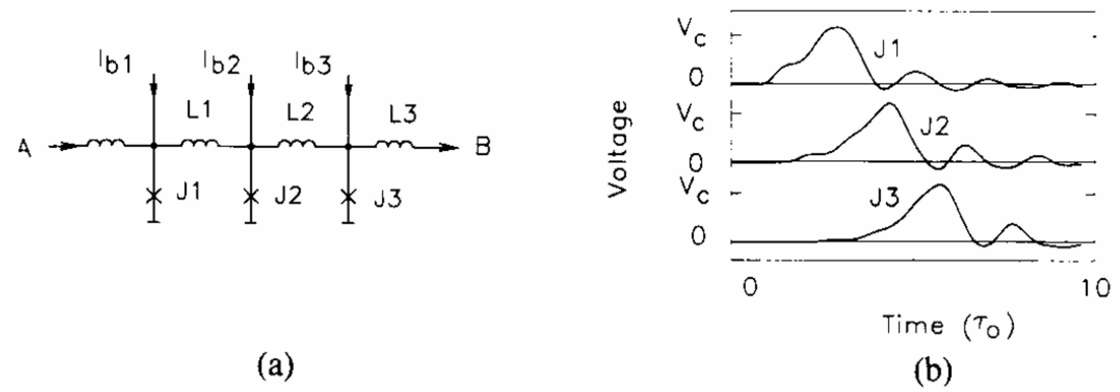


Figure 1.2: (a): A circuit diagram of a 3-stage Josephson transmission line, used to propagate and amplify SFQ pulses. $I_b i$ and $Li$ are the bias currents and inductances associated with the Josephson junctions $Ji$ respectively. (b): Simulation results showing how the pulses are produced after each junction. $V_c$ is the characteristic voltage of the junction, and $\tau_0$ is the time for the junction to undergo a $2\pi$ phase slip. Figure reproduced from [15] ©1991 IEEE.

Overall, it is clear that low temperature is still a requirement for a number of applications and scientific investigations. In particular, it will always be essential for superfluid research, which has analogues to superconductivity. Regarding electronics at low temperature, there are benefits associated with low thermal noise and Joule heating. Additionally, many low temperature superconductors are well understood in terms of their properties and because many of them are metals they can be easily fabricated into functional devices. This makes low temperature superconductors the likely candidates for new developments related to superconducting devices for the foreseeable future.

## 1.2 Nanomaterials and electronically confined systems

There are a few definitions surrounding low-dimensional materials and nanomaterials which first need to be explained for context. A simple definition that is based on the raw size of a material says that nanomaterials are those for which at least one spatial dimension is shorter than 100 nm. This is a very broad definition which is best used to group anything of a sufficiently small size, whether that is an individual layer of material or a collection of nanoparticles. It can be useful for communicating across multidisciplinary aspects of nanoscience as it gives a straightforward indication of scale and type of low-dimensional system, alongside more specific nomenclature. It has also been featured as the definition used in local safety documentation while studies into the effects of inhalation, ingestion, or skin absorption are ongoing.

More specifically, two dimensional materials (2DMs) are usually considered to be those for which a single layer (or monolayer) of a particular material can be isolated. The monolayer could be formed using either top-down processes such as exfoliation from a layered crystal, or bottom up processes like chemical vapour deposition (CVD). The quintessential 2DM and one of most relevance to this work, graphene, lies in one plane. But other collections of 2DMs like transition metal dichalcogenides (TMDs) have monolayers that are not entirely on one plane. The definition of a 2DM is extended to multiple layers of the materials to the extent that the multilayer material still displays notably different properties to the bulk material. For example, a bulk crystal of the TMD $WSe_2$ has an indirect band gap but in a monolayer the band gap becomes direct[23].

However, this is still distinctly different to how low-dimensional systems are handled in condensed matter physics terms, as this is with regard to electron transport rather than the literal geometry. A 2D system with regard to electronics uses the idea of 'confinement' where the movement of charge carriers is restricted to two, one, or no spatial dimensions. This confinement tends to happen over ranges less than 10 nm as this is the approximate size of the de Broglie wavelength in electrons. At these length scales, the dimensionality of the density of states is reduced and the available energy states in the direction of the confinement are quantised. This is smaller than the broad 100 nm definition but shows that an effective 2D system can exist in multilayered materials, thin films and heterostructures.

### 1.2.1 Graphene and the 2D material family

As an atomically flat honeycomb lattice of carbon atoms, graphene is the thinnest possible solid material, and remains the quintessential 2DM. Despite being known about since the 1920s[24] graphene was first isolated in 2003 by Andre Geim and Kostya Novoselov[25]. It has been regarded as a wonder material due to an array of remarkable properties. An intensity of research has started to produce applications. Some are using graphene's innate strength as a way to improve or maintain the durability of other materials while reducing weight, such as in concrete[26] and rubber[27]. Graphene has also showed promise as a membrane for water filtration[28] or resistive coatings[29], making use of the physical spacing of the atoms in the lattice.

It is worth noting that some of these types of applications will actually use graphene precursors like flakes of highly-oriented pyrolytic graphite (HOPG) which are easier to produce but will still contribute a similar effect. It is often difficult to determine exactly what is meant by commercial products that claim to incorporate graphene because there is currently no standardisation around the types and quality of graphene-like materials. The quality of graphene can vary on the production method used to obtain it. The mechanical exfoliation method which was originally used to isolate graphene remains the best way to get the highest quality graphene (in terms of reducing the number of defects), but this method is low yield, presenting a challenge for scaling graphene-based technologies.[30].

Other 2DMs similar to graphene make up a class of 'van der Waals' (vdW) materials[31, 32]. These are nanomaterials which are layered crystals analogous to how graphene layers make up HOPG. As well as semimetal graphene there is coverage of other material classes including electronic insulators and semiconductors.

The first of two major examples of non-graphene 2DMs that are frequently used are transition metal dichalcogenides (TMDs). TMDs are semiconductor 2DMs which are formed in a 1:2 ratio of transition metal M and chalcogen X (found in group 6 of the periodic table), $MX_2$ (see figure 1.3). Particularly common examples are $MoS_2$ and $WSe_2$ but many other combinations exist using other materials, a notable example being the 2D superconductor $NbSe_2$[33]. The structure of a TMD monolayer actually consists of three interlinked atomic planes. The metal atoms lie in the central plane and are bonded to chalcogen atoms in the planes above and below them. These materials are naturally occurring crystals where the monolayer can be isolated by mechanical exfoliation in the same way as when graphene monolayers are exfoliated from HOPG. Viewed from above the atoms are arranged in a hexagonal lattice shape, again very similar to graphene.

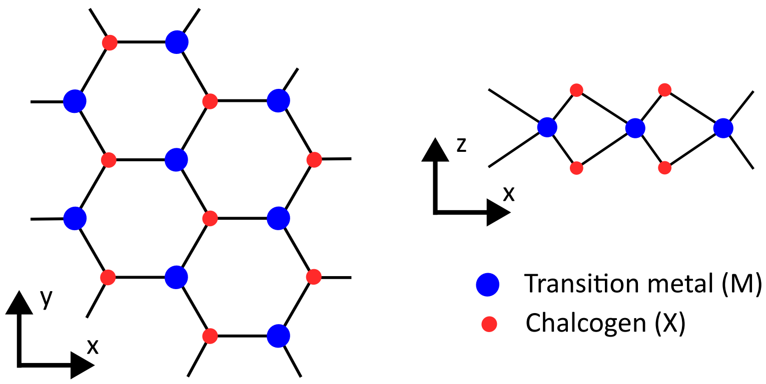


Figure 1.3: General lattice structure of a transition metal dichalcogenide. Larger blue circles represent the transition metal atoms and smaller red circles represent the chalcogen atoms. The y-x axis shows the plane of the 2DM monolayer while the z-x axis shows a cut perpendicular to the plane of the 2DM, indicating that the monolayer is structured as three interlinked atomic planes.

The second important example is hexagonal boron nitride (hBN). It shares a number of geometric properties with graphene including the shape of the lattice and how it can be exfoliated from a crystal into atomically flat sheets. The lattice of hBN is quite similar to graphene, but it is an electrical insulator, making it favoured as a dielectric component of 2D electronic devices.

Different 2DMs can be combined into circuits in a way which is unique to layered materials. When in the bulk crystals, the individual layers experience a relatively strong van der Waals force, which is overcome to exfoliate the layers from the bulk. But it is also possible to use the same principle to stack different 2DMs on top of each other to make electronic devices, held together by vdW forces. Different classes of materials can be easily combined in this way. These van der Waals heterostructures avoid some of the problems encountered in semiconductor growth where the materials you can grow next to each other are restricted by the necessity to match lattice constants. This allows heterostructures to be built with a huge flexibility in their properties[31].

## 1.3 Graphene in superconducting electronics

Research around graphene in electronics searches for an application or device that graphene enables better than anything else. Its high conductivity makes it appealing to be generally substituted into many circuits. It can be tuned by electrostatic gating, making it viable for roles that might usually be taken by semiconductors. The most unique potential brings in the rest of the 2DM family, which is in making flexible circuits and building van der Waals heterostructures. This is a new way of building devices which often remains compatible with existing nanofabrication techniques.

If an application is found, the next concern is about scaling the production of high-quality graphene. Mostly, high-quality material is obtained via mechanical exfoliation, but this only yields small areas of graphene. Graphene grown by CVD is a popular route for obtaining larger areas of the material, and is accessible from commercial sources. Recent research into CVD growth of graphene has claimed quality similar to that of exfoliated graphene by excluding oxygen from the growth environment[34]. If this is the case, it would make the scaling up of graphene-based devices in general a more realistic prospect, including superconducting devices. The Josephson effect in a graphene JJ was initially reported in 2007[35], but since then a number of developments have been made in device design. Typically for these types of devices, graphene is used as the 'normal metal' component of SNS style JJs. They use a vdW heterostructure of hBN encapsulating a monolayer of exfoliated graphene. The heterostructure is located on a typical substrate such as $Si/SiO_2$, and the electrical contacts are made using standard nanolithography and thin-film growth techniques, showing how 2DM circuits can be integrated with other electronic systems. This is the primary topic of section 2.2, where these points will be greatly expanded.

At the start of the work for this thesis, it was intended that graphene Josephson junctions (GJJ)s could be explored in the context of SFQ logic circuits. Operation of SFQ circuits requires precise engineering of the critical current of the JJs making up the circuit. While this can largely be controlled through junction geometry, graphene junctions have a tuneable critical current, allowing for precise optimisation. Additionally, more advanced circuits could be developed with enhanced functionality using the tunablility of the graphene. For example, branches of a circuit could be switched 'on' or 'off' by changing the critical current to direct SFQ pulses to different parts of the circuit. Lastly, because of the atomic flatness of am hBN encapsulated graphene vdW heterostructure, it can be placed on top of any substrate, which can have particular benefits in devices which operate with RF signals, as substrates with favourable loss characteristics can be chosen with less concern for the fabrication of the circuit itself.

Due to limitations, the scope of the project changed to focus on the behaviour of superconducting quantum interference devices (SQUIDs) fabricated with graphene JJs under irradiation from high frequency signals. The characteristics of these devices were explored through simulation and experiment.

## 1.4 Scope of the thesis

This thesis is an investigation into the properties of dc SQUIDs which use monolayer graphene as the material bridging the gap between the superconducting electrodes of the parallel Josephson junctions. The devices tested experimentally were fabricated using a combination of a van der Waals heterostructure and more typical lithography and metallisation techniques.

Graphene's electronic properties allow the properties of the SQUID to be changed while active using electrostatic gating. As well as the general characteristics of the devices and how they change when the graphene is gated, a focus of the thesis is on the behaviour of graphene SQUIDs in the presence of microwave radiation. In typical JJs and SQUIDs, quantised voltage steps called Shapiro steps appear under these conditions. The literature suggests firstly that the behaviour of Shapiro steps can be related to the current-phase relationship (CPR) of the JJ[36], the property which controls the supercurrent allowed through the junction. In particular, it is shown that a skewed, non-sinusoidal CPR, present in ballistic JJ, gives rise to fractional quantisation of the voltage steps.

Secondly, it has been shown that ballistic graphene JJs have skewed CPRs where the skewness depends on the charge carrier concentration in the graphene, with a high charge carrier density corresponding to high transmission of charge carriers across the junction[37]. This can be controlled by electrostatic gating.

If a graphene SQUID has a tuneable CPR that can be placed into either lowly or highly skewed regimes, it would be expected that fractional Shapiro steps would only be visible in highly skewed case, and not when the CPR is close to sinusoidal. Therefore, it is hypothesised that measuring changes in the appearance of Shapiro steps in such a device would be a way of evidencing the changing current-phase relation and the ballistic nature of the charge transport.

The important physical theory underpinning these types of devices will be explained in chapter 2, alongside discussion of related work in the literature.

In parallel with experimental analysis of physical devices, a theoretical investigation of similar systems is done using a numerical simulation of the resistively and capacitively shunted junction (RCSJ) model. The simulation represents generic SQUID systems using dimensionless parameters. The intrinsic properties of the SQUID can be varied and the devices can be put under different test conditions including noise and ac currents. The derivation of the numerical model and its results are contained within chapter 3.

The devices under investigation, and the experimental apparatus used to measure them, will be shown in chapter 4. The sample environment part of the setup includes a dry dilution refrigerator with a base temperature of $\approx 15$ mK, necessary for the superconducting devices. This is connected to a variety of laboratory grade electronic instruments to control and read out the SQUIDs. The main measurement instrument is a lock-in amplifier, which allows both differential and dc measurements to be taken. The experimental setup allows for operation of the devices in the dc regime as well as under microwave irradiation.

Chapter 5 contains the results and analysis of the experimental measurements. This covers a wide array of properties used to characterise SQUIDs both in the dc regime and under microwave irradiation. The investigation into the appearance of fractional Shapiro steps is featured in both the simulation and experimental results chapters.

Finally, there will be summary and conclusions of the overall thesis, and discussion looking forward to how this work can be continued in the future.

# Chapter 2

# Ballistic graphene-based SQUIDs

In this chapter, graphene will be introduced first alongside other significant nanomaterials, before then moving straight into the history and development graphene-based Josephson junctions and superconducting quantum interference devices (SQUIDs). Following that, the phenomenon of Shapiro steps will be introduced with discussion about how they can vary depending on the type of Josephson junction and its properties.

## Contents

## 2.1 Graphene and its electronic properties

As a 2D material, graphene can be compared to other low-dimensional systems which demonstrate electronic confinement. The most prolific examples come from thin layer growth using methods like molecular beam epitaxy for semiconductor device fabrication. Early examples of electronic confinement reduced electron transport to a 2D system by forming a quantum well inside a semiconductor heterostructure. The classic example is growing a thin layer of GaAs between two layers of AlGaAs[38]. The AlGaAs has a wider bandgap that the GaAs, such that the conduction band in the GaAs lies inside the bandgap of the AlGaAs. This means that electrons inside the well are confined to the plane of the GaAs, until they can escape the quantum well. Further developments led to examples of semiconductor quantum wires[39] (1-dimensional confinement) and quantum dots (0-dimensional confinement)[40, 41].

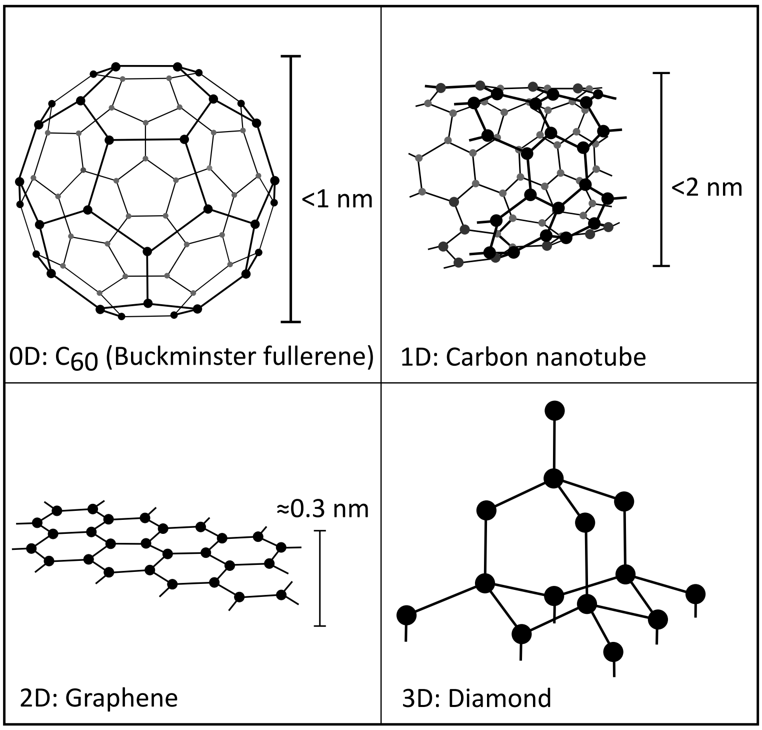


Figure 2.1: Different allotropes of carbon are shown. Diamond can exist with its dimensions on nanometer scale but its crystal structure can extend arbitrarily far in 3 dimensions. The other structures with lower dimensionality always have one or more of their spatial dimensions restricted to nanometer-scale. The Buckminster fullerene is an example of a 0D nanomaterial[a]

[a]The Buckyball figure is based on an image by wikimedia user 'designism' which is published under the Creative Commons 4.0 licence.

Carbon allotropes include examples of materials of each dimensionality, shown in figure 2.1, and they are each used for different applications due to their different properties. Diamond is considered valuable when cut appropriately to scatter light, though also has applications in cutting and drilling because of its mechanical hardness. Additionally, colour centres caused by defects in the diamond lattice are being explored for quantum technologies[42].

The Buckminster fullerene (buckyball), is a ball-shaped arrangement of carbon atoms. Most of its potential applications involve adapting the material in some way, either by functionalising it for nanomedicine[43], or implanting other atoms inside it to make an endohedral fullerene for quantum applications such as a clock transition in $^{14}$N@C$_{60}$[44].

Graphite was left out of the figure as it can be explained in context with graphene, the material relevant to this work. Highly oriented pyrolytic graphite (HOPG) is a precursor crystal from which 2DM graphene is exfoliated. Common applications for graphite are in lubricants and pencils because of its layered structure (see figure 2.2). The layers are easily able to slide over each other and detatch from the bulk because they are only held together with weak van der Waals forces. The layers are each a hexagonal lattice of carbon atoms, with reasonable electrical conductivity in plane, so it is also used in electrodes, for example in electrochemistry. This property is also what makes isolating graphene straightforward using scotch tape.

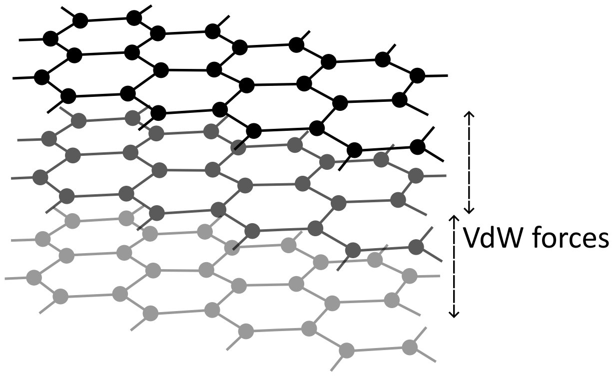


Figure 2.2: Graphite shown as layers of graphene which are held together by van der Waals forces between the layers, indicated by the dashed arrows. Graphite is considered to be in bulk form with 10 or more layers of graphene.

This top-down isolation is in contrast to the bottom-up fabrication methods used for 2D electronic systems in semiconductors. A more detailed diagram of graphene's honeycomb lattice structure is in figure 2.3.

The initial report on the field effect in graphene revealed a new avenue for the scaling down of electronic devices in part due to graphene's nature as a 2DM but also the remarkable results of the electronic characterisation which showed it could support high current densities, ballistic charge carrier transport, and ohmic behaviour [25]. To help explain the behaviour of the graphene-based nanoelectronic devices studied in this work, the electronic properties of graphene will be discussed further.

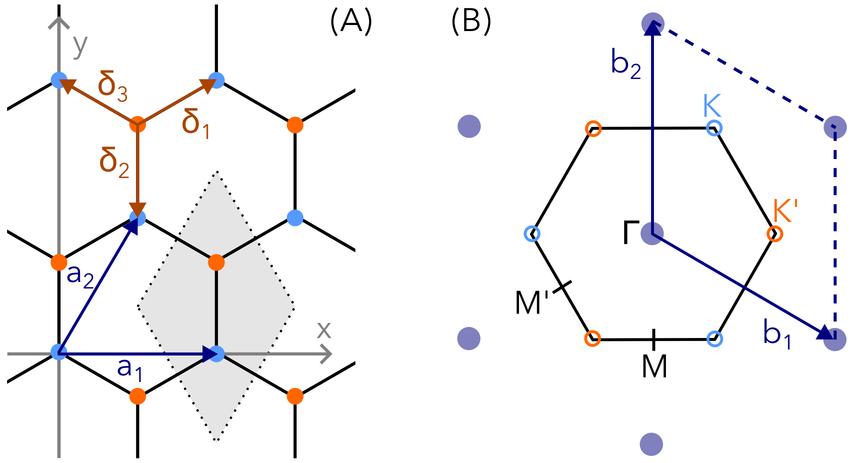


Figure 2.3:

(A) The 'real space' representation of graphene's lattice. It is a hexagonal lattice formed of two triangular sub-lattices, indicated by the blue and orange points respectively. The bond length is $1.42$ Å. The basis vectors for one sublattice are $\vec{a}_1$ and $\vec{a}_2$. The vectors $\delta_{1,2,3}$ represent translations between sublattices. The unit cell contains two carbon atoms, one from each sublattice. The grey shaded area represents the Wigner-Seitz unit cell.

(B) The reciprocal lattice of graphene, with reciprocal lattice vectors $\vec{b}_1$ and $\vec{b}_2$ which define the reciprocal Bravais lattice. The first Brillouin zone (BZ) is constructed by the intersections between the perpendicular bisectors of the reciprocal lattice vectors, and is marked out by the black hexagon. The centre of the BZ is denoted as $\Gamma$. M and M' represent the middle of each edge of the BZ. K and K' are positioned at the vertices of the BZ. K and K' are particularly notable in graphene as the Dirac points where the conical conduction and valence bands meet.

### 2.1.1 Electronic properties

Graphene's electronic properties are described by its electronic band structure, which features 'Dirac points', which have two interesting qualities. Firstly, as the name implies, the charge carriers in this region act as Dirac-like particles[45] because of the linear dispersion curve in the vicinity of the Dirac point. A linear energy-momentum relation is also seen in relativistic massless particles, and experiments have shown that this behaviour is common to charge carriers in graphene due to observations of effects such as half-integer quantum hall effect[46] and Klein tunnelling[47]. Secondly, there is no band gap between the cones of the conductance and valence bands. This puts graphene in the category of a semimetal and is the reason why graphene can be gated to great effect. Shifting the Fermi level through electrostatic gating makes states in the conduction band extremely accessible for electrons to move into. This is illustrated in figure 2.4.

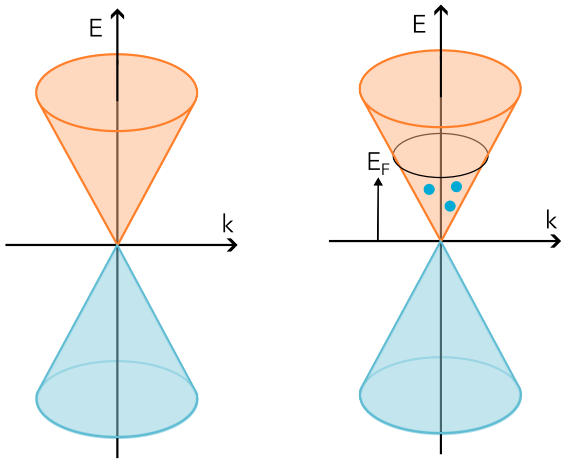


Figure 2.4: The sketches depict the electronic band structure of graphene in the vicinity of the K and K' (Dirac) points. The conduction band (orange, upper cone) and valence band (blue, lower cone) have a distinctive conical shape such that the dispersion relation is linear. This means that the charge carriers in this regime act as if they are massless. Furthermore, there is no band gap, giving graphene the characteristics of a semimetal. The right hand sketch indicates that if the Fermi energy is increased from the midpoint of the bands (for example, through electrostatic gating of the graphene) it is very easy for charge carriers to enter the conduction band from the valence band, as the minimum energy requirement is negligible.

In the original measurements by Geim and Novoselov, the charge carrier concentration in few layer graphene was $10^{13}$ cm$^{-2}$, with mobility of the order $\approx 10^4$ cm$^2$ V$^{-1}$ s$^{-1}$. In 'multi-layer' (about 5 nm thick) graphene the mobility increased from $1.5 \times 10^4$ to $6.0 \times 10^4$ cm$^2$ V$^{-1}$ s$^{-1}$ when cooled from 300 to 4 K[25].

With tuneable properties in-situ, graphene has potential for use in several areas of electronics, including optoelectronics[48] and bolometers[49], superconducting devices[50], qubits[51], and transistors[52]. Some of these applications use graphene JJs of the same style as the devices measured in this thesis, but before they are discussed in any more detail the background of graphene JJs will be covered.

## 2.2 Development of graphene-based Josephson junctions

The aim of this section is to show how the types of devices used in the experimental section have been developed and discuss the theoretical concepts behind them. For context, this means first introducing the Josephson equations and superconductor-insulator-superconductor (SIS) or 'tunnel' junctions. Then most of the section will talk about ballistic SNS JJs, which is an important class of junction that graphene Josephson junctions (GJJs) can belong to.

### 2.2.1 The Josephson effects and tunnel junctions

Superconductors are materials which exhibit zero resistance and expel magnetic fields when below their critical temperature. The microscopic theory developed by Bardeen, Cooper and Schrieffer [53–55] in the 1950s came up with a description of the charge carriers in superconducting materials to explain the dissipationless 'supercurrent' flow. At the low temperatures required to be below the superconducting phase transition, electrons would form Cooper pairs of equal but opposite momentum, and this bosonic bound state would condense into the material's ground state energy. The supercurrent wavefunction $\Psi$ is described by the concentration of superconducting charge carriers $n_s$ and the phase $\varphi$ of the condensate.

$$\Psi = \sqrt{n_s}e^{i\varphi} \tag{2.1}$$

Each of the Cooper pairs in the condensate is bound by an energy defined as $E_g(0) = 2\Delta(T)$, where $\Delta(T)$ is the superconducting energy gap at temperature $T$[1]. Zero resistance is achieved because the condensate moves in a coordinated manner and any single scattering event would not have enough energy to separate one the Cooper pairs from the condensate. The range of the Cooper pairs is described by the coherence length $\xi_0$.

Josephson predicted how the supercurrent would behave if its route along a superconducting wire was interrupted by an insulating tunnel barrier[12, 56] (see figure 2.5 A). This was shortly confirmed experimentally[57] and has since been a Nobel prize-winning prediction supported by a wealth of experimental evidence. The prediction came with two equations which displayed the electronic properties of the supercurrent and the junction. One of these was for the zero-voltage case, and the other was for the finite voltage case.

In the zero-voltage case, supercurrent $I_s$ can flow through the tunnel barrier because of the difference of phase in the superconductor either side of the barrier. The magnitude of the supercurrent is dependent on the difference in phase either side of the barrier $\Delta\varphi$.

$$I_s = I_c \sin(\Delta\varphi) \tag{2.2}$$

The maximum supercurrent supported by the junction is given by the critical current of the junction $I_c$. It should not be confused with the critical current of the superconducting material. This equation is known either as the dc Josephson effect or the current-phase relation (CPR).

The second equation describes how a finite voltage $V$ across the junction is related to the time-evolution of the phase difference. This is the ac Josephson effect or voltage-phase relation, where $\hbar$ is the reduced Plank's constant, $t$ is time, and $e$ is the magnitude of the charge of an electron.

$$\frac{2eV}{\hbar} = \frac{\mathrm{d}(\Delta\varphi)}{\mathrm{d}t} \tag{2.3}$$

The finite voltage means that regular dc current can flow as normal but there is an additional ac supercurrent generated as the phase difference evolves. A related quantity is the Josephson frequency. As the phase difference rotates periodically, the frequency $f$ is found by integrating (2.3) from 0 to $2\pi$, resulting in equation (2.4). Notably, the ac Josephson equation and its frequency contain the magnetic flux quantum $\Phi_0$, an important constant which will be discussed further in section 2.2.4.

$$f = \frac{2eV}{h} = \frac{V}{\Phi_0} \tag{2.4}$$

These are the basic equations which describe the dynamics of the simplest Josephson junctions. This is the case where the CPR is sinusoidal as in equation (2.2), and is best described by the tunnel junctions Josephson initially conceived. This type of junction is called a superconductor-insulator-superconductor (SIS) junction. The superconducting transport through a tunnel barrier is limited by the thickness of the barrier. The superconducting wave function decays exponentially in the insulator, but if the wavefunctions from each side of the junction overlap then the superconducting state can be maintained across the junction.

These junctions are commonly made in a vertical orientation by depositing a superconductor (for example, aluminium), oxidising the surface, and then depositing a second layer of the superconductor[58–60] (see figure 2.5 B). Aluminium SIS junctions are a popular choice for trying to scale up production of superconducting qubits[13, 61].

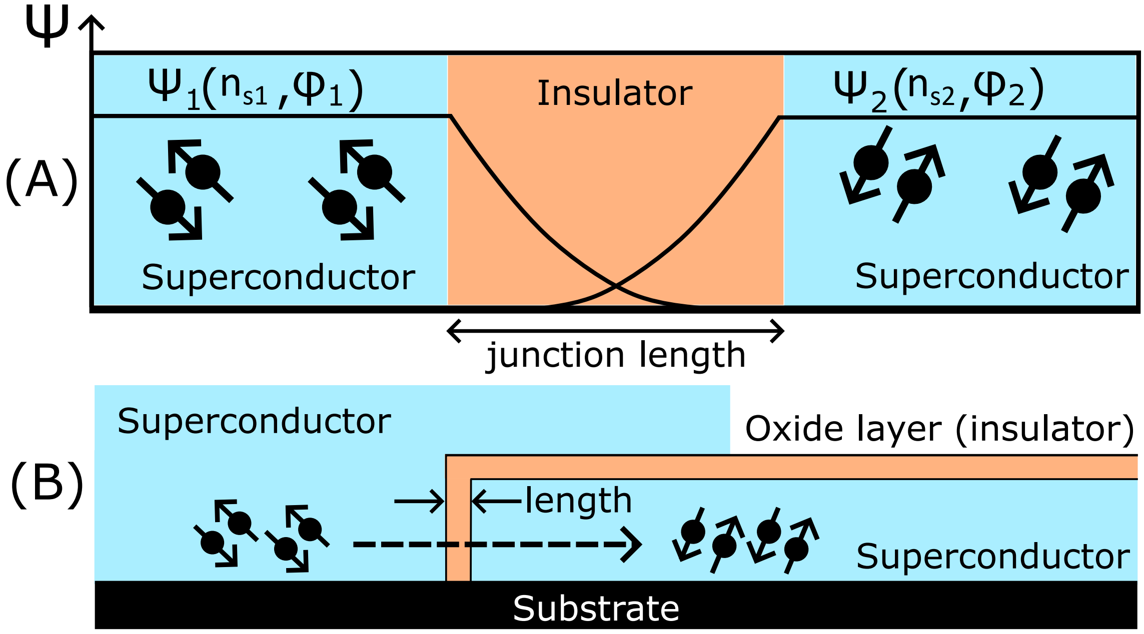


Figure 2.5: Sketches of SIS JJ concepts. (A): Schematic representation of the wavefunctions $\Psi_{1,2}$ in an SIS JJ. The wavefunctions associated with each superconducting electrode have superconducting charge carrier concentrations $n_{s1,s2}$ and phases $\varphi_{1,2}$ respectively. Where the two wavefunctions overlap, Cooper pairs can tunnel through the insulator between the two superconducting electrodes, changing phase. (B): A sketch of a typical SIS junction made by growing an oxide layer (orange) on top of an initial superconducting film (blue) and then the second superconducting electrode is deposited on top. The thickness of the oxide layer in (B) is equivalent to the length of the insulator in (A).

A graphene Josephson junction is a JJ which uses graphene as the weak link between the superconducting electrodes. The usual layout is similar to a superconductor-normal metal-superconductor (SNS) junction, and they behave similarly in terms of their charge transport, even though graphene is a semi-metal. The structure of the devices measured in this work is shown schematically in figure 2.6. The graphene monolayer is encapsulated between two crystals of hBN, forming a van der Waals heterostructure. This can be transferred on top of most typical substrates, in this case silicon is used so that the substrate can also be used as a gate. Contacts to the graphene are made using superconducting NbTi, in such a way as to contact the 1D edge of the graphene and slightly on top, leading to SN interfaces with high transparency (high transmission probability of charge carriers). The significant difference between GJJs and SNS junctions is that the graphene is an 'active' material in the junction, meaning that its properties can be changed in-situ. As described in section 2.1.1, the field effect can be applied to change the charge carrier concentration in the graphene, affecting the properties of the GJJ. Some work has also been done on graphene junctions built vertically like an SIS junction as a way of attaining ballistic transport[62].

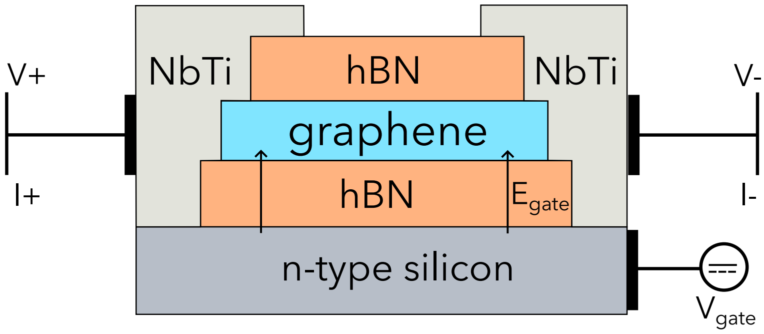


Figure 2.6: Illustration of a graphene junction in an SNS-type configuration. The superconducting electrodes are made of NbTi, and monolayer graphene is the weak link, encapsulated in hBN. The graphene is proximitised, allowing Cooper pairs to be transported between the two superconducting electrodes NbTi electrodes. In a 4-terminal measurement setup one electrode is connected to the positive voltage and current terminals $V+$ and $I+$, and the other electrode is connected to the corresponding negative terminals $V-$ and $I-$. The lower hBN flake acts as a dielectric between the graphene and the Si substrate, which can be used as a gate to apply the field effect to the graphene. A voltage $V_{\text{gate}}$ is applied to the gate to create a field of strength $E_{\text{gate}}$ between the gate and the graphene. The gate voltage can be changed to tune the charge carrier concentration in the graphene.

SNS junctions are usually longer than SIS junctions, because transport through tunnelling necessitates that barriers are thin. This means they more often use alternative mechanisms such as the proximity effect for supercurrent transport. Overall, charge transport depends on the properties of the materials in the junction and the junction geometry, and it is possible to have contributions from different mechanisms.

### 2.2.2 Charge transport in SNS Josephson junctions

In a normal, non-superconducting metal, Cooper pairs cannot form, and supercurrent will not flow. However, supercurrent can flow through a normal metal bounded by superconductors in an SNS Josephson junction. The length that the normal metal section can be to allow Cooper pairs to be transported depends on several factors associated with the properties of the superconductors, the normal metal, and the NS boundaries between them.

Fundamentally it is single electrons which can travel in normal conductors. There are two regimes, which are classified based on the length $L$ of the material the charge carrier is travelling through, and the mean free path $l$ of the material in question. The mean free path is the average distance over which electrons can travel without scattering in the material. This means that, if the mean free path is significantly larger than the length of the conductor, all the electrons can travel without scattering. This is called ‘ballistic’ transport. Alternatively, if the mean free path is shorter, the junction is instead ‘diffusive’ because the electrons interact with the lattice as they move through the material.

Whether the junction is ballistic or diffusive impacts the description of the junction’s conductivity. In the ballistic case, conductivity is quantised based on the area of the junction, which determines how many superconducting channels can be supported, each with conductivity equal to the conductance quantum $2e^2/h$, where $h$ is Plank's constant. However, resistance of the wider system is determined at the interface in and out of the ballistic conductor. Incoming charge carriers are either transported through the interface, or are reflected. This is the transmission probability or 'transparency' of the interface. In the diffusive regime, the rate of current transport is instead scaled by a diffusion constant $D$ which is characteristic of the material.

Graphene can be in either the diffusive[63] or ballistic[64] regime, depending on the disorder in the material, doping, or geometry. Large amounts of disorder create locations where scattering is likely, compared to pristine graphene. In either case, we can observe the transmission of supercurrent in SNS junctions. A junction being ballistic or diffusive does not independently explain how the supercurrent transport is possible, though they can influence the properties of the junction.

The proximity effect is the term commonly used to describe how supercurrent is supported in SNS junctions. It broadly describes how superconductivity 'leaks' from the superconductor into the normal metal, over a length determined by the superconductor's coherence length $\xi_0$, which is defined in terms of the Fermi velocity $v_F$ and the superconducting energy gap $\Delta$.

$$\xi_0 = \frac{\hbar v_F}{\pi \Delta} \tag{2.5}$$

Andreev reflection is the mechanism underpinning the proximity effect, occurring in both ballistic and diffusive SNS junctions[63, 65–67]. Andreev reflection occurs at NS interfaces and indeed GS interfaces. The basic principle of Andreev reflection is that an electron with energy below the superconducting gap incident on the NS boundary is retroreflected as a hole, and a Cooper pair is generated in the superconductor. The $2e$ charge created in the superconductor is balanced by the charge of the incoming electron and the oppositely charged hole moving in the opposite direction. Multiple Andreev reflection (MAR) is the process through which an electron reflects from each NS boundary either end of the junction repeatedly, accumulating enough energy to access a state in the opposite superconductor's conduction band[68]. This is illustrated in figure 2.7. In graphene, as well as retroreflection, electrons can also undergo specular reflection, where the hole does not travel back along the same path that the incident electron came from[69–71].

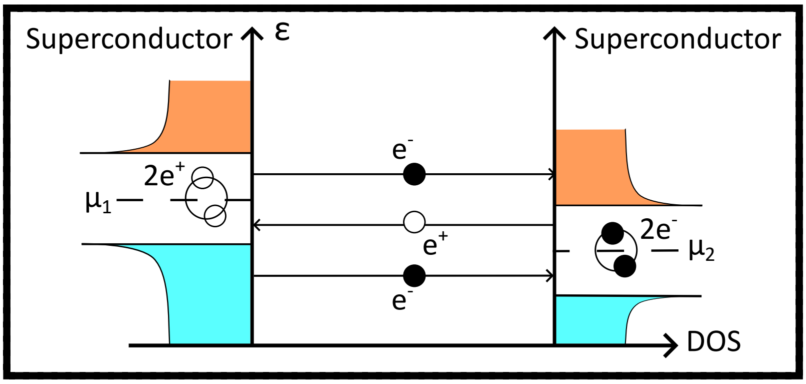


Figure 2.7: Illustration of multiple Andreev reflection. An electron can only move from the valence band of one superconductor to the conduction band of another superconductor by reflecting at the link-superconductor boundary as a hole, creating a cooper pair in the superconductor as a result. The produced hole may also reflect at the opposite boundary, creating a hole pair in the other superconductor. More than one reflection may be required for the electron to have sufficient energy to enter the conduction band of the superconductor. The net effect is that an effective $2e$ charge is transmitted across the junction as supercurrent.

Andreev reflection is the mechanism which facilitates the transport of superconducting charge carriers in SNS junctions, but whether or not the charge transport can occur depends on the energy scales involved in the system. These are related to the critical current of the junction, which is an upper limit on the current that can be transported without breaking superconductivity. The Thouless energy is an energy scale related to the transit time in diffusive and ballistic conductors, and is also applied to SNS Josephson junctions[72]. In diffusive junctions, the Thouless energy takes the form

$$E_{\mathrm{Th}} = \frac{\hbar}{\tau_c} = \frac{\hbar D}{L^2} \tag{2.6}$$

where $\tau_c$ is the diffusion time, $D$ is the diffusion constant and $L$ is the length of the conductor. In a ballistic conductor, it is described in terms of the Fermi velocity $v_F$ instead:

$$E_{\mathrm{Th}} = \frac{\hbar v_F}{L}. \tag{2.7}$$

For SNS junctions, the Thouless energy has significance in context with the superconducting energy gap $\Delta$. While $\Delta$ determines some of the properties of the Cooper pairs, $E_{\mathrm{Th}}$ governs the individual charge carriers. The overall determination of the coupling energy between superconducting electrodes over a normal conducting gap is defined by the smaller of the Thouless energy or the superconducting energy gap. This leads to the Thouless energy limiting the critical current in diffusive junctions, while the superconducting energy gap sets the limit in ballistic junctions. The consequence of this in graphene Josephson junctions is that when the graphene is weakly doped, electrons with energy below the Thouless energy can undergo multiple Andreev reflection when the junction is in its finite voltage regime, leading to oscillations representing the Andreev states.

Early GJJs worked on the principle of the proximity effect over short distances, with the earliest practical devices from Heersche et al.[35] featuring electrode separations of 100-500 nm. In this case, aluminium was the superconducting contact which has a long coherence length greater than 1 μm. Therefore the whole junction was able to be proximitised. They showed that changing the charge carrier concentration of the graphene through electrostatic gating affected the critical current of the device (figure 2.8).

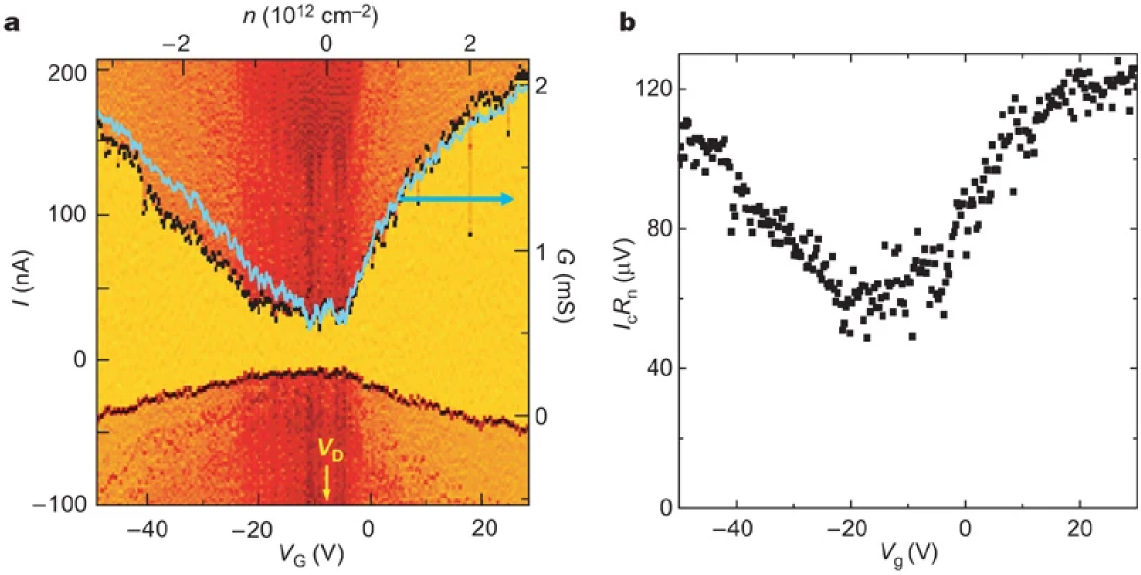


Figure 2.8: (a) Dependence of the differential resistance of a graphene Josephson junction (indicated by the colour scale where yellow is 0) on the bias current and charge carrier concentration/gate voltage. The blue line is the normal state conductance. (b) Dependence of the characteristic voltage of the JJ on the gate voltage. Reproduced from [35] with permission from Springer Nature.

Additionally, oscillations were observed in the differential resistance for currents above $I_c$, showing evidence of multiple Andreev reflection. From this point, the focus of development for GJJs became on producing higher quality ballistic junctions.

The transmission probability of the boundary between the superconductor and graphene is an important parameter in a ballistic SGS junction. A significant development leading to extremely transparent junctions was the realisation of a one-dimensional contact between a graphene monolayer and the superconducting electrode. Wang et al.[73] etched a stack of monolayer graphene encapsulated in hBN to expose the edge of the graphene before metallisation. This meant that electrical contact was made only along the one-dimensional edge of the graphene, rather than being deposited on top of the two-dimensional surface which was the previous approach being taken (figure 2.9A shows the new process). This was very significant because as well as giving a very low resistance contact of $\approx 100\ \Omega$ and high mobility at room temperature, it presented a new approach to fabrication using 2DM. They were able to create the 2DM stack separately from the metallisation process, whereas previously the graphene would have been transferred using a polymer and then left exposed for metallisation before the top hBN flake was transferred[64].

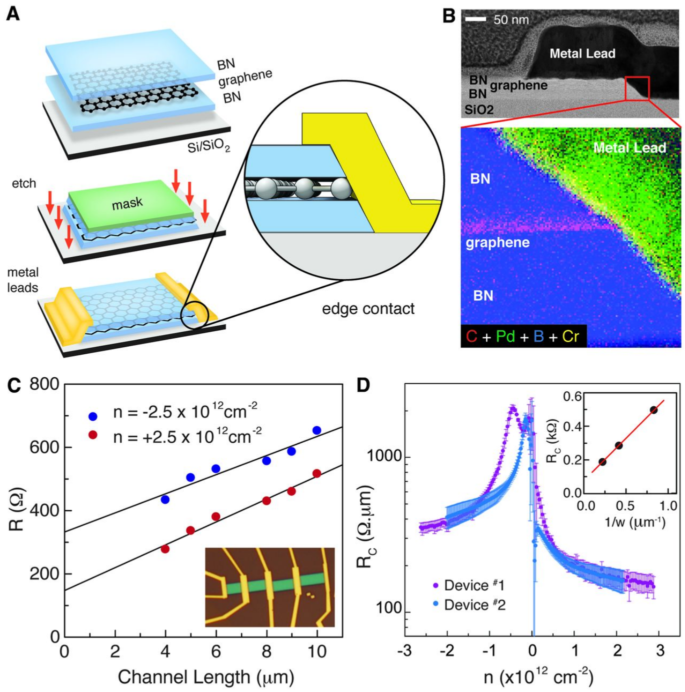


Figure 2.9: (A) Fabrication of edge-contacts to encapsulated graphene. (B) Scanning tunnelling electron microscopy (STEM) image of the contact geometry, and a false colour electron energy-loss spectroscopy (EELS) which expands on the junction interface region to show the 1D contact between graphene and the metal. (C) Two-terminal resistance measurements of the junction against its width. (D) Dependence of contact resistance on charge carrier density. From [73]. Reprinted with permission from AAAS.

The next development was by Moshe Ben Shalom in which the etching of the hBN/Gr/hBN stack was adjusted so that part of the top of the graphene monolayer was also exposed[74] as shown in figure 2.10. Metallisation on this structure led to an even lower resistance junction of $\approx 50\ \Omega$.

There are many further examples of ballistic GJJs. The majority of recent devices are based on exfoliated graphene encapsulated in hBN with various superconducting contact materials including Nb[75] or NbTiN[50], and MoRe[76]. Additionally, Li et al. made ballistic GJJs from CVD graphene, with the possibility of mass production in mind for their fabrication process.[77].

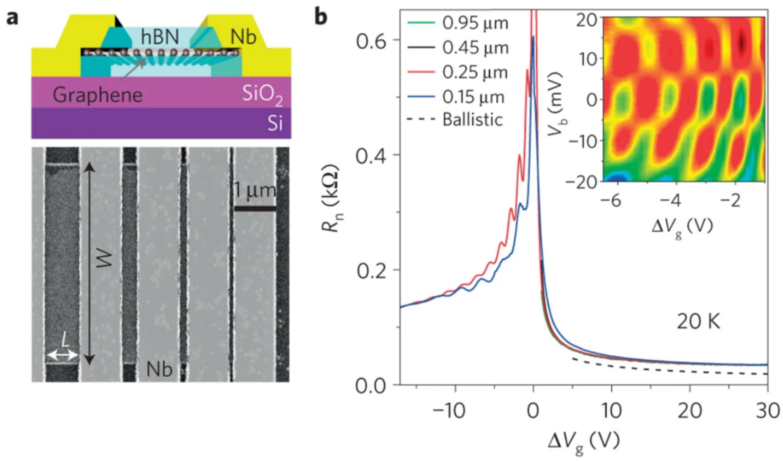


Figure 2.10: (a) Schematic of the junctions showing how the metal contact is both on the 1D edge and on top of the graphene. Below that is an electron microscope image of four junctions with different lengths, but the same width of 5 µm. (b) Resistance against gate voltage for each of the different length junctions. The sharp peak at $\Delta V_{\mathrm{g}} = 0$ V shows the charge neutrality point. The dashed 'ballistic' curve is the theoretically calculated resistance in the quantum ballistic limit as a function of the charge carrier density. The inset colourplot shows a map of the differential conductance for the 0.25 µm long junction. The colour scale ranges from -1 to 1 mS (red to blue). Reproduced from [74] with permission from Springer Nature.

Having established that GJJs are now able to be consistently produced in the ballistic charge transport regime, their properties can be assessed in more detail in comparison with ballistic SNS junctions. The main property of interest for this work is the current-phase relation.

### 2.2.3 Variations in the current-phase relation

The current-phase relation is a periodic function which describes how the supercurrent passing through a Josephson junction depends on the phase difference across the junction. In an ideal JJ the CPR is sinusoidal with phase as shown by the dc Josephson effect given in equation (2.2). This sets a limit on the values of supercurrent that can be supported by a Josephson junction, with a minimum of zero and a maximum equal to the critical current of the JJ. If the phase of each individual electrode can be somewhere between $0$ and $2\pi$, the maximum phase difference in the junction would be $\pi$, which is equivalent to $0$ because of the periodicity of the system. So the minimum $I_s$ (no supercurrent) occurs when both sides of the JJ have the same phase. This implies that supercurrent can only flow if there is some phase difference, with the maxima occurring at $\pi/2$, midway between the minima.

This is the behaviour in the ideal junction, but there are many JJ systems where the CPR is different, usually skewed away from the sinusoidal shape such that the maximum and minimum points no longer align with integer multiples of $\pi/2$. This is one of the main differences which is observed when measuring ballistic SNS JJs.

One model to reflect this is based on the 'transparency' $T_n$ of the junctions, describing the transmission probability of superconducting particles across a normal-superconducting boundary. Specifically this is for multiple channels of ballistic transport across a Josephson junction[78], where $e$ is the electron charge, $\Delta_0$ is the superconducting energy gap, $N$ is the number of ballistic transport channels, $k_B$ is the Boltzmann constant, $T$ is the temperature, and $\gamma$ is the phase difference.

$$I_s = \frac{e\Delta_0}{2\hbar} \sum_{p=1}^{N} \frac{T_n \sin\gamma}{\sqrt{(1 - T_n \sin^2(\gamma/2))}} \tanh\left(\frac{\Delta_0}{2k_B T}\sqrt{(1 - T_n \sin^2(\gamma/2))}\right) \tag{2.8}$$

The transparency term affects equation (2.8) in two ways. Firstly, it determines the amplitude of the supercurrent. The greater the transparency, the more charge carriers are being transmitted across the junction, and so the supercurrent increases. Secondly, it controls the phase at which the maximum supercurrent is found, due to the $\gamma/2$ term in the denominator. The shift in phase maximum is what determines the skew of the CPR. Physically, this is related to the Andreev bound states and scattering states in the SNS junction. The fewer backscattering events occurring at the interfaces (i.e. more transparent interfaces) the more skewed the CPR becomes, with Andreev states having more influence over the total supercurrent[79, 80]. There is a discontinuity at $T_n = 1$ as the denominator approaches 0. On the other hand, as $T_n \to 0$ the denominator approaches 1 and so the supercurrent returns to the sinusoidal dependence on phase controlled by the numerator.

Equation (2.9) is a phase-dependent approximation which is valid at low temperature as the hyperbolic tangent function will be approximately 1 when $\Delta_0 \gg k_B T$. This will be used in the simulation chapter 3. Comparing the approximation (2.9) to the CPR component of the full equation 2.8 at different temperatures is shown in figure 2.11. It shows that at low temperatures substantially below $T_c$ (when the superconducting gap $\Delta_0$ is assumed to be similar to that of niobium, the order of 1 meV) the approximation matches the full equation well at both low and high values of $T_n$. In the approximated model, the plots will be in the same place each time as they lack a temperature dependence. At an intermediate temperature, the sinusoidal case still holds well, but the skewed model has started to retreat, but not by a huge amount. Once at temperatures comparable with the critical temperature of Nb, the skewed model has retreated significantly, almost perfectly matching the sinusoidal case. This confirms that low-temperatures should be assumed for any work involving the approximated equation, such as in the later simulations, though the exact temperature at which the model no longer holds has not been determined precisely, and some use could be justified up to around 1 K where the difference between models is not large.

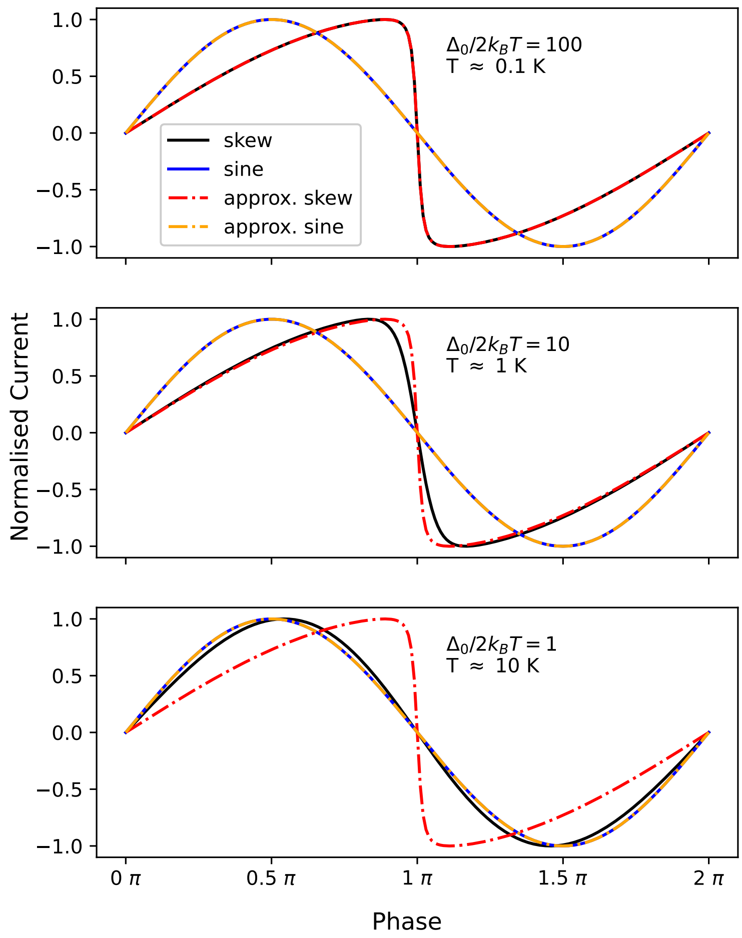


Figure 2.11: Plots comparing the appearance of the full skewed CPR equation (2.8) to the approximation (2.9) roughly corresponding to temperatures of 0.1, 1, and 10 K. Plots labelled 'skew' have $T_n = 0.999$, and plots labelled 'sine' have $T_n = 0.001$. The plots show that the approximate equation (2.9) breaks down for high skewness at high temperature.

$$CPR = \frac{T_n \sin(\gamma)}{\sqrt{(1 - T_n \sin^2(\gamma/2))}} \tag{2.9}$$

In junctions with very low transparency the denominator of the equation will tend to 1, reducing the relation back to the sinusoidal form of the ideal junction CPR. On the other hand, high $T_n$ junctions are quite heavily skewed, corresponding to ballistic transport. At perfect $T_n = 1$ in the limit of 0 temperature, the CPR becomes sawtooth in shape due to the transport being exclusively determined by Andreev bound states[79]. Different levels of skewed CPRs due to transmission probability are shown in figure 2.12. A significant review of CPRs in different JJ systems was written by Golubov[81].

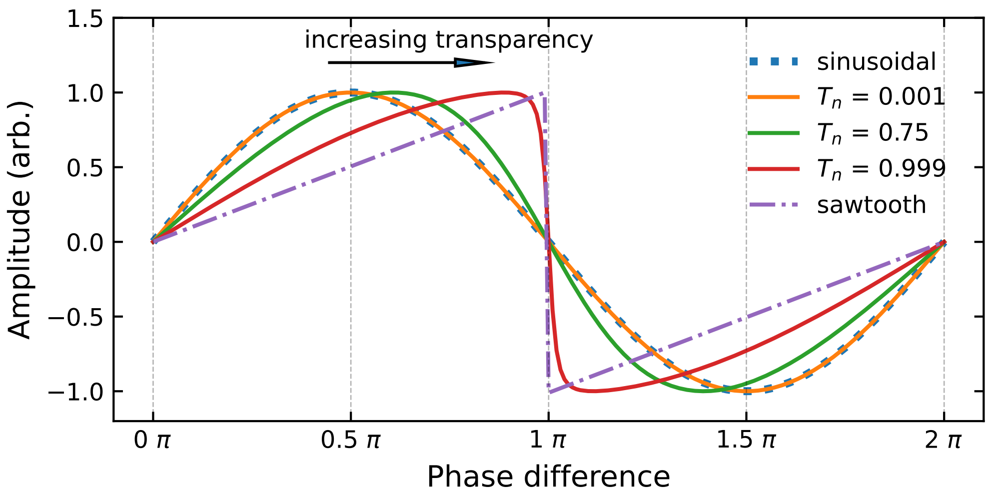


Figure 2.12: Plots of different CPR functions, where $T_n$ are transparencies used for a skewed CPR (equation (2.9)). Each curve is normalised to its maximum amplitude. The maximum moves from $\pi/2$ towards $\pi$ as the skewness increases. All plots pass through 0 amplitude at integer values of $\pi$ phase difference. The negative amplitude current implies that which electrode has the larger phase has switched such that the supercurrent travels in the opposite direction. When the junction is current biased in one direction, only the values in one half of the graph are accessed (based on the convention taken for the current direction). The sawtooth function is due to perfect transparency characterised by the discontinuity at $T_n = 1$.

The work by Nanda et al. [37] at Delft University of Technology investigates this idea in GJJs and SQUIDs, confirming the change in CPR with changing transparency of the JJ. The significance of the work by the Delft group is that by gating each junction independently they could make the SQUID asymmetric and extract the CPR directly to characterise the skewness $S$. The skewness was defined as

$$S = \left(\frac{2\phi_{\text{max}}}{\pi}\right) - 1 \tag{2.10}$$

where $\phi_{\text{max}}$ is the phase at which the supercurrent is maximised. This gives the position of the maximum on a scale between 0 when the CPR is unskewed (sinusoidal), and 1 when the maximum current is fully skewed to $\pi$ on the phase axis. The effect of temperature on the CPR was also investigated, as shown in 2.13. The contribution to the supercurrent by Andreev bound states is suppressed at higher temperatures [82].

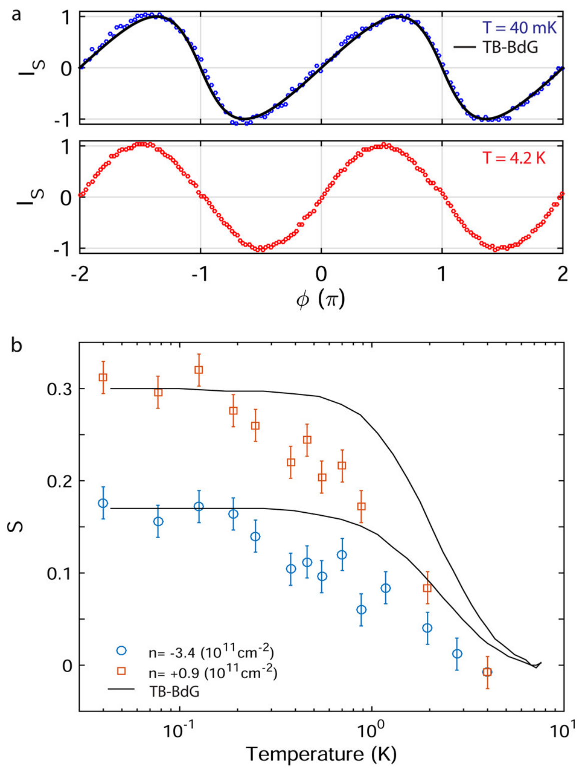


Figure 2.13: (a): Shows the current-phase relation of the left junction which is biased at 1 V, slightly above charge neutrality of 0 V. The plots are of how the supercurrent depends on phase difference. It is shown at 40 mK and 4.2 K. The low temperature CPR is clearly skewed while the room temperature CPR appears unskewed. (b): The skewness $S$ of the CPR against temperature at different charge carrier concentrations. Negative charge carrier concentrations are skewed less than positive charge carrier concentrations, and the skewness reduces with temperature. The black lines in both plots are the results of tight-binding model calculations. Reproduced without modification from [37], which is published under a Creative Commons Non-Commercial No Derivative Works (CC-BY-NC-ND) Attribution License. © 2017 American Chemical Society. ACS disclaims all warranties with respect to the article except that it is entitled to grant the license agreement described.

This is consistent with the effect of the model which will be used in the simulations. The full model has often been included in consideration of ballistic JJs including GJJs[36, 62, 83]. This gives confidence that devices used in this investigation will share the properties of the other devices, and that they will display the behaviour expected by the presumed CPR.

### 2.2.4 SQUIDs

Superconducting quantum interference devices (SQUIDs) are loops of superconducting material broken by Josephson junctions. They are extremely sensitive to magnetic fields, so many of their applications are as magnetometers or gradiometers. The devices are capable of detecting magnetic fields produced by living creatures, leading to their use in biomedicine measuring heart and brain activity[84, 85]. They are also used in materials science, by constructing the SQUID on the tip of a probe akin to atomic force microscopy, or placing samples of interest inside a SQUID loop[86].

In this section some of the devices which were initially invented around the same time as the dc SQUID will be described. Then, the behaviour of JJs and SQUIDs in magnetic fields will be discussed, because that behaviour is intrinsic to the devices' sensitivity to magnetic fields. Then, the main parameters describing SQUID electronics and performance will be shown. Finally, some examples of the most current SQUIDs being researched that are not graphene-based will be given. 3 will go into more detail about how dc SQUIDs work using a mathematical description of the resistively and capacitively shunted junction (RCSJ) model for a numerical simulation.

### SQUID history

SQUIDs have been researched since the 1960s[87]. There are two varieties, shown schematically in figure 2.14: RF SQUIDs where one side of the loop contains a JJ, and dc SQUIDs, where both sides contain a JJ. The first publication concerning the RF SQUID was the work of A H Silver and J E Zimmerman published in 1967 [88]. In the RF SQUID, the voltage is measured across the tank circuit, and would be periodic with applied magnetic flux through the superconducting loop as long as the RF current applied to the tank circuit was kept constant. As it only contained one JJ, the RF SQUID was easier to fabricate, but it is less sensitive than the dc SQUID.

Another early device related to the invention of JJs and SQUIDs was the Superconducting low-inductance undulatory galvanometer (SLUG). SLUGs were made by forming a JJ between Sn-Pb solder and Nb wire, with the oxidation layer of the Nb acting as the insulating barrier. This device was able to measure voltage with a resolution on the order of fV[89].

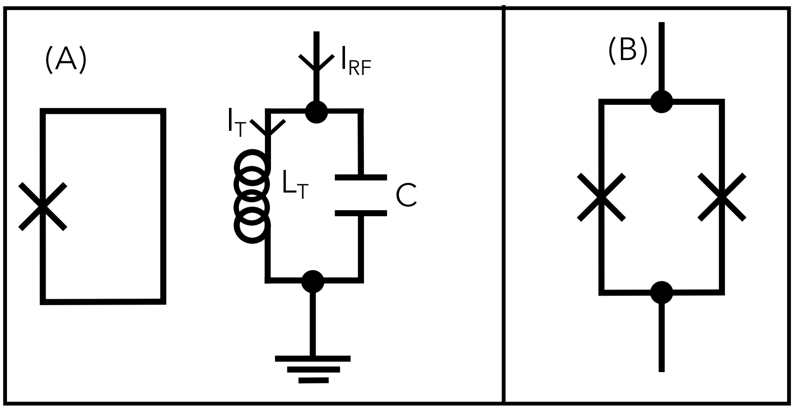


Figure 2.14: (A) Circuit diagram of an RF SQUID. The SQUID loop is on the left side with one JJ on one side of the superconducting loop. To the right is the tank circuit where an RF current is driven through an inductor to couple with the superconducting loop. (B) Circuit diagram of a dc SQUID, where both sides of the loop contain a JJ.

### Flux quantisation and the effects of magnetic fields on Josephson junctions

The discussion of Josephson junctions so far has been focused on the current-phase relation. Part of the CPR is the phase difference $\Delta\varphi$, which is important to reconsider in the context of magnetic fields.

The descriptions given here are brief, for a more fully-derived explanation see references [1, 90]. Firstly, $\Delta\varphi$ cannot generally be used to determine the supercurrent $I_s$ as described by (2.2). This is because $I_s$ is a gauge-invariant quantity, while $\Delta\varphi$ is not. It is necessary to replace $\Delta\varphi$ with an alternative gauge-invariant phase difference $\gamma$[1]:

$$\gamma \equiv \Delta\varphi - (2\pi/\Phi_0) \int \vec{A} \cdot d\vec{s} \tag{2.11}$$

where $\vec{A}$ is the vector potential and $d\vec{s}$ is the vector line differential. Having introduced $\vec{A}$ allows the effects of the magnetic field to be assessed. In the case of no magnetic field, $\vec{A} = 0$, allowing the simple substitution of $\Delta\varphi = \gamma$ giving

$$I_s = I_c \sin(\gamma) \tag{2.12}$$

With this mention of phase-invariance in place, the effects of magnetic fields can be discussed, starting with flux quantisation. The concept of flux quantisation is integral to describing the behaviour of Josephson junctions and SQUIDs. The constant value of the magnetic flux quantum $\Phi_0 = h/2e$ appears in several places in the theory surrounding superconductors and superconducting devices, coming from how magnetic fields behave inside superconducting rings. Starting with a ring which is above its critical temperature, a magnetic field is applied parallel to the ring's axis (figure 2.15a). If the superconductor is then cooled below $T_c$ the Meissner effect will take hold and expel any field lines from inside the superconducting ring (figure 2.15b). Field lines are still able to pass around the ring on the inside or outside. Then the field is removed, but the flux that was passing through the hole of the ring is trapped, as a persistent supercurrent has been generated inside the superconductor (figure 2.15c). Quantifying the amount of flux around the ring is done by integrating the vector potential of the field over a line contour around the centre of the ring. Doing so corresponds to a full rotation around the superconducting ring, and because the superconducting wavefunction is gauge-invariant it has the same value at the start and end. So the phase part of the wavefunction has simply precessed by $2\pi$ in one rotation. This adds an extra $2\pi$ per rotation $n$ to the phase, so the flux becomes

$$\Phi = n\frac{2\pi\hbar}{2e} \tag{2.13}$$

where the flux quantum $\Phi_0 = h/2e$, so

$$\Phi = n\Phi_0 \tag{2.14}$$

shows that the flux in the loop is quantised.

The first appearance of flux quantisation was in mixed-state type-II superconductors, where the penetrating flux is arranged into a triangular array of supercurrent vortices[91]. Each tube is bounded by circulating supercurrent corresponding to an amount of flux equal to the magnetic flux quantum that is allowed to penetrate. In the interior where the flux penetrates, there are no superconducting charge carriers so the material is resistive. The tubes form in energetically favourable locations, so defects in the material can pin the vortices in place so that the triangular array is not entirely consistent across the superconductor. These pinning sites which are almost always present in real materials hold the flux vortices in place so that they are not moved by nearby current flow inducing a Lorentz force and thereby a resistance. This means that supercurrent can usually still flow while the superconductor is in the mixed state. It is possible to engineer pinning sites when designing devices so that these disrupted areas are kept away from the functional part of the device. In the ac Josephson effect (2.2), $\Phi_0$ is part of the definition the Josephson frequency (the frequency of the alternating current generated by the evolution of the JJ's phase difference). The Josephson frequency (2.4) is proportional to the voltage across the junction and determines the energy change of a Cooper pair moving across the junction.

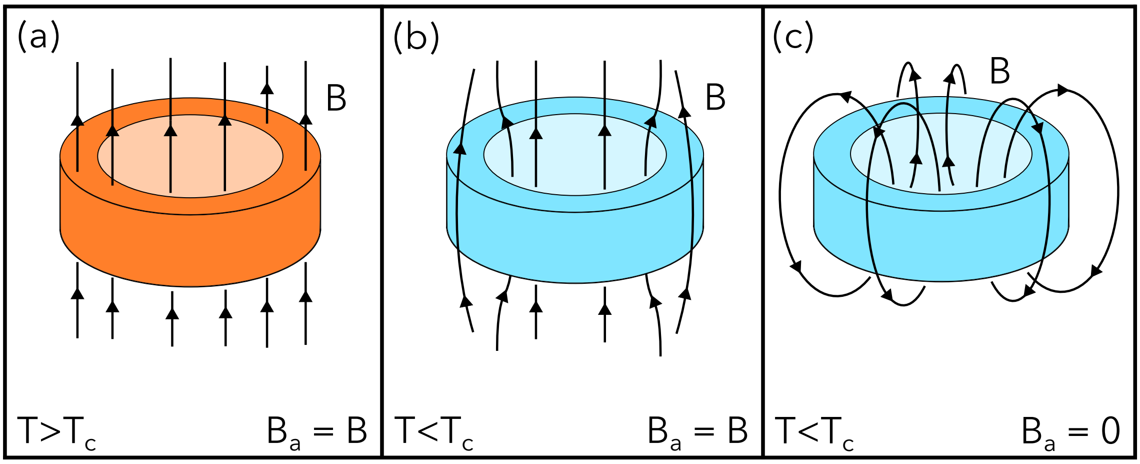


Figure 2.15: Illustration of the behaviour of magnetic flux inside a superconducting ring. The three frames should be considered in sequence. In (a) the ring is above its transition temperature, so the applied magnetic field $B_a$ passes through the material normally. In (b) the superconductor has been cooled to below its transition temperature, so all the magnetic field lines are deflected either through the ring hole, or outside the ring. In (c), the applied magnetic field has been removed, but the magnetic field has been sustained by a persistent current circulating in the ring.

Following flux quantisation, the effect of magnetic flux on JJs and SQUIDs will now be considered. Both cases are examples of quantum interference effects. The magnetic flux in the junction affects the phase such that the maximum flux-dependent critical current $I_J$ becomes defined by an equation analogous to the Fraunhofer pattern produced by single-slit interference:

$$I_J = I_0 \left| \frac{\sin\left(\pi \frac{\Phi_J}{\Phi_0}\right)}{\pi \frac{\Phi_J}{\Phi_0}} \right| \tag{2.15}$$

where $I_0$ is the maximum critical current at 0 magnetic field. This constitutes a tall peak at $\Phi_J/\Phi_0 = 0$, then oscillations with peaks at much lower values (the first at close to $0.2 I_0$)) that subsequently get smaller. The minima between peaks are located at integer values of $\Phi_J/\Phi_0$.

Following the 'single-slit' case, SQUIDs are analogous to the 'double-slit' case. In the case of a symmetrical SQUID, the critical current $I_m$ is shown to vary in a cosine manner:

$$I_m = 2I_c \left| \cos\left(\frac{\Phi_J}{\Phi_0}\right) \right| \tag{2.16}$$

where $I_c$ is the maximum critical current of the junctions in the SQUID. The oscillations this time are at the same height, with maxima at integer values of $\Phi_J/\Phi_0$, and minima and half-integer values.

SQUIDs can show both types of interference effects, visible on different scales. For a relatively large applied field, the Fraunhofer-like interference pattern is visible, but at higher resolution, smaller flux oscillations can be seen following the path of the interference pattern. To get the maximum critical current the applied field needs to place the device at the peak of the central Fraunhofer, and then also at the top of a more localised oscillation. If away from the centre of the interference pattern the flux oscillations on the local scale will appear to be sloping. Equations (2.15) and (2.16) are plotted in figure 2.16. The flux oscillations will be discussed further in a more practical sense in the next section.

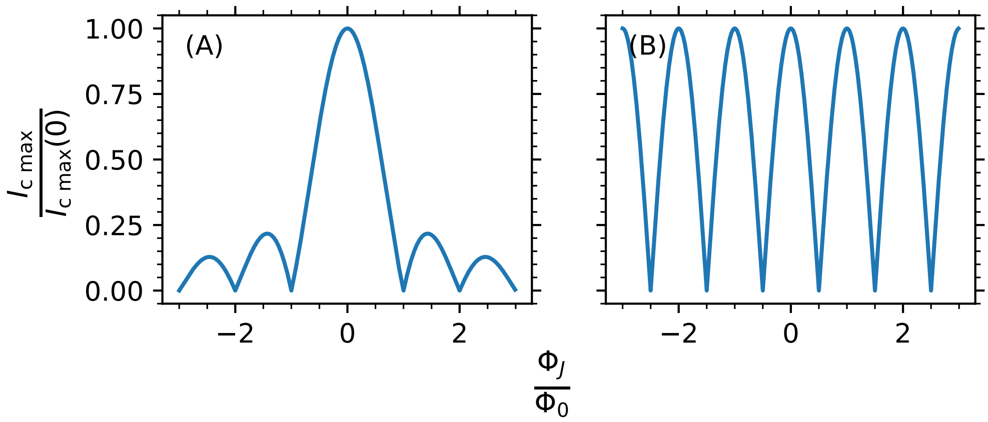


Figure 2.16: Plot of the dependence of the normalised maximum critical current against the ratio of applied magnetic flux to the magnetic flux quantum, in a single JJ configuration (A), and a dc SQUID configuration (B).

#### Oscillation of the critical current of the SQUID

Flux oscillations are a behaviour in dc SQUIDs where the critical current oscillates periodically as a function of the magnetic flux enclosed in the SQUID loop. The oscillation period in terms of magnetic field is equal to the magnetic flux quantum. In other words, each period seen corresponds to an additional quantum of magnetic flux passing through the loop. In the experimental measurements, a superconducting magnet is used to apply a vertical magnetic field perpendicular to the SQUID loop, so that the magnetic flux is straightforward to quantify.

When the amount of flux in the SQUID loop changes it influences the phase difference of the Josephson junctions, which itself impacts the critical current of the SQUID. This is because the SQUID loop has an inductance and this causes a circulating current to be induced in the SQUID loop. This current effectively adds to one junction and takes away from the other as it passes through them in opposite directions. The maximum critical current occurs when there is an integer value of flux quanta inside the loop, and the minimum is when there is half-integer flux quanta[1]. Experimentally it can be difficult to guarantee that any given SQUID is perfectly symmetrical or particularly that both junctions have the same critical current. The cause of asymmetry in the critical current can be related to fabrication if the junctions are not made uniformly, but may also be because of residual charge trapped on the device which is highly unlikely to affect both junctions equally.

Critical current asymmetry can be compensated for in devices where both junctions are independently tuneable [75] though this is not seen often due to added complication for fabrication and the reduced possibility for scaling production in more complex device designs. In a two-junction device, both junctions would require their own gates to be tuned separately. This increases the number of fabrication steps needed, which increases the chance of failed devices. Additionally, each additional contact requires its own wiring and power supply, which will eventually mean that feasible devices are constrained by the electronics in the experimental setup and cooling power of the refrigerator when more complex devices are required. These types of devices are also useful because instead of making the device symmetrical they can also force it to be highly asymmetrical, allowing junctions to be measured independently [37].

To ensure that the oscillation period of the SQUID is behaving as expected it is useful to reframe the applied magnetic field to be in terms of the flux quantum. Therefore it is necessary to know the coil constant of the magnet $k$ (where $k$ has dimensions of current per field strength) to obtain the applied magnetic field. The flux through the loop is the product of the field $B_a$ and the effective loop area $A_{\text{eff}}$. Finally, the applied flux can be divided by the flux quantum to 'count' the individual flux quanta. This conversion is summarised in equation (2.17).

$$\frac{\Phi}{\Phi_0} = \frac{BA}{\Phi_0} = \frac{kI_m A_{\text{eff}}}{\Phi_0} \tag{2.17}$$

An effective loop area is used because the superconducting wires expel flux and therefore adjust its path. This means that there is more flux passing through the SQUID loop than just the internal area of the loop would suggest for a uniform field. Roughly it is expected that half of the flux incident on the wires is directed into the loop and half is directed out of the loop. This allows an estimation of $A_{\text{eff}}$ to be calculated to try and verify the period of the flux oscillations.

This can be approached from the opposite angle as well. If the period of the oscillations is measured and assumed to match the integer flux quantum, the effective area can be reverse engineered. If there is reasonable agreement between the two values then that provides satisfactory confirmation that the SQUID is behaving as expected.

#### SQUID parameters and optimisation

SQUIDs are described by a set of parameters tying together their electronic characteristics. These lead to figures of merit which determine the SQUID's performance and noise characteristics. The noise produced by a SQUID is important because SQUIDs are often intended for use as extremely sensitive magnetometers, and the noise would put a limit on the resolution achievable in a given device.

Electronically, SQUIDs can be generally described by their Stewart-McCumber parameter $\beta_C$ and their screening parameter $\beta_L$ which include the electronic properties of the SQUID, with the former containing the capacitance $C$ while the latter contains the inductance $L$. Both also include the normal state resistance $R$ and the critical current of the junctions $I_c$. As $\beta_C$ and $\beta_L$ define the SQUID properties, they inherently affect the figures of merit and noise, so they will be discussed first.

The Stewart-McCumber parameter $\beta_C$ is associated with the Josephson junctions in the SQUID. It is linearly dependent on $I_c$ and $C$, and quadratically dependent on $R$, as shown in equation (2.18). In a symmetrical SQUID, both junctions have the same value of $\beta_C$.

$$\beta_C = \frac{2\pi I_c R^2 C}{\Phi_0} \tag{2.18}$$

This property is related to damping in the JJ, which affects the observation of hysteresis its IV curve. In the overdamped case where $\beta_C \leq 1$, sweeping the bias current up from the superconducting region to above $I_c$ and then back down again will have the superconducting phase transition at $I_c$ each time. However, if the JJ is underdamped such that $\beta_C > 1$, on the returning sweep the transition back to superconducting will occur at a retrapping current $I_r$ less than the critical current[1]. This concept is important in practical devices for SFQ logic, which requires that JJs are overdamped to avoid 'latching logic'[15]. The capacitance of the junction is more complex to determine in SNS JJs than just the geometric capacitance defined by the junction electrodes, which is much smaller than in SIS tunnel junctions. It is likely that SNS and gated junctions have additional sources of capacitance from their substrates and measurement wires. To create a junction with a desired $\beta_C$, each of the electronic parameters need to be considered. It difficult to calculate the capacitance of the junction precisely for the reasons mentioned, but it should be possible to engineer $I_c$ through a combination of the design of the device geometry and the material choices. In tuneable junctions such as GJJs, $I_c$ can be further controlled over a range which could allow for moving between the overdamped and underdamped states. The resistance will also depend on the charge transfer mechanisms occuring in the junction.

The second parameter is the screening parameter $\beta_L$ which is a function of the SQUID inductance.

$$\beta_L = \frac{2LI_c}{\Phi_0} \tag{2.19}$$

An appropriate value of the screening parameter $\beta_L \leq 1$ is needed to avoid magnetic hysteresis. The screening parameter affects the ratio of the maxima and minima in flux oscillations[92]. In low $\beta_L$ SQUID loops the oscillations become very deep, while they are shallower when $\beta_L$ is high. This can be defined as the modulation depth $I_d$

$$I_d = \frac{I_{c\ \max} - I_{c\ \min}}{I_{c\ \max}} \tag{2.20}$$

where $I_{\mathsf{c\ max}}$ and $I_{\mathsf{c\ min}}$ are the maximum and minimum critical current values respectively, due to the oscillation of magnetic flux. The modulation depth can take values in the range $0 \leq I_d \leq 1$ depending on the relative size of $I_{c\ \min}$. If the minimum critical current is reduced to 0, that is the maximum depth by this metric, normalised to 1. This corresponds to $\beta_L = 0$. As $\beta_L$ increases, the oscillations get flatter. A point of significance is $\beta_L = 1$ corresponding to $I_d = 0.5$. Above that $I_d$ continues to reduce at a linear rate[92], implying that eventually flux oscillations can be completely suppressed by high $\beta_L$. The screening parameter is linearly dependent on inductance but also on critical current. Geometric inductance is constant for a particular device if the geometry is permanent. But the critical current does not have to be in tuneable junctions. Therefore $\beta_L$ can be tuned in graphene SQUIDs by controlling $I_c$ through electrostatic gating, causing the depth of the flux oscillations to change as well. A SQUID also has a kinetic inductance contribution $L_k$, primarily from the superconducting electrodes, which is summed with the geometric inductance $L_g$ to give the total, as shown in equation (2.21).

$$L = L_g + L_k \tag{2.21}$$

Related to the critical current, the coupling energy $E_J$ is a measure of the strength of the superconducting phase coherence. Its dependence on $I_c$ essentially provides a limit against thermal energy in the system[1].

$$E_J = \frac{\hbar I_c}{2e} \geq 5kT \tag{2.22}$$

Additionally, the flux in a SQUID loop provides a fluctuating noise depending on the inductance of the loop, which grants another constraint:

$$L \leq \frac{\Phi_0^2}{4kT} \tag{2.23}$$

The constraints on $\beta_L$ and $\beta_C$ are to avoid forms of hysteresis, but the latter constraints on thermal energy are stricter as they will determine whether the SQUID will be able to function.

In SFQ logic devices, the value of $\beta_L$ required varies on the role of the junction in the circuit. For example, a simple flux storage circuit required $\beta_L \approx 10$, while a transmission line required a smaller value of $\beta_L \approx 1$[15]. Being able to tune $\beta_L$ with GJJs would therefore allow more flexibility in the fabrication of such circuits and give the opportunity to optimise their performance.

Having discussed the parameters which define a SQUID, the key quantities which characterise its performance can be discussed. A primary figure of merit is the transfer function $V_\Phi$ which describes the sensitivity of a SQUID, which refers to how large a change in magnetic flux can be detected as a change in voltage. It is defined as the maximum of the absolute value of the partial derivative of the voltage $V$ with respect to the applied magnetic flux $\Phi_a$[92]

$$V_\Phi = \max\left(\left|\frac{\partial V}{\partial \Phi_a}\right|\right). \tag{2.24}$$

A larger transfer function implies that the voltage changes more for a smaller change in flux, and hence has a greater sensitivity. This is a key parameter when a SQUID is being considered for use as a magnetometer. The transfer function can be affected by the $\beta_L$ with values close to 1 usually being optimal[92]. Simulations have also shown larger transfer functions for SQUIDs with highly skewed CPRs[93]. Graphene SQUIDs have been measured with maximum transfer functions of 300 µV/$\Phi_0$[75]. 100 µV/$\Phi_0$ is considered typical for a SQUID[92] so this shows that graphene SQUIDs can attain reasonable transfer function values.

Lastly, the noise of a SQUID can be assessed. One noise term is linked to the transfer function: the flux noise power $S_\Phi$. This is defined as $S_\Phi = S_V/V_\Phi^2$, where $S_V$ is the spectral density of the voltage noise power. The flux noise power then defines the energy resolution (minimum detectable energy) of the SQUID $\epsilon = S_\Phi/2L$ and the magnetic field noise power $S_B = S_\Phi/A_{\text{eff}}^2$, where $A_{\text{eff}}$ is the effective area of the SQUID loop. These noise parameters are calculated from Johnson-Nyquist noise (in the form of white noise) of the device resistance. The main other source of noise is $1/f$ noise which comes either from trapped flux vortices in the SQUID material, or from fluctuations of the critical current of the JJs due to defects or impurities in the material. However, $1/f$ noise is only relevant when operating at extremely low frequencies, whereas the thermal noise component sets a limit on the SQUID sensitivity over a wide frequency range[92], and is therefore much more applicable to general use. The description of Johnson-Nyquist noise in SQUIDs is discussed in more detail as part of the simulation in section 3.8.

#### Modern Josephson junction technologies

For applications of JJs or SQUIDs where a large quantity of devices is required, or where batch production is required, $Al_2O_3$ tunnel junctions remain the go-to design. They are currently the main technology being used to scale superconducting quantum computers, for example in Google's Sycamore processor[13]. They remain popular because superconducting aluminium has a long coherence length and the manufacturing process is very straightforward. They also have low loss for high-frequency applications.

In the research space, there is more variety in the types of JJs being constructed and the kinds of devices they are integrated in. The main superconductors being used are Nb alloys like NbTi and NbTiN. Nb has a critical temperature about 10 times larger than Al, making devices much more accessible as sub-kelvin temperatures are not needed. The types of materials being used for the weak link is what changes more frequently. Notably, there are relatively few examples of studying SQUIDs made from these materials than individual junctions. This is likely related to how the fabrication process is less straightforward to produce a pair of parallel junctions compared to a single junction, especially considering some of the gating requirements which greatly increase the number of fabrication steps required.

Semiconductors are used in some cases to explore the possibility of integrating superconductor and semiconductor technology for computing[94]. InAs is commonly seen in semiconductor-based JJs because it has favourable field-effect characteristics [95]. In this way use of semiconductors has a similar rationale to the use of graphene. Semiconductor devices usually use nanowires[36, 96] which lack the benefits of graphene's 2DM properties for the device design. However, there are examples of InAs-based SQUIDs with planar junctions. In one case, the device was shown to have a dominant second harmonic in the CPR, potentially useful for extending relaxation time in qubits[97]. Another example displays highly skewed CPRs and potential in superconducting spintronics due to a large anomalous phase difference which is tuneable through gating of the device.

Other semiconductor-based JJs have been made using 2D $MoS_2$ of various numbers of layers[98, 99], which are interesting because of the 1.8 eV direct band gap in the visible part of the electromagnetic spectrum. In this case, graphene still has a benefit of the order of 100 times higher mobility of charge carriers[100]. Between semiconductors and graphene, there are enough differences in the materials that the research can be complementary, with different applications or designs encouraging use of different materials.

Another interesting and distinct class of JJs are those which use ferromagnetic materials as the weak link. There are interesting interactions at these boundaries because of the interplay between magnetism and superconductivity[101, 102]. One example of a device using a superconductor-ferromagnet-superconductor (SFS) junction is a spin valve, which can be used for computer memory[7]. This subfield is extensive so a recent review of ferromagnetic $\pi$ junctions, which could be used in superconducting logic circuits and certain types of qubits, is referenced for interest[103].

Lastly, Unconventional superconductivity was discovered in bilayer graphene when the layers were twisted to a 'magic angle' of 1.1°[104]. This has been used in JJs and SQUIDs in different ways to the typical weak link. This form of graphene has been used as the entire JJ in a single junction and SQUID by gating the graphene locally to maintain the unconventional superconductivity in the 'electrodes' while switching it off in the 'weak link'[105, 106].

It is clear that there is a wealth of research into a variety of JJ technologies for different purposes. In general, the applications of a particular type of JJ are highly specialised. Graphene-based JJs retain high potential in these types of superconducting devices due to its 2D nature, field effect, and high mobility.

### 2.2.5 Applications of graphene Josephson junctions and SQUIDs

Graphene and 2D materials research searches for advantages of using the materials which would lead to broader implementation of the technology. In superconducting devices there are a few potential benefits.

Heterostructures of graphene with hexagonal boron nitride are atomically flat, allowing them to be placed onto any substrate, enhancing their potential for integration with other types of circuits. Graphene being an active material gives potential for devices which can be switched into different modes of operation or in-situ optimisation. Layered materials have consistent thickness potentially giving more control over the uniformity of fabricated devices compared to grown thin films or heterostructures.

The following subsections are some examples of applications in which graphene JJs or SQUIDs are being considered.

#### Parametric amplifiers

Parametric amplifiers are devices used in particular to detect weak signals. In electronics they require a non-linear impedance medium[107]. A pump signal is mixed with the weak signal, and if the impedance is increased the voltage also increases, enhancing the the signal. Some designs of travelling wave parametric amplifiers (TWPAs) use Josephson junctions in their design because of their non-linear inductance[108], which comes from the Josephson inductance's inverse dependence on the cosine of the phase difference between its superconducting electrodes. These types of amplifiers aim to be used to detect the weakest signals with energies close to the quantum noise limit[109]. Recent work has incorporated graphene JJs because the inductance is also tuneable by gating the graphene which changes the critical current of the junction and hence the inductance. This gives a wider bandwidth of frequencies that the resonator can then be used for, making it more practical to use[110, 111].

### Bolometers

Graphene based Josepshon junctions can also be used as bolometers for detecting low-energy photons, such as those with microwave energies. One example from Gil-Ho Lee et al. shows that graphene's low electron heat-capacity means it can detect low energy photons down to 32 GHz. The associated small thermal time constant meant that the bolometer could operate $10^5$ times faster than other technologies at the time[49].

### Qubits

The previous applications of parametric amplifiers and bolometers both share a lot in common with qubits. They are fundamentally similar as they are all based on the Josephson junction, the base element of superconducting electronics. All three can have use in quantum computing circuits, depending on the combination of technologies being used to prepare, transmit, and measure qubit states. Transmon qubits have previously been made using GJJs[51], though a comparison of different superconducting qubits showed that graphene gatemons did not have a long lifetime in comparison to other technologies[112].

## 2.3 High frequency effects in Josephson junctions and SQUIDs

Many of the applications for superconducting circuits will inevitably either incorporate or be exposed to high-frequency signals up to the range of optical radiation[113, 114]. This is particularly the case for qubit control and signal transport for quantum computing, a major research area.

As different technologies are developed and investigated for use in these applications, it is important that their characteristics are well understood under all feasible conditions, as this will allow strengths and weaknesses of devices to be identified and inform future projects which could benefit from certain behaviours or performance levels.

The high-frequency phenomenon of Shapiro steps is well established, but the exact behaviour can vary depending on the geometry and materials of any given JJ or SQUID. This means that measurements of Shapiro steps always provides valuable information. These types of measurements will represent a large portion of this work, both by simulation (chapter 3) and experiment (chapter 5), so the key aspects of the background theory will be included.

### 2.3.1 Shapiro steps

Quantisation effects were observed in Josephson junctions driven by electromagnetic radiation by Sidney Shapiro in 1963[115]. The result of the effect is that steps appear in the IV of a Josephson junction at quantised voltages $V_n$ proportional to the drive frequency $\nu$ and magnetic flux quantum $\Phi_0$, where $n$ is the integer corresponding to the $n^{\text{th}}$ step.

$$V_n = n\frac{h}{2e}\nu \tag{2.25}$$

The effect comes from how the voltage across the junction is described in the ac Josephson effect (2.3). The junction is typically biased by a dc current, which above the critical current creates a voltage drop across the junction and causes the phase difference of the junction to oscillate. Certain bias currents correspond to voltages which are equal to a Shapiro step. In a junction which is not being driven by an additional ac source, these are all one-to-one values, each bias current gives a different voltage response. The driving current introduces additional dc current components so that at a Shapiro step voltage, the same voltage response is produced across a range of bias current values.

Real electronic measurements can be offset, such that the 0 gradient region in the IV curve corresponding to the superconducting region is not at 0 voltage. This means it is sometimes useful to characterise the steps in terms of their spacing $\Delta V$ rather than the specific voltage values.

$$\Delta V = \frac{h\nu}{2e} = \Phi_0\nu \tag{2.26}$$

Of more interest now are half-integer and fractional Shapiro steps, which can be observed in ballistic JJs with skewed CPRs.

### 2.3.2 Half-integer Shapiro steps

Shapiro steps are the expected outcome of exposing a Josephson junction to high-frequency radiation. They are quantised voltage steps appearing at integer spacing equal to the product of the frequency of an applied high-frequency electric field and the magnetic flux quantum (see equation (2.26)). However, the appearance of steps at fractional intervals has been observed both in simulation and experiment[36, 83, 102, 116, 117]. There are two main cases where half-integer steps can appear in SQUIDs: due to a skewed CPR, and due to half-integer flux in the SQUID loop. The latter case is only possible in SQUIDs, while the former can also be observed in single junctions.

#### Half-integer steps due to half-integer flux

One mechanism is that half-integer Shapiro steps will appear when a half-integer value of magnetic flux is applied through a SQUID. This mechanism would seem to be present specifically in SQUIDs and not individual Josephson junctions because the effect is linked to the difference in phase differences of the JJs in a SQUID[117]. The physical interpretation is that a symmetric SQUID with integer flux in the loop has no circulating current, and the phase differences of the two JJs are the same (see equation (3.28)). Therefore the phases are locked and they evolve in step while the device operates, as if it was a single junction. When an RF field is applied, they similarly undergo their evolution at the same rate, so any steps that appear are only quantised at the integer level. On the other hand, when there is a non-integer fraction of magnetic flux quanta in the loop, the circulating current is established by the SQUID's loop inductance. This means there are different amounts of current flowing through each junction, and so the phase differences of the individual junctions change at different rates. This means that in one cycle of the RF field, the different junctions have evolved by a different amount. This is maximised at half-integer flux. In particular, the number of rotations the junctions complete in a period of the drive signal is supposed to correspond to the integer of the related Shapiro step. So if one junction has completed 2 oscillations and the other 3, then a half-integer step at $n = 2.5$ should be visible. Thinking about this in terms of the bias current on an IV curve, with the circulating current, the actual bias through each junction are $\pm J$ from the recorded bias. This could put one junction in the region of one Shapiro step, and the other in the region of the next. Averaging these voltages in the measurement would give values halfway between.

#### Fractional steps due to a skewed CPR

The second mechanism is related to a skewed CPR. An ideal junction with a sinusoidal CPR will not show fractional Shapiro steps, but junctions in several systems with skewed CPRs have displayed fractional Shapiro steps. Graphene JJs have been shown to have a CPR which can be tuned via electrostatic gating[37]. When the graphene has low transparency the CPR is very sinusoidal, but when gated into the n-type region the transparency increases and the CPR becomes skewed.

A general way of expanding the CPR of a JJ is as a Fourier series summing increasing harmonics

$m$ of sinusoidal waveforms

$$I = \sum_{m=1}^{\infty} c_m \sin(m\gamma) \tag{2.27}$$

where $c_m$ is the amplitude of harmonic $m$, usually decreasing with increasing harmonic[97]. These higher harmonics can be coupled to by a high-frequency signal to induce fractional Shapiro steps at voltages evenly spaced between integer Shapiro steps. For example, for $m = 3$, fractional steps appear at $(n/3)$ and $(2n/3)$ multiples of the voltage spacing given in (2.26).

Another source of fractional Shapiro steps can be a finite capacitance in the junction such that $\beta_C > 0$, although these can appear even in junctions with a sinusoidal CPR. Most real devices will have some capacitance, and $\beta_C$ is defined by multiple quantities including the critical current [see (2.18)]. Nevertheless, it is a possible confounding factor to consider when analysing fractional Shapiro steps, and minimising $\beta_C$ will reduce its contribution compared to other mechanisms[118]. This is already a desired property in many cases to avoid hysteresis in the junction, so it is not at odds with junction design.

### Fractional Shapiro steps in graphene Josephson junctions

Integer and fractional Shapiro steps have been observed in graphene Josephson junctions in different geometries. There are examples of graphene JJs constructed laterally like SNS junctions, and vertically where superconducting contacts to the graphene are made on the top and bottom of the plane of the monolayer, rather than at the edges. Vertical graphene JJs are not widely used, because it is difficult to get good contact between the superconductor and the surface of graphene, especially compared to the extremely low-resistance contacts seen in lateral junctions like those discussed in section 2.2.2. Gil-Ho Lee et al. have published work on vertical graphene JJs [62, 119]. The supplementary information from the 2015 publication[120] contains figure 2.17, which shows spikes in the differential conductance of their junctions corresponding to Shapiro steps. Visible with smaller magnitude are steps at half-integer positions, as well as $n/3$ and $2n/3$. These steps appear because the junction is ballistic and has a skewed CPR.

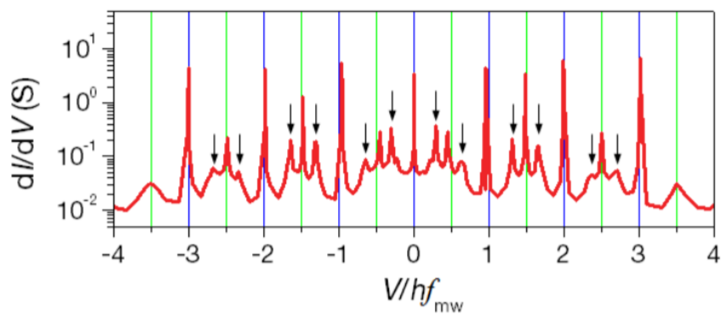


Figure 2.17: Differential conductance against Shapiro step number in vertical graphene Josephson junctions. The x-axis shows the voltage of the JJ in terms of Shapiro step quantisation. Green vertical lines are at $n/2$ values where peaks corresponding to half-integer steps are present, and the black arrows mark the position of $n/3$ and $2n/3$ fractional step peaks. Reproduced from [120] where the article is published under a Creative Commons Attribution 4.0 International License.

For lateral junctions, recent work was published by Huang et al. [83] in which half-integer Shapiro steps were observed. Their junctions were also using hBN encapsulated graphene, but with Ti/Al contacts. Performing an experiment conceptually similar to one of the measurement done here in section 5.2.3, they suggest that their results link the transparency of the graphene junctions to the appearance of half-integer Shapiro steps, which would be consistent with the skewed CPR equation (2.8) that is generally used. Figure 2.18 shows an example of measurements their measurements which are similar in form to those which were being done for this thesis before the publication of [83], showing the Shapiro steps in the form of a histogram and the dependence of the steps on the microwave power applied.

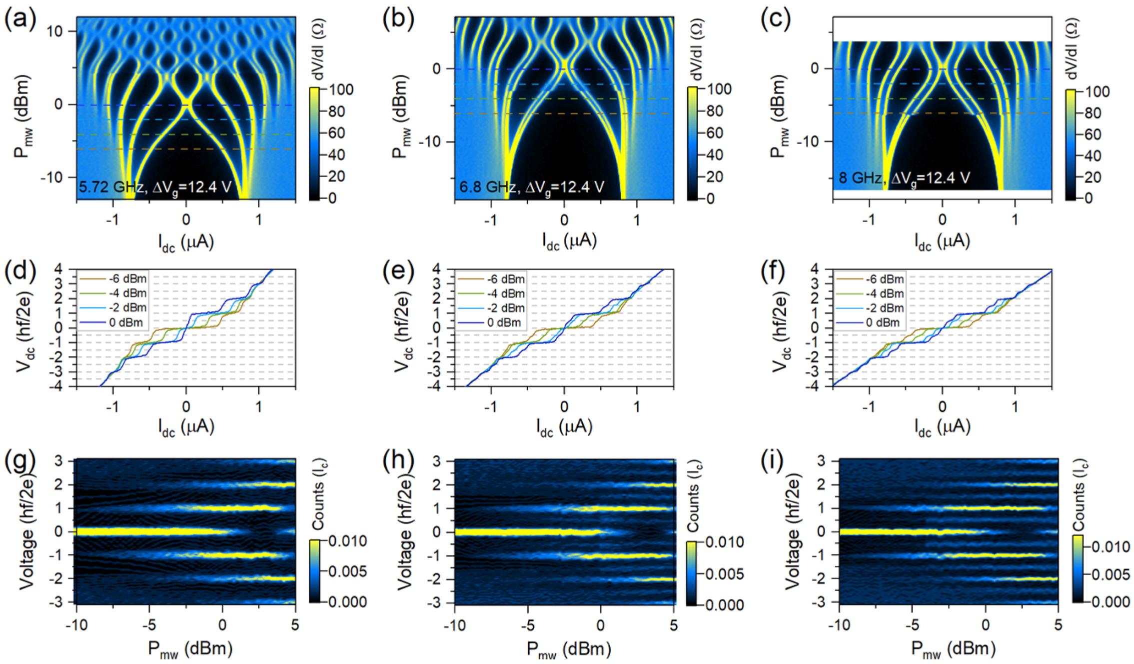


Figure 2.18: Plots showing ac characterisation of a graphene JJ at a fixed gate voltage (12.4 V) but irradiated with different microwave power. (a), (b), and (c) are Shapiro maps which show the position of Shapiro steps by the regions of 0 differential voltage. Fewer step regions are visible as frequency increases. Power slices from (a), (b), and (c) are shown in (d), (e), and (f) respectively. Half-integer steps are clearly visible in (f). (g), (h) and (i) are histograms of voltage responses against power from (a), (b) and (c) respectively, showing that there are integer and half-integer Shapiro steps due to a higher frequency of points at those voltages compared to the background. (g) only shows integer steps, and the half-integer steps are clearest in (i). Reproduced from [83] with the permission of AIP Publishing.

The work in this thesis differs significantly from [83] in two major ways. Firstly, the measurements shown in this thesis are on a graphene SQUID rather than a single JJ, allowing for consideration of a second mechanism causing the appearance of half-integer Shapiro steps. Secondly, a greater consideration of how the half-integer Shapiro steps change with temperature is given in this thesis, because of how the CPR has been shown to return to a sinusoidal shape with increasing temperature (section 5.2.2). The basis for this expectation comes from the model in figure 2.11 and the work by Nanda et al.

## 2.4 Chapter summary

In this chapter the progress made on the topic of superconducting devices and low-dimensional materials has been discussed, showing the variety of work being done to progress the field.

The work shown in this thesis explores a niche implementation of graphene SQUIDs. Whilst a lot of prior work focuses on Josephson junctions, in reality many superconducting circuits are more complicated than that, and will likely also include SQUIDs. Therefore it makes sense to extend the investigation of device properties to these structures.

In particular, many devices will be operated under high frequency conditions or using high frequency signals, especially if working towards integration with optical circuits but also commonly in quantum computing applications. Shapiro step behaviour in SQUIDs has previously been observed, along with half-integer steps when there is a non-integer quantity of magnetic flux in the SQUID loop[117] or skewed CPR.

With tuneable graphene devices, it is possible to observe differing Shapiro step behaviours depending on the skewness of the current-phase relation, as well as the magnetic flux in the SQUID loop. This work moves towards assessing the different half-integer Shapiro step phenomena in one device.

# Chapter 3

# Numerical simulation of RCSJ SQUIDs

This chapter is about numerically simulating a superconducting quantum interference device using the resistively and capacitively shunted junction (RCSJ) model. The first few sections will be about deriving the equations that are needed to build the simulation. Then, the method and algorithm used to solve the differential equations numerically will be shown. After that, additional derivations will be included to show how ac current and thermal noise can be added to the system and the differences they make to the results. Following that is discussion about the different types of SQUID measurements that can be simulated with the setup, and some of the general trends observed in the SQUID's behaviour.

The base simulation code was originally implemented by Jonathan Prance as published recently [93]. This code was used by the author to produce the results included and modifications were made by the author to include an additional current source from an external RF signal (section 3.7).

The main objective of the simulations is to investigate the appearance of half-integer Shapiro steps, such that the simulated model may be able to support the experimental results. However, additional observations are made which provide significant motivation for further exploration of the simulation in future work.

## Contents

## 3.1 Resistively and capacitively shunted junction model

The resistively and capacitively shunted junction (RCSJ) model is formed of a Josephson junction in parallel with a shunt resistor and a shunt capacitor, as seen in figure 3.1a. This allows the JJ to be studied when the ac Josephson effect is contributing to the junction dynamics (i.e. the finite voltage state). When the junction is in the finite voltage state there will be dissipation of energy coming from the non-zero resistance $R$. The RCSJ model puts the shunt resistor in parallel so that when the junction is in the finite voltage regime, the dissipation can be modelled without interfering with the lossless part through the JJ itself. The capacitance $C$ is an approximation of the capacitance in the circuit. In a tunnel junction this would usually be dominated by the geometric capacitance because of the very thin tunnel barriers and comparatively large electrode areas, but in SNS junctions this assumption does not hold up, with other effects such as the capacitance between the electrodes and the substrate, or other parallel capacitances present in an extensive electronics setup potentially wielding non-negligible influence. This does not stop the model from working: those sources of capacitance are still effectively included in $C$ whatever the exact nature of the experimental system, and other work has shown that the RCSJ model can be applied to SNS graphene systems[121]. What it does mean, is that it is harder to accurately quantify the capacitance of the junction itself. This model does not take into account any geometric effects, and as such the junctions are considered point-contacts. The model also assumes that resistance is linear.

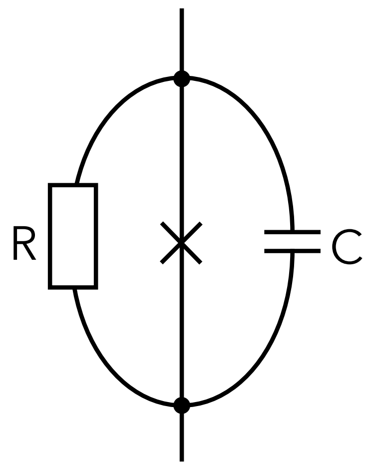


(a) Circuit diagram of the resistively and capacitively shunted junction model. The Josephson junction is in parallel with the shunt capacitor and shunt resistor.

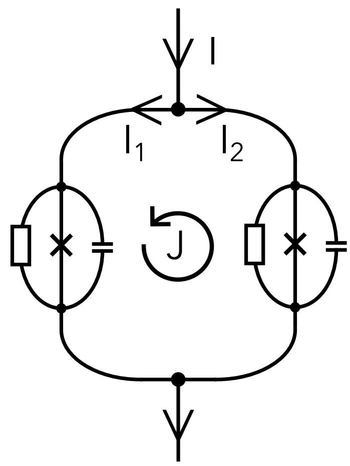


(b) SQUID diagram showing components of current flow through resistively and capacitively shunted JJs. Total bias current $I = I_1 + I_2$. $J$ is the circulating loop current due to the inductance of the SQUID geometry.

Figure 3.1: Diagrams of a Josephson junction and SQUID in the context of the RCSJ model.

## 3.2 SQUID current in the RCSJ model

In the implemented simulation, two RCSJ JJs are combined to form a SQUID as in 3.1b. The objective of the simulation is to calculate the average voltage response of the SQUID. To derive the equations for the simulation, one starts by considering the current $I$ through one JJ. In the RCSJ model we can apply Kirchoff's current law to determine the current passing through each parallel arm of the circuit shown in figure 3.1a. The total current $I$ is therefore a sum of the currents through the shunt resistor, shunt capacitor, and the current defined by the current-phase relation (CPR) of the JJ. The CPR current takes the form $I_c \cdot \overline{CPR}(\gamma)$ where $I_c$ is the critical current and $\gamma$ is the gauge-invariant phase difference. In the simulation the CPR can be defined as any dimensionless periodic function, normalised such that the maximum value is 1, as in the examples shown in figure 3.2. The CPRs plotted in the figure are implemented in the completed simulation, and shown in Table 3.1. It was primarily the skewed equation which was used in this work, as the transparency (transmission probability) $T_n$ could be set to high and low values close to 1 and 0 respectively to model situations where the CPR was skewed close to the sawtooth or sinusoidal CPRs. For full discussion of this CPR equation and skewed CPRs, see section 2.2.3.

For the resistor, the current is calculated with Ohm's law where $V$ is the voltage drop across the junction, and the current through the capacitor is its capacitance multiplied by the rate of change of the voltage drop $V$ with time $t$.

$$I = I_c\overline{CPR}(\gamma) + \frac{V}{R} + C\frac{\mathrm{d}V}{\mathrm{d}t} \tag{3.1}$$

| CPR | Equation |
|---|---|
| Sinusoidal | $\sin(\gamma)$ |
| Skewed | $\dfrac{T_n \sin(\gamma)}{\sqrt{1 - T_n \sin^2(\frac{\gamma}{2})}}$ |
| Sawtooth | $\dfrac{(\gamma - \pi) \mod 2\pi}{\pi}$ |

Table 3.1: Equations used in the RCSJ simulation as the current-phase relation. In the sinusoidal (ideal junction) and sawtooth (extreme case of skewed junction) equations they take only the phase difference $\gamma$ as an argument. In the skewed equation the transparency (or transmission probability) parameter $T_n$ can also be varied (taking values $0 < T_n < 1$).

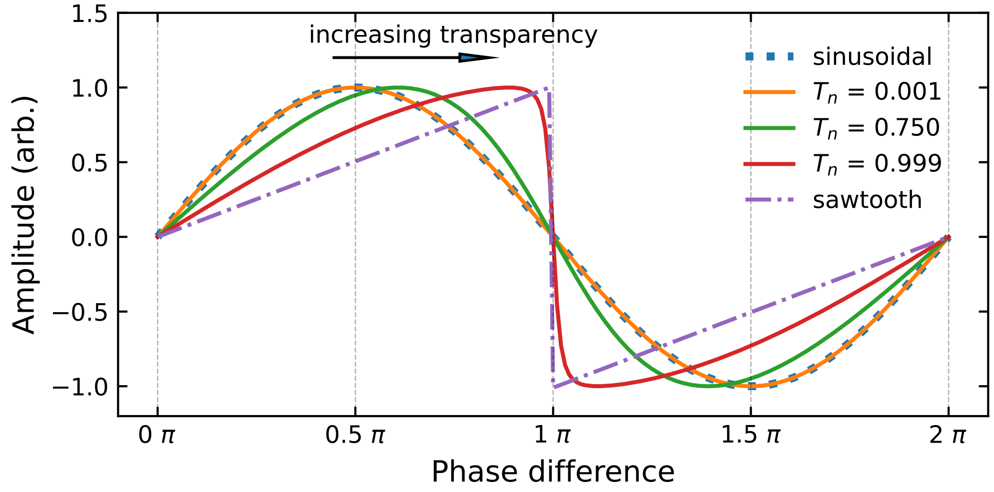


Figure 3.2: Plots of different CPR functions that can be used in the numerical simulation. As in the simulation, each plot is normalised by its maximum value. The plots are produced by the equations in table 3.1, where the transparency (or transmission probability) $T_n$ values are for plots using the skewed CPR. The sinusoidal plot is superimposed with the $T_n = 0.001$ skewed function. This confirms that in the low transparency limit the skewed CPR reduces back to the sinusoidal behaviour, making it a good choice of function to study these junctions with a tuneable CPR. At the higher values of $T_n$ the skewness becomes increasingly prominent. The sawtooth function represents the ideal case of perfectly ballistic and uniform JJ[93]. The vertical dashed lines highlight multiples of $\pi/2$ as reference points so that the changing shape of the curves can be clearly interpreted. In particular, the stationary points at maximum amplitude are shown to occur at greater phase difference for greater transparency.

To extend this to a SQUID a second equation is included to represent the parallel junction and it is assumed that the bias current will split between the two branches, such that $I = I_1 + I_2$, as shown in figure 3.1b. Asymmetry terms will be added later which makes it possible to investigate devices with asymmetric JJs. Both junction equations look similar, based on the form given in (3.1), but they are related to one another by the circulating current $J$, and the relationship between their phase differences. The circulating current is travelling in a different direction through each junction, so $J$ is added to the total current through one junction and subtracted from the total through the second junction.

$$\begin{aligned} I_1 &= \frac{I}{2} + J = I_{c1}\overline{CPR}(\gamma_1) + \frac{V_1}{R_1} + C_1\frac{\mathrm{d}V_1}{\mathrm{d}t} \\ I_2 &= \frac{I}{2} - J = I_{c2}\overline{CPR}(\gamma_2) + \frac{V_2}{R_2} + C_2\frac{\mathrm{d}V_2}{\mathrm{d}t} \end{aligned} \tag{3.2}$$

The phase differences are related to the total flux $\Phi_T$ through the SQUID loop and the magnetic flux quantum $\Phi_0$.

$$\gamma_2 - \gamma_1 = \frac{2\pi}{\Phi_0}\Phi_T \mod 2\pi \tag{3.3}$$

These are the basic forms of the equations describing the current through the SQUID, but they are currently not very useful for this simulation because of the large number of unknown variables. The next sections will show how the base equations can be manipulated into differential equations with dimensionless parameters which can be solved numerically and model SQUID systems very generally.

## 3.3 Dimensionless parameterisation of a SQUID

In this section equations (3.2) will be manipulated into a general form by converting to a set of dimensionless parameters. The only notable difference in the two equations is the direction of the circulating current $J$. Therefore for simplicity the derivation will only be shown for the first branch, and then the result for the second branch will be quoted.

Firstly applying the ac Josephson effect (2.3) removes the voltage terms $V$ and $\mathrm{d}V/\mathrm{d}t$ from equation (3.2).

$$I_1 = \frac{I}{2} + J = I_{c1}\overline{CPR}(\gamma_1) + \frac{1}{R_1}\frac{\hbar}{2e}\frac{\mathrm{d}\gamma_1}{\mathrm{d}t} + C_1\frac{\hbar}{2e}\frac{\mathrm{d}^2\gamma_1}{\mathrm{d}t^2} \tag{3.4}$$

The first major substitution to make is converting to dimensionless units of time $\tau$, which affects the derivatives found in the equation. $\tau$ is based on the characteristic frequency $\omega_c$ of the junction such that $\tau = \omega_c t$. The characteristic frequency is the Josephson frequency $\omega_J = 2\pi V/\Phi_0$ when the voltage is equal to the junction characteristic voltage $V_c = I_c R$.

$$\tau = \frac{2eI_cR}{\hbar}t \tag{3.5}$$

$$\frac{\mathrm{d}\tau}{\mathrm{d}t} = \frac{2eI_cR}{\hbar} \tag{3.6}$$

The definitions in (3.5) and (3.6) use critical current $I_c$ and resistance values $R$ which are defined as a combination of the values representing both junctions in the SQUID.

$$I_c = \frac{I_{c1} + I_{c2}}{2} \tag{3.7}$$

$$R = \frac{2R_1R_2}{R_1 + R_2} \tag{3.8}$$

Using (3.6), $\mathrm{d}\gamma/\mathrm{d}t$ can be expressed in terms of $\mathrm{d}\gamma/\mathrm{d}\tau$, allowing the conversion into dimensionless time by substituting the resulting equations (3.9) and (3.10) into (3.4)

$$\frac{\mathrm{d}\gamma}{\mathrm{d}t} = \frac{2eI_cR}{\hbar}\frac{\mathrm{d}\gamma}{\mathrm{d}\tau} \tag{3.9}$$

$$\frac{\mathrm{d}^2\gamma}{\mathrm{d}t^2} = \left(\frac{2eI_cR}{\hbar}\right)^2\frac{\mathrm{d}^2\gamma}{\mathrm{d}\tau^2} \tag{3.10}$$

changing (3.4) into

$$\frac{I}{2} + J = I_{c1}\overline{CPR}(\gamma_1) + \frac{1}{R_1}\frac{\hbar}{2e}\frac{2eI_cR}{\hbar}\frac{\mathrm{d}\gamma_1}{\mathrm{d}\tau} + C_1\frac{\hbar}{2e}\left(\frac{2eI_cR}{\hbar}\right)^2\frac{\mathrm{d}^2\gamma_1}{\mathrm{d}\tau^2} \tag{3.11}$$

Cancelling of terms can be done immediately for the resistance term but the capacitance term requires the Stewart-McCumber parameter $\beta_C$ and the SQUID capacitance $C$ to be fully simplified. A substitution for the magnetic flux quantum $\Phi_0 = h/2e$ has been included in (3.12) so that the subsequent cancelling of terms from (3.11)is clearer.

$$\beta_C = \frac{2\pi I_cR^2C}{\Phi_0} = \frac{2eI_cR^2C}{\hbar} \tag{3.12}$$

where $C$ is the average capacitance of the two junctions.

$$C = \frac{C_1 + C_2}{2} \tag{3.13}$$

Now the result of the substitution of (3.12) into (3.11) and the cancelling of terms associated with both the resistance and capacitance components is shown.

$$\frac{I}{2} + J = I_{c1}\overline{CPR}(\gamma_1) + \frac{RI_c}{R_1}\frac{\mathrm{d}\gamma_1}{\mathrm{d}\tau} + \beta_C\frac{C_1 I_c}{C}\frac{\mathrm{d}^2\gamma_1}{\mathrm{d}\tau^2} \tag{3.14}$$

The dimensionless current is defined as the raw current being divided by $I_c$:

$$i = \frac{I}{I_c} \tag{3.15}$$

$$j = \frac{J}{I_c} \tag{3.16}$$

So dividing (3.14) by $I_c$ removes the non-dimensionless current terms $I$ and $J$ and the total critical current terms $I_c$, leaving:

$$\frac{i}{2} + j = \frac{I_{c1}}{I_c}\overline{CPR}(\gamma_1) + \frac{R}{R_1}\frac{\mathrm{d}\gamma_1}{\mathrm{d}\tau} + \beta_C\frac{C_1}{C}\frac{\mathrm{d}^2\gamma_1}{\mathrm{d}\tau^2} \tag{3.17}$$

To further generalise the SQUID and remove the junction-specific variables, systems with asymmetric junctions are considered. Asymmetry terms are defined for the junction critical current, resistance, and capacitance.

$$\alpha_I = \frac{I_{c2} - I_{c1}}{I_{c1} + I_{c2}} \qquad \alpha_R = \frac{R_2 - R_1}{R_1 + R_2} \qquad \alpha_C = \frac{C_2 - C_1}{C_1 + C_2} \tag{3.18}$$

While the asymmetry terms contain both of the specific values of variables related to the individual junctions, one of them [e.g. $I_{c2}$ in the $\alpha_I$ equation from (3.18)] can be eliminated by combining the equation with its generalised definition [(3.7) for $I_c$], in this case simplifying to a result of $I_{c1}/I_c = (1 - \alpha_I)$. Some equivalent working can be carried out for each variable and for each branch to give the overall results that follow.

$$\frac{i}{2} + j = (1 - \alpha_I)\overline{CPR}(\gamma_1) + (1 - \alpha_R)\frac{\mathrm{d}\gamma_1}{\mathrm{d}\tau} + \beta_C(1 - \alpha_C)\frac{\mathrm{d}^2\gamma_1}{\mathrm{d}\tau^2} \tag{3.19}$$

$$\frac{i}{2} - j = (1 + \alpha_I)\overline{CPR}(\gamma_2) + (1 + \alpha_R)\frac{\mathrm{d}\gamma_2}{\mathrm{d}\tau} + \beta_C(1 + \alpha_C)\frac{\mathrm{d}^2\gamma_2}{\mathrm{d}\tau^2} \tag{3.20}$$

## 3.4 Relation between junction phase differences

In a SQUID, each junction has its own phase difference $\gamma_1$ and $\gamma_2$. They are themselves related because of how the applied magnetic flux and inductance of the SQUID cause a circulating current to be induced in the loop, passing through both junctions. The basic relation is based on the quantisation of magnetic flux in the SQUID loop and its relation to phase.

$$\gamma_2 - \gamma_1 = \frac{2\pi}{\Phi_0}\Phi_T \mod 2\pi \tag{3.21}$$

$\Phi_T$ is the total amount of magnetic flux in the SQUID loop, comprised of the applied flux $\Phi$ and the self-induced flux due to the inductances $L_{1,2}$ and currents $I_{1,2}$.

$$\gamma_2 - \gamma_1 = \frac{2\pi}{\Phi_0}\left(\Phi + L_1 I_1 - L_2 I_2\right) \tag{3.22}$$

The difference in phase differences is always zero when $\Phi_T$ is an integer multiple of $\Phi_0$. The difference is maximised when the two phase differences are separated by $\pi$, which corresponds to a half-integer amount of total flux through the SQUID loop. It is easier to intuit these conditions visually, see figure 3.3.

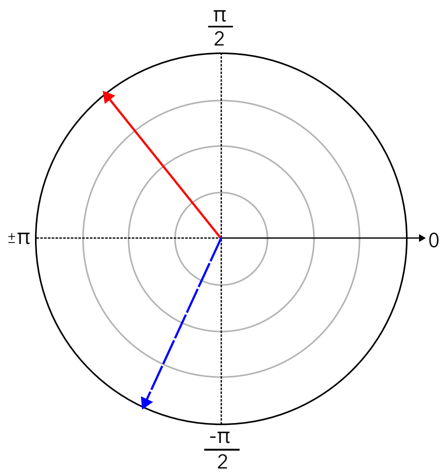


Figure 3.3: The red and blue arrows each represent the phase difference of one of Josephson junctions in a SQUID. This shows intuitively that the maximum magnitude of the difference in phase differences is equal to $\pi$.

For the simulation it is desirable to treat the components of $\Phi_T$ individually. The phase difference is already effectively a dimensionless quantity but the equation still contains several variables with dimensions. This is addressed with a few substitutions and re-definitions. Firstly, the screening parameter $\beta_L$ is introduced, and used to eliminate the $\Phi_0$ terms associated with the inductance. Secondly, the dimensionless magnetic flux $\phi$ is defined,

$$\phi = \Phi/\Phi_0 \tag{3.23}$$

representing the fraction of a flux quantum being externally applied. Thirdly, recall that $I_{1,2}/I_c = i/2 \pm j$ (section 3.2). Lastly, the inductance asymmetry $\alpha_L$ and total inductance $L$ are combined to remove

$L_1$.

$$L = L_1 + L_2 \tag{3.24}$$

$$\beta_L = 2LI_0/\Phi_0 \tag{3.25}$$

$$\alpha_L = \frac{L_2 - L_1}{L_1 + L_2} \tag{3.26}$$

Applying these conversions gives

$$\gamma_2 - \gamma_1 = 2\pi \left[ \phi + \frac{1}{4}\beta_L(1-\alpha_L)\left(\frac{i}{2} + j\right) - \frac{1}{4}\beta_L(1+\alpha_L)\left(\frac{i}{2} - j\right) \right] \tag{3.27}$$

Finally, expanding brackets and simplifying gives the equation

$$\gamma_2 - \gamma_1 = 2\pi \left[ \phi + \frac{1}{2}\beta_L \left( j - \frac{\alpha_L}{2} i \right) \right] \tag{3.28}$$

## 3.5 Average voltage across the SQUID

The previous sections 3.3 and 3.4 have provided differential equations for the current in an RCSJ SQUID and the relationship between the individual junctions' phase differences. The overall goal of the simulation is to calculate the voltage response at different current biases for a particular set of parameters.

Similarly to how the current through each arm was assessed earlier, an equation can be constructed for the voltage drop over each SQUID branch. It is assumed that the voltage drop over each branch is the same. The total voltage drop in one branch is made up of components from the junction and inductance in that branch.

$$V = V_1 + L_1 \frac{\mathrm{d}I_1}{\mathrm{d}t} = V_2 + L_2 \frac{\mathrm{d}I_2}{\mathrm{d}t} \tag{3.29}$$

This is made dimensionless in the same way as the other equations derived so far. Initially the inductance will be converted using the inductance asymmetry relation to substitute $L_{1,2} = L(1 \mp \alpha_L)/2$.

$$V = V_1 + \frac{L}{2}(1 - \alpha_L)\frac{\mathrm{d}I_1}{\mathrm{d}t} = V_2 + \frac{L}{2}(1 + \alpha_L)\frac{\mathrm{d}I_2}{\mathrm{d}t} \tag{3.30}$$

The next step will be converting the differential current terms. $I_{1,2}$ are the actual current values passing through each branch of the SQUID, defined as half of the total bias $I$ plus/minus the circulating current $J$. If it is assumed that the current bias across the SQUID is constant, such that $\mathrm{d}I/\mathrm{d}t = 0$ then the individual branch currents are eliminated leaving just the circulating current. This assumption is valid because the SQUID is being measured in a current-biased experimental configuration. Therefore the voltage being calculated is intended to be associated with a single current bias value.

$$\frac{\mathrm{d}I_{1,2}}{\mathrm{d}t} = \frac{\mathrm{d}}{\mathrm{d}t}\left(\frac{I}{2} \pm J\right) = \pm \frac{\mathrm{d}J}{\mathrm{d}t} \tag{3.31}$$

Substituting the resulting relations in (3.31) back into (3.30) for each branch and then applying the methods previously shown in section 3.2 gives the dimensionless form in (3.32).

$$\begin{aligned}
V &= V_{1,2} && \pm \frac{1}{2}(1 \mp \alpha_L) L \frac{\mathrm{d}J}{\mathrm{d}t} \\
V &= \frac{\hbar}{2e}\frac{\mathrm{d}\gamma_{1,2}}{\mathrm{d}t} && \pm \frac{1}{2}(1 \mp \alpha_L) L \frac{\mathrm{d}J}{\mathrm{d}t}\frac{2I_c}{\Phi_0}\frac{\Phi_0}{2I_c} \\
V &= I_c R \frac{\mathrm{d}\gamma_{1,2}}{\mathrm{d}\tau} && \pm \frac{1}{2} I_c R (1 \mp \alpha_L)\beta_L \frac{h}{2e}\frac{e}{\hbar}\frac{\mathrm{d}j}{\mathrm{d}\tau} \\
v &= \frac{\mathrm{d}\gamma_{1,2}}{\mathrm{d}\tau} && \pm \frac{\pi\beta_L}{2}(1 \mp \alpha_L)\frac{\mathrm{d}j}{\mathrm{d}\tau}
\end{aligned} \tag{3.32}$$

Next, $v$ can be expressed in terms of $\gamma_1$ and $\gamma_2$ by adding the branches together.

$$v = \frac{1}{2}\left[\frac{\mathrm{d}\gamma_1}{\mathrm{d}\tau} + \frac{\pi\beta_L}{2}(1 - \alpha_L)\frac{\mathrm{d}j}{\mathrm{d}\tau} + \frac{\mathrm{d}\gamma_2}{\mathrm{d}\tau} - \frac{\pi\beta_L}{2}(1 + \alpha_L)\frac{\mathrm{d}j}{\mathrm{d}\tau}\right]$$

$$v = \frac{1}{2}\left[\frac{\mathrm{d}\gamma_1}{\mathrm{d}\tau} + \frac{\mathrm{d}\gamma_2}{\mathrm{d}\tau} - \pi\alpha_L\beta_L\frac{\mathrm{d}j}{\mathrm{d}\tau}\right] \tag{3.33}$$

To also eliminate $j$, the equation describing the relationship between the phase differences (3.28) is written as

$$j = \frac{\gamma_2 - \gamma_1 - 2\pi\phi}{\pi\beta_L} + \frac{\alpha_L}{2} i \tag{3.34}$$

Reasserting the previous assumption that $\mathrm{d}I/\mathrm{d}t = 0$ (and therefore that $\mathrm{d}i/\mathrm{d}\tau = 0$, and introducing a further assumption that the amount of applied flux is constant (also reasonable to obtain a voltage response) such that $\mathrm{d}\phi/\mathrm{d}\tau = 0$, allows the derivative of $j$ to be taken and simplified to

$$\frac{\mathrm{d}j}{\mathrm{d}\tau} = \frac{1}{\pi\beta_L}\left(\frac{\mathrm{d}\gamma_2}{\mathrm{d}\tau} - \frac{\mathrm{d}\gamma_1}{\mathrm{d}\tau}\right) \tag{3.35}$$

This can then be substituted into (3.33).

$$v = \frac{1}{2}\left[\frac{\mathrm{d}\gamma_1}{\mathrm{d}\tau} + \frac{\mathrm{d}\gamma_2}{\mathrm{d}\tau} - \frac{\pi\alpha_L\beta_L}{\pi\beta_L}\left(\frac{\mathrm{d}\gamma_2}{\mathrm{d}\tau} - \frac{\mathrm{d}\gamma_1}{\mathrm{d}\tau}\right)\right]$$

$$v = \frac{1}{2}\left[(1-\alpha_L)\frac{\mathrm{d}\gamma_2}{\mathrm{d}\tau} + (1+\alpha_L)\frac{\mathrm{d}\gamma_1}{\mathrm{d}\tau}\right] \tag{3.36}$$

## 3.6 Calculating the numerical solution of the RCSJ SQUID model

The aim of the simulation is to calculate the average voltage of the SQUID for a given set of conditions. The voltage equation (3.33) requires solutions to $\dot{\gamma}_{1,2}$ to calculate a value. This is done by numerically integrating the second order differential equations $\ddot{\gamma}_{1,2}$ using the `integrate.solve_ivp` function in the SciPy 1.1.0[122] Python (version 3.7.1) library. The python function implements a Runge-Kutta method (`"RK45"`) [123] to the equations (3.39) with a set of initial conditions to solve the differential equations, allowing the voltage to then be calculated using the solutions.

A high-level overview of this process for a single voltage data point in the overall simulation script is given by the flowchart in figure 3.4.

Equation (3.19) contains the variables $\ddot{\gamma}_{1,2}$ to integrate. First, the circulating current $j$ is eliminated from by substituting (3.34).

$$0 = \left(-\frac{i}{2} \mp \frac{\gamma_2 - \gamma_1 - 2\pi\phi}{\pi\beta_L} \mp \frac{\alpha_L}{2} i\right) + (1 \mp \alpha_I)\overline{CPR}(\gamma_{1,2}) + (1 \mp \alpha_R)\dot{\gamma}_{1,2} + \beta_C(1 \mp \alpha_C)\ddot{\gamma}_{1,2} \tag{3.37}$$

Rearranging for $\ddot{\gamma}$ as the subject gives

$$\ddot{\gamma}_{1,2} = \frac{1}{\beta_C(1 \mp \alpha_C)}\left[\frac{\gamma_2 - \gamma_1 - 2\pi\phi}{\pi\beta_L} + \frac{i}{2} \pm \frac{\alpha_L}{2} i - (1 \mp \alpha_R)\dot{\gamma}_{1,2} - (1 \mp \alpha_I)\overline{CPR}(\gamma_{1,2})\right] \tag{3.38}$$

To break down the four equations:

$$\begin{aligned}
\frac{\mathrm{d}\gamma_1}{\mathrm{d}\tau} &= \dot{\gamma}_1 \\
\frac{\mathrm{d}\dot{\gamma}_1}{\mathrm{d}\tau} &= \frac{1}{\beta_C(1 - \alpha_C)}\left[\frac{\gamma_2 - \gamma_1 - 2\pi\phi}{\pi\beta_L} + (1 + \alpha_L)\frac{i}{2} - (1 - \alpha_R)\dot{\gamma}_1 - (1 - \alpha_I)\overline{CPR}(\gamma_1)\right] \\
\frac{\mathrm{d}\gamma_2}{\mathrm{d}\tau} &= \dot{\gamma}_2 \\
\frac{\mathrm{d}\dot{\gamma}_2}{\mathrm{d}\tau} &= \frac{1}{\beta_C(1 + \alpha_C)}\left[\frac{\gamma_2 - \gamma_1 - 2\pi\phi}{\pi\beta_L} + (1 - \alpha_L)\frac{i}{2} - (1 + \alpha_R)\dot{\gamma}_2 - (1 + \alpha_I)\overline{CPR}(\gamma_2)\right]
\end{aligned} \tag{3.39}$$

The differential equations contain four variables $\gamma_1$, $\dot{\gamma}_1$, $\gamma_2$, and $\dot{\gamma}_2$ to solve for a given set of constants $i$, $\beta_C$, $\beta_L$, and $\phi$. The time steps for the integration are controlled by $\tau$.

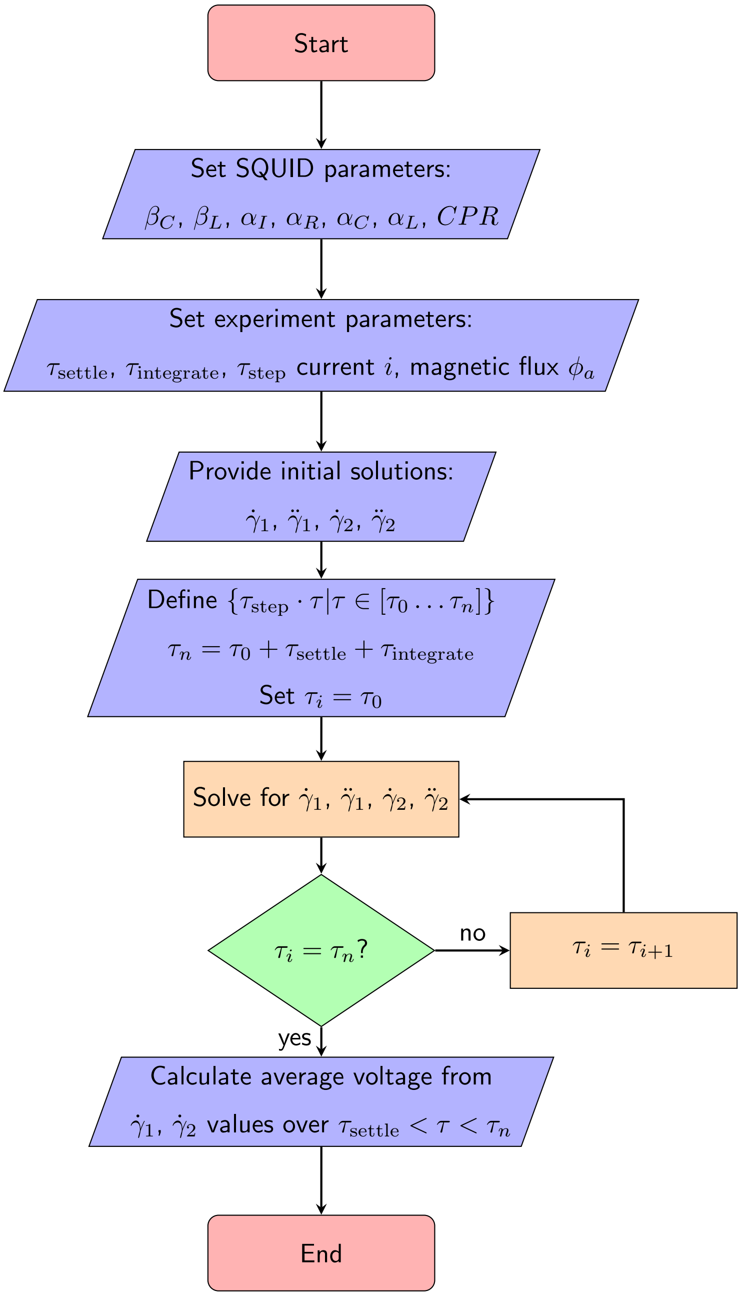


Figure 3.4: A flowchart showing the high-level operation of the algorithm for the numerical solution to the RCSJ SQUID model. Before the simulation begins properly the parameters for the SQUID object are passed from a parameters file, along with the parameters for the experimental conditions. The SQUID parameters are $\beta_C$, $\beta_L$, SQUID type (CPR), and the asymmetry terms $\alpha_{I,R,C,L}$. The experiment parameters are the settling time, integration time, current, applied flux $\phi_a$. The initial solutions to each of the differential equations are first set to zero. A list of time steps is generated based on the settling and the integration time. A voltage is calculated for each time step using the SciPy `solve_ivp` function. The voltage results taken during the settling time are discarded and the remainder are averaged to create the average voltage result for this set of parameters.

Rather than just calculating a single average voltage it is desirable to vary one of the parameters and find out how the system changes its behaviour as a result. Many of the simulations loop through a range of current bias values, imitating the main structure of the experimental measurements, which are mostly based on taking current-voltage characteristic curves.

Beyond that, adding an extra dimension to the measurements is also very useful. To model flux oscillation measurements for example, a IV characteristic is taken at different steps of applied flux $\phi$, as shown in 3.5. Nesting these loops for a simulation will start to take an extremely long time. If each calculation takes an average of 1 minute to complete, a sweep of 1000 points would take about 17 hours. If this were to be repeated through sweeping a second parameter 100 times, it would take about 70 days to complete. Those are rough numbers, but it shows that a nested loop style of simulation is not practical for obtaining detailed results. Instead, parallel computing available through Lancaster University's High End Computing (HEC) cluster was used. This means that in the magnetic flux example, the IV at each flux value is simulated roughly at the same time, depending on the HEC's available resources.

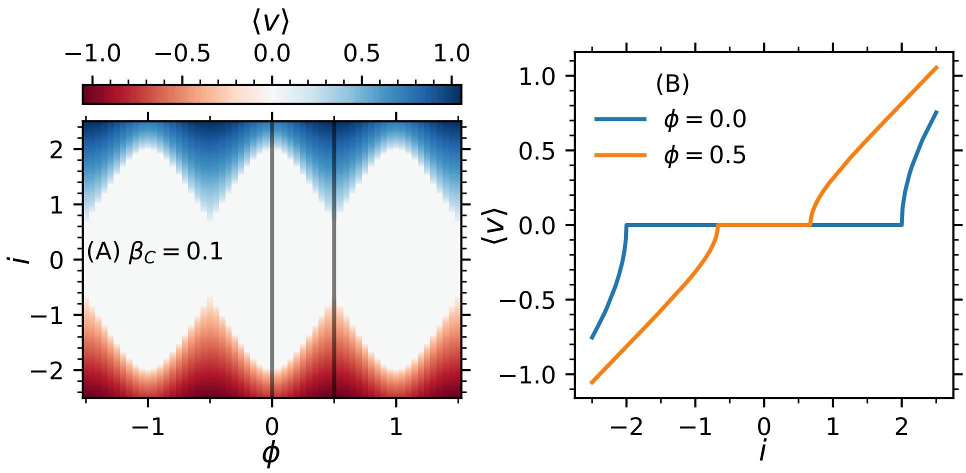


Figure 3.5: Left, a simulated colour plot of an RCSJ SQUID with an ideal current-phase relationship. Flux has been varied to show multiple flux oscillations. Vertical lines show slice positions which are displayed in the line plot to the right. Parameters: $\beta_L = 0.5$, $\beta_C = 0.1$, $\Delta\phi = 0.05$, $\Delta i = 0.01$, $\Gamma = 0$, $i_P = 0$.

## 3.7 Expanding the simulation to include ac current

Shapiro steps in graphene junctions have been measured experimentally, but a question remains as to whether the results shown are supported by current theory, or which theoretical models fit best. To study the potential Shapiro steps in SQUIDs the model needs to be expanded to include an RF driving signal. A similar derivation to section 3.5 will be shown including the new RF component. Then how this was integrated into the Python code will be explained. This part of the code was added to the simulation by the author.

### 3.7.1 Derivation of average voltage with RF driving signal

The practical measurement setup uses a signal generator which produces an ac signal of the form $P\sin(\omega_{\mathsf{RF}}t)$, where $P$ is the amplitude of the signal, $\omega_{\mathsf{RF}}$ is the frequency of the signal and $t$ is time. In the signal generator the user would set the amplitude as a power in dBm and the frequency in GHz. To integrate that into the simulation model it is assumed that the current induced in the SQUID is proportional to the power, resulting in an alternating current defined in terms of a current amplitude and a frequency. In the simulation the induced current is treated as part of the overall current bias, such that the total bias $I = I_{dc} + I_{ac}$. Propagating this adjustment through the derivation is initially straightforward reaching the point of equation (3.19) when converted to dimensionless units.

$$\frac{i_{dc}+i_{ac}}{2} \pm j = (1 \mp \alpha_I)\overline{CPR}(\gamma) + (1 \mp \alpha_R)\frac{\mathrm{d}\gamma}{\mathrm{d}\tau} + \beta_C(1 \mp \alpha_C)\frac{\mathrm{d}^2\gamma}{\mathrm{d}\tau^2} \tag{3.40}$$

The dimensionless ac component $i_{ac}$ is derived by letting $I_{ac} = I_P \sin\omega_{RF}t$, where $I_P$ is the current amplitude due to the power $P$. The current terms are reduced as previously by dividing by $I_c$. The dimensionless time $\tau$ and dimensionless frequency $\nu$ are defined as $\tau = \omega_c t$ and $\nu = \omega_{RF}/\omega_c$. Substituting these into the equation for current gives the dimensionless form

$$i_{ac} = i_P \sin(\nu\tau) \tag{3.41}$$

To continue the derivation of the average voltage, the differential equations which include the ac current term are needed. To do this fully the definition of $j$ needs to be considered again. Earlier, equation (3.34) was determined but this can no longer be considered fully valid because it includes $i$ which has now been redefined. The new starting point is a simple substitution but the derivative $\mathrm{d}j/\mathrm{d}\tau$ cannot be simplified as fully as in (3.35). It is still assumed that the dc bias current and magnetic flux are constant but the ac bias is changing by definition.

$$j = \frac{\gamma_2 - \gamma_1 - 2\pi\phi}{\pi\beta_L} + \frac{\alpha_L}{2}(i_{dc} + i_{ac}) \tag{3.42}$$

$$\frac{\mathrm{d}j}{\mathrm{d}\tau} = \frac{1}{\pi\beta_L}\left(\frac{\mathrm{d}\gamma_2}{\mathrm{d}\tau} - \frac{\mathrm{d}\gamma_1}{\mathrm{d}\tau}\right) + \frac{1}{2}\frac{\mathrm{d}i_{ac}}{\mathrm{d}\tau} \tag{3.43}$$

Substituting this $j$ into (3.40) for junction 1 and gathering some terms together,

$$(1+\alpha_L)\frac{i_{dc}+i_{ac}}{2} + \frac{\gamma_2-\gamma_1-2\pi\phi}{\pi\beta_L} = (1-\alpha_I)\overline{CPR}(\gamma_1)+(1-\alpha_R)\frac{\mathrm{d}\gamma_1}{\mathrm{d}\tau} + \beta_C(1-\alpha_C)\frac{\mathrm{d}^2\gamma_1}{\mathrm{d}\tau^2} \tag{3.44}$$

In this case the equation reduces down to the same form as before the ac was included, except that $i$ has been redefined to include the ac component. Therefore the differential equations are the same as (3.39). The remaining aspect to consider is the average voltage response. Picking back up from (3.30) we have $I$ terms which are redefined.

$$V = V_1 + \frac{L}{2}(1-\alpha_L)\frac{\mathrm{d}}{\mathrm{d}t}\left(\frac{I_{dc}+I_{ac}}{2}+J\right) = V_2 + \frac{L}{2}(1+\alpha_L)\frac{\mathrm{d}}{\mathrm{d}t}\left(\frac{I_{dc}+I_{ac}}{2}-J\right) \tag{3.45}$$

Once again the dc component is assumed to be constant and so can be eliminated when differentiated. This equation also needs to be made dimensionless using the familiar conversions. For clarity the derivation will be shown only for the first junction because the steps are identical for deriving the second junction.

$$\begin{aligned}
V &= V_1 + \frac{L}{2}(1-\alpha_L)\left[\frac{1}{2}\frac{\mathrm{d}I_{ac}}{\mathrm{d}t} + \frac{\mathrm{d}J}{\mathrm{d}t}\right] \\
V &= \frac{\hbar}{2e}\frac{\mathrm{d}\gamma_1}{\mathrm{d}t} + \frac{L}{2}(1-\alpha_L)\left[\frac{1}{2}\frac{\mathrm{d}I_{ac}}{\mathrm{d}t} + \frac{\mathrm{d}J}{\mathrm{d}t}\right]\frac{2I_c}{\Phi_0}\frac{\Phi_0}{2I_c} \\
V &= \frac{\hbar}{2e}\frac{\mathrm{d}\gamma_1}{\mathrm{d}\tau}\frac{2eI_0R}{\hbar} + \frac{L}{2}(1-\alpha_L)\left[\frac{1}{2}\frac{\mathrm{d}I_{ac}}{\mathrm{d}\tau} + \frac{\mathrm{d}J}{\mathrm{d}\tau}\right]\frac{2eI_cR}{\hbar}\frac{2I_c}{\Phi_0}\frac{\Phi_0}{2I_c} \\
V &= I_cR\frac{\mathrm{d}\gamma_1}{\mathrm{d}\tau} + \frac{\beta_L}{2}(1-\alpha_L)\left[\frac{1}{2}\frac{\mathrm{d}i_{ac}}{\mathrm{d}\tau} + \frac{\mathrm{d}j}{\mathrm{d}\tau}\right]\frac{2eI_cR}{\hbar}\frac{\Phi_0}{2} \\
V &= I_cR\frac{\mathrm{d}\gamma_1}{\mathrm{d}\tau} + \frac{\beta_L}{2}(1-\alpha_L)\left[\frac{1}{2}\frac{\mathrm{d}i_{ac}}{\mathrm{d}\tau} + \frac{\mathrm{d}j}{\mathrm{d}\tau}\right]\pi I_cR \\
v &= \frac{\mathrm{d}\gamma_1}{\mathrm{d}\tau} + \frac{\pi\beta_L}{2}(1-\alpha_L)\left[\frac{1}{2}\frac{\mathrm{d}i_{ac}}{\mathrm{d}\tau} + \frac{\mathrm{d}j}{\mathrm{d}\tau}\right] \qquad (3.46)
\end{aligned}$$

and for the second junction

$$v = \frac{\mathrm{d}\gamma_2}{\mathrm{d}\tau} + \frac{\pi\beta_L}{2}(1+\alpha_L)\left[\frac{1}{2}\frac{\mathrm{d}i_{ac}}{\mathrm{d}\tau} - \frac{\mathrm{d}j}{\mathrm{d}\tau}\right] \tag{3.47}$$

so combining the two branches

$$v = \frac{1}{2}\left[\frac{\mathrm{d}\gamma_1}{\mathrm{d}\tau} + \frac{\mathrm{d}\gamma_2}{\mathrm{d}\tau} + \frac{\pi\beta_L}{2}(1-\alpha_L)\left[\frac{1}{2}\frac{\mathrm{d}i_{ac}}{\mathrm{d}\tau} + \frac{\mathrm{d}j}{\mathrm{d}\tau}\right] + \frac{\pi\beta_L}{2}(1+\alpha_L)\left[\frac{1}{2}\frac{\mathrm{d}i_{ac}}{\mathrm{d}\tau} - \frac{\mathrm{d}j}{\mathrm{d}\tau}\right]\right] \tag{3.48}$$

$$v = \frac{1}{2}\left[\frac{\mathrm{d}\gamma_1}{\mathrm{d}\tau} + \frac{\mathrm{d}\gamma_2}{\mathrm{d}\tau} + \frac{\pi\beta_L}{2}\left[(1-\alpha_L)\left[\frac{1}{2}\frac{\mathrm{d}i_{ac}}{\mathrm{d}\tau} + \frac{\mathrm{d}j}{\mathrm{d}\tau}\right] + (1+\alpha_L)\left[\frac{1}{2}\frac{\mathrm{d}i_{ac}}{\mathrm{d}\tau} - \frac{\mathrm{d}j}{\mathrm{d}\tau}\right]\right]\right] \tag{3.49}$$

$$v = \frac{1}{2}\left[\frac{\mathrm{d}\gamma_1}{\mathrm{d}\tau} + \frac{\mathrm{d}\gamma_2}{\mathrm{d}\tau} + \frac{\pi\beta_L}{2}\left[\frac{\mathrm{d}i_{ac}}{\mathrm{d}\tau} - 2\alpha_L\frac{\mathrm{d}j}{\mathrm{d}\tau}\right]\right] \tag{3.50}$$

Now substituting for $\frac{\mathrm{d}j}{\mathrm{d}\tau}$:

$$\begin{aligned}
v &= \frac{1}{2}\left[\frac{\mathrm{d}\gamma_1}{\mathrm{d}\tau} + \frac{\mathrm{d}\gamma_2}{\mathrm{d}\tau} + \frac{\pi\beta_L}{2}\left[\frac{\mathrm{d}i_{ac}}{\mathrm{d}\tau} - 2\alpha_L\left[\frac{1}{\pi\beta_L}\left(\frac{\mathrm{d}\gamma_2}{\mathrm{d}\tau} - \frac{\mathrm{d}\gamma_1}{\mathrm{d}\tau}\right) + \frac{\alpha_L}{2}\frac{\mathrm{d}i_{ac}}{\mathrm{d}\tau}\right]\right]\right] \\
v &= \frac{1}{2}\left[\frac{\pi\beta_L}{2}(1-\alpha_L)\frac{\mathrm{d}i_{ac}}{\mathrm{d}\tau} + \frac{\mathrm{d}\gamma_1}{\mathrm{d}\tau} + \frac{\mathrm{d}\gamma_2}{\mathrm{d}\tau} - \alpha_L\frac{\mathrm{d}\gamma_2}{\mathrm{d}\tau} + \alpha_L\frac{\mathrm{d}\gamma_1}{\mathrm{d}\tau}\right] \\
v &= \frac{1}{2}\left[\frac{\pi\beta_L}{2}(1-\alpha_L)\frac{\mathrm{d}i_{ac}}{\mathrm{d}\tau} + (1+\alpha_L)\frac{\mathrm{d}\gamma_1}{\mathrm{d}\tau} + (1-\alpha_L)\frac{\mathrm{d}\gamma_2}{\mathrm{d}\tau}\right] \qquad (3.51)
\end{aligned}$$

This is now the same as equation (3.36) except for the additional $i_{ac}$ term. However it can be justified that this term can be removed. It is straightforward to compute $\mathrm{d}i_{ac}/\mathrm{d}\tau$ given the definition $i_{ac} = i_P \sin(\nu\tau)$. The result is a cosine waveform that has an amplitude symmetric around 0. Therefore, or for a large enough number of periods (controlled here by the settling and integration times) the average of the function will be very close to 0. This allows the ac term to be neglected in the average voltage calculation. This is assuming that an integer number periods are or not exactly completed, in which case the average would be exactly 0.

$$\langle v \rangle = \left\langle \frac{1}{2}\left[(1+\alpha_L)\frac{\mathrm{d}\gamma_1}{\mathrm{d}\tau} + (1-\alpha_L)\frac{\mathrm{d}\gamma_2}{\mathrm{d}\tau}\right]\right\rangle \tag{3.52}$$

With the result of the average voltage calculation remaining the same as it was previously, including the RF signal is actually quite straightforward, as its impact on the results is wrapped up in $\mathrm{d}\gamma_1/\mathrm{d}\tau$ and $\mathrm{d}\gamma_2/\mathrm{d}\tau$, which are themselves individually calculated in the simulation.

Regarding implementation, the equation to be added to the simulation introduces two new variables, the RF amplitude and RF frequency. Initial changes to the code could be considered 'administrative' which includes setting the new variables up so that they are included as parameters in the SQUID models and can be defined when setting up the experiment parameters, or used as variables to be swept through. The equation will use the same $\tau$ that governs the progress of the rest of the simulation, so no changes are needed in relation to $\tau$. The more 'active' change to the code is how the ac signal will affect the calculations. The ac component will act as part of the total bias current, such that $i = i_{\mathrm{dc}} + i_{\mathrm{ac}}$. In the simulation this corresponds to the $i$ in the ODEs (3.39). Therefore the edit requires redefining the current to add the RF component, changing it from `i = self.i` (where `self.i` is the current value of dc bias) to `i = self.i + (self.rf_amplitude * np.sin(self.rf_frequency * tau))` (where `tau` is the instantaneous time value and `np.sin` is referencing the Numpy library's sine function[124]). This is done in every time step just before the ODEs are calculated. Finally, this format also means that the simulation remains general for the case where no RF is being used. By setting `rf_amplitude` to 0, $i$ reduces back down to only the dc component.

## 3.8 Expanding the simulation to include thermal noise

This section justifies the manner in which noise has been implemented into the simulation. The code for this was already implemented by Jonathan Prance before the author began to work on the simulation.

### 3.8.1 Johnson-Nyquist noise currents in SQUIDs

In experiments noise is limited as much as possible but it is always present in some form. At minimum any signal that is being detected needs to be significantly stronger than the noise floor. It would be useful to know if noise is able to strongly influence the outcome of SQUID experiments. In particular, the effects of temperature are of interest to understand in superconducting systems, so attention moves towards Johnson-Nyquist (JN) noise. This type of thermal noise comes from electrons fluctuating randomly due to additional thermal energy. Generally, the thermal energy of a system receives a contribution of

$$E = \frac{1}{2} k_B T \tag{3.53}$$

per degree of freedom, where $k_B = 1.38 \times 10^{-23}$ J K$^{-1}$ is the Boltzmann constant and $T$ is the temperature. An RCSJ Josephson junction contains a shunt resistor which can be used to model the voltage noise contribution. The resistor gives a power spectral density $S_V$ of

$$S_V(f) = 4 k_B T R \tag{3.54}$$

where $R$ is the resistance [125]. Introduce noise parameter $\Gamma$ which is defined as the ratio of the thermal energy (3.53) to the Josephson coupling energy. This parameter sets a physical limit on how the coupling energy needs to be larger than the thermal energy otherwise the phase difference in a JJ will become unstable and the supercurrent would no longer be supported.

$$\Gamma = \frac{2\pi k_B T}{I_c \Phi_0} \tag{3.55}$$

The noise added to the simulation is based on how the SQUID handbook [92] considers thermal fluctuations in dc SQUIDs (section 2.2.3 of that text). To normalise $S_V$ it is divided by $V_c^2/\omega_c$ which reduces to

$$s_v = 4\Gamma \tag{3.56}$$

To convert to a noise current instead of a noise voltage, one just has to divide (3.54) by the resistance $R$, and then normalise with $I_c^2/\omega_c$, producing an equivalent $s_i = 4\Gamma$.

The random fluctuations of the current due to noise can be modelled as normally distributed additions or subtractions from the bias current. To maintain the power spectral density of $s_i = 4\Gamma$, the width of the distribution $\sigma$ is

$$\sigma = \sqrt{\frac{2\Gamma}{\tau_N}} \tag{3.57}$$

where $\tau_N$ is the time step between noise sampling (set as 0.1 in the simulation).

Thermal noise can be modelled as a kind of Gaussian white noise because it possesses the statistical properties of having zero mean and constant power spectral density. Here, it can be considered as a probability distribution of the dimensionless noise current. Therefore the rms amplitude of a noise signal can be considered proportional to the width of the distribution $\sigma$. To confirm the relationship between the width of the white noise Gaussian and the power spectral density one just needs to consider the bandwidth. The product of the PSD and the BW is equal to the power in the dimensionless case.

$$4\Gamma\frac{1}{2\tau_N} = i_{\text{rms}}^2 \tag{3.58}$$

The bandwidth here is halved to account for the Nyquist frequency which means that the sampling rate ($\tau_N$) needs to be twice as fast as the highest frequency signal being measured. The Gaussian being sampled is the probability that the noise contributes a particular value of current to the system. The rms value of a current is found by averaging the squares of each value the periodic function takes, and then square-rooting the result. Given the mean of zero for Gaussian white noise, this is the same process as calculating the standard deviation. Therefore we can conclude that the standard deviation is equivalent to the rms current, and that (3.57) is true. If still unconvinced, one can sample the current values from a normal distribution with the stated standard deviation, and then calculate the corresponding PSD using Welch's method[126].

To build this into the simulation model, a noise current is added to each branch of the SQUID, because each individual Josephson junction produces its own noise current. The currents $i_{N1}$ and $i_{N2}$ are added to branch 1 and 2 respectively as separate current terms. They are produced every time interval $\tau_N$ by randomly selecting from a normal distribution (`numpy.random.normal`) and scaling the result by the width (3.57). The two noise currents are generated independently so they affect the overall branch currents differently.

$$\frac{i}{2} + j = i_{N1} + (1-\alpha_I)\overline{CPR}(\gamma_1) + (1-\alpha_R)\frac{\mathrm{d}\gamma_1}{\mathrm{d}\tau} + \beta_C(1-\alpha_C)\frac{\mathrm{d}^2\gamma_1}{\mathrm{d}\tau^2} \tag{3.59}$$

$$\frac{i}{2} - j = i_{N2} + (1+\alpha_I)\overline{CPR}(\gamma_2) + (1+\alpha_R)\frac{\mathrm{d}\gamma_2}{\mathrm{d}\tau} + \beta_C(1+\alpha_C)\frac{\mathrm{d}^2\gamma_2}{\mathrm{d}\tau^2} \tag{3.60}$$

This change follows through to appear in the differential equations used in the simulation.

$$\begin{aligned}
\frac{\mathrm{d}\gamma_1}{\mathrm{d}\tau} &= \dot{\gamma}_1 \\
\frac{\mathrm{d}\dot{\gamma}_1}{\mathrm{d}\tau} &= \frac{1}{\beta_C(1-\alpha_C)}\left[\frac{\gamma_2-\gamma_1-2\pi\phi}{\pi\beta_L} + (1+\alpha_L)\frac{i}{2} - (1-\alpha_R)\dot{\gamma}_1 - (1-\alpha_I)\overline{CPR}(\gamma_1) - i_{N1}\right] \\
\frac{\mathrm{d}\gamma_2}{\mathrm{d}\tau} &= \dot{\gamma}_2 \\
\frac{\mathrm{d}\dot{\gamma}_2}{\mathrm{d}\tau} &= \frac{1}{\beta_C(1+\alpha_C)}\left[\frac{\gamma_2-\gamma_1-2\pi\phi}{\pi\beta_L} + (1-\alpha_L)\frac{i}{2} - (1+\alpha_R)\dot{\gamma}_2 - (1+\alpha_I)\overline{CPR}(\gamma_2) - i_{N2}\right]
\end{aligned} \tag{3.61}$$

The current noise is generated at a slower rate than the voltage is calculated. So when calculating an average voltage, each voltage in the set will have been calculated with the same noise current as several others. This means that the integration time has to be long enough that the distribution of noise currents used will be representative of the Gaussian white noise. The standard values used mean that there will be 10 voltages calculated at each noise current value, but 200,000 voltage values are being calculated in total, so 20,000 samples from the noise model are taken which is adequate to be representative.

## 3.9 Simulated results of varying SQUID parameters

In this section, the parameter space of the simulated RCSJ SQUID will be explored in a way analogous to the experiments performed on the physical devices (chapter 5). In the following simulated results, some parameters are standardised across most of the presented plots. The model parameters are partly characteristic parameters intrinsic to the SQUID, and partly the conditions that the SQUID is being exposed to.

In the former case there are three parameters that can be controlled, $\beta_L$, $\beta_C$, and the CPR. The screening parameter $\beta_L = 0.50$ is selected as it is close to the estimate for the high-transparency regime of the Double SQUID from the experimental characterisation in section 5.1.1. The Stewart-McCumber parameter $\beta_C = 0.005$ is chosen because a low capacitance is necessary to ensure Shapiro steps are not suppressed, and that there is no hysteresis. The CPR is a function which can be changed, but mostly the 'skewed' CPR will be used. The skewed function (shown in table 3.1) has a transparency parameter $T_n$ which will be controlled. The usual values will correspond to very high skewness $T_n = 0.999$ and very low skewness $T_n = 0.001$ (see figure 2.12). Comparing high and low transparency of the CPR will be the focus of section 3.9.1.

In the case of measurement conditions there are several more parameters to control. Applied magnetic flux $\phi$ is defined as the number of flux quanta in the SQUID loop, as in (3.23). The value is set to either $0$ or $0.5$ representing integer and half integer flux quanta respectively. Due to constraints on time and scope, the focus is largely on the effects taking place at integer flux quantum where additional effects of half-integer flux like additional fractional steps are avoided.

The noise parameter is set to $\Gamma = 0$ for simulations which are excluding noise. Noise is only used in simulations which are intended to explore the effects of the noise, in which case the values are specified.

There are two parameters associated with applying an RF signal: the dimensionless power $i_P$ and frequency $\nu$. When an RF signal is not being applied, $i_P = 0$. If Shapiro steps are being measured, $i_P = 10$ will be typical so that steps are clear, unless the power is being varied. The typical dimensionless frequency value $\nu = 1$ mostly for convenience, because it means that the average voltages calculated are already spaced for their corresponding Shapiro step values. It also affects the range and step size of bias currents required to view multiple Shapiro steps. These default values have been summarised in table 3.2, but the parameters are also included in the plot captions.

| Parameter | Default Value |
|---|---|
| $\beta_L$ | 0.50 |
| $\beta_C$ | 0.005 |
| $\phi$ | 0 |
| $\Gamma$ | 0 |
| $i_P$ (RF Amplitude) | 10 (0) |
| $\nu$ (RF Frequency) | 1 |

Table 3.2: Default values for simulations when the parameter is not otherwise shown in a plot. RF signal power $i_P$ is set to 0 when no RF signal is desired. All asymmetry parameters $\alpha_I = \alpha_R = \alpha_C = \alpha_L = 0$ for all simulations.

Finally, the main independent variable in the model is the dimensionless bias current $i$, and the output value from the model is the average voltage for a particular combination of parameters. This makes the basis of each simulation a IV characteristic curve, with additional dimensions depending on how the other experimental parameters are varied and controlled.

### 3.9.1 Effect of transmission probability

The skewness of the CPR is controlled by using the skewed CPR function (from table 3.1) and varying the transparency parameter $T_n$. The range of values is $0 < T_n < 1$. This section shows the effect of very high and very low skew in three situations. Firstly, the effect on a flux oscillation plot with no RF signal. Then, the equivalent but with a constant RF signal. After that, the magnetic flux is fixed and the amplitude of the RF signal is varied. Using these plots, the qualitative effects of changing the skewness of the CPR are shown.

#### Flux oscillations with only dc bias

To show the basic effect of changing the transparency one can look at the flux dependence of the critical current. Figure 3.6 shows that at low transparency (sinusoidal CPR) there is very small superconducting gap at the critical current minima compared to the high transparency case. In effect, the 'depth' of the oscillation $i_d$ is reduced for high skewness.

$$i_d = \frac{i_{c\ \mathrm{max}} - i_{c\ \mathrm{min}}}{i_{c\ \mathrm{max}}} \tag{3.62}$$

This is similar to what happens from increasing the value of $\beta_L$, which also shows an increased critical current minimum. The other notable change is in the shape of the boundary between the superconducting region and the resistive region. The critical current dependence is clearly parabolic in the low transparency case whereas it appears to have more linear regions when highly transparent.

As seen experimentally in figure 5.1, increasing transparency of the junctions correlates with an increase in the maximum critical current of the SQUID. This is not apparent in the simulated data because the simulation parameters are normalised in such a way that the maximum critical current stays the same. In the dc flux oscillation plots in figure 3.6, the expected behaviour of a SQUID is shown. The critical current maximum is found at integer multiples of the magnetic flux quantum, which is the expected value of 2 for this model. The minimum critical current values are at half-integer flux quantum values. The minimum can depend on the screening parameter $\beta_L$ and the skewness of the SQUID's current-phase relation. This is a periodic behaviour with a period of one flux quantum.

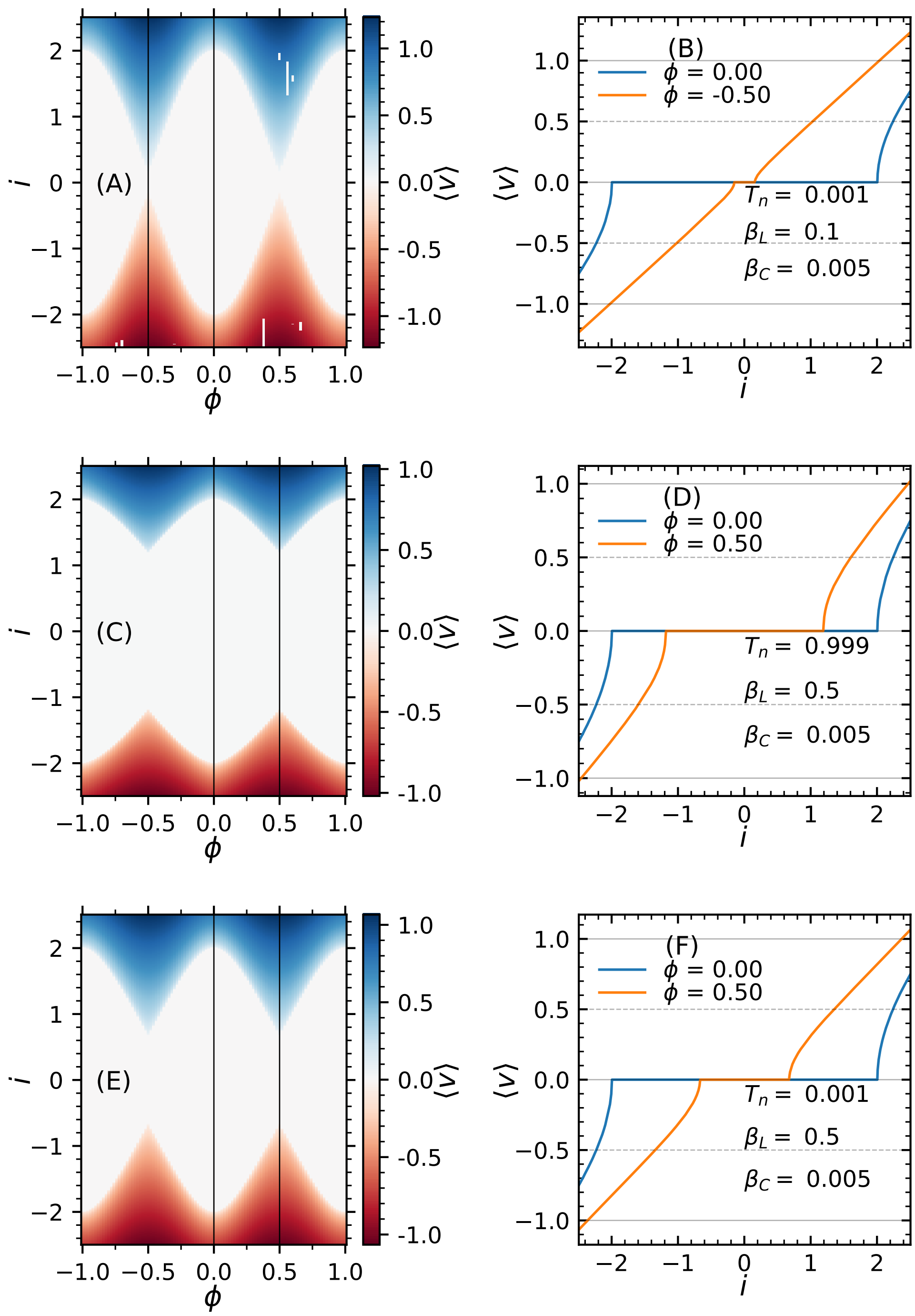


Figure 3.6: Colour plots of the average voltage response of a SQUID depending on magnetic flux and bias current. Vertical black lines indicate the slices shown in the associated line plots. On the line plots, the blue and orange lines correspond to integer and half-integer values of flux respectively. Subplot pairs have different combinations of CPR skewness and $\beta_L$. Plots (A) and (B) have $\beta_L =$ 0.1 and transparency $T_n =$ 0.001. This can be compared to (E) and (F) which also have $T_n =$ 0.001 but have $\beta_L =$ 0.5. Plots (C) and (D) compare with (E) and (F) with the same $\beta_L$ but (C) and (D) and highly transparent with $T_n =$ 0.999. Graph (A) is sliced at the equivalent point of $-0.5$ rather than $0.5$ to avoid artifacts in the simulation. For the slice at $+0.5$ see figure A.1 in the appendix. Constant parameters: $\beta_C = 0.005$, $\Delta\phi = 0.02$, $\Delta i = 0.005$, $\Gamma = 0$, $i_P = 0$.

#### **Flux oscillations with RF signal**

The simulations of most interest include ac current components, where Shapiro steps can be observed. In practice, a comparison of different $T_n$ can be achieved by comparing IV characteristics at different gate voltages in a graphene SQUID. It is expected that fractional Shapiro steps can be observed in a system with a highly skewed CPR[116].

Performing the flux oscillation plots again but with an RF signal applied allows a pair of effects to be investigated. It is expected that half-integer Shapiro steps will appear in any SQUID that has a half-integer flux quantum passing through it[117]. This is a separate mechanism to the one which causes half-integer steps to appear due to the CPR.

Figure 3.7 contains the plots which show flux oscillations under RF irradiation. In the low transparency case, at integer flux, Shapiro steps appear only in integer steps. At half-integer flux, half-integer steps also appear. The size of the steps at half-integer flux steps is small compared to the steps at integer flux. This is seen quite clearly on the colourplots, when the colour is constant it corresponds to a step. One can also see that the half-integer Shapiro step grows gradually from not being visible at integer flux, to their maximum width at half-integer flux.

In the high transparency case, half-integer steps are visible for both integer and half-integer flux. The width of the half-integer steps at half-integer flux is larger than the equivalent steps at integer flux. This could be because the step is appearing from multiple sources: the mechanism associated with half-integer magnetic flux, and the mechanism associated with a skewed CPR. The integer steps are still larger for the integer flux, like in the low transparency case.

The other notable effect in the highly skewed case is the apparent further fractionalisation of Shapiro steps, which seems to show steps present down to the resolution of the current step size. This verifies simulations by other groups that show fractional steps in skewed CPR JJs which are qualitatively similar in appearance[83]. For now, it is at least possible to highlight the steps appearing at $\pm 0.25$ and $\pm 0.75$. These are wide enough that they are certainly made up of more than one point on the $i$ scale, so are not artifacts of the simulation. They are also seen in both flux slices, being consistently larger for half-integer flux. This could be again be because they are benefiting from two voltage quantisation mechanisms, as mentioned for the regular half-integer steps. However, given that no fractional steps below half-integer are visible in the low-transparency case suggests that it is the skewed CPR which is the main cause.

Within one integer step there is not symmetry around the half-integer step. However, the fractional steps are symmetrical around 0. One explanation for this could be related to the RF amplitude, as it is shown in Shapiro maps such as in figure 3.8 that plateaus corresponding to Shapiro steps appearing at increasing currents are offset along the RF amplitude axis. This is also reflected in the experimental measurements, as shown figure 5.27). Additionally, only the first step is shown in figure 3.7, which also contains the transition from the superconducting state, which is different to the way the IV normally transitions out of a Shapiro step. Fractional steps smaller than $1/2$ have been reported previously in simulations and experiments on Josephson junctions[120, 127, 128] in experiment and simulation, but this model is a promising way to investigate them further in SQUIDs because the conditions can be made completely arbitrary.

Overall, these plots make it clear that there is a substantial effect of changing the skewness of the CPR of an RCSJ SQUID. Both plots have the same resolution of bias current step, confirming that the steps are not just hidden in the low skewness case.

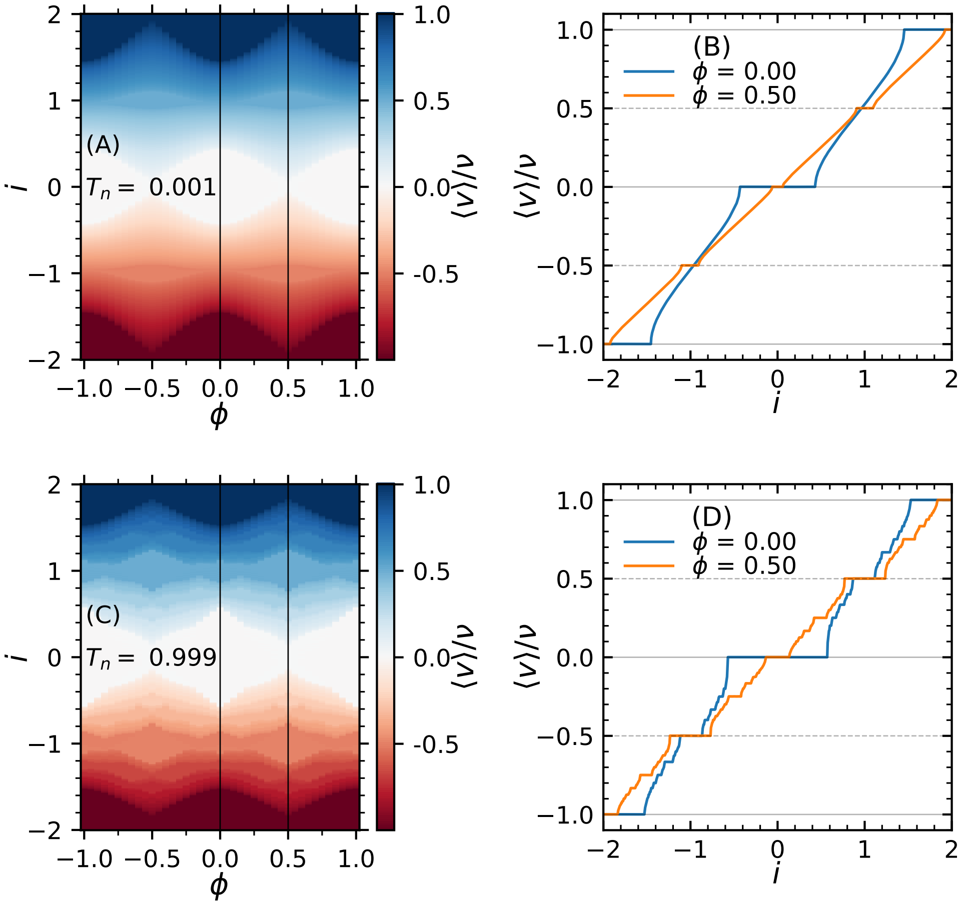


Figure 3.7: Colour plots of the applied flux dependence of the average voltage of a current-biased SQUID, under irradiation by an ac signal. The upper pair of plots are simulated results for low $T_n = 0.001$, while the lower plots are for high $T_n = 0.999$. The slices taken are indicated by the vertical black lines on the colour plot, and are shown on the line graphs to the right. On the line plots, the blue lines correspond to integer values of flux, and the orange lines correspond to half-integer values of flux. Parameters: $\beta_L = 0.5$, $\beta_C = 0.005$, $\Delta\phi = 0.05$, $\Delta i = 0.005$, $\Gamma = 0$, $i_P = 10$, $\nu = 1$.

#### Maps of IV against RF signal amplitude

The RF amplitude dependence of the IV characteristic shows bands corresponding to different $n$ integer Shapiro steps. This is shown in figure 3.8 along with slices to show Shapiro steps observed at a particular RF signal amplitude. These plots are all at integer values of magnetic flux, which have already been shown not to display half-integer steps when at low skewness. As with 3.7, half-integer steps are only visible for high $T_n$, once again with some apparent steps at smaller fractional quantities.

The shape of RF amplitude-IV maps with different transparency CPRs is consistent for if they each have a large enough range of current and amplitude to show two main regimes. At low amplitude, the superconducting region extends out with the critical current variation following a curve which levels out at the critical current value for the SQUID when not exposed to an RF signal. At higher amplitudes, small oscillations of the size of voltage plateaus are seen, and as the corresponding step sizes appear to get smaller as the amplitude increases. These plots are qualitatively similar to the experimental data shown for low skewness in figure 5.27. It is difficult to compare them directly, especially as their respective current ranges cover a different number of Shapiro steps. In principle, however, it should be possible to make the experimental results dimensionless following the same principles used for the simulation, as long as all of the relevant device parameters are calculated. One parameter which would be more difficult to know well for the measured devices is the skewness of the CPR, which instead may need to be treated as a fitting parameter.

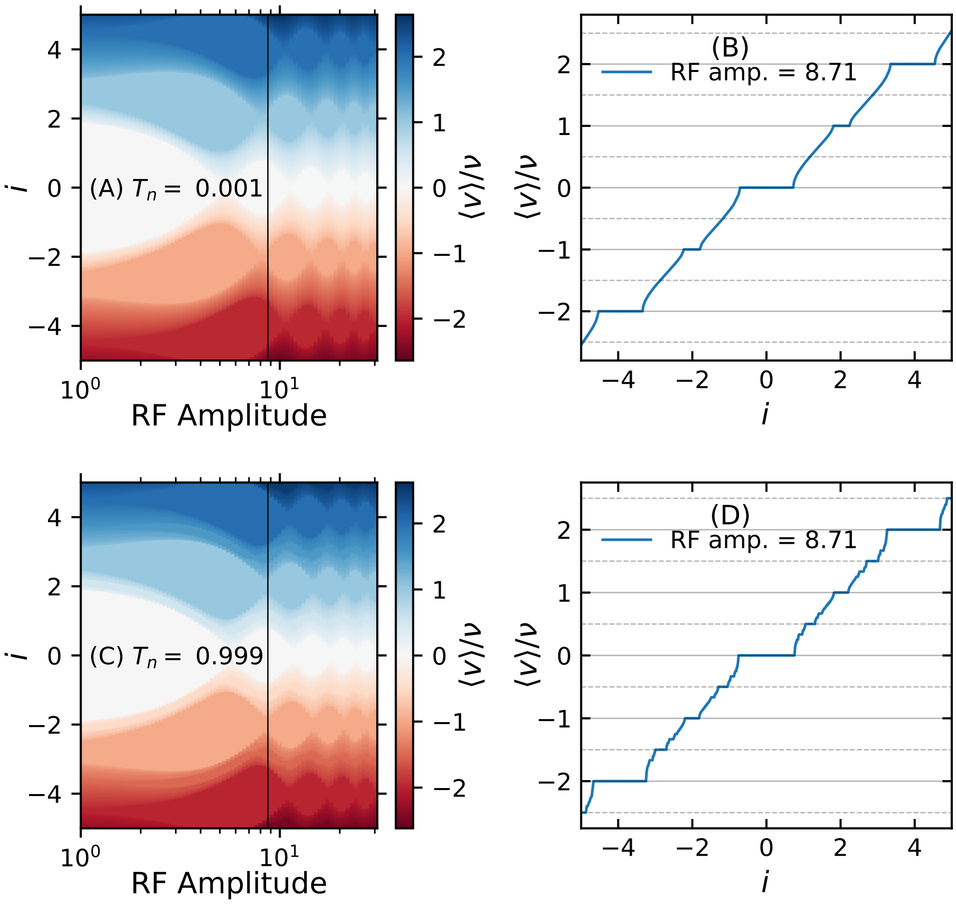


Figure 3.8: Colour plots showing simulated power dependent IVs for different $T_n$ values. To the right of each colour plot is a slice taken at the point indicated by the black vertical line. The upper plots are for low $T_n = 0.001$ corresponding to an effectively sinusoidal CPR. The lower plots correspond to a highly skewed CPR with $T_n = 0.999$. Horizontal lines indicate the expected positions of integer (solid) and half-integer (dashed) Shapiro steps. Parameters: $\beta_L = 0.5$, $\beta_C = 0.005$, $\phi = 0.0$, $\Delta i = 0.005$, $\Gamma = 0$, $\Delta i_P = 0.02$, $\nu = 1.0$.

Figure 3.9 shows slices at $i_P = 6.31$ for three different transparency values. As the transparency of the CPR increases, half-integer steps appear and get wider. Additional fractional steps also appear at the highest $T_n$ values. This clearly shows that the characteristics of fractional Shapiro steps are at least partly related to the skewness of the SQUID CPR, as that is the only parameter which is changed.

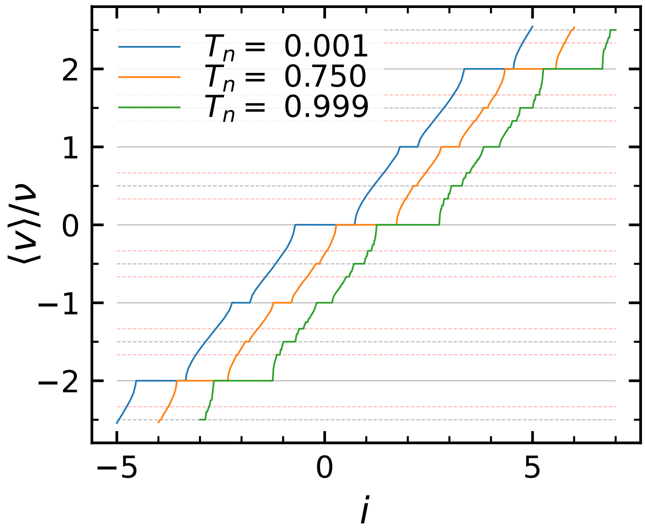


Figure 3.9: Line plots of simulated SQUID voltage scaled for Shapiro steps against bias current for a fixed RF power and integer flux. To convert to Shapiro step spacing, the average voltage $\langle V \rangle$ is divided by the frequency $\nu$ of the ac current component. Individual lines are for different $T_n$ values in the skewed CPR. Lines have been offset in the x-direction by $+0$, $+1$, and $+2$ respectively for clear comparison. Black dashed lines indicate the position of half-integer Shapiro steps, visible in the $T_n =$ 0.750 and $T_n =$ 0.999 plots. Red dashed lines indicate the position of one and two thirds-integer steps, visible for $T_n =$ 0.999. Slices are taken from the equivalent plots in figure 3.8 at an RF amplitude of 6.31. Parameters: $\beta_L = 0.5$, $\beta_C = 0.005$, $\phi = 0.0$, $\Delta i = 0.005$, $\Gamma = 0$, $\nu = 1.0$.

The RF amplitude is clearly a very important parameter in determining the behaviour of Shapiro steps. The periodicity in the step size it creates means that it is not simple to correlate, for example, a small power with large steps. This means that taking a Shapiro map like this is very useful for planning further measurements where viewing Shapiro steps is part of the objective.

The largest steps are close to the point where the superconducting region closes in on zero current, at the lower end of the power scale. To measure steps in this vicinity it would be possible to use a lower current resolution, but a wider range of bias values would be needed to see multiple steps compared to the higher power regions. It is not usually preferred to take lower resolution measurements but it might be a consideration made if measurement or simulation time was limited.

### 3.9.2 Effect of noise current

Thermal noise in the SQUID can be modelled using the noise current parameter $\Gamma$. In general, adding noise to the simulation adds a smoothing or broadening effect to the data. This effect is greater for a larger noise current, and this would correspond to a higher temperature in a real device. It is expected

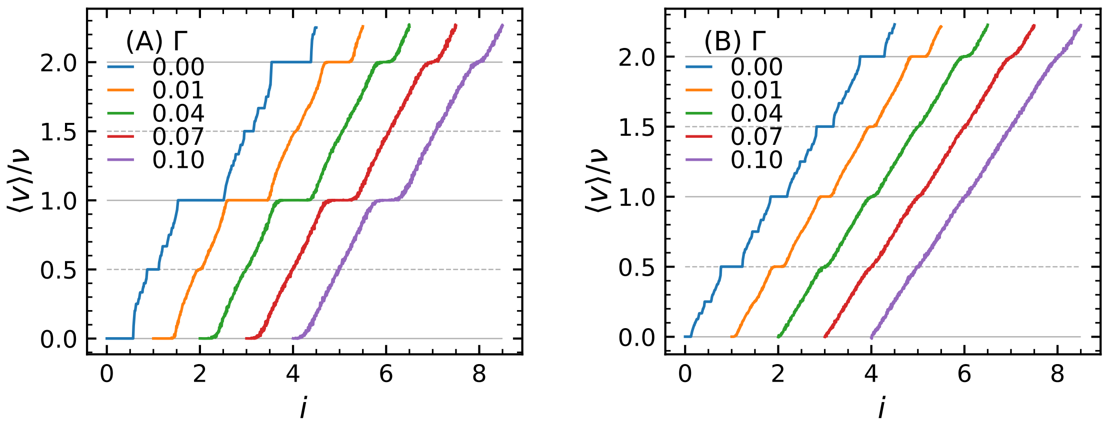


Figure 3.10: Line plots of simulated SQUID voltage scaled for Shapiro steps against bias current for a fixed $i_P = 10$ and $\nu = 1$. (A): integer flux ($\phi = 0.0$). (B): half-integer flux ($\phi = 0.5$). Individual lines are for different $\Gamma$ values in the skewed CPR ($T_n = 0.999$). Lines after the first (blue, $\Gamma = 0.00$) are offset by $+1$ in the x-axis with respect to the previous line. Parameters: $\beta_L = 0.5$, $\beta_C = 0.005$.

that the dominant source of noise would be Johnson-Nyquist noise, so a corresponding temperature should be straightforward to calculate using (3.55).

The main objective of testing the noise in the simulation is to get an idea of how increasing noise in the SQUID affects integer and half-integer Shapiro steps which were previously observed. The noise quantity will give an approximation of the thermal noise, which could be useful when interpreting the results of temperature-dependent experimental data.

Figure 3.10 shows the effect of increasing thermal noise current on Shapiro steps in a SQUID with a highly skewed CPR. The lines with no noise ($\Gamma = 0$) show familiar features. There are integer, half-integer and further fractional steps visible. Adding a small noise current has an immediate and obvious effect. Transitions into and out of steps are smoothed, which has the effect of hiding any smaller fractional steps. As noise increases this effect also increases, quickly the half integer steps also appear to vanish. Steps which were initially wider remain visible for longer. These curves with noise present are much more representative of the curves which are observed in the experimental data. For comparison, figure 5.16 shows the smoothing and suppression of the steps as temperature increases. Results for integer and half-integer flux are both relevant in this system, as the flux values affect the size of the Shapiro steps. At integer flux, the integer steps are very wide compared to the half-integer steps. But at half-integer flux, both types of steps are similar in width.

Another interesting effect of the noise current is the apparent suppression of the critical current. At low noise there are clear regions where the SQUID is superconducting, but as the noise increases, the transition takes places over a longer range, and the range that the average voltage stays at zero is reduced. This effect may be seen more clearly if the simulations were repeated from negative bias through to positive, so that the full range of the superconducting state can be seen.

The width of a Shapiro step appears as the range of bias currents which produce the same quantised voltage. The current values displayed on the x-axis are the dc components of the bias current which don't include the components from the RF signal or noise. The ac and noise values change with time so the total current producing the SQUID voltage is unknown but must be confined within the width of a step, as a current which could fluctuate beyond a step would create voltage spikes in the IV. The steps are the only part of the IV which receive a contribution from the RF signal resonating with the junction. So everywhere else should only be influenced by the noise, though the noise will also affect the step.

A possible drawback with these results is that at high temperature the highly skewed CPR used in the simulation is no longer completely valid (see section 2.2.3), and would need to be modelled with a less skewed model, or eventually an ideal sinusoidal model. However, it is also unclear what temperature the parameter $\Gamma$ corresponds to, so it could be that here the skewed CPR is still a reasonable approximation. Additionally, there may be other sources of noise in a real device. This could include $1/f$ noise[129, 130], but it is not expected to be significant compared with the thermal noise. Thermal noise takes effect over a much wider range of frequencies than $1/f$ noise meaning that for the majority of applications it is the most relevant noise source to consider[92]. Furthermore, the RCSJ simulation presented here assumes an ideal device with point-contact JJs. The origin of $1/f$ noise is trapped flux or defects and impurities in the superconducting material or the JJs[92]. Therefore, it would be complex to implement this source of noise here, whereas the thermal noise is intrinsic to the device and can be well described. As seen in figure 3.10, thermal noise is itself sufficient to modify the appearance of Shapiro steps, so additional noise sources would be unlikely to add much to these results.

#### Temperature estimate from noise current

It can be useful to have an idea of the rough temperature that the noise value in the simulation would correspond to in a real device. A simple estimation can be made from the definition of $\Gamma$ in (3.55). Most of the values are constants, with only the temperature $T$ and the critical current $I_c$ that could be different. For a specific characterised device it should be possible to estimate the critical current to an order of magnitude which would therefore enable the temperature estimate.

Rearranging (3.55) gives

$$T = \frac{I_c \Phi_0 \Gamma}{2\pi k_B} \tag{3.63}$$

and using broadly rounded values of $\Phi_0 = 2 \times 10^{-15}$ Vs, $k_B = 1 \times 10^{-23}$ J K$^{-1}$, and $\pi = 3$ the resulting formula is

$$T \approx 3 \times 10^7 I_c \Gamma \quad \text{K} \tag{3.64}$$

For the Double SQUID at high gating, $I_c = 10$ μA will be assumed. From figure 3.10(A), half-integer steps are already being reduced substantially for $\Gamma = 0.01$, and are gone by $\Gamma = 0.04$. This corresponds to a temperature range of 3-12 K. This order of magnitude is not unreasonable given the temperature measurements taken in section 5.2.2, but the range based on the simulations performed is too large. It also highlights limitations with the simulation model, which are from the simulation having no temperature parameters. This means the integer steps will continue up to temperature implied by the noise which are much higher than critical temperature of an actual SQUID.

### 3.9.3 Effect of RF frequency

Simulations were performed in the highly-skewed CPR regime, varying the RF frequency. All other parameters took default values. This was to see if the simulation would yield any different behaviours over a range of frequencies. Fundamentally it was expected that Shapiro steps should continue to appear, but spaced proportionally to the frequency value used. This can be verified in this dimensionless space by dividing the voltage response by the frequency value $\nu$, equivalent to dividing by $hf/2e$ for an experimental device.

In general, the variation of frequency gave the expected outputs. Integer and half-integer Shapiro steps appeared in all cases for both flux values. Results for $\nu = 0.5$ and $\nu = 2.0$ are shown in figure 3.11. It is difficult to compare these curves directly because of the different current ranges required to resolve the steps at different frequencies. However, for the lowest frequency tested ($\nu = 0.1$) the results featured an offset in the dc voltage. This offset was approximately 0.25 above the corresponding voltage step integer. This effect was reproduced in a simulation with the same parameters but higher resolution to confirm that it was not 'accidental', or a result of error processing the data. Additionally, reversing the direction of the current sweep led to identical results, as shown in figure 3.12. The presence of an offset raises a point of interest because dc offsets have been seen in the results of the experimental measurements. These were previously considered an experimental artifact associated with the measurement but may warrant further investigation.

Further simulations were performed to explore this more. By varying the frequency used in the simulation it was found that offset gets smaller until vanishing as the frequency used increased. This is summarised in tables 3.3 and 3.4.

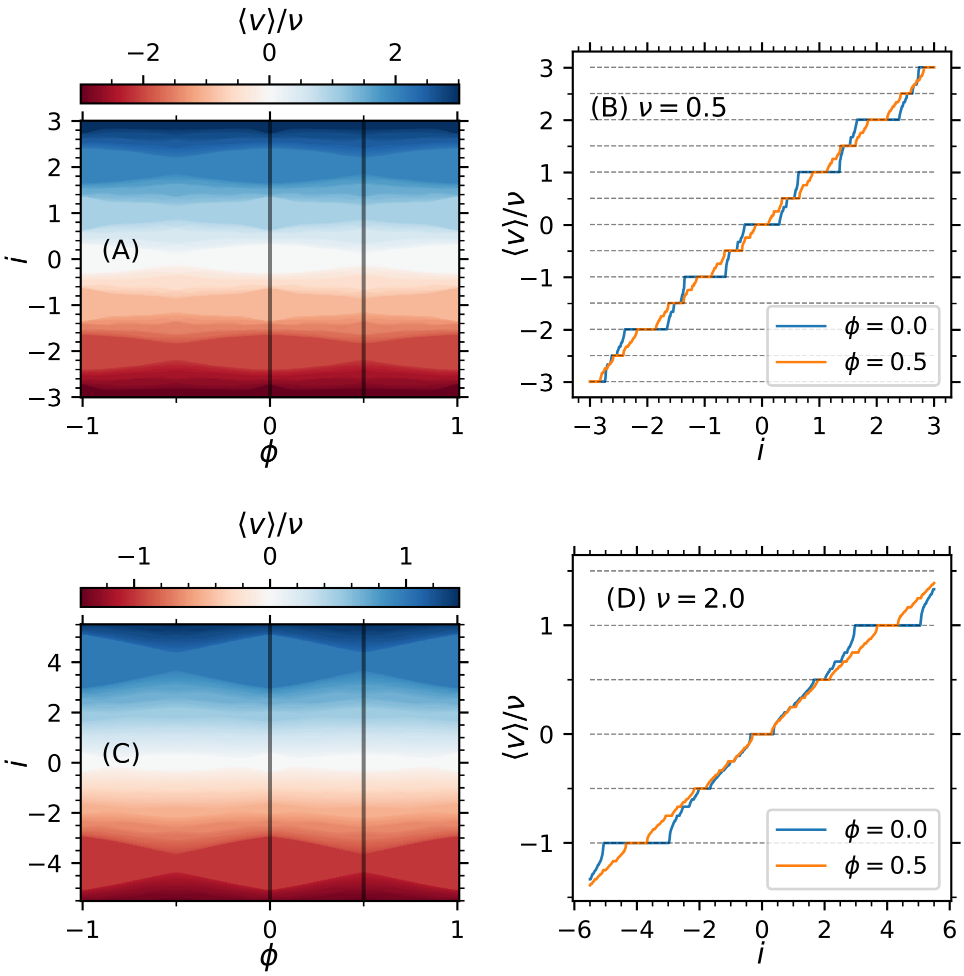


Figure 3.11: Colour plot and slices of voltage response dependence on current and flux under RF irradiation for $\nu = 0.5$ (top) and $\nu = 2.0$ (bottom). The slices are taken at integer and half-integer flux quanta, and are displayed on the right hand side. The horizontal dashed lines indicate the position of integer and half-integer voltage steps. Parameters: $\beta_L = 0.5$, $\beta_C = 0.005$, $\Gamma = 0$, $i_P = 10$.

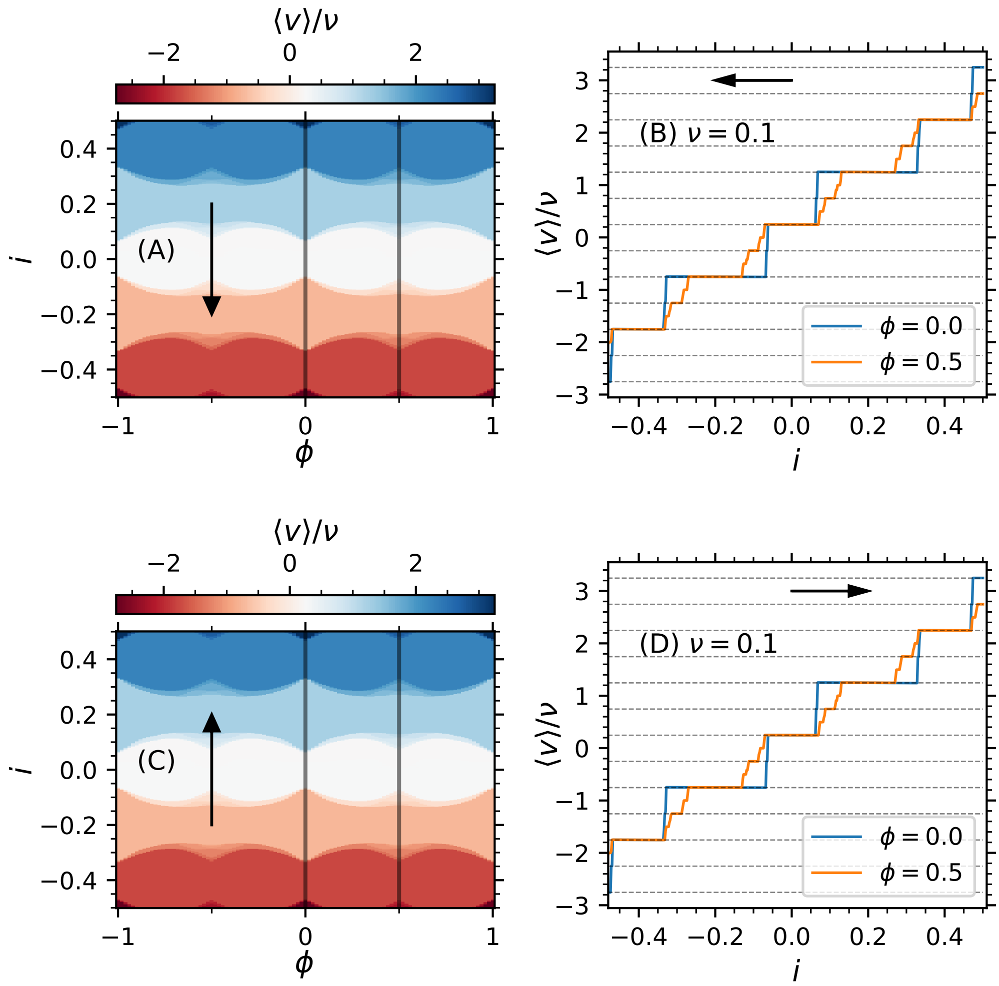


Figure 3.12: Colour plot and slices of voltage response dependence on current and flux under RF irradiation for $\nu = 0.1$. The slices are taken at integer and half-integer flux quanta, and are displayed on the right hand side. The horizontal lines denoting integer and half-integer steps are aligned with the voltage steps rather than the integers on the y-axis scale. This is to highlight the appearance of an offset in the dc voltage response while still confirming the correct spacing between steps. The black arrows show the direction of the $i$ parameter sweep. Parameters: $\beta_L = 0.5$, $\beta_C = 0.005$, $\Gamma = 0$, $i_P = 10$.

| Frequency | Integer steps | Half-integer steps | Fractional steps | Offset |
|---|---|---|---|---|
| $0.05$ | Even only | No | No | 1.36 |
| $0.08$ | Yes | No | No | 0.29 |
| $0.1$ | Yes | Barely resolved | No | 0.22 |
| $0.15$ | Yes | No | No | 0.1 |
| $0.5$ | Yes | Yes | Yes | 0.0 |
| $2.0$ | Yes | Yes | Yes | 0.0 |

Table 3.3: Summary of the appearance of integer, half-integer, and further fractional steps for different frequencies of ac drive current, for RCSJ SQUID with integer flux in the loop. Half-integer and further fractional steps are visible for higher frequencies of 0.5 and above. The voltage offset gets smaller at higher frequency, and is not present for frequency of 0.5 and above. Corresponding plots are in section 3.9.3 and appendix A.1.

| Frequency | Integer steps | Half-integer steps | Fractional steps | Offset |
|---|---|---|---|---|
| $0.05$ | Yes | Yes | No | 1.36 |
| $0.08$ | Yes | Yes | No | 0.29 |
| $0.1$ | Yes | Yes | Yes | 0.22 |
| $0.15$ | Yes | Yes | Yes | 0.1 |
| $0.5$ | Yes | Yes | Yes | 0.0 |
| $2.0$ | Yes | Yes | Yes | 0.0 |

Table 3.4: Summary of the appearance of integer, half-integer, and further fractional steps for different frequencies of ac drive current, for RCSJ SQUID with half-integer flux in the loop. Half-integer steps are visible for frequencies of 0.05 and above, and further fractional steps are visible for higher frequencies of 0.1 and above. The voltage offset gets smaller at higher frequency, and is not present for frequency of 0.5 and above. Corresponding plots are in section 3.9.3 and appendix A.1.

## 3.10 Simulation chapter conclusions and future work

The simulation supported the hypothesis that half-integer steps can appear in devices with either a weakly or strongly skewed current phase relationship by applying magnetic flux that is a non-integer multiple of the magnetic flux quantum, to maximum effect at half integer flux. The simulations also show that there are combinations of SQUID parameters which cause half-integer Shapiro steps to appear through a separate mechanism, only in devices with strongly skewed current-phase relationships.

Additional observations would require further work to understand fully. Firstly, the appearance of further fractional Shapiro steps, which are linked to the strongly skewed CPR, and likely to emerge from higher harmonics of the CPR matching the driving frequency. These steps could be difficult to study in an experimental system because they appear to be quite short, especially if the IV curve is being quantised at many points. Resolving the steps would require extremely high resolution current control, but would more likely be limited by the thermal noise in the system, which has been shown to quickly suppress small steps. Therefore, simulation may offer a more convenient way to study these features in more detail, as frequency and current values can be set arbitrarily.

This leads into the second extension of the investigation. The frequency dependence testing so far has revealed an effect that has not been accounted for: a dc offset of the low frequency Shapiro steps. It was found that with high enough frequency the offset disappears, but it is not clear how this originates from the model, and whether it corresponds to the experimental offsets observed. This next needs to be investigated from the experimental side.

Another requirement in general will be to characterise the Shapiro steps in better detail by measuring their width. This can be dependent on many factors, including frequency. Determining these behaviours in as much detail as possible is necessary to understand the full picture of SQUID behaviour. For example, it has been reported that fractional steps below half are more likely to appear for higher frequencies[116], though for the frequencies tested here down to $\nu = 0.1$ apparent quarter steps are still visible. These two cases are not directly comparable for several reasons, but the important point is that the exact behaviour of the system is dependent on multiple factors. This complicates the task because the number of variables that can be controlled creates a huge parameter space to explore. One limitation of the simulation is that trying to do extremely high resolution measurements may mean that very small numbers need to be used in the simulation which can extend the simulation time and sometimes a solution will not be found for a particular combination of parameters.

Overall, general RCSJ SQUIDs are well modelled by the simulation, which shows promise for a detailed exploration of these systems, particularly by being able to customise the current-phase relation. The next chapter contains experimental work investigating fractional Shapiro steps in graphene SQUIDs. In relation to that, it would also be valuable to convert between the dimensionless simulation and real device parameters for more direct comparison between the simulations and experiment.

# Chapter 4

# Fabrication and measurement of graphene SQUIDs.

This chapter will detail the construction of two graphene SQUIDs and the experimental apparatus used to measure them. It will also summarise the types of measurements performed to characterise the devices. The experiment setup includes the low temperature sample environment and electronic circuits used for the measurements. The experiment types can be broadly categorised as 'dc' and 'radio frequency' (RF). There is a lot of common ground between the two but they serve different purposes, and it is important to consider both because of the applications that RF electronics are used in. While RF is a common term used for high-frequency electronics, it should be noted that the components used in this work could also support microwave frequencies up to 18 GHz.

## Contents

## 4.1 Fabrication details of measured devices

Both of the devices discussed in this thesis were fabricated by collaborators at the National Graphene Institute (NGI) at the University of Manchester, UK. The 'Double SQUID' was designed and made by Moshe Ben Shalom in the group of Andre Geim, and the 'Big SQUID' was designed by the author and made by Wendong Wang in the group of Roman Gorbachev.

They share some common characteristics in their fabrication which will be explained here to save repetition. They both use a stack of monolayer graphene encapsulated in hexagonal boron nitride (hBN) on top of a silicon substrate. The hBN flakes and graphene monolayer are mechanically exfoliated and stacked to form a van der Waals heterostructure. The same heterostructure is used for both superconductor-graphene-superconductor (SGS) junctions in the SQUID. The graphene is mechanically exfoliated to maximise the quality of the material, and encapsulating it with hBN serves a few different purposes. Firstly, the hBN can act as a protective layer on either side, stopping the graphene from being contaminated. Secondly, more control is possible when forming the contacts between the electrodes and the graphene to make very low resistance edge-contact. To do this, electron-beam lithography (EBL) is used to pattern the hBN for reactive ion etching (RIE) which exposes the very edge of the graphene. Because hBN is atomically flat, this ensures that the graphene monolayer is also flat, so that when the superconductor is sputtered to make the electrodes it forms a very thin 1D contact with the graphene. Thirdly, the hBN flake between the graphene and the substrate is a dielectric which allows the substrate to be used as a gate to apply an electric field to the graphene and control the charge carrier concentration. However, the silicon dioxide layer on top of the substrate is thicker than the lower hBN layer with a similar dielectric constant, so this contributes more to the field effect, and would mean that the hBN is not essential to enable the gating in this case.

### 4.1.1 Double SQUID

The 'Double SQUID' is a device with two similar SGS SQUIDs. Measurements were performed on the 'top' SQUID of this pair, see figure 4.1. The full photo showing all the devices is included in the appendix in figure B.1.

The overall structure of the device is $50$ nm thick niobium-titanium electrodes on a silicon dioxide substrate ($290$ nm oxide layer on doped silicon) forming a SQUID loop with the junctions formed by making edge contact with monolayer graphene encapsulated in hexagonal boron nitride. The junctions made this way are $5$ µm wide and $250$ nm long. Lastly, the bottom flake of hBN acts as a dielectric between the doped silicon substrate and the graphene, allowing the substrate to be used as a gate to apply an electric field to the graphene and control its carrier concentration.

This sample also has flux bias lines which run alongside the SQUIDs and can be used to generate a localised magnetic field by applying a current to them. The generated magnetic field lines would be perpendicular to the substrate as they pass through the SQUID loop because the flux bias lines lie on the same plane. The flux bias line has a field constant of approximately $200$ µA per $\Phi_0$, so the number of flux oscillation periods which could be measured is limited to about 10 if the maximum current in the bias line is $\pm$ 1 mA, chosen to avoid excess heating of the device. This would be an adequate number of flux quanta for some investigations, but the small loop area allows the superconducting magnet to be used and still obtain very stable traces.

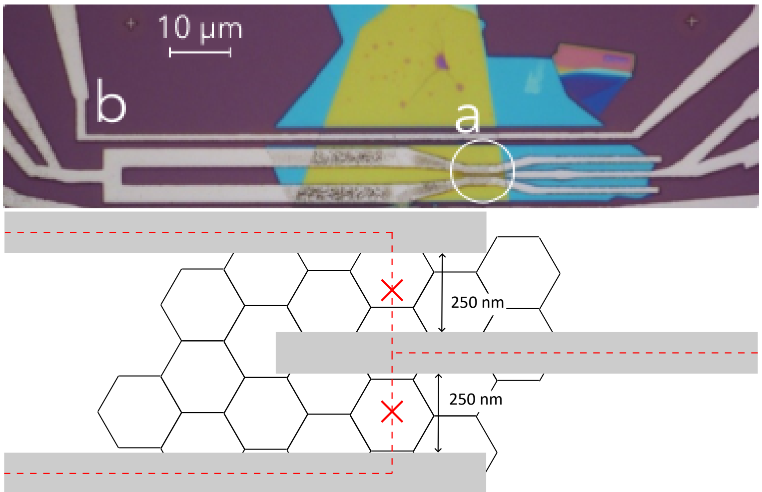


Figure 4.1: A modified optical photograph of the Double SQUID, originally taken by Moshe Ben Shalom at the NGI. Feature A is the location of the graphene Josephson junctions, and a schematic view of the junction layout is shown below the photograph. In the schematic, the grey bars are the superconducting NbTi electrodes, and the red dashed line shows the path of current in the device, with the red crosses indicating the JJs which are 250 nm long. Feature B is a flux bias line which can be used to produce a local magnetic field in the SQUID.

The original idea behind the Double SQUID was to measure the circulating current in one of the SQUIDs. There were three flux bias lines, one beside each SQUID and one between them. The SQUIDs are in close enough proximity to affect each other, so the middle bias line was used to screen the flux in one of the SQUIDs when changing the flux in the other.[1] As that experiment did not work as intended, the device was available for the experiments shown in this thesis, as it contains the required SGS junctions.

### 4.1.2 Big SQUID

The "Big SQUID" has very large wires and SQUID loop because it was designed to be impedance matched to 50 Ω in a microstrip geometry to carry microwave signals. The electrodes are 200 μm wide and the loop area is about 200,000 μm$^2$. The original purpose was to try and make a device that would work like a two-stage Josephson transmission line (see figure 1.2). It would be possible to bias the junction from the vertical wire, and apply an input pulse from the left wire and measure the output on the right wire. This is why the junctions were designed to be asymmetrical, one is 2 μm wide and the other is 3 μm which would ideally lead to amplification of a signal. This experiment was not performed because the experimental apparatus required was not ready, so the work investigating half-integer Shapiro steps in graphene SQUIDs was prioritised instead.

[1]Private communication with M Thompson

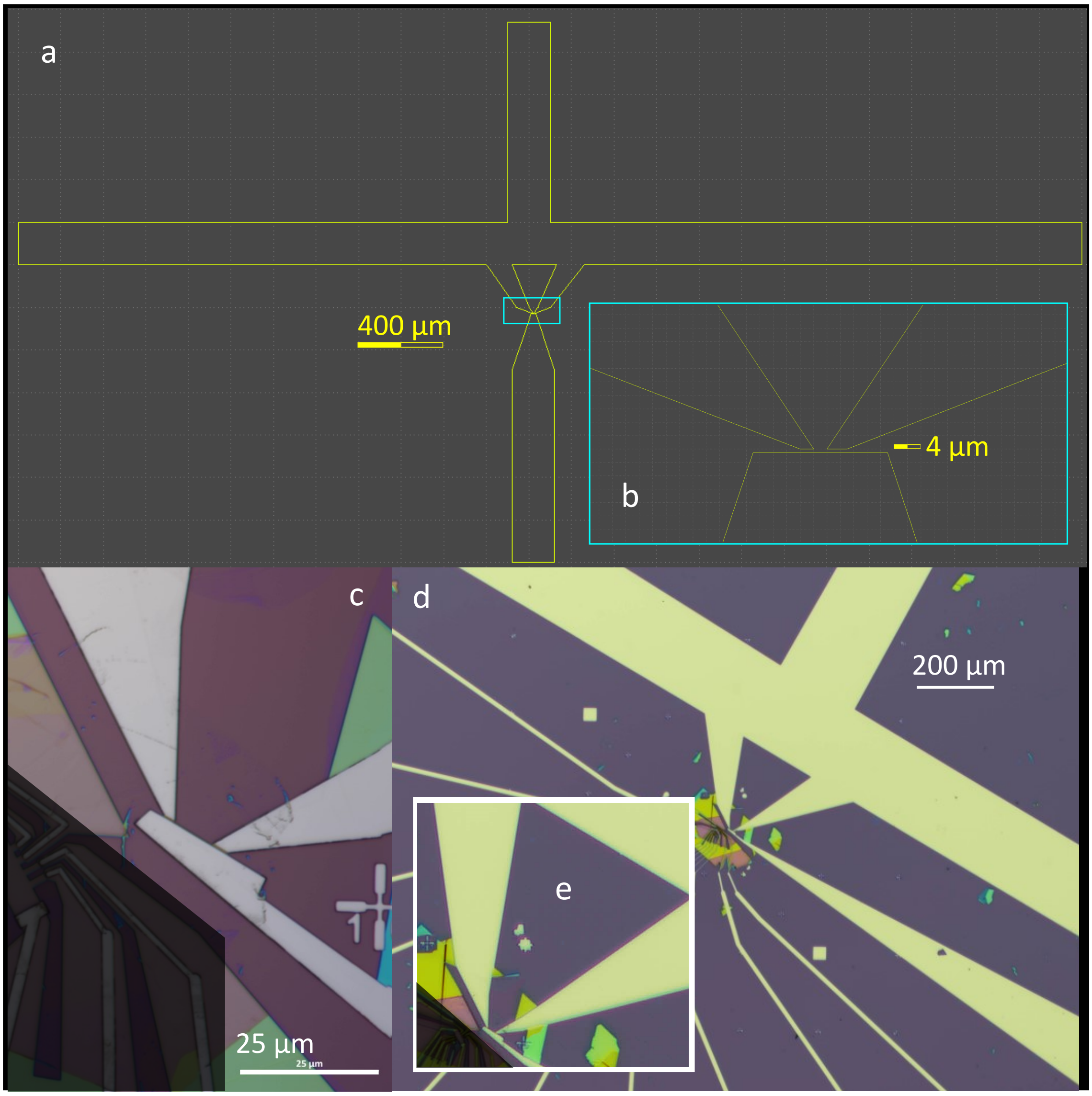


Figure 4.2: Big SQUID CAD images and photos from after fabrication. The CAD design was by the author. Device fabrication and original photos were taken by W Wang at the National Graphene Institute. The photos have been adapted by the author. (a): Initial design of the SQUID. The inset (b) shows an enlarged version of the position of the Josephson junctions, while the other lines are for electrical connections. (b): The junctions are separated laterally by $1$ µm, and their widths are $2$ µm (left) and $3$ µm (right). The gap between the junction electrodes is $532$ nm. (c): Optical image of the fabricated junctions. The design was adapted by W Wang before fabrication, moving the ground electrode for space considerations. (d): Optical image of the wider space of the device, with different filters. (e): Close up of the junction area, showing that there is also a difference in how the right-hand branch of the SQUID was fabricated compared to the initial design.

Both junctions in the Big SQUID are $0.532$ µm long. The contacts are an initial 5 nm adhesion layer of Ta followed by 50 nm of NbTi, capped with a further 5 nm of Ta and finally 10 nm of Pt. The lower hBN flake is 88 nm thick and the upper flake is 35 nm thick. The Big SQUID shares a substrate with another Hall-bar style structure which is part of an unrelated experiment. This is a holdover from how the coronavirus pandemic impacted production at the NGI. Sharing this substrate was necessary at the time to have a new device to test, however it led to rushed design and unideal material choices dictated by the design of the Hall-bar device.

In the end, this device was not studied as thoroughly as the Double SQUID, in part because the large loop area meant that the device was quite susceptible to flux jumps and the signal was often unstable as a result. Despite this, the device was used for a brief investigation of SQUID inductance, detailed in section 5.1.4.

## 4.2 Low-temperature electronic measurement setup

The typical methods of measuring and characterising non-superconducting electronic devices can be applied to graphene SQUIDs. An electronic device's current-voltage characteristic (IV curve) encodes a lot of information about it. In a voltage-biased regime a series of voltages are applied across the device under test and the current passing through is measured. Devices can also be tested in a current-biased regime, where the current is applied and the voltage is measured.

The SQUIDs tested here were current-biased and their voltage response is measured to form the IV curves, from which quantities such as the critical current and normal state resistance can be extracted. Additional variables were also applied to the devices to add an extra dimension to the measurements and see how those parameters affected the device characteristics, including applied magnetic field, temperature, electrostatic gating, and RF electric field. These will be discussed further in section 4.2.2.

As they are superconducting electronic devices, a low temperature sample environment is needed to be able to access and measure the properties of interest. This complicates the electronics setup because of the balancing act between keeping stable low temperatures while also running electronic cables to the device from room temperature. For this investigation, these challenges were met using a dry dilution refrigerator.

### 4.2.1 Dry dilution refrigerator

The measured devices have NbTi wires as the superconductor, which typically have a critical temperature of 9 - 10 K. The critical temperature of the SQUIDs themselves is greater than 6 K as they were shown to maintain behaviour characteristic of the superconducting phase up to that point. A commercial dry dilution refrigerator with a base temperature of 15 mK was used to provide the necessary low-temperature sample environment. The model was an Oxford Instruments Triton 400, which will be referred to as 'the Triton'. Samples are housed in a detachable sample holder or 'puck' which is attached to the mixing chamber plate at the bottom of the Triton. The base of the puck which connects to the mixing chamber plate is gold-plated copper, and the outer shell is brass. The copper provides thermal contact between the sample and the coldest part of the refrigerator. Figure 4.4 shows an illustrated schematic of an equivalent dilution fridge system. The Triton has two stages of dc wiring. The wiring is Cu from room temperature to the 4 K plate, and NbTi from there to the mixing chamber plate. At the 4 K plate there is a low-pass R-C-R filter with 200 Ω resistance and 1 nF capacitance.

The RF wiring used in this work was the first use of RF wiring in the Triton, although the plates in the Triton were designed to accommodate the wiring in the form of a 'coax stick'. The coax stick is made up of five sections of coaxial wiring. The joints between each section could be clamped to the plates in the Triton. The design and start of the construction work was performed by Joshua Chawner, and then the completion of the construction, testing and installation in the Triton was performed by the author. There were two sections of CuNi coaxial wire from room temperature to the 4 K plate, then three sections of NbTi from the 4 K plate to the mixing chamber. A schematic of the coax stick is shown in figure 4.3. The coax stick could support up to six RF lines. Four lines were constructed, three of which had a total of 36 dB of attenuation, and one of which was unattenuated. The attenuation and continuity of the lines was tested using a vector network analyser. In the experiments conducted for this work, only the single unattenuated line was used, as the objective was just to deliver an ac signal to the device via an antenna. In other experiments, the attenuated lines would likely be used for input signals, while the output would be received on the unattenuated line, as the lower power output would otherwise be suppressed.

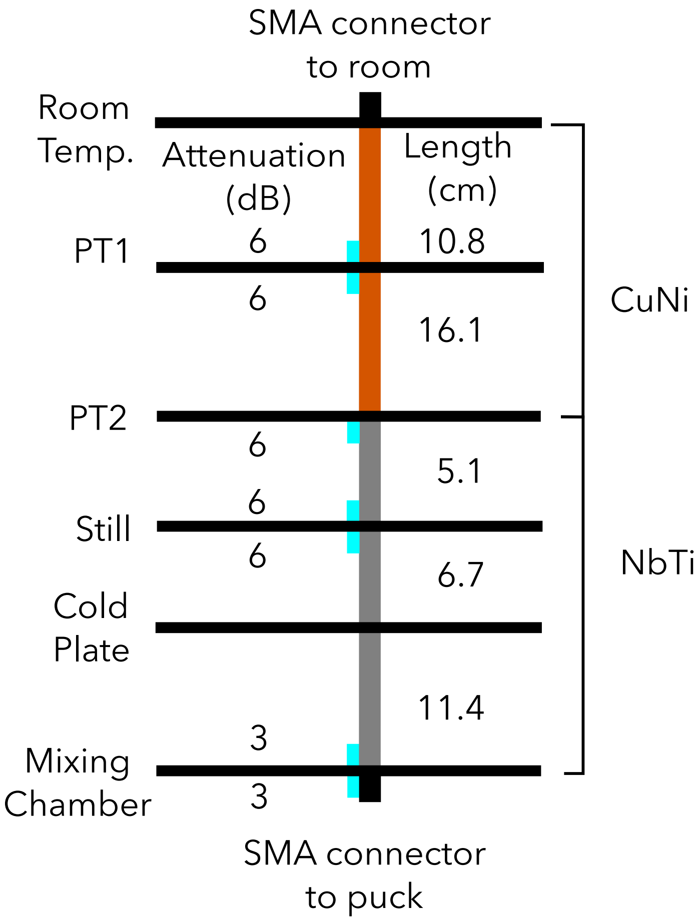


Figure 4.3: Schematic of the RF wiring setup used for the measurements involving high-frequency signals. The labels on the far left indicate which plate of the Triton each section fits between. The orange and grey vertical lines in the centre represent the CuNi and NbTi coaxial wire respectively. The total length of wiring is 50.1 cm, not including the connections between wire sections, which bring the total length to 72.1 cm. The blue squares indicate the position of the attenuators. The total attenuation is 36 dB. For unattenuated lines, the attenuators are replaced with 0 dB attenuators. SMA connectors are at each end to connect to room temperature electronics or the sample puck.

Having a base temperature that is significantly lower than the critical temperature of the superconductor is useful and necessary. Firstly, the critical temperatures of JJs and SQUIDs are substantially lower than the superconductor by itself. In graphene JJs, the graphene acts like a normal metal, so the proximity effect is active in the vicinity of the boundary between the electrode and the graphene. While this makes the graphene superconducting, it also weakens the superconductivity of the electrode, lowering the critical temperature. Being sufficiently low in temperature also means there is a range of temperatures over which the temperature dependencies of the device properties of interest are small.

Secondly, superconducting devices are very sensitive to noise sources, so minimising the temperature helps to minimise thermal (Johnson-Nyquist) noise[125], as it is known that thermal energy is proportional to temperature (this topic is discussed in more detail in 3.8.1). Another way that noise in the devices was reduced was by having the Triton mounted on air springs to reduce vibration.

Having established the benefits of the temperatures attainable by the fridge, additional features that are made use of will also be detailed. The fridge is equipped with a superconducting magnet orientated to apply a magnetic field along the 'z' (vertical) axis (shown in figure 4.4). The magnet is needed for measurements on SQUIDs which depend on the magnetic flux passing through the SQUID loop (section 2.2.4).The magnet has a field constant of $k_{\mathrm{M}} = 13.72$ AT$^{-1}$. The product of $k_M$ and the current through the magnet $I_{\mathrm{M}}$ gives the applied magnetic field strength $B_{\mathrm{z}} = k_{\mathrm{M}} I_{\mathrm{M}}$.

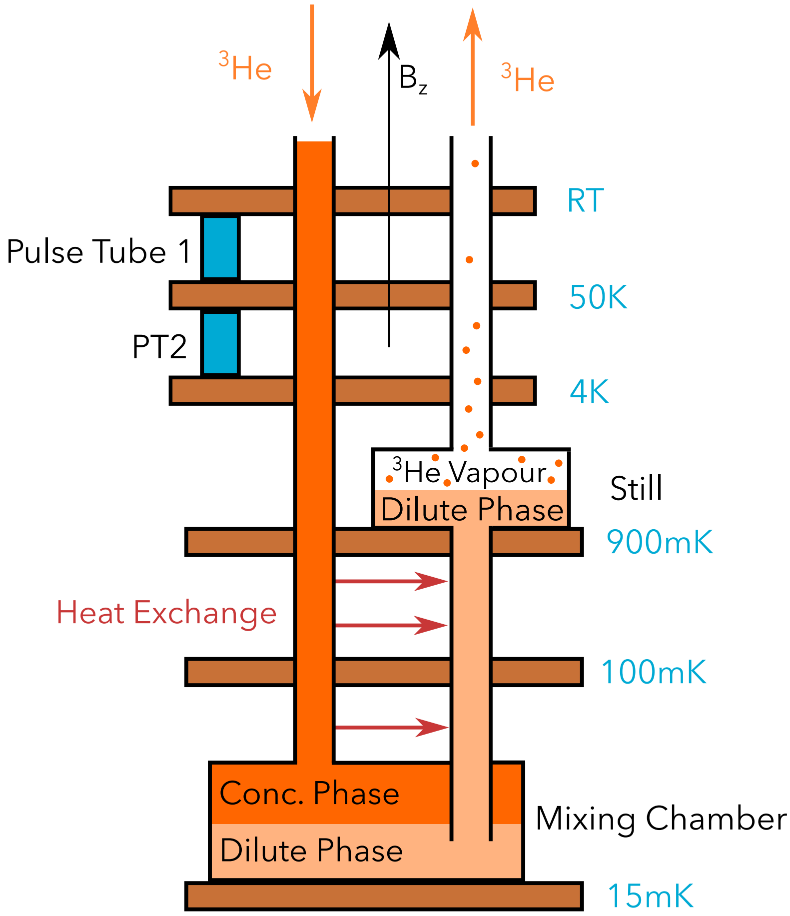


Figure 4.4: A schematic of the dilution circuit of a typical dry dilution refrigerator. The schematic is a vertical slice where the room temperature plate is at the top of the cryostat and the mixing chamber is at the bottom. $B_z$ shows the direction of the superconducting magnet built into the cryostat. Prior to operation, a gaseous mixture of $^4$He and $^3$He is pumped from a storage tank into a pre-cooling circuit (not shown explicitly here), bringing the fridge down to 10 K allowing the condensation process to begin. Then it is moved to the dilution circuit for further cooling. The final cooling stage is in the mixing chamber. Here, both isotopes of helium are liquid and they are separated by density, with most of the less-dense $^3$He at the top. The concentrated and dilute phases refer to the concentration of $^3$He. In the still, $^3$He vapour boils off, which acts to put the system out of equilibrium. To balance this loss, $^3$He crosses the phase boundary in the mixing chamber from concentrated to dilute. It takes heat away from the mixing chamber travelling up towards the still. The gaseous $^3$He circulates through the refrigerator, returning to the dilution circuit through the other line. Its excess heat is transferred back to the still line by heat exchangers (assisting with the evaporation) as it re-enters the mixing chamber in the concentrated phase.

When investigating a SQUID it is useful to speak in terms of the amount of magnetic flux in the loop, rather than the raw field strength. Applied flux $\Phi_a$ is the product of the field strength $B_z$ and the effective area of the SQUID loop $A_{\text{eff}}$. Therefore, in a smaller SQUID a stronger field is needed to produce an equivalent amount of flux. Then one is able to investigate small scale flux oscillations, or the larger Fraunhofer pattern, knowing the appropriate range and resolution of field to apply.

For these SQUIDs the maximum field size needed was on the order of 1 mT, and the smallest resolution is on the order of 1 μT. These are relatively small fields so the magnet was run non-persistently from a current source (Keithley 2400) to enable stable high-resolution measurements.

The other useful function of the Triton is a heater and proportional-integral-derivative (PID) controller so that temperature dependent measurements can be performed. The temperature can be set to cover the full range of interest, from base temperature to above the $T_c$ of NbTi.

### 4.2.2 Differential electronic measurements

The main parameters that can be obtained from the IV of a JJ are the critical current and the normal state resistance. These allow the characteristic voltage of the junction to be calculated. Knowledge of the device geometry then gives access to quantities like the critical current density. Additional independent variables can be included in this characterisation on a contextual basis. These are additional parameters which affect the result of the regular IV curve. For SQUIDs this includes magnetic field, back gate voltage, temperature and RF signals.

All of the electronic measurements are performed using a four-terminal arrangement from a lock-in (LI) amplifier (Zurich Instruments MFLI), eliminating resistance contributions from the measurement leads so that the IV characterisation reflects only the device itself. As the device should be superconducting, it is expected that while in its superconducting state there should be no resistance. At these points any signal from the MFLI vanishes compared to the noise floor, which is typically two orders of magnitude smaller than the peak signal in the resistive state.

Figure 4.6 shows schematically how the measurements are set up. To supply current through the device, two voltage outputs on the MFLI are used in conjunction with a current supply (made in-house by Steve Holt in the Lancaster University physics department electronics workshop). The current supply takes one ac and one dc voltage input and converts them into a current output with the two components added together. The ac component is from the LI signal output and the dc component is from the LI auxiliary output. The current supply can be set to convert the input voltages into a current defined by one of three ratios; $1$, $10$, or $100$ μA V$^{-1}$ dc and nA V$^{-1}$ ac. The output from the current supply is passed through a splitter to provide a positive and ground connection for the four-terminal measurement. These are connected to a breakout box which is the interface to the Triton's internal wiring down to the sample puck.

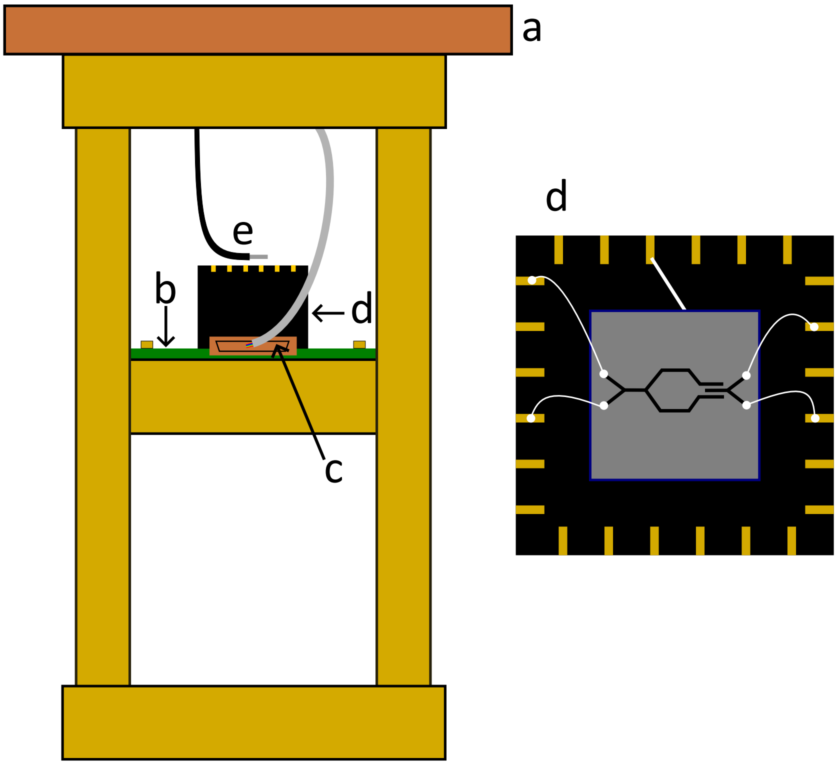


Figure 4.5: Schematic of the puck which is used to house the device inside the dilution refrigerator. The puck is screwed to the bottom of the mixing chamber plate through a bottom-loading mechanism (a). It is made of copper to aid with thermalisation of the sample. The circuit board (b) is bolted to the puck, and houses a chip carrier. A 24-pin connector (c) is wired to the top of the puck. The connector at the top of the puck couples with an equivalent connector attached to the bottom of the mixing chamber plate, from which wiring traverses the length of the refrigerator to the room temperature electronic instruments. On the right is a top-down view of the black chip carrier (d) which is attached to a circuit board bolted to the puck. The Au fingers are connections which run to the 24-pin connector on the circuit board. Silver epoxy is used to bond Nb wire from the fingers to make contacts to the device (NbTi sputtered wires). Silver epoxy also connects a finger to the Si substrate of the sample, to allow it to be gated. A stripped piece of flexible coaxial wire (e) is positioned parallel above the device as an antenna for RF signals to be applied.

For the voltage measurement, the '+V' and '-V diff' terminals of the MFLI are used and connected directly to the breakout box. Differential measurement is enabled so that the differential resistance can be measured directly, rather than calculated from the dc response. The differential voltage signal is extracted from the small changes in the response caused by the modulation of the bias current provided by the ac component.

A second demodulator is used at 0 Hz so that the dc voltage signal can also be measured. This measures the 'Y' component of the signal corresponding to the peak voltage, which is divided by $\sqrt{2}$ to obtain the root-mean-square (rms) voltage. The simultaneous measurement of the dc and differential responses mean that the typical IV curve and the differential $\mathrm{d}V/\mathrm{d}i - I$ curve can both be accessed directly, where $i$ is the amplitude of the ac component of the bias current. The latter is a differential resistance against current plot. The normal state resistance can also be estimated from the dc voltage characteristic curve by differentiating it, but the resolution is limited by the bias current step size and would not match the differential resistance unless the step size matched the amplitude of the modulating current. For this reason, it is usually preferable to use the directly measured differential resistance, which is also more useful for accurately locating the critical current of the device, as the transition from zero to finite resistance is extremely sharp.

Varying additional parameters is done in different ways. The graphene in the devices can be electrostatically gated using the sample substrate as a back gate. A voltage is applied to the gate using a sourcemeter (Keithley 2400) in series with a $100\ \mathrm{k}\Omega$ resistor to protect the gate from large transients. The build up of charge on the gate creates an electric field between the gate and the conductive graphene monolayer. The main effect of this is that the charge carrier density in the graphene is changed, with further discussion in section 5.1.1.

The magnetic field through the SQUID loop can be controlled as previously discussed using the inbuilt superconducting magnet in conjunction with either a sourcemeter or dedicated power supply unit depending on the size of field required. SQUIDs are extremely sensitive to magnetic fields, so this is an important element of their characterisation that would be directly relevant to most applications involving the device. Similarly, the Triton has an inbuilt heater that serves a dual purpose of being a necessary part of its operation when warming and cooling as well as directly controllable by the user for temperature dependent measurements. Seeing how the device responds with temperature has significance for its practical operating range.

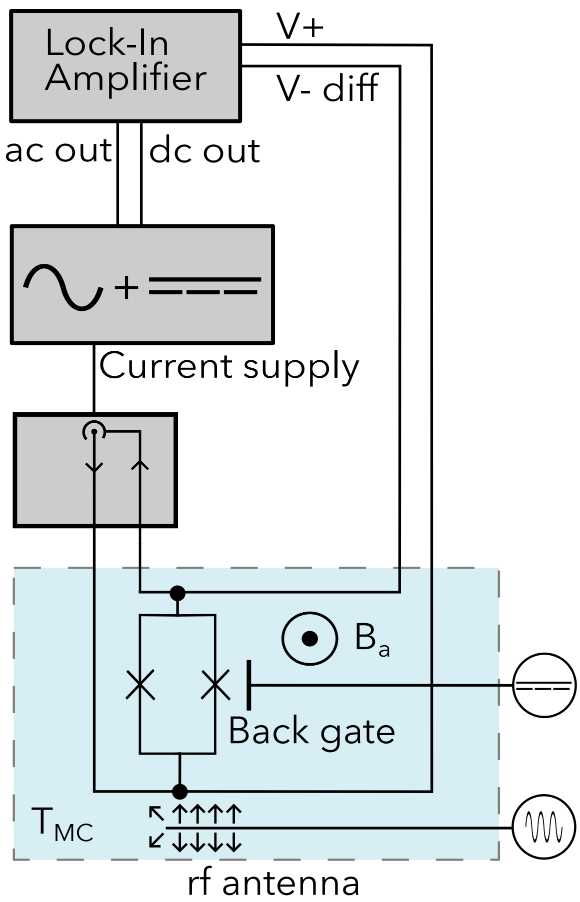


Figure 4.6: Schematic drawing of the general measurement setup for the electronic characterisation of the graphene SQUID device. The SQUID is current biased by a current supply which outputs a dc current with modulation from a small ac signal, defined by voltage outputs from the lock-in amplifier. Unless otherwise stated the conversion is $10$ µA V$^{-1}$ dc and $10$ nA V$^{-1}$ ac. The device is in thermal contact with the mixing chamber of a dry dilution refrigerator. The temperature of the mixing chamber $T_{\mathrm{MC}} \approx 15$ mK under normal operation at base temperature. The cold area is indicated by the dashed box with a pale blue background. Applied magnetic field $B_a$ is from a NbTi superconducting magnet built into the fridge, and the perpendicular field would pass both through and around the device. The field constant is $13.72$ A T$^{-1}$. The magnet is either controlled by a dedicated current supply for strong fields (order 1 T) or a current sourcemeter for higher resolution steps. The back gate is controlled with a voltage applied from a sourcemeter. The RF antenna has a continuous high-frequency signal supplied from a signal generator.

The last set of parameters are related to the effects of irradiating the SQUIDs with microwave signals, inducing ac currents into the devices. This uses a short length of flexible coaxial wire which is placed inside the puck, connected to the Triton's unattenuated RF wiring. The end of the coaxial wire is stripped so that about 1 cm of the inner core is exposed. This is positioned above the device like a monopole antenna, parallel to the plane of the SQUID. A signal generator (Anritsu MG3692B) is connected to the antenna and is used to apply a continuous microwave signal. The voltage at the end of the antenna oscillates creating an alternating electric field in the puck. Attenuation was applied to the RF wiring at room temperature to reduce the power incident on the device and reduce heating in the mixing chamber. This also helped to optimise the range of input powers used for the measurements so that features of interest such as superconducting phase changes were visible over more of the parameter space. The main aim of this type of measurement is to view Shapiro steps in the IV response. This is more obvious in the dc voltage response than the differential response, though the latter does give some insight into the nature of the steps, as will be discussed in section 5.2.

# Chapter 5

# Electronic characterisation of graphene SQUIDs

In this chapter, the experimental work done measuring the graphene SQUIDs is presented. The majority of work was done on the Double SQUID. There are two core sections: characterisation of the devices with and without irradiation from a high-frequency RF signal. First, the dc-bias only section (5.1) will characterise the typical graphene SQUID characteristics including the dependence of the critical current on gating, the presence of flux oscillations, and estimates of the inductance and capacitance of the device. Section (5.2), shows measurements of Shapiro steps under changing RF signal parameters, magnetic field, and temperature. In particular, the appearance of half-integer Shapiro steps is the topic of interest here. This chapter ends with the overall conclusions and future work resulting from this thesis in section 5.3.

## Contents

## 5.1 Characterisation with dc biasing

This subsection addresses electronic characterisation which does not involve the use of the RF antenna. The basis of these measurements is taking an IV characteristic to determine the critical current while a third variable is varied. In these measurements the critical current is identified on a plot of differential voltage against bias current by a sharp transition from 0 to finite differential voltage. The differential voltage is converted to resistance by dividing by the amplitude of the modulating ac signal applied to the dc bias.

Firstly, the Double SQUID will have its critical current dependence assessed with respect to the voltage applied to its back gate. This will establish if gating the graphene is working as expected. Then, the dependence of the critical current on the magnetic flux through the SQUID loop will be tested, which will allow the period of the flux oscillations to be measured. Those are the two most fundamental measurements.

In addition to these, attempts have been made to establish methods for estimating a SQUID's capacitance and inductance. These are important parameters influencing the Stewart-McCumber parameter $\beta_C$ and screening parameter $\beta_L$ respectively.

The magnetic field was controlled by the Triton's superconducting magnet and the gating was controlled with a voltage sourcemeter. Details of the experimental setup are described in chapter 4.

### 5.1.1 Back gate dependence of critical current

It has been comprehensively established in the literature that applying a voltage to the back gate of a graphene SQUID creates an electric field which dopes the graphene in the Josephson junctions with additional electrons or holes. The increased charge-carrier density leads to increased SQUID critical current [35, 37, 50, 66, 67, 74–77, 83, 110, 131, 132]. Measuring the IV characteristics of the SQUIDs at different gate voltages shows the range of accessible critical currents in the devices, and indicates the charge neutrality point. The charge neutrality point is not necessarily at 0 V, as there could be residual charge trapped on the device. It is identifiable by a significant increase in differential resistance, and the critical current is minimised. The thickness of the dielectric places a limit on the gate voltage from its breakdown field threshold, above which current will leak through the material[133]. Generally, the greater the thickness of the dielectric, the greater the field strength it can sustain.

The measurements in the Double SQUID are primarily to check that it displays the expected critical current dependence seen in other devices. Here, typically the largest gate voltage used was 5 V, because above this flux jumps were more likely, leading to more unstable measurements.

Figure 5.1 shows a back gate dependence on the differential IV characteristic of the Double SQUID device (4.1.1). The back gate voltage was incremented and measuring a differential voltage IV characteristic curve at each back gate value. At charge neutrality, the critical current is about 3.5 μA, which increases to approximately 11.5 μA at 5 V gating. There is a slight asymmetry visible in this plot: on the negative side, the values range from -3.0 to -10.0 μA. Clearly, the critical current increases much more for increasing the back gate above 2 V compared to decreasing it below 2 V. This shows that doping the graphene with electrons leads to more transparent SN junction interfaces, and is consistent with measurements of similar devices.

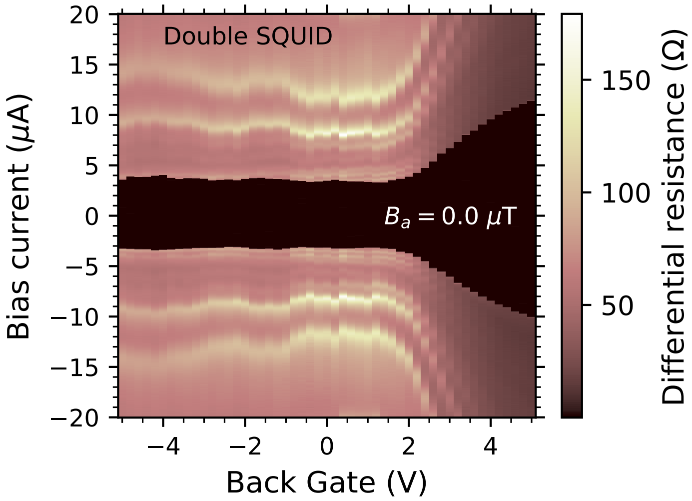


Figure 5.1: Colour plot showing the dependence of differential resistance of the Double SQUID on the bias current and back gate. The sharp difference in colour indicates the switching critical current of the SQUID between the superconducting (dark region around 0 bias current) and resistive phases (light region). There is an extended region of low transparency contacts at low back gate voltages starting close to 2 V. The normal state resistance decreases at higher gate voltage, because the junction becomes more transparent when charge carrier density between the graphene and superconductor is more equivalent. Gate step size = 0.2 V. Bias current step size = 0.05 μA.

#### Critical current extraction

To understand the characteristics in more detail, critical current values can be extracted from the differential IV at each gate voltage. To extract the critical current, a threshold value was set that is below the normal state response of the SQUID but substantially above the superconducting state response. Starting from inside the superconducting region and moving either positively or negatively depending on which critical current is being determined, the critical current is found as the last data point below the threshold. Figures 5.2 (A) and (C) respectively show the positive and negative critical current values extracted from figure 5.1, with (B) and (D) showing a slice at a back gate of 3 V to highlight the position of the extracted critical current and other features of the differential IV curve. Regarding the differential resistance plots, the critical current is indicated by the sharp transition from 0 resistance to a finite value. As in figure 5.2 (D) the spike at the superconductor-normal transition often goes to higher resistance before returning to a lower resistance at the next current step. Continuing to increase the bias current, additional peaks are visible which are evidence of Andreev reflection.

Looking at the extracted critical current values, they are monotonically increasing from a back gate of 1.4 V as the back gate increases. Moving in the opposite direction, there is an overall increasing trend, but there are also small peaks and troughs which could be evidence of Fabry-Perot oscillations, which have been observed in similar graphene JJ devices. The Fabry-Perot oscillations are due to ballistic transport of charge carriers in the cavity defined by the boundaries between the superconducting electrodes and the graphene[132]. The uncertainty in the critical current is small enough to not be visible in figures 5.2 (A) and (C), so the variation is not due to random fluctuations.

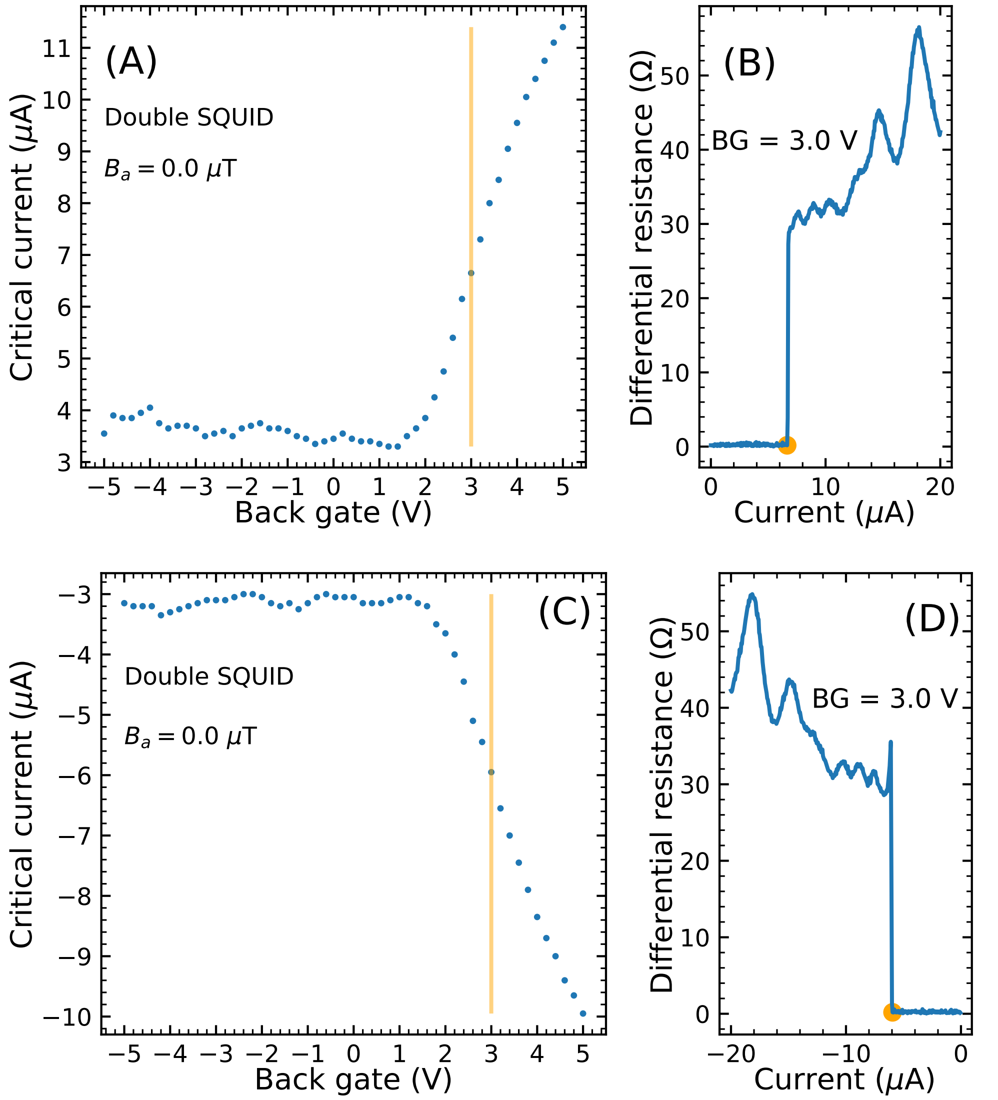


Figure 5.2: Plots showing extracted critical current dependence on back gate voltage, and a slice to show the position found by the extraction algorithm. This corresponds to figure 5.1. Plot (A) shows the positive critical current values and (C) shows the negative critical current values. A slice is taken at a back gate voltage of 3 V in each case, shown in (B) for the positive $I_c$ and (D) for the negative $I_c$. $I_{c+} = 6.65 \pm 0.05$ μA, $I_{c-} = -5.95 \pm 0.05$ μA. The applied field $B_a = 0$ μT. Bias current step size = 0.05 μA.

The uncertainty in the critical current values will typically be equal to the interval between the current values, unless the transition itself is noisy, which would be evident in the line plot by the transition taking place over multiple data points before settling. In figure 5.1 the superconducting region is very high contrast to the resistive region, so there is little ambiguity in the position of the critical current.

To avoid artifact peaks in the superconducting region, setting the critical current condition to require that two consecutive points lie above the threshold is a way of confirming the transition.

#### Explaining the asymmetry

The colourplot in figure 5.1 and extracted critical current values in figure 5.2 indicate an asymmetry between the positive and negative critical currents. The Double SQUID was designed to have geometrically symmetrical JJs. This should lead to symmetrical critical current, resistance, capacitance and inductance in the device. To characterise the apparent asymmetry, the ratio of the positive to negative critical current values at each back gate is plotted in figure 5.3. It shows the size of the asymmetry increasing above and below the minimum at about 2 V. The uncertainties in the ratio $I_{c+}/I_{c-}$ were determined by summing the fractional uncertainties of the two values in quadrature. The combined uncertainty is smaller at higher positive back gate voltages because the critical current itself is larger.

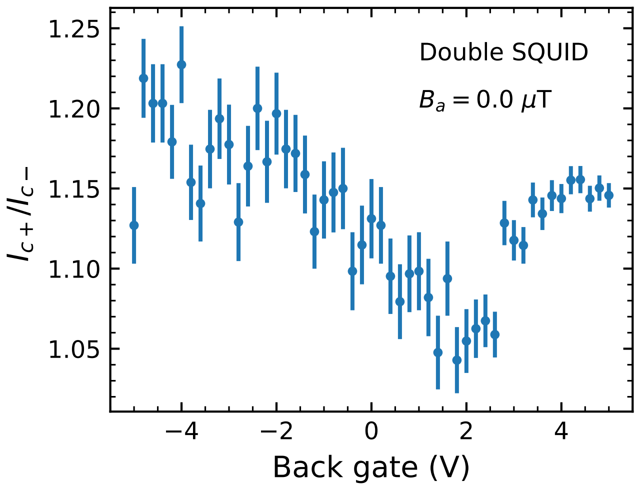


Figure 5.3: The ratio of the absolute values of the positive and negative maximum critical current against back gate voltage of the Double SQUID. The magnitude of the positive critical current is always slightly larger than the magnitude of the negative critical current, so the ratio is always greater than 1. There is a trend in the size of the ratio, with a minimum at approximately 1.5 - 2 V. This corresponds to the point in figures 5.1 and 5.2 where the gating starts to have an increase impact on increasing the critical current of the SQUID.

There are a number of factors which can influence the relative critical currents of the junctions in each arm of the SQUID. While in this device the junctions were designed to be identical, it is possible that there is some unevenness introduced during fabrication, or defects introduced at that stage or over extended use of the device. If there is residual flux trapped in the loop, that would introduce a circulating current which would therefore create an asymmetry. There could also be residual charge which would not necessarily be equivalent over each junction. The mostly likely explanation here, however, is that the asymmetry comes from how the device was measured, and is a result of hysteresis in the IV characteristic. As the bias current for figure 5.1 started at negative and then passed through

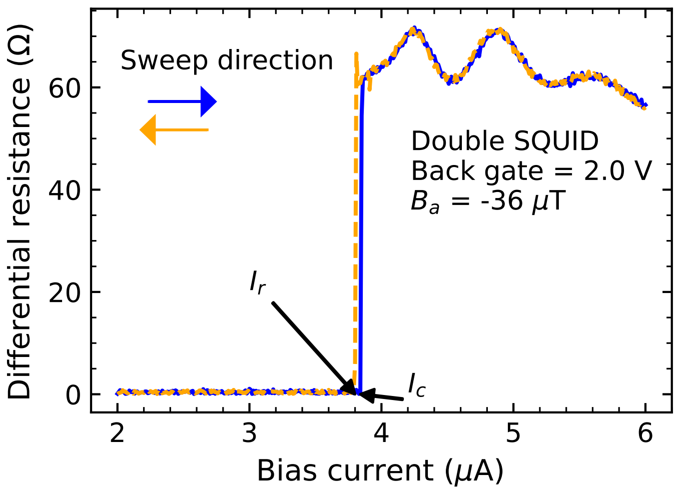


Figure 5.4: Hysteresis plot at the minimum hysteresis point. Solid blue lines show the switching (critical) current $I_c$ where the current is increased from inside the superconducting region to the resistive region. The dashed orange lines show the retrapping current $I_r$ where the current is reduced from the resistive region into the superconducting region. The back gate at 2 V, close to charge neutrality. The magnetic field is -36 μT, corresponding to the maximum critical current of the overall flux dependence. The critical current is 3.84 μA and the retrapping current is 3.80 μA. The current step size is 0.01 μA.

zero to end at positive, it would be consistent that the apparent critical current is smaller when crossing the transition in the 'retrapping' direction (resistive state to superconducting state) compared to the 'switching' direction (superconducting to resistive). This can be seen in hysteresis measurements taken on the device. The smallest hysteresis is seen at 2 V (shown in figure 5.4) with the hysteresis getting larger moving away from that point. Taking two points as examples, shown in figure 5.5, at 0.0 V the difference between the switching and retrapping current is $\approx$ 0.2 μA, and at 4.0 V this difference is $\approx$ 0.7 μA. These are comparable differences to the extracted values in figures 5.2 A and C. They do not correspond exactly, because in figure 5.5 the data were taken at a different applied magnetic field such that the critical currents were ensured to be maximised and that there was no asymmetry of flux in the SQUID loop (this is explained further in section 5.1.3). The similarity in the size of the asymmetry and the size of the hysteresis shows that hysteresis is likely to be the main contribution. It would be expected that if the bias current were swept in the opposite direction, the asymmetry would be inverted. To properly measure the positive and negative critical currents, the transitions should both be approached from inside the superconducting region in separate measurements.

As well as helping to explain the asymmetry seen here, hysteresis measurements of the SQUID can also be used to estimate its capacitance, as will be shown in section 5.1.2.

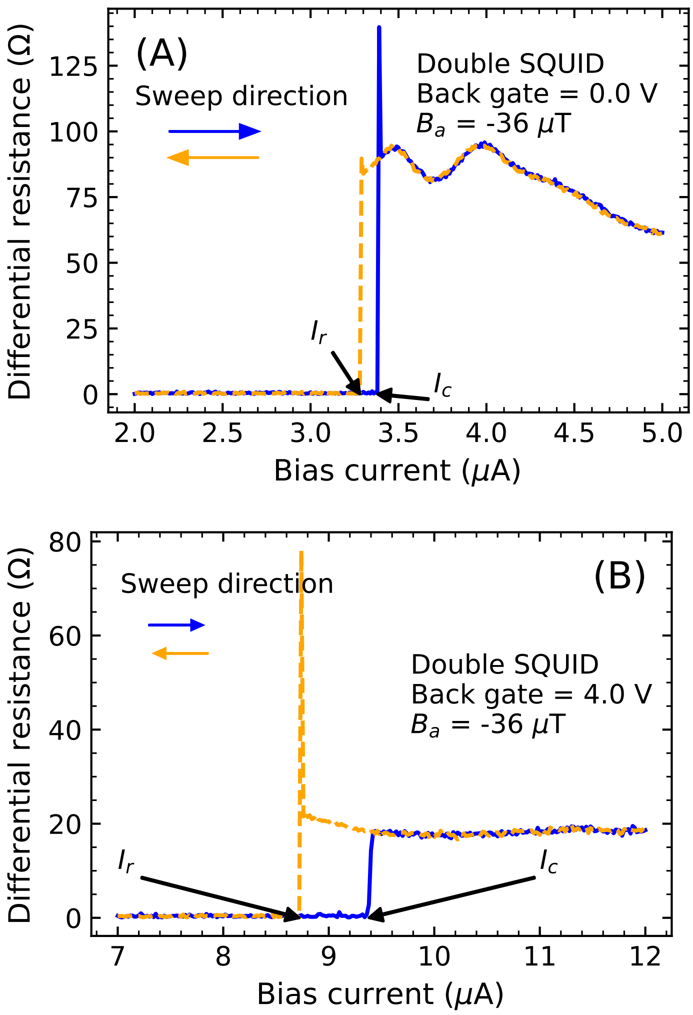


Figure 5.5: Hysteresis plots at back gate voltages away from charge neutrality. Solid blue lines show the switching (critical) current $I_c$ where the current is increased from inside the superconducting region to the resistive region. The dashed orange lines show the retrapping current $I_r$ where the current is reduced from the resistive region into the superconducting region. Plot (A) is in the p-type region with the back gate at 0 V and (B) is in the n-type region with the back gate at 4 V. In (A) the critical current is 3.38 μA and the retrapping current is 3.28 μA. The current step size is 0.01 μA. In (B) the critical current is 9.38 μA and the retrapping current is 8.72 μA. The current step size is 0.02 μA. In both the magnetic field is kept constant at -36 μT, corresponding to the maximum critical current of the overall flux dependence.

### 5.1.2 Hysteresis effects and link to SQUID capacitance

The capacitance $C$ of a SQUID is a quantity of interest because of its impact on the hysteresis of the IV characteristic. Hysteresis in the IV curve is when the retrapping current $I_r$ is smaller than the critical current $I_c$, after sweeping the bias current up and down across the transitions (see figure 5.6). Usually, SQUIDs are designed to have a small enough capacitance that no hysteresis is observed, with the McCumber parameter limited to $\beta_C \leq 1$. Having already observed an apparent hysteresis in the Double SQUID, it would be useful to estimate the capacitance that has caused it. This will be done using the return current $i_r$, which is the ratio of the retrapping current to the switching current, shown in equation (5.1). It can be related to $\beta_C$ by an analytical equation (5.2) given in the SQUID handbook[92].

$$i_r = \frac{I_r}{I_c} \tag{5.1}$$

$$\beta_C = \frac{2 - (\pi - 2)i_\mathrm{r}}{i_\mathrm{r}^2} \tag{5.2}$$

In the Double SQUID, it was shown in section 5.1.1 that the critical current of the SGS SQUID can be varied by changing the back gate voltage. This means that values of $i_r$ can be measured experimentally for different values of $I_c$, and be used to calculate values of $\beta_c$ to set limits on the possible values of capacitance.

**Experimental and analytical SQUID capacitance estimate**

The experimental part of this investigation involved measuring $I_c$ and $I_r$ at 1 V back gate intervals from 0 to 5 V. Examples of these measurements are shown in figures 5.4, 5.5, and 5.6, with the remaining plots in the appendix A.4. The bias current was increased moving from the superconducting region to the resistive region, and then swept back again to transition to the superconducting region. The transition points were determined in the same way the critical currents were extracted for figure 5.2. These values of $I_r$ and $I_c$, labelled in the hysteresis curve figures, allow the return current $i_r$ to be calculated using equation (5.1).

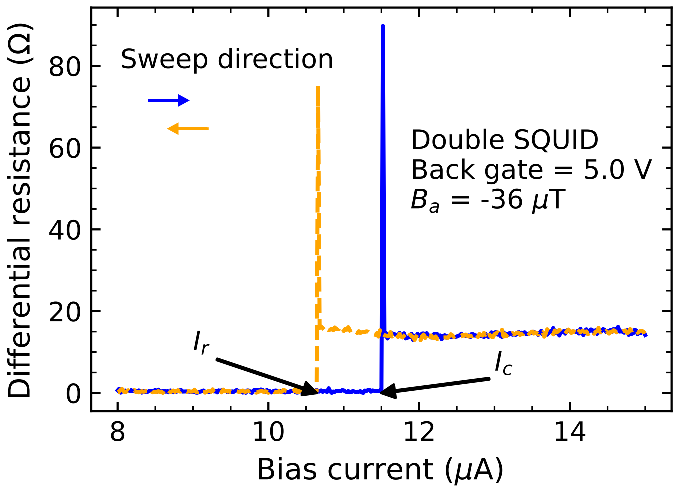


Figure 5.6: Hysteresis measurement of the Double SQUID at magnetic flux corresponding to maximum critical current and with a back gate voltage of 5 V. The critical current is $11.50$ μA and the retrapping current is $10.64$ μA. The current step size is 0.02 μA.

The full results of the hysteresis measurements are shown in figure 5.7, where $i_r$ is plotted on the left, black axis against back gate voltage. On the right, red axis are values of $\beta_c$ calculated from the corresponding $i_r$ using the analytical equation 5.2. Equation (5.2) is valid in the range

$0.05 \leq i_r \leq 0.95$[92]. The upper limit is marked on figure 5.7 by a horizontal dashed black line. Higher return currents close to 1 (where the return current is almost the same as the critical current) correspond to $\beta_c$ values less than 1 (indicated by the red dashed line) where no hysteresis is expected. There is significant disagreement between the two measurements taken at 5 V. The larger error bars on one measurement are due to a larger bias current step size of 0.05 μA compared to 0.02 μA. The difference in step size means that the measurement with the larger step size will be changing bias current at a faster rate. The idea that this could affect the retrapping current is supported by the two measurements at 3 V. Again, a larger step size was used for one measurement, which again led to a smaller return current and larger $\beta_C$. This time, the larger step size was 0.02 μA compared to 0.01 μA. The smaller difference in step size may be reflected in the smaller difference in $i_r$ and $\beta_C$. More measurements would be able to confirm this relationship, but in general it would be good practice to keep the step size constant to ensure these measurements are comparable.

The uncertainties in figure 5.7 for the return current are calculated by adding the fractional uncertainties in $I_r$ and $I_c$ in quadrature, using the current step size as the absolute uncertainty. The uncertainties in $\beta_C$ were found by applying equation (5.3) to equation (5.2) where $\beta_C$ is a function of $i_r$.

$$\alpha_{f(x)} = \sqrt{\left(\frac{\partial f}{\partial x}\alpha_x\right)^2} \tag{5.3}$$

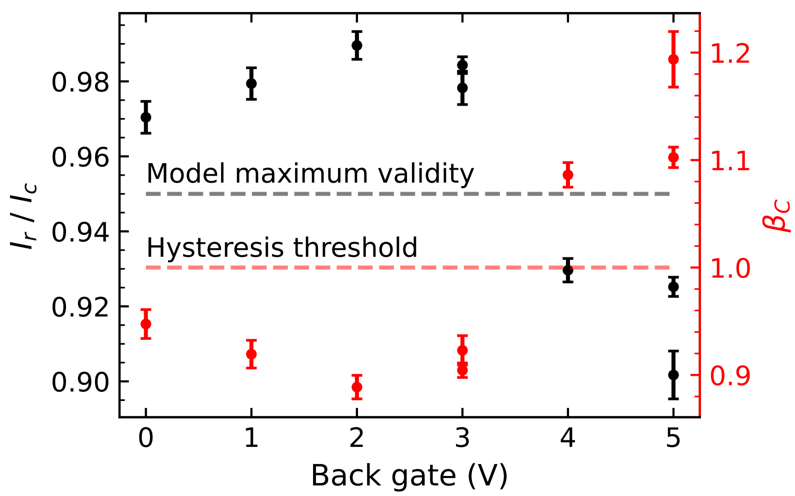


Figure 5.7: Left axis and black points show the return current against gate voltage, reflective of the hysteresis observed in the Double SQUID. The right axis and red points show values of $\beta_c$ calculated using an analytical model which depends on the return current (5.2). The model is only reliable for the three return current values below the maximum indicated in black. This corresponds to values where hysteresis is expected due to $\beta_C \geq 1$.

For the maximum capacitance estimate for the range of back gate voltages tested, the largest $\beta_c$ value is used, corresponding to a back gate of 5 V, which is in the region where the return current analytical equation is valid, and $\beta_c > 1$. Using the definition of $\beta_c$ rearranged for $C$ (equation (5.4)), at a back gate of 5 V this produces a capacitance of $C = 37.9$ fF, using $\beta_C = 1.19$, $I_c = 11.5$ μA and $R = 30$ Ω (critical current and resistance from figure 5.6).

$$C = \frac{\Phi_0 \beta_C}{2\pi I_c R^2} \tag{5.4}$$

The resistance was doubled from the value in the plot, because the parameters in (5.4) apply to a single JJ, while the SQUID value includes two junctions in parallel, assumed to be symmetrical and thus have equal resistance. To get an estimate of the capacitance of the SQUID, assuming the parallel, symmetrical junctions dominate the capacitance in the circuit, this value can be doubled to 75.8 fF.

### Geometrical estimate of SQUID capacitance

To check the validity of the measured value, a simple estimate of the dominant geometric capacitance contribution in GJJs can be calculated. In SNS junctions this is usually considered to be the 'parallel plate' capacitance between the electrodes. In the Double SQUID the electrodes of a single JJ are 5 μm wide by 50 nm high, separated by 250 nm of hBN. This is like a parallel-plate capacitor of area 0.25 μm$^2$. The capacitance can be calculated using equation (5.5). In the equation, $\epsilon$ is the dielectric constant $k$ multiplied by the permittivity of free space $\epsilon_0 = 8.85$ pF m$^{-1}$, $d$ is the thickness of the dielectric, and $A$ is the area of the 'plates'.

$$C = \frac{\epsilon A}{d} \tag{5.5}$$

The dielectric constant of hBN will be taken as 6.93 due to its bulk thickness and in-plane orientation[134]. The resulting capacitance is $\approx$ 61.3 aF. This is clearly not the dominant capacitance, as it is three orders of magnitude smaller than the calculated upper limit from the hysteresis measurements. Another likely source is the capacitance of the SQUID loop with the conductive substrate. The substrate's silicon dioxide layer is the dielectric in this case, with a dielectric constant of 3.9. The NbTi leads cover a much larger area overall compared to the size of the junctions themselves. The specific capacitance is 119 μF m$^{-2}$, which is similar to the value of 100 μF m$^{-2}$ quoted by Huang et al. in a similar device[83]. The area of the loop can be approximated as about 100 μm in length and 3 μm wide, for a total of $A =$ 300 μm$^2$ which is 300 $\times 10^{-12}$ m$^2$, corresponding to 35.7 fF.

### Capacitance estimate comparison and discussion

The measured capacitance value of 75.8 fF is about 2.1 times larger than the capacitance estimated from the loop geometry of 35.7 fF. These values are of the same order of magnitude and quite comparable, however there are some other factors to consider. One other way that the apparent capacitance could be influenced could come from the critical current being suppressed by overheating of the graphene. Graphene has a low specific heat capacity of $2\times10^{-21}$ J K$^{-1}$ μm$^{-2}$ [135] and because of this has potential use in bolometers (section 2.2.5). It has been shown in work by I.V. Borzenets et al. that hysteresis in GJJs can be caused by electron overheating[136], and this explanation has also been assumed by G. Lee et al. in their work on using hBN-encapsulated GJJs as bolometers. This suggests that the electron overheating effect is likely to contribute to observed hysteresis, with the heating coming from the bias current in the dissipative regime of the SQUID.

Where the balance lies between the possible capacitance and overheating cannot be determined without a more deliberate investigation. This could be done on the Double SQUID because there are two devices. One of the devices has a heating current passed through it to heat the graphene while the other SQUID is measured for the switching and retrapping currents. These values are compared to those found by measuring the same SQUID by sweeping the bias current as in a normal IV measurement with no additional heating. This is analogous to Borzenets' work[136] using two graphene single junctions. This would be a useful test to better understand the capacitance of these junctions.

### 5.1.3 Flux oscillations

Flux oscillations are a behaviour in dc SQUIDs where the critical current oscillates periodically as a function of the magnetic flux enclosed in the SQUID loop. The oscillation period in terms of magnetic field is equal to the magnetic flux quantum $\Phi_0$. In other words, each period corresponds to an additional quantum of magnetic flux passing through the loop. In these measurements, a superconducting magnet is used to apply a vertical magnetic field perpendicular to the SQUID loop, so that the magnetic flux is straightforward to quantify. The period of the Double SQUID will be determined by measuring a few flux oscillations and calculating the difference in applied magnetic field between the maxima or minima. Then, for verification, the effective area of the SQUID loop can be calculated, and compared to the geometrical area of the loop.

#### Flux oscillation period and loop area

For this measurement only the positive bias direction was used. The main purpose of the measurement was to check the magnetic field strength required to apply integer or half-integer quantities of flux, corresponding to the maxima and minima of the oscillations. It also allows checking that the critical current values are the expected size and that the period is consistent with previous measurements, so that any problems with the measurement setup or the device are detected.

The flux oscillations of the Double SQUID were measured by driving the Triton's superconducting magnet with a current sourcemeter (Keithley 2400) to change the magnetic flux inside the SQUID loop. Differential IV curves were measured at each magnetic field strength. The field was offset to ensure the maximum critical current at the peak of the Fraunhofer pattern was being measured. The results are shown in figure 5.8. The critical current of the SQUID is indicated by the bright front separating the superconducting and resistive phases. The critical current oscillates with a period of $\approx 6.1$ μT which corresponds to 1 magnetic flux quantum when the effective area of the SQUID loop is defined as 338 μm$^2$ which accounts for flux focusing effects, where the magnetic flux incident on the superconducting wires is deflected into the loop by the Meissner effect. This is close to the area that would be enclosed if the path were traced along the centre of the SQUID wires forming the loop, approximately[1] 350 μm$^2$. This is close enough to be confident that the SQUID is operating correctly. It is difficult to calculate the effective area of the loop exactly from the geometry, especially if the device geometry is complex.

[1]Value estimated previously by J. Prance and M. Thompson, provided in private communication.

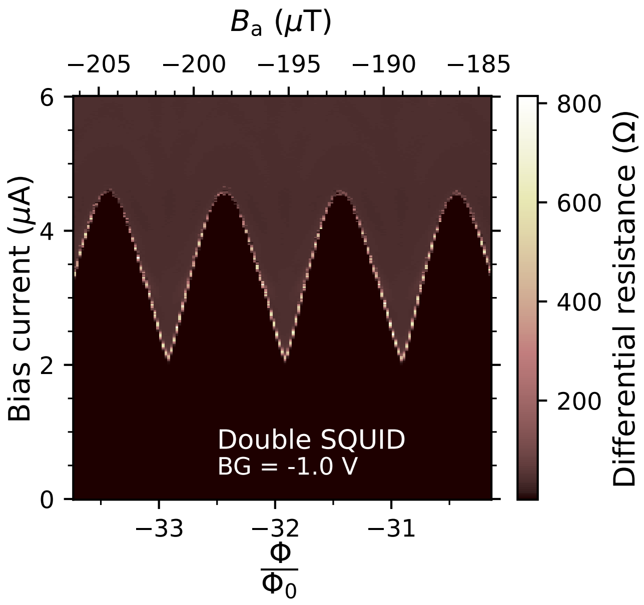


Figure 5.8: Colour plot showing the differential resistance measurement of the Double SQUID depending on bias current through the SQUID and the applied magnetic field and flux. The back gate is -1 V. The bottom x-axis is scaled to show the magnetic field as a proportion of a flux quantum. The top x-axis shows the equivalent applied magnetic field.

It has also been shown with simulations in section 3.9.1 that the CPR of the SQUID can effect the appearance of the flux oscillations, with more a more skewed CPR corresponding to critical current minima being further from 0. This affects the modulation depth of the flux oscillations.

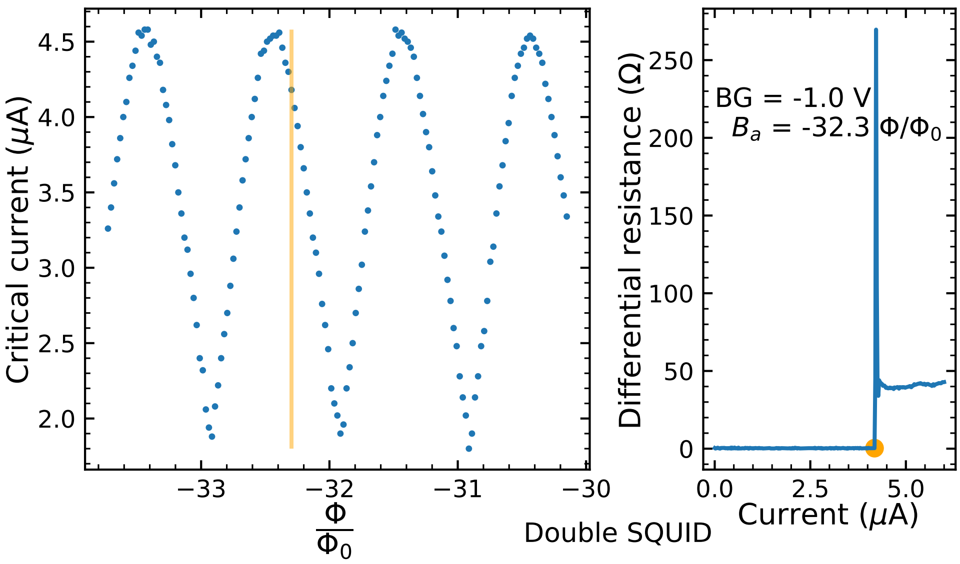


Figure 5.9: Extracted critical currents against flux in terms of the flux quantum from the flux oscillation data shown in figure 5.8. The orange vertical line on the left is the slice shown on the right, and the orange point shows the position of the extracted critical current. The back gate was -1 V.

**Trapped flux**

It is useful to know at which point on a flux oscillation the device is located when performing measurements because the critical current of the device is an important parameter when assessing a device's performance. Usually, the device would want to be placed at the maximum critical current, corresponding to an integer quantity of flux, as this means that there is no net circulating current in the SQUID loop caused by the magnetic field.

A complication with these measurements that makes the understanding and measuring of the interference pattern more important is that flux can be trapped in the SQUID during thermal cycling, creating a significant field offset which should be compensated for. Applying no external field does not guarantee that the SQUID loop contains no circulating current. It is expected that when 0 magnetic field strength is applied, that there is 0 flux in the SQUID loop, because there is no circulating current. This should also correspond to the maximum in the SQUID's Fraunhofer pattern. However, in the Double SQUID, the critical current maxima decreased with increasing positive field strength. This indicated that the centre of the Fraunhofer was offset and that there must be another source of flux causing the measurements to be off-centre. Figure 5.10 shows the positive current bias flux oscillations are not symmetric around 0 and the critical current maxima are larger at larger negative field strengths. The slice at 2 µA is shown in the lower plot. The spikes in the line plot correspond to critical current values intersected by the slice. As the critical current maxima increase, the superconducting region covered by the slice gets longer. This means that the centre of the Fraunhofer can be identified by varying the applied magnetic field at a fixed bias current below the central maximum critical current. This is the approach taken in figure 5.11, where for the applied bias current close to the maximum $I_c$, the field strength associated with the peak is evident in the region around -200 µT. This method is preferable to the full two-parameter sweeps simply because it is much more efficient, especially if there appears to be a large offset, as was the case here. If the peak is broad, neighbouring oscillations can have effectively the same maxima and minima, giving multiple field strengths that can be used. Here, the inset of figure 5.11 shows a good location to check for the precise maximum critical current, as was done to produce figure 5.8 in the previous section, showing the full size flux oscillations.

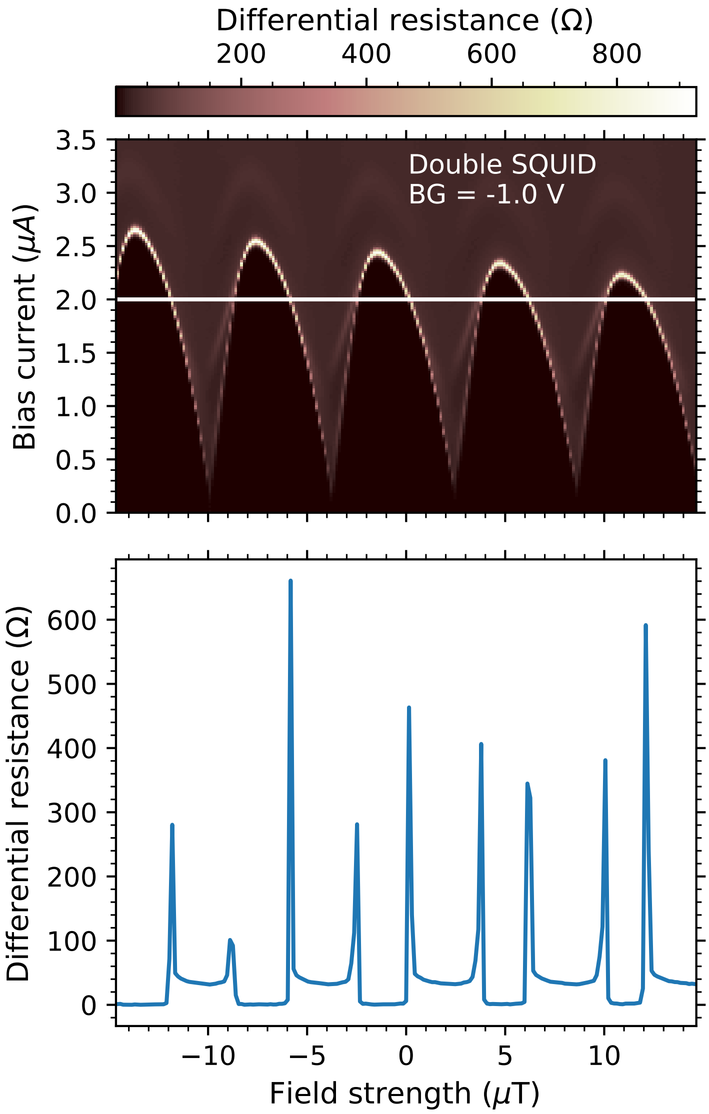


Figure 5.10: Flux oscillations of the Double SQUID showing critical current maxima which are not symmetrical about 0 μT magnetic field strength. A slice at a bias current of 2.0 μA is shown by the horizontal white line on the upper plot, and is displayed on the lower plot, showing that the superconducting regions get wider for the negative field and narrower for the positive field, due to the shift in the position of the critical current. Faint lines to the left of and above each peak are Andreev reflections.

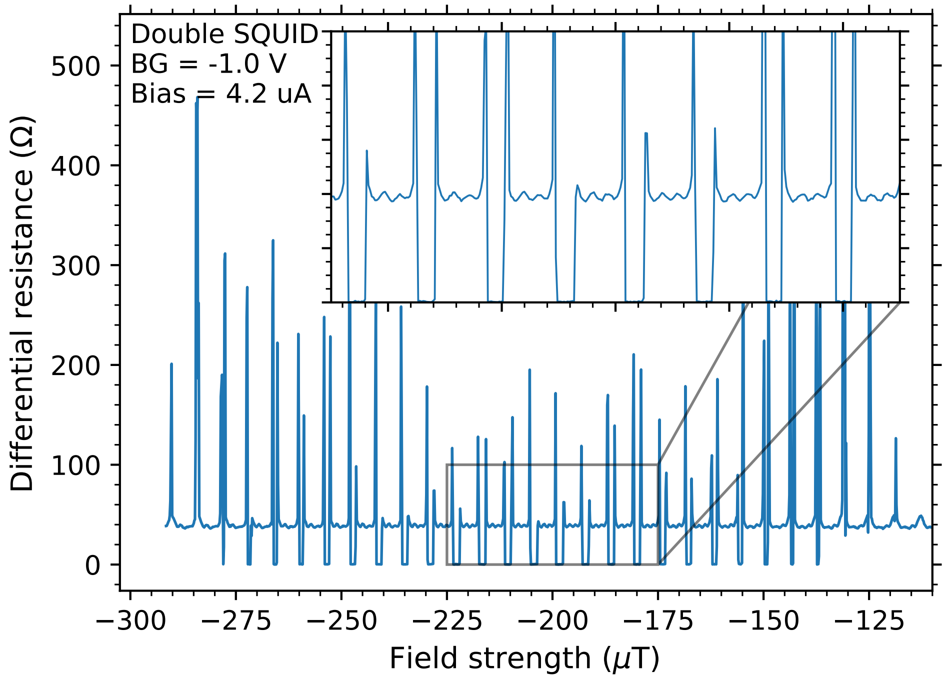


Figure 5.11: With constant current bias of 4.2 μA, magnetic current is varied and the differential resistance of the SQUID is measured, so that the effective point of 0 magnetic flux can be determined. The back gate voltage was 1 V. The inset zooms in on the point where the superconducting regions are the largest, corresponding to an effective 0 magnetic field. Above -135 μT and below -280 μT, the bias current is greater than the maximum critical current.

### 5.1.4 Estimating SQUID inductance using flux oscillations

The inductance of a SQUID is an important parameter because it influences the size of the circulating current in the SQUID. Recalling section 2.2.4, the SQUID parameter defined by the inductance is the screening parameter $\beta_L$, which is proportional to both the inductance $L$ and the critical current $I_c$, as shown in (5.6).

$$\beta_L = \frac{2LI_c}{\Phi_0} \tag{5.6}$$

If the inductance is already known then it is straightforward to calculate corresponding values of $\beta_L$ for each critical current measured. But complicated SQUID geometries can make the inductance values more difficult to estimate accurately.

In this section, a method based on the modulation depth $I_d$ of the Big SQUID (section 4.1.2) is used to estimate its inductance. The modulation depth describes the difference between the critical current maxima $I_{\text{c max}}$ and minima $I_{\text{c min}}$ due to the critical current's dependence on applied magnetic flux. It is defined as

$$I_d = \frac{I_{c\ \max} - I_{c\ \min}}{I_{c\ \max}}, \tag{5.7}$$

and is influenced by $\beta_L$. The minimum critical current of a SQUID increases from close to 0 to approaching the maximum critical current as $\beta_L$ increases. As $\beta_L$ is dependent on the maximum critical current $I_c$ it should be possible to estimate the inductance of a graphene SQUID. This is because in a graphene device, $I_c$ is tuneable by the field effect, as shown in figure 5.1, allowing a relation between the back gate voltage and $\beta_L$ to be established.

Experimentally, the modulation depth was measured at back gate voltages from -5.0 to 5.0 V, providing a set of values of $I_d$ and $\beta_L/L$. The values were determined using equations (5.7) and (5.6) with the maximum and minimum critical current values extracted by finding the switching current of the Big SQUID. Both positive and negative critical currents were used.

A simulation of the modulation depth against $\beta_L$ was performed using a sinusoidal CPR using the model described in chapter 3, to fit to the experimental data. The experimental data was used to calculate $\beta_L$ for different $L$, with the best fit determined by a least-squares method. This value should represent the total inductance of the device, including geometric and kinetic contributions.

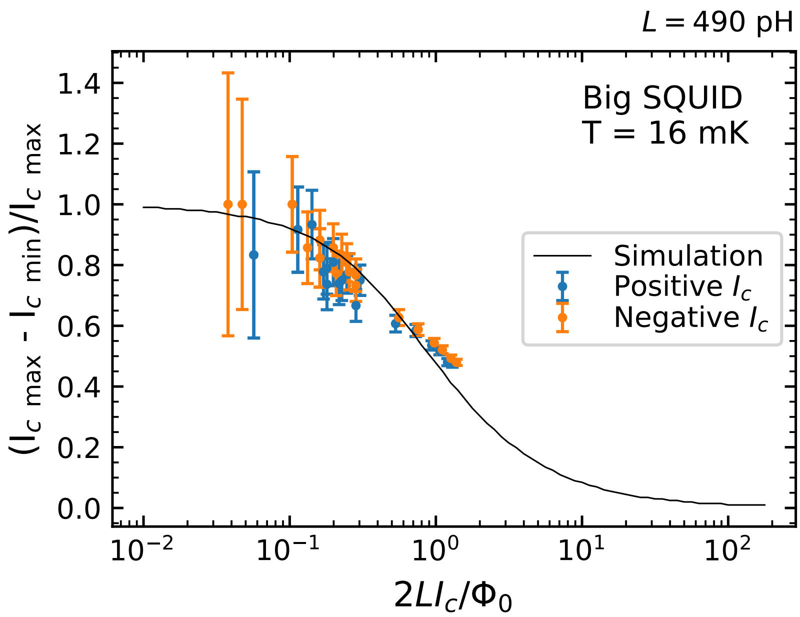


Figure 5.12: A plot of flux oscillation depth plotted against $\beta_L$. The orange and blue data points are calculated from experimental data at various back gate values corresponding to different $\beta_L$, calculated from $I_c = I_{c\text{max}}$. The blue and orange points are for critical currents from applying positive and negative current biases respectively. The grey line is the simulated results for an inductance $L = 490$ pH, using a symmetrical SQUID with a sinusoidal current-phase relation and $\beta_C = 0.1$.

Figure 5.12 shows the resulting plot comparing the experimental data and simulation. The best fit of inductance was $L = 490 \pm 40$ pH, considering the data derived from both the positive and negative critical currents together. The y error bars are from the step size of the bias current giving uncertainty in the recorded position of the critical current, and the uncertainty in the inductance fit is estimated from the size of x-error bar required for the larger $\beta_L$ values to agree with the simulation, as $L$ affects the position of the data on the x-axis.

To verify the result, this inductance was compared with separate estimates of the geometric and kinetic inductances. Kinetic inductance values for Nb-related materials are usually on the order of 10 pH[75]. The kinetic inductance $L_K$ can be estimated based on the geometry and properties of the superconducting loop[137]

$$L_K = \frac{\mu_0 \lambda^2 l}{wh} \tag{5.8}$$

where $\mu_0$ is the magnetic permeability of the vacuum and $\lambda$ is the penetration depth of the superconducting film. The variables $l$, $w$, and $h$ are the length of the SQUID loop, and the width and thickness of the film, respectively. The constant values are $\mu_0 = 4\pi \times 10^{-7}$ H m$^{-1}$, $h = 50$ nm, and $\lambda = 235$ nm[138]. The Big SQUID's geometry is not straightforward to analyse, but based on the values defined so far the relation is $L_K = 1.39(l/w)$ pH. The length of the SQUID loop will be taken through the centre of the superconducting film as approximately 1100 µm. The width will be taken as an average value of approximately 65 µm, giving a result of $L_K = 24$ pH. This is a similar result to other similar junctions.

To estimate the geometric inductance the finite-element model FastHenry [139] was used, giving a value of 315 pH. Summing the kinetic inductance with the geometric inductance gives a total inductance of 339 pH. This is an underestimate in comparison with the value of 490 $\pm$ 50 pH calculated from fitting the experimental data to the simulation. The most likely explanation for this is that the simulated model used to fit the data was not entirely reflective of the experimental device. Considering that the SQUID was fabricated in the same way as to produce ballistic graphene junctions, it would be expected that they exhibit skewing of the CPR. By plotting the dependence of the modulation depth against $\beta_L$ for different transparencies of junction, it can be determined if the skewed SQUID model makes a better fit in the case of the lower inductance estimate.

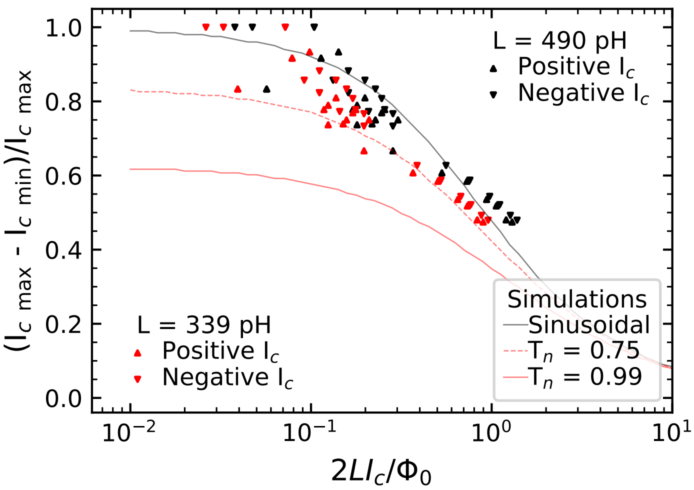


Figure 5.13: Plot of modulation depth against $\beta_L$. The data in black are the same as presented in figure 5.12, corresponding to the best fit to the sinusoidal CPR SQUID model with inductance $L =$ 490 pH. The solid black line is the corresponding simulation. The red points are the same data but calculated for inductance $L = 339$ pH, the value estimated from the Big SQUID geometry and kinetic inductance. The red lines are the SQUID model with a skewed CPR, with transparencies of 0.75 and 0.99 shown by the dashed and solid lines respectively.

Increasing the skewness of the CPR reduces the modulation depth, as shown in figure 5.13. Using $\beta_L$ values calculated for $L = 339$ pH, the sinusoidal CPR fits better for the data where the SQUID is close to charge neutrality. This is where the critical current is smallest and therefore $\beta_L$ is also at its smallest. As $\beta_L$ increases, the skewed models appear to fit better, but no individual curve matches the data perfectly. If the skewness of the CPR is increasing as $\beta_L$ increases, then increasingly skewed models would make better fits to corresponding parts of the data. This is supportive of the idea that ballistic graphene SQUIDs have a skewed CPR. It also presents a method which, given confidence in the inductance value of the SQUID, could give another way of assessing the transparency and skewness of the junctions in SQUIDs. Given the values from the two methods, a reasonable overall estimate of the Big SQUID inductance would be $\approx 400$ pH.

## 5.2 Observation of half-integer Shapiro steps

It has been shown in sections 5.1.1 and 5.1.3 that the Double SQUID exhibits the tuneable critical current and flux oscillations expected of a graphene SQUID. This allows for an interesting exploration of the fractional Shapiro steps phenomena. As shown in the simulations and literature, a SQUID displays half-integer Shapiro steps when there is a non-integer quantum of flux in the SQUID loop. These half-integer steps should be visible regardless of the gating of the SQUID. Additionally, a graphene SQUID should have a skewed CPR when the junctions are tuned to high transparency, resulting in fractional Shapiro steps. Both origins of fractional Shapiro steps should be visible in the Double SQUID, and could be switched on and off by changing the relevant parameters. A secondary hypothesis which further reinforces the presence of mechanisms associated with graphene SQUIDs and skewed CPRs is how the CPR should return to the sinusoidal shape at higher temperature. This is consistent with the model for the CPR in equation (2.8).

In this section, firstly the coupling of the RF signal to the SQUID will be discussed. This is to show how the optimal region of the power-frequency parameter space to measure Shapiro steps was found.

Following that, the measurements of half-integer Shapiro steps will be shown. The two hypotheses mentioned were both investigated: temperature and gating. In both cases, the magnetic flux was also varied.

The introduction of the high-frequency signal does introduce complications into the measurements, most notably heating of the mixing chamber and sample. It cannot be guaranteed that the temperature of the device is consistent throughout these measurements, especially if the power of the RF signal is varied, because only the temperature of the mixing chamber was monitored. This was one limitation of the setup which would ideally be improved upon for future measurements, but measuring the temperature of a device would require the 'thermometer' to be built into the device itself, and need additional wiring and measurement apparatus. A second improvement would be the addition of a second RF antenna to act as a receiver and give a better estimate of the power being delivered to the device, rather than just the power sent from the signal generator.

### 5.2.1 Assessing the coupling of the RF signal to the SQUID

Fundamentally it should be possible to observe Shapiro steps at any frequency – they simply appear at particular corresponding voltage values defined by (2.26). In the current-biased setup that is being used, the alternating current drives the rotation of the junction phase at the frequency of the current, so the drive frequency always matches the junction frequency. There are matters of practicality and a lack of ideal conditions for experiment which determine which frequencies are best to use. Shapiro steps are separated by a quantised voltage value, so the resolution of the measurement instruments must be sufficient to distinguish neighbouring steps. This will put a minimum value on the frequency that can be used. However, the actual minimum may also be determined by the apparatus that one has access to. In this case, the signal generator had a frequency range from 2 - 20 GHz. This was further restricted at the upper end by the rating of the attenuators used which had a maximum frequency of 18 GHz. This upper limit is no problem as it is substantially below the characteristic frequency of the SQUID. The normal state resistance of the devices also impacts the instrumental resolution needed, but for the current biasing. This is because sharper gradients imply smaller differences in bias current between voltage steps. In graphene SQUIDs the normal state resistance depends on the doping of the junctions, with the largest resistance tending to be where the device is at charge neutrality. Therefore it is this regime which places the experimental limit. A rule of thumb conversion is that 1 GHz roughly corresponds to a 2 μV step spacing (2.26). This means that in a device like the Double SQUID where the order of magnitude of voltage responses is 10 μV, it makes sense to use an RF frequency which would give well spaced and easily resolved steps over that range. The current step size should produce changes in voltage substantially smaller than the Shapiro step size that is being targeted. In general it seems sensible to use as high a frequency as possible to increase the gap between steps to make resolving them as easy as possible. Additionally, when considering the possibility of fractional Shapiro steps, the highest resolution possible will be needed, as shown in the simulations in section 3.9.3.

The frequency used is actually determined by geometric factors associated with the sample stage. For these measurements the device is mounted inside a cylindrical metal puck (see section 4.2). The electric field output by the antenna has a wavelength on the order of centimeters, which is comparable to the size of the sample environment. Therefore it is likely that standing waves are set up between the closed ends of the puck. Depending on the exact positioning of sample with respect to the antenna and frequency of the signal, the nodes and antinodes will be positioned differently. The best frequency coupling to the device will occur when the device is at a point of constructive interference. Preliminary measurements are needed to optimise the coupling of the device to a particular frequency in the determined range.

Two techniques have been used for this device. First, a colour map of the differential voltage response is produced with dependence on the RF power and frequency parameters. To do this, the SQUID is biased at zero volts and then the power is swept down at a fixed frequency[2]. This is repeated, stepping the frequency between power sweeps. The aim is to find frequencies where the differential signal response clearly oscillates as the RF power changes, indicating coupling between the signal and the device. This method also helps to determine the level of power needed to be applied. Ideally the

[2]This technique was shared with the author by D. Wielens, in private communication, August 2022.

power is minimised to limit heating inside the low-temperature environment but a minimum power is required in order to resolve the Shapiro steps, as the power impacts the width of the step parallel to the current axis. Figure 5.14 shows an example of this process repeated for different back gate voltages. Particularly in the higher-frequency regions the columns clearly change between a higher and lower signal response, indicating oscillations. Four plots were included here so that the coupling can be assessed with respect to the back gate voltage. This addresses a potential inconsistency associated with the changing characteristic frequency of the SQUID due to the dependence of the critical current and normal state resistance on the gating of the graphene. At lower gate voltages the resistance is greater, shown by the brighter colour in the plots. This clearly diminishes as the back gate voltage is increased. This is expected from the typical back gate dependence of a graphene SQUID (figure 5.1). The figures also display both resistive and superconducting regions, though not as clearly separated as in other measurement schemes. This is because the superconducting state of the device is sensitive to the power and frequency combination. The RF signal deposits heat into the system (which can be seen by a rise in the mixing chamber temperature) though the actual temperature of the device is unknown, not necessarily equivalent to the mixing chamber itself. It would be reasonable to expect that the power of the signal is not dissipated uniformly through the sample environment, because of the geometrical arguments discussed previously. As well as being susceptible to magnetic fields, it is reasonable to consider firstly that because Cooper pairs are charged they can also be influenced and potentially broken by electric fields. Secondly, the electric field is generated by an unsophisticated methodology and it would be difficult to rule out that there is no magnetic field also generated, possibly by a secondary source in the sample environment induced by the original signal.

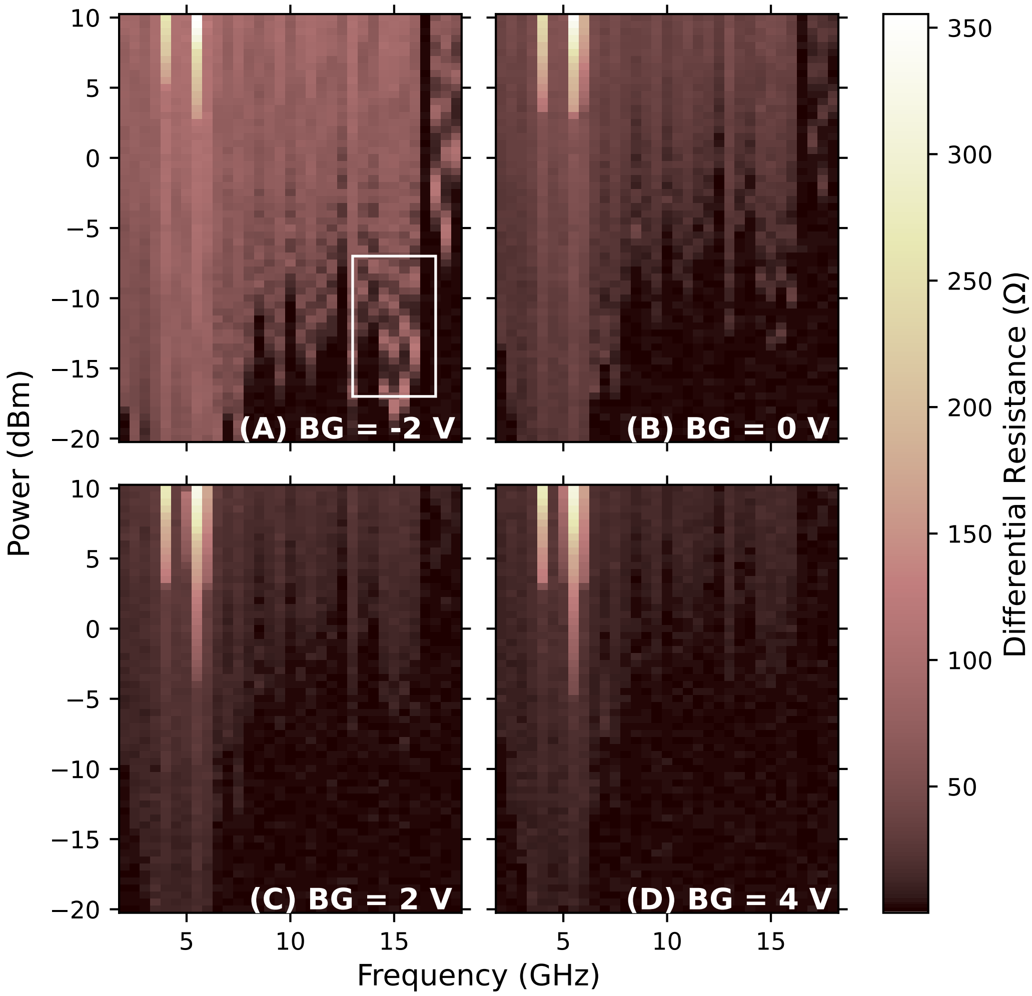


Figure 5.14: Differential resistance response of the Double SQUID for power against frequency at 0 current bias for different back gate voltages. The differential resistance is generally largest for (A) and decreases sequentially as the doping of the junctions is increased. Features also retreat to be visible at higher powers, leaving more superconducting region at lower powers as the doping is increased. In (A) the white rectangle highlights a location where oscillations are clearly visible.

It is important to pay attention to the superconducting regions because it is expected that the critical current of the device will increase as the back gate voltage increases. This effect explains the slight differences in the plots shown, and is clear when comparing slices from different back gates at a particular frequency, as in figure 5.15. The overall shape and pattern of the colourplot remains very similar for each back gate value, particular key features include the very strong signals in the upper left hand corner of each plot, and how for those low frequencies the device is resistive across almost the whole power range. From medium to high frequencies the superconducting region is more pronounced, except for the area around 15 GHz. This general pattern is maintained, but it is clear for medium to higher frequencies that the resistive region is ending at lower power. A qualitative description might be that the colour plot is 'creeping up' with back gate voltage. This is consistent with the idea that the critical current is increasing, as seen in the dc-only measurements.

It is clear that back gate tuning and subsequent change of charge carrier concentration affects the power-frequency plots in predictable ways explained by the effect on the transparency of the junctions and the critical current. Otherwise, distinct features in the plots remain consistent, suggesting that back gate tuning does not directly influence the effects caused by the high-frequency irradiation when at 0 bias current.

The second technique is more direct but slower to perform. It is good for improving precision once a rough frequency has been found using the first technique. A power level is chosen at which oscillations were visible, then the bias current is swept up from zero while measuring the dc voltage response. This is repeated across a higher resolution but smaller band of frequencies compared to the first assessment. Shapiro steps should appear obvious in the individual IV sweeps, and the sharpest and most robust traces can be identified to select the frequency to use.

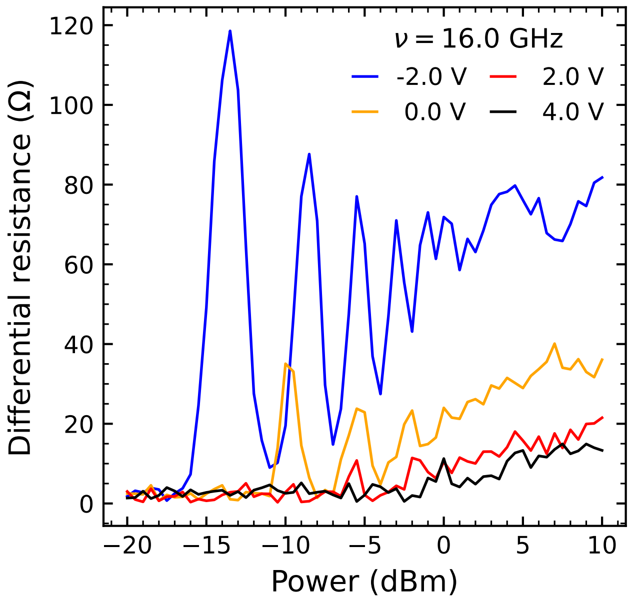


Figure 5.15: Frequency slices at 16 GHz from each of the back gate voltages shown in figure 5.14 for comparison. Oscillations are much more visible when the graphene is more p-doped. The first oscillation in the increasing power direction appears at a higher power for more n-type configurations. The device is superconducting before the first oscillation.

Once a frequency has been identified where Shapiro steps are reliably visible, the experiment will proceed. The typical frequency used for the measurements of the Double SQUID shown here was 16.6 GHz.

### 5.2.2 Temperature dependence of half-integer Shapiro steps

The investigation of the CPR of graphene junctions by Nanda et al.[37] shows how a CPR which is skewed at 20 mK returns to a sinusoidal shape at 4.2 K. As the skewed CPR can give rise to half-integer Shapiro steps in graphene SQUIDs, it follows that the half-integer steps would be suppressed when moving from low temperature to high temperature because of this change in the CPR. The half-integer steps caused by half-integer flux ($n\Phi_0/2$) in the SQUID loop would not be suppressed due to the change in the CPR. However, the difficulty here is that increasing temperature increases the thermal noise in the circuit, which can prevent short steps from being resolved as shown in the noise simulations (section 3.9.2). But while half-integer steps from the half-integer flux can be resolved, it is known that there is sufficient resolution to observe half-integer steps from the skewness of the CPR. Therefore, if the half-integer steps from the CPR vanish at a particular temperature but those from the half-integer flux are still visible, the change in the CPR would be verified.

#### Temperature dependence results

To test the hypothesis, a robust half-integer step was identified, and measured at mixing chamber temperatures from 20 mK to 6 K. Flux was applied through the SQUID to ensure that the flux-dependent critical current is at a maximum, so half-integer steps should only appear due to the CPR. The frequency used was 16.6 GHz and the applied power was -4 dBm (attenuated by 20 dB at room temperature). The actual power delivered to the device is unknown because it depends on the precise positioning of the antenna above the sample and other attenuation sources, but was kept constant for this experiment.

Figure 5.16 shows the plots of the Shapiro steps themselves up to 5 K. From 20 mK up to 2.1 K there is no real change in the characteristic. Though it appears that initial temperature increases from 20 to 2100 mK cause the trace to shift to higher current, this is likely explained by experimental drift. The implied difference in the critical current over this range is about 0.1 µA. At 3000 mK and beyond the half integer steps are clearly suppressed while the integer steps are still visible.

It is also notable that the critical current of the SQUID is being reduced with temperature, due to the shift along the current axis. This implies that the transparency of the junction is being reduced, even though the gate voltage is kept constant. These initial results support the hypothesis that half-integer steps are being suppressed by increasing temperature, and that this is due to the temperature reducing the skewness of the CPR, because of the reduced transparency.

The stability of the SQUID until beyond 2.1 K shows a good operation range for the device, and that the small changes in temperature seen due to heating from the RF signal that keep the mixing chamber below 40 mK (see appendix figure A.35) are not likely to affect the measurements.

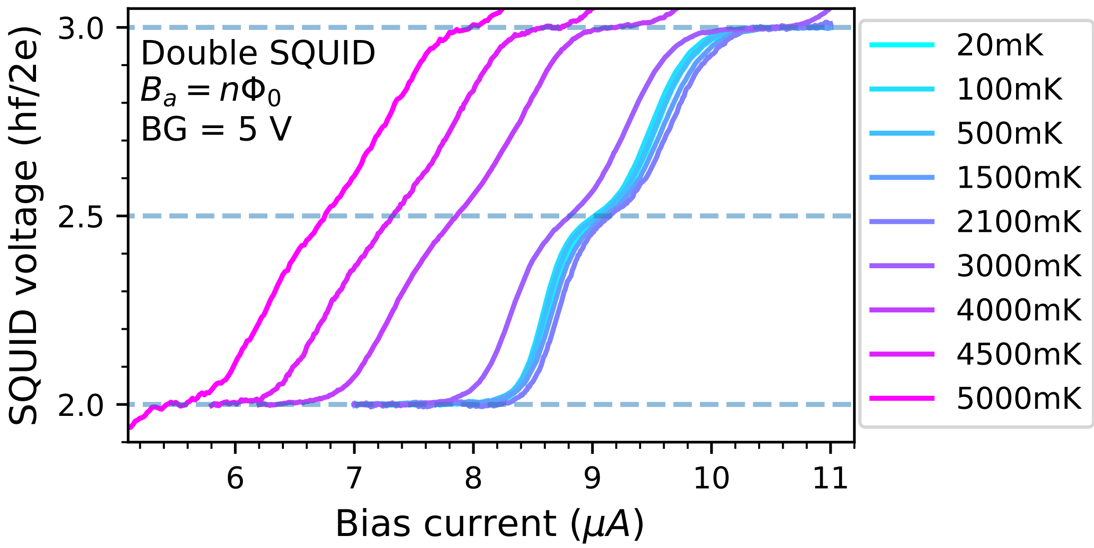


Figure 5.16: Plot of the IV characteristics of the Double SQUID in the region of the second to third integer Shapiro step at different temperatures from 20-5000 mK. For all measurements the back gate was 5 V, the magnetic flux corresponded to an integer flux quantum, the RF frequency was 16.6 GHz, and the RF power was -4 dBm, attenuated by 20 dB at room temperature.

#### Step characterisation

To better characterise the half-integer Shapiro steps and evidence the changes with temperature, the differential resistance data was used. The differential resistance is calculated from the differential voltage which was measured at the same time as the dc voltage with the lock-in amplifier.

In a plot of differential resistance against bias current, a half-integer Shapiro step looks like a pair of peaks with a trough between them, with clear zero differential resistance regions on the outside of the peaks, corresponding to well-defined integer steps.

While the dc trace shows the actual appearance of the Shapiro steps which can be mapped nicely to the predicted quantisation (equation (2.26)), the differential signal encodes more quantifiable characteristics which can be used to start comparing different steps. Differentiating the dc signal, we would expect step features to have a gradient of 0 because they are constant in voltage. The linear sections between the steps would ideally have a constant gradient greater than zero, corresponding to the normal-state resistance of the SQUID. The transitions between the neighbouring steps where the dc response moves from a step into a linear gradient and back into a step will be characterised by a peak in the differential curve.

Figure 5.17 gives an example by showing both the dc and differential results of a measurement focused on a half-integer Shapiro step between two integer Shapiro steps. The black line shows the dc measurement, the original voltage values have been expressed in units of $hf/2e$ where $h$ is Planck's constant, $f$ is the RF signal frequency, and $e$ is the magnitude of the charge on an electron. The spacing of the steps matches the predicted values extremely closely. While the half-integer step is not completely flat, it is certainly present. The curving of the step indicates a lack of resolution in the measurement, as the curve is being forced to transition into the next integer step before being able to complete the half-integer step. The differential curve is consistent with expectations – the differential is 0 for the well-defined integer steps, and the double peak between the zero regions indicate the transitions in and out of the half-integer step. The trough does not reach 0 as the half-integer step did not exhibit a constant voltage.

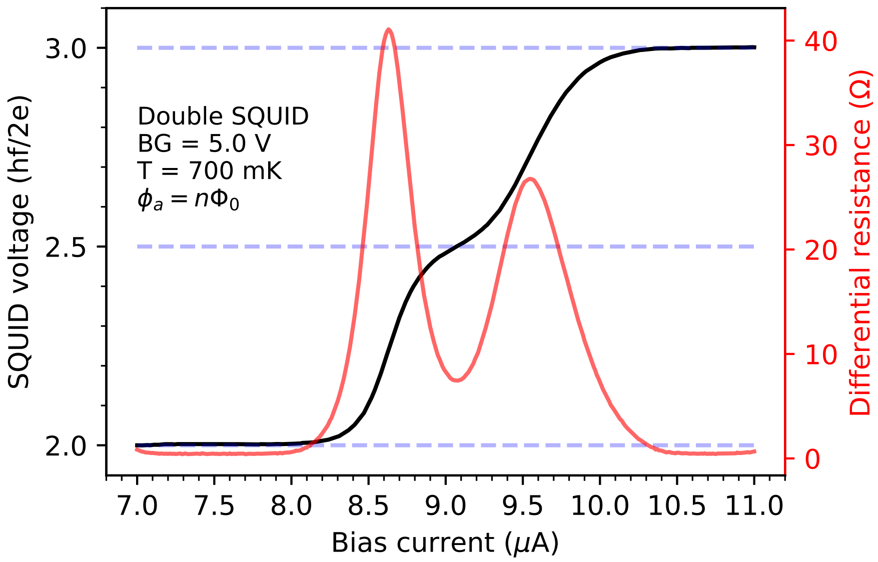


Figure 5.17: The black line is the dc voltage response with current, showing the second and third Shapiro steps, and the half-integer step between them. The red line is the differential resistance response of the same data. The temperature was 700 mK and the back gate was at 5 V. The RF signal had a frequency of 16.6 GHz and an amplitude of -4.0 dBm. The applied magnetic flux was an integer multiple of $\Phi_0$.

The majority of the observed half-integer steps measured did not completely flatten out, leaving the trough feature between the peaks above 0. Extracting the corresponding minimum point is one way to characterise the step in a quantifiable way, as it would give an indication of how 'step-like' the feature is in comparison to others. The peaks are also of interest because they act as markers for the transition periods between steps. Figure 5.18 shows the application of these characterisation techniques to the differential curve from figure 5.17. The peaks and troughs were extracted using the SciPy function `scipy.find_peaks`. The trough depth is useful to compare between half-integer steps to determine if a step is being suppressed by differing conditions. The peak separation could be used as a way of quantifying the width of the half-integer step, given that it is often the case that there is not a sharp transition into the half-integer steps, and that the half-integer steps do not tend to have extended ranges of 0 differential resistance. One drawback is that the shapes of the two peaks are usually not symmetrical, so the implication is that more of the bias current range is spent on either the transition into or out of the step. As it is difficult to establish any point in a half-step which is not also in the transition, there are no other consistent features which can be used in this data.

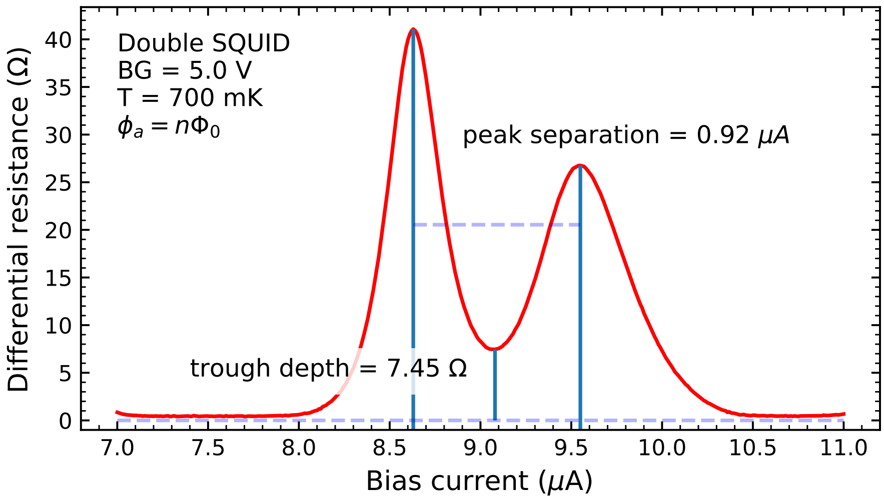


Figure 5.18: Plot showing the differential resistance of the Double SQUID over a half-integer Shapiro step between two integer steps. The temperature was 700 mK and the back gate was at 5 V. The RF signal had a frequency of 16.6 GHz and an amplitude of -4.0 dBm. The applied magnetic flux was an integer multiple of $\Phi_0$. The 'trough' depth shown on the plot is measured from the minimum of the curve to 0. The 'peak separation' is measured between the peak maxima.

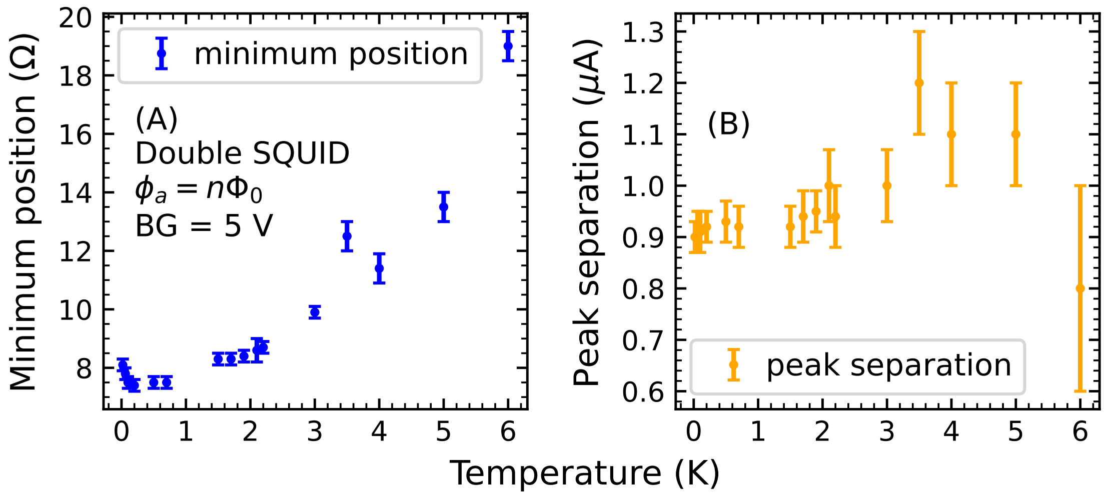


Figure 5.19: Plots of the values of quantifiable features of a half-integer Shapiro steps against temperature. The RF signal had a frequency of 16.6 GHz and an amplitude of -4.0 dBm. The applied magnetic flux was an integer multiple of $\Phi_0$. (A): The position of the minimum corresponding to the gradient of the half-integer step. The smaller the value, the flatter the step. (B): The separation between maxima corresponding to the beginning and end of Shapiro steps. The larger the separation, the longer the step.

These features of the differential plot were used to attempt to characterise the half-integer steps shown in the temperature dependent measurements (figure 5.16). The results are shown in figure 5.19. In plot 5.19 (A), the minimum position reached by the half-integer steps is shown to get higher up after around 1 K, increasing non-linearly with temperature. In plot 5.19 (B), the peak separation is shown to stay fairly constant until about 3 K, indicating that the transitioning around the half-step was in the same place until that point. The peak separation does not appear to change as significantly as the minimum position. Uncertainty gets larger with temperature as the noise increases making the positions of the maxima and minima less clear. By 6 K, the steps are suppressed to the point that the peaks were very unclear, leading to the significantly larger uncertainty, possibly indicating the temperature limit of Shapiro step observation. This may be more indicative of the stability of the integer steps, as their end and beginning are what underpin the peaks. Even if there is no half-integer step visible, the integer steps still perform the transition into and out of the linearly increasing voltage between steps. Therefore it is still possible to observe a minimum point when there is no half-integer step. An improvement to this characterisation could be to calculate the relative difference between the maxima and minima for determining if there is a fractional Shapiro step.

So far, these results are indicative of the expected temperature-dependent behaviour of half-integer Shapiro steps due to a skewed CPR. However, they do not conclusively rule out the possibility that steps are being lost to thermal noise. To do that, measurements were taken which varied the magnetic flux in the SQUID loop, allowing half-integer steps to be produced which would not be suppressed due to a changing CPR, and could therefore be used as a reference to establish when the thermal noise is high enough to suppress half-integer steps.

#### Magnetic field Shapiro maps

In these measurements, colourplots were produced which show the IV characteristic against the applied magnetic flux, allowing for comparison between the integer and half-integer flux regimes, such as in figure 5.20. These are analogous to the flux oscillations plots earlier in the chapter (section 5.1.3) in terms of characterising the oscillation period of the SQUID. They can also be compared qualitatively to the simulated plots in section 3.9.1. They are qualitatively similar in the positioning of features such as the peaks and plateaus. The simulation current range from 0-2 in figure 3.7(A) corresponds to 0-1.2 μA in the experimental data, suggesting that future simulations should have an extended current range to check the features beyond that point.

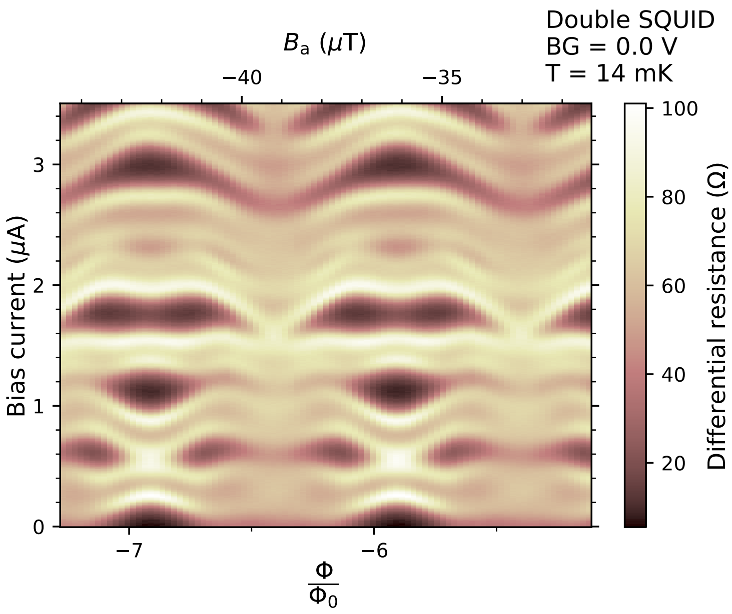


Figure 5.20: Magnetic flux dependence of the differential resistance of the Double SQUID under RF irradiation at 14 mK. The periodicity of the SQUID is still visible under RF irradiation, which is consistent with the values with no RF signal. The points of integer magnetic flux are in line with the peak-like features such as at -42 μT, and the half-integer flux points are in line with the channel-like features such as at -39 μT. The back gate voltage is 0 V.

The plots used for the analysis are taken over the same range of flux values as figure 5.20, but the back gate is increased to 5 V. The following plots are shown for temperatures of 4, 5 and 6 K. Notably, a basic level of SQUID behaviour is visible in the colourplots up to 6 K where small Shapiro step plateaus are still visible, showing that the critical temperature of the SQUID is greater than this temperature. Despite this, lower temperatures would definitely be preferred as the thermal noise is getting more significant at this point. In figure 5.21, it is already difficult to distinguish the half-integer Shapiro steps, though the integer steps are still very visible. Half-integer steps are also not very visible at half-integer flux. This trend continues with increasing temperature to 5 K in figure 5.22 and 6 K in figure 5.23. To better attempt to view the steps at high temperature, the differential measurements were used.

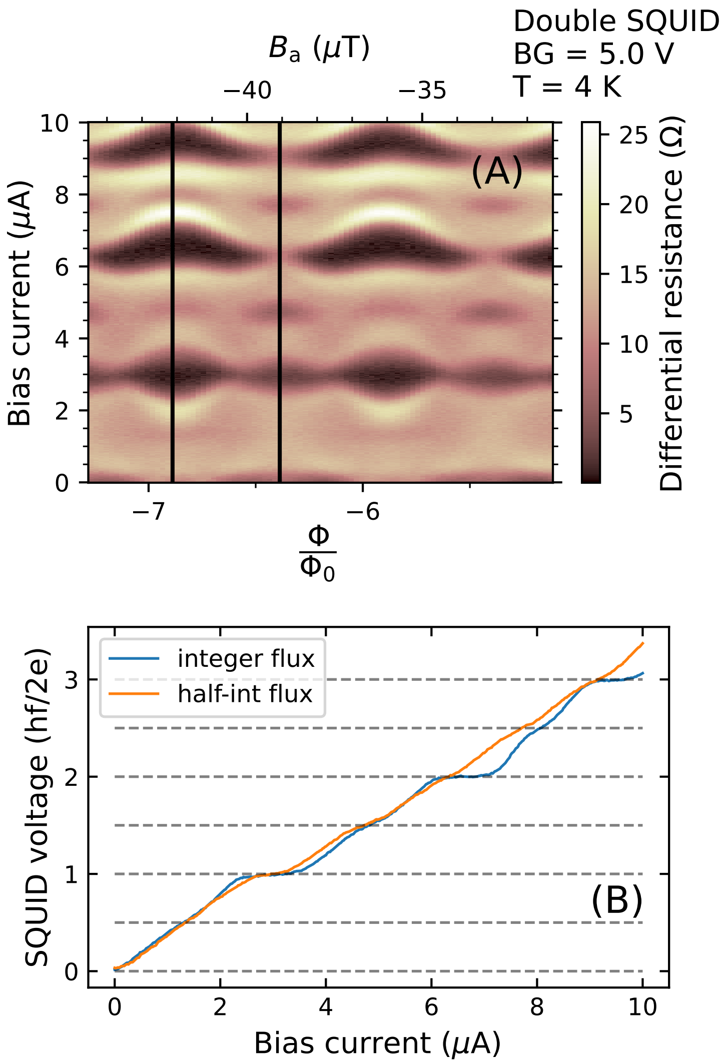


Figure 5.21: Colourplot of differential resistance against bias current and applied magnetic flux. The Double SQUID has its back gate biased to 5 V and the mixing chamber temperature is 4 K. An RF signal is applied at 16.6 GHz and -4.0 dBm with 20 dB attenuation at room temperature. Slices are taken at integer and half-integer flux quanta. The dc response is offset in the y-direction to align the steps with their corresponding quantised voltage value.

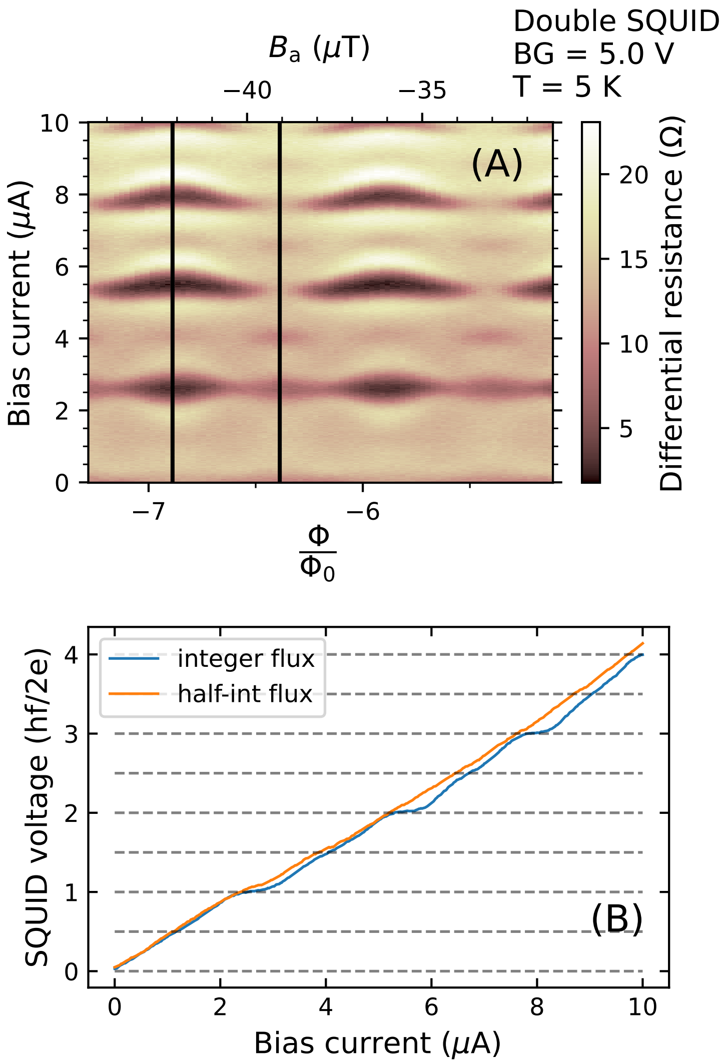


Figure 5.22: Colourplot of differential resistance against current and applied magnetic flux. The Double SQUID has its back gate biased to 5 V and the mixing chamber temperature is 5 K. An RF signal is applied at 16.6 GHz and -4.0 dBm, with 20 dB attenuation at room temperature. Slices are taken at integer and half-integer flux quanta. The dc response is offset in the y-direction to align the steps with their corresponding quantised voltage value.

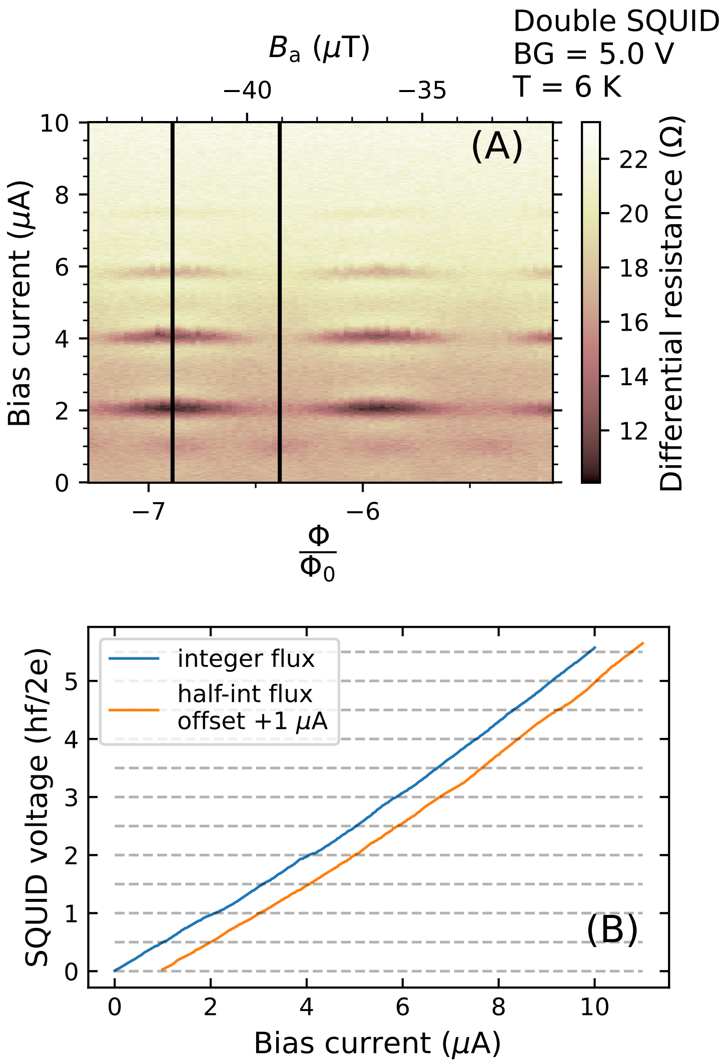


Figure 5.23: Colourplot of differential resistance against current and applied magnetic flux. The Double SQUID has its back gate biased to 5 V and the mixing chamber temperature is 6 K. An RF signal is applied at 16.6 GHz and -4.0 dBm with 20 dB attenuation at room temperature. Slices are taken at integer and half-integer flux quanta. The dc response is offset in the y-direction to align the steps with their corresponding quantised voltage value.

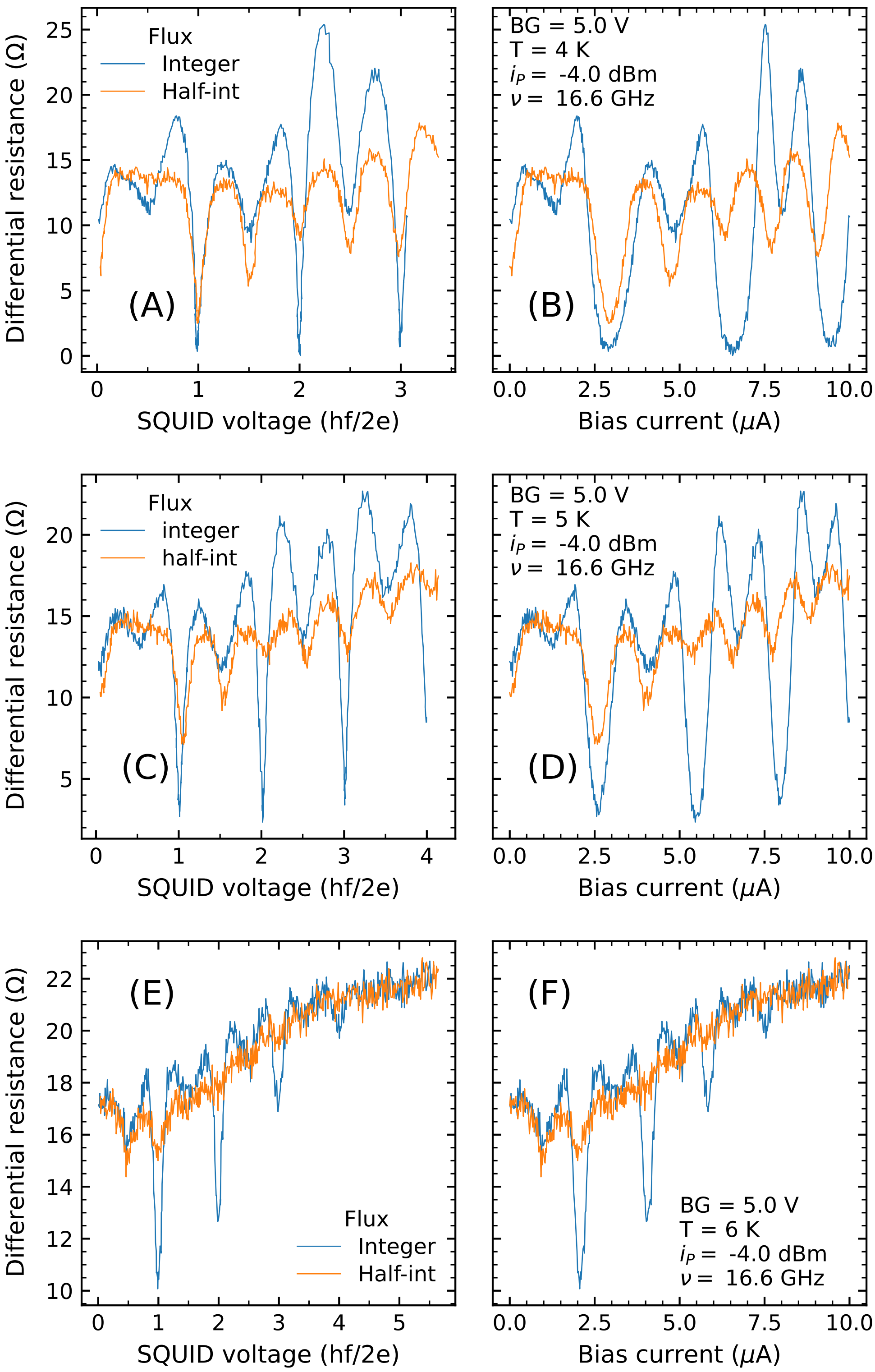


Figure 5.24: Line plots of differential resistance against dc voltage in terms of Shapiro step number (A, C, E) and differential resistance against the corresponding current bias (B, D, F). Plots are given for integer (blue lines) and half-integer (orange lines) flux at temperatures of 4 (A and B), 5 (C and D) and 6 K (E and F). Data are from the Double SQUID and correspond to the plots in figures 5.21, 5.22, and 5.23.

The differential measurements are shown in figure 5.24, corresponding to the plots in figures 5.21, 5.22, and 5.23. Together, these give insight into the behaviour of the SQUID when the thermal noise is beginning to have a large effect on the measurement. Plots (A), (C), and (E) align the differential resistance measurements with their corresponding dc voltage response, scaled to Shapiro step units. In these plots, thin deep troughs correspond to larger Shapiro steps rather than wide troughs which would be seen in the corresponding plots (B), (D), and (F) of differential resistance against bias current. Because of the plots against dc voltage, it is clear that the troughs in the plot against bias current correspond to Shapiro steps, with the deeper troughs being integer steps, and the smaller troughs in between corresponding to half-integer Shapiro steps.

At 4 K, integer Shapiro steps remain very visible at integer flux, though at half-integer flux they are less visible. Half-integer steps are difficult to see in the dc response, but the corresponding troughs are still visible in the differential plot. Heating up to 5 K, the integer Shapiro steps are still clear in the differential for integer flux, but at half-integer flux all steps are diminishing compared to at 4 K. Finally at 6 K, with integer flux the troughs corresponding to the integer steps are still visible but are diminishing, and steps above the first get smaller until they disappear into the noise completely after $n = 4$. Very small troughs at half-integer Shapiro step voltages can be resolved in the differential plot for integer flux. The dip in the differential resistance shows a change in gradient, but is not sufficient to evidence a half-integer step rather than the transition between two integer steps. For half-integer flux, all steps are lost to noise after $n = 1$.

This shows that the integer flux state is the most resilient state of the SQUID for Shapiro steps under heating. As there is still evidence of half-integer steps at integer flux (at least at 4 K) it could suggests that there is a skewed CPR which has not completely returned to a sinusoidal shape at this point.

Another observation is with regard to the relative sizes of the half-integer step troughs with integer and half-integer flux. In each plot against SQUID voltage, the bottom of the integer flux troughs are at a higher differential resistance than the bottom of the half-integer flux troughs. The increasing differential resistance of the minima mean the half-integer steps are further from being completely flat steps, indicating that they are becoming suppressed. This is especially relevant comparing the relative depths of the troughs for half-integer flux to the corresponding integer flux trough. At 4 K, they are similar in depth. But as temperature increases,

The corresponding troughs against bias current are slightly wider for half-integer flux than integer flux. This is consistent with how the simulations showed wider Shapiro steps for half-integer flux when at high transparency.

To supplement the investigation into the effects of temperature on the SQUID, figure 5.25 shows how the flux oscillations of the SQUID appear at 4 K, with no RF signal, at 5 V back gate. This is evidence that the current-phase relation is now very close to if not sinusoidal, because the depth of the flux oscillations has reached its maximum, with the positive and negative minima meeting. The reduced critical current is close to the measured critical currents in figures 5.4 and 5.5 (A) which correspond to gating the device close to charge neutrality, when in fact the device is gated at 5 V. This is evidence that the current-phase relation has been returned to a low-transparency regime despite gating.

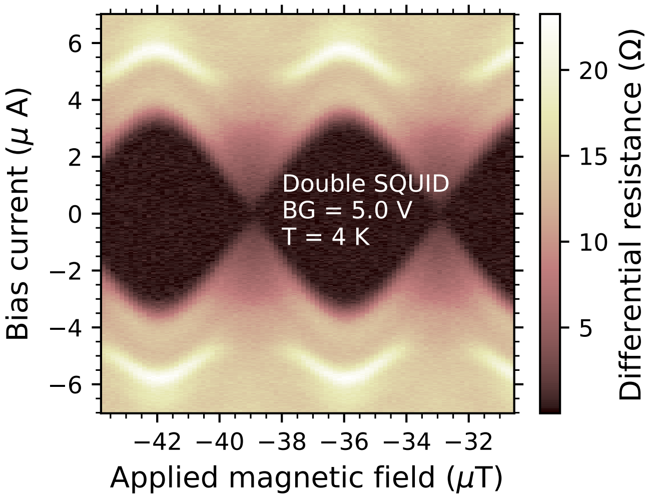


Figure 5.25: Flux oscillations of the Double SQUID at 4 K temperature and 5 V back gate. No RF signal applied. The critical current minima meet close to 0, evidencing a sinusoidal CPR.

Figure 5.25 is also a useful confirmation that the correct integer and half-integer flux values are being used in the RF measurements, where the oscillations have a different appearance with less clear peaks. From the figure, integer flux corresponds to $I_c$ maxima, which are at -42 μT and -36 μT. The complementary half-integer flux values at the minima are at -33 μT and -39 μT. A period of approximately 6 μT is consistent with the value extracted from the low temperature measurement in figure 5.8. The periodicity is maintained in the high temperature measurements with RF irradiation, shown in the colourplots in figures 5.21, 5.22, and 5.23, where the positions of integer and half-integer flux still clearly correspond to the applied field quantities in the no-RF measurement of the flux oscillations at 5 K.

Overall, more time is needed to complete these measurements comprehensively. Flux oscillation plots at lower temperatures than 4 K would have been useful to properly track the reduction of the Shapiro steps. Additionally, measurements at a back gate corresponding to low junction transparency are necessary to fully compare the appearance of half-integer steps potentially originating from either the CPR or the magnetic flux. Nevertheless, the results obtained do point in the direction of a skewed CPR at high transparency, which is reduced with temperature, even if the evidence is not conclusive at this stage.

### 5.2.3 Back gate dependence of half-integer Shapiro steps

This experimental section investigates the appearance of half-integer Shapiro steps in the Double SQUID due to the gating of the GJJs. The gating controls the transparency of the junctions which in this type of SQUID should affect the skewness of the CPR. When the skewness is increased, half-integer Shapiro steps should appear. Additionally, the magnetic flux can also be changed to integer $n$ and half-integer multiples of the magnetic flux quantum, with half-integer Shapiro steps appearing at half-integer flux ($n\Phi_0/2$). Assessing these factors in combination gives further insight into the behaviour of graphene SQUIDs under RF irradiation. It was expected that at low transparency, corresponding to low skewness of the CPR, only integer Shapiro steps could be observed if there is also integer ($n\Phi_0$) flux in the SQUID loop. Then if the magnetic flux was changed to $n\Phi_0/2$, half-integer Shapiro steps would become visible. Repeating these measurements but at high transparency and skewness, it would be expected that the half-integer Shapiro steps are visible in both cases. However, the integer and half-integer flux cases would still exhibit differences, because of how the magnetic flux in the SQUID loop changes its response, such as in figure 5.20 from the experimental data or figure 3.7 from the simulated data. The case where no half-integer steps are visible is important as a control for the appearance of the half-integer steps in the other cases.

#### Back gate dependence results

Initially, Shapiro steps were measured at different back gate voltages with constant RF signal parameters and integer magnetic flux. The measurements shown in figure 5.26 show the fourth and fifth integer steps and the half-step that lies between them. The same step was measured for consistency but each measurement has to use a different range of bias currents. This is because changing the back gate significantly changes the resistance and critical current in the SQUID so the gradient of the IV curve increases as gate voltage is reduced, and the curve is shifted to lower bias currents.

There are drawbacks to doing the measurement this way: the higher gradient associated with higher junction resistance at doping close to charge neutrality means that the step size of the bias current needs to be small enough to resolve half-integer steps at low doping, as they will have a smaller width. The steps are likely to be less well defined in this case, which can make comparison difficult. In 5.26 it is seen that the integer steps are also shorter at lower back gate, which could also be due to the gradient.

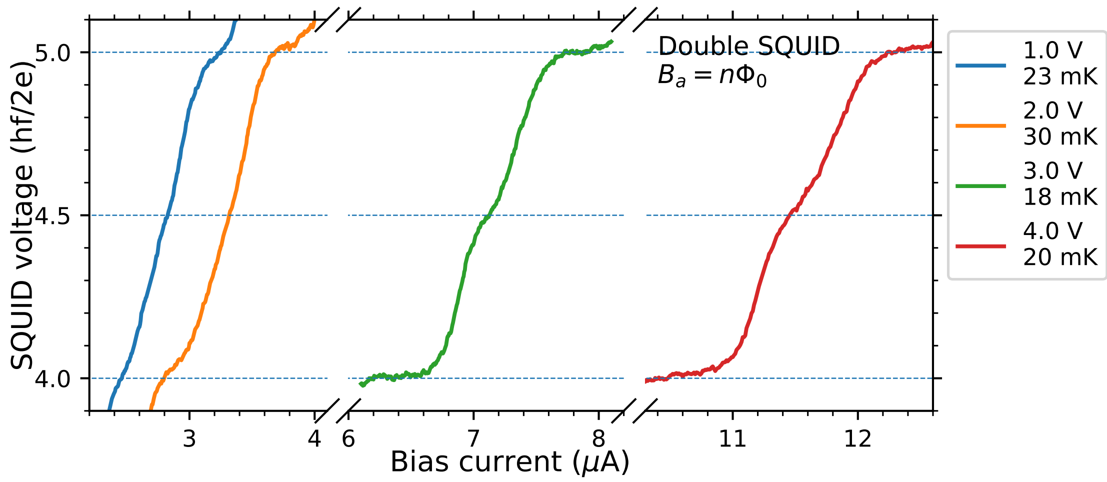


Figure 5.26: Plot comparing the appearance of the fourth and fifth Shapiro steps taken at different back gate voltages in the Double SQUID. Higher back gate voltage shows the appearance of half-integer Shapiro steps which are not visible at lower gating. Horizontal dashed lines show the expected position of integer and half integer Shapiro steps. Data points have been translated in the y direction to account for dc offset. Each sweep had a slightly different temperature due to the RF signal over a range of 12 mK. With a maximum temperature of 30 mK the characteristics of the trace would not be significantly affected by the small temperature differences.

However, changing the back gate changes how the SQUID responds at a particular power, as initially observed in figure 5.14. This means that results which keep the power constant at different back gate voltages might not be directly comparable, with steps seeming to appear or disappear because of the position in the power parameter space rather than the gating itself. As such, the is therefore more useful to look at the space as a whole with a 2D colourplot of the IV against RF signal power.

**Power dependent Shapiro maps**

The power-dependent Shapiro map plots IV characteristics under RF irradiation for different RF power but at the same RF frequency. To be concise this type of plot will from now on be referred to as a P-IV (power-current-voltage characteristic). The RF frequency is kept constant at 16.6 GHz because the frequency which couples to the device best is largely determined by the sample environment geometry as discussed in section 5.2.1. Measurements were taken at -1 V and 5 V for the low and high junction transparencies respectively, for integer and half-integer magnetic flux. The range of RF power varied because the differing flux and gating caused the position of the superconducting region to shift.

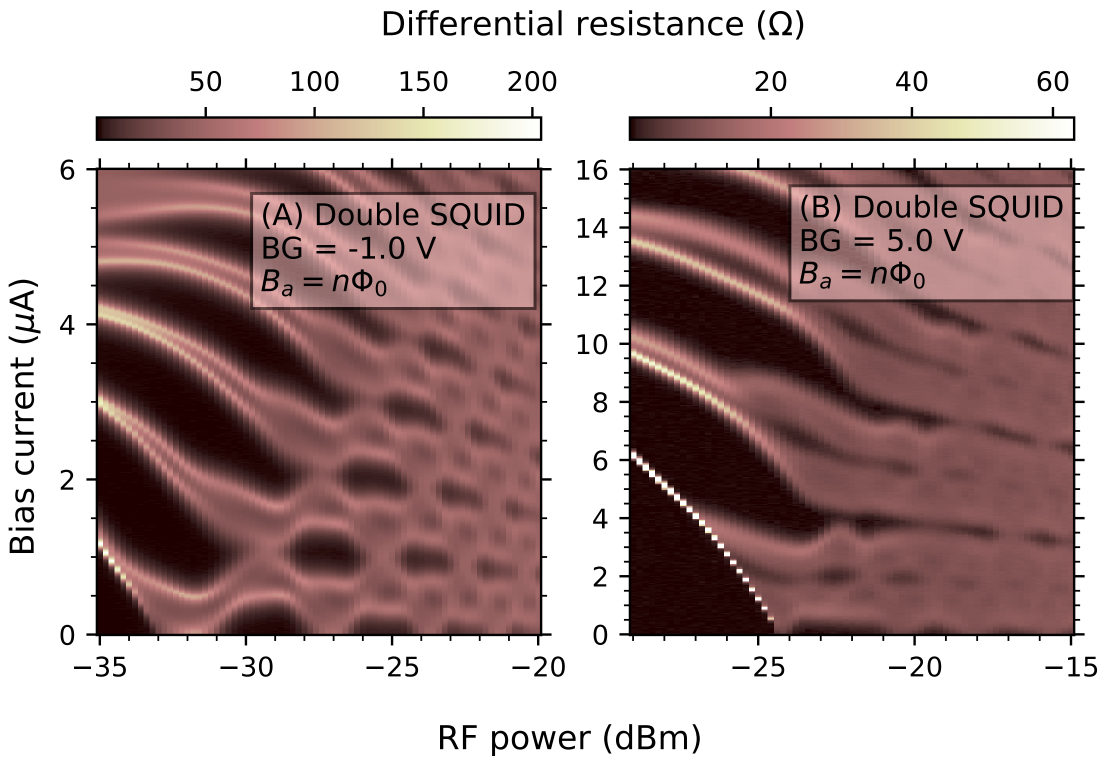


Figure 5.27: Double SQUID P-IV curves with differential voltage converted to differential resistance. The applied magnetic flux is an integer multiple of $\Phi_0$. (A) Back gate voltage = -1.0 V (low transparency case). Temperature range 18-38 mK. (B) Back gate voltage = 5.0 V (high transparency case). Temperature range 22-53 mK The maximum value of the colour bar in (B) is scaled by a factor of 0.2 to stop the detail being washed out by a high intensity superconducting transition. 0 Ω differential resistance corresponds to Shapiro step regions, or the superconducting region in the case of the lowest bias current and power data.

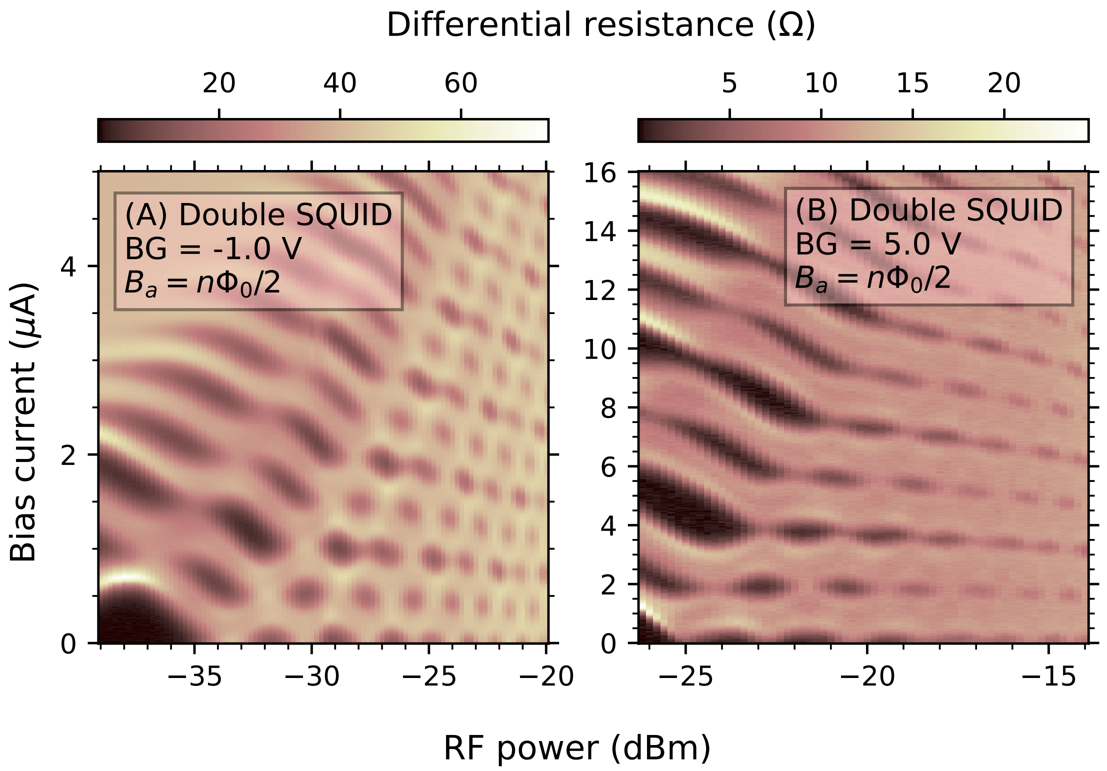


Figure 5.28: Double SQUID P-IV curves showing differential voltage converted to differential resistance. The applied magnetic flux is a half-integer multiple of $\Phi_0$. (A): Back gate voltage = -1.0 V (low transparency case). Temperature range 16-37 mK. (B): Back gate voltage = 5.0 V (high transparency case). Temperature range 26-57 mK. 0 Ω differential resistance corresponds to Shapiro step regions.

Firstly, figure 5.27 shows the P-IV characteristics for integer flux at different junction transparency. There is a clear qualitative difference in the visible features, with dark areas corresponding to 0 differential resistance - a voltage plateau. In the low transparency case, plateaus corresponding to integer Shapiro steps are visible, with subsequent plateaus appearing diagonally at greater bias current and power, showing that the choice of power will strongly affect which steps are visible. In the high-transparency case there are fewer round plateaus visible as instead the curved bands appear to split, forming trenches which correspond to half-integer Shapiro steps. The equivalent plots for half-integer flux are in figure 5.28. They have the same types of features as the plots at integer flux, particularly the round plateaus at low transparency and the trenches at high transparency. This suggests that the shape of these features is linked to the transparency of the junctions. The plots with the same back gate were measured over similar current and power ranges, but the half-integer flux plots have about twice as many plateaus in the low transparency case, implying the presence of half-integer steps due to to half-integer magnetic flux. In the high transparency case, the half-integer steps are more pronounced in the half-integer flux case than the integer flux case. Comparing the integer flux plots with the simulations in figure 3.8, very similar features are visible in general, especially the round plateaus. The trench-like features are less visible here. A feature like the trenches was observed once in a test simulation but that simulation's parameters were not controlled in line with the other simulations in this thesis. For information, it has been included in the appendix in figure A.6, but the resolution would need to be improved to draw strong conclusions.

There is still a difficulty with the interpretation of the P-IV plots, because depending on where a power or current slice is taken, certain Shapiro steps can be missed, and looking only at the colourplots is less conclusive without scaling the voltage to be in terms of Shapiro steps. It is very clear that keeping the power constant does not provide consistency for observing different Shapiro steps, because to show the integer and half integer steps most clearly a diagonal slice through the plateaus in figures 5.27 and 5.28 would be needed. To account for this, it can be easier to interpret the presence of Shapiro steps by plotting histograms of the dc voltage responses converted to Shapiro step units. The histograms produced correspond to the P-IV plots presented. Figure 5.29 corresponds to 5.27, and 5.30 corresponds to 5.28.

#### P-IV histograms

The histograms are dealt with in pairs: the integer flux pair and the half-integer flux pair. For each pair, the histograms are constructed by taking each power slice and binning the data in bins of size 0.05$(hf/2e)$. This is small enough that integer and half-integer values will be unambiguous. The data are then normalised. Firstly, each individual dataset is divided by the total number of data points in the dataset (number of bins multiplied by number of power slices). This is to account for differences in the sizes of the datasets, which would influence the relative heights of histogram peaks. Then to compare a pair of histograms, all data points are divided by the largest data point between the two, placing all points on a consistent scale of 0 to 1.

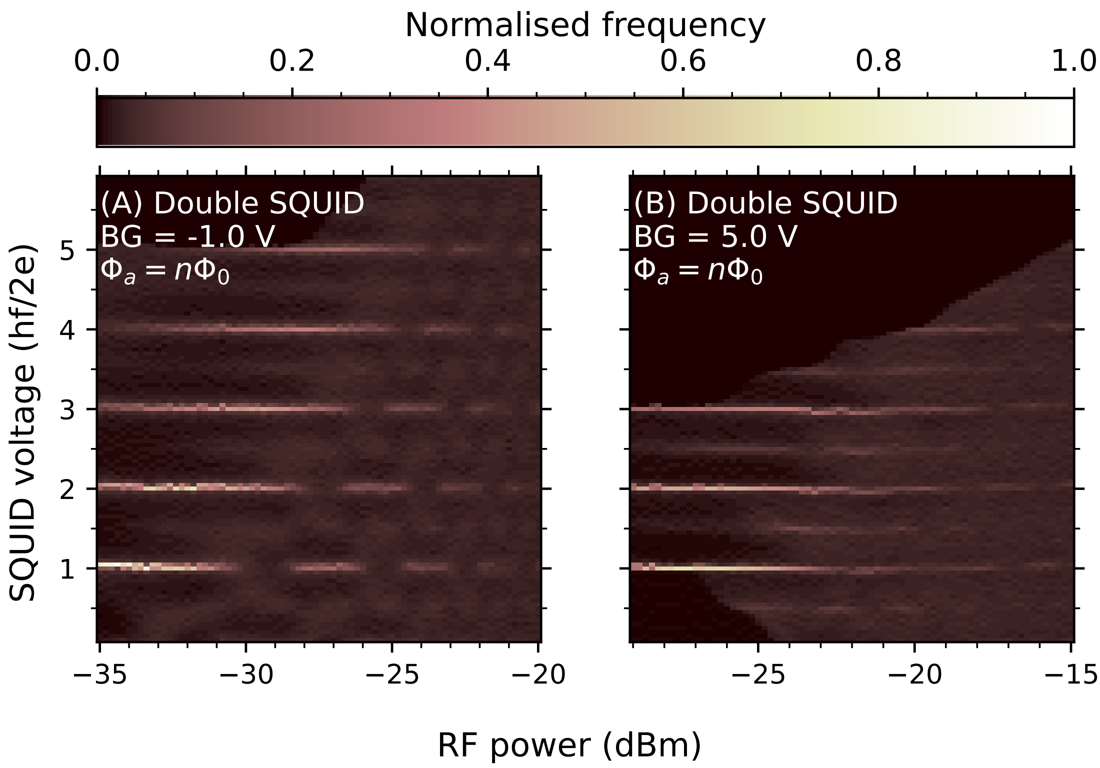


Figure 5.29: 3D histograms of the Shapiro step voltage against power, for integer flux, in the Double SQUID. Corresponds to data in figure 5.27. RF frequency = 16.6 GHz. (A): Back gate voltage = -1.0 V (low transparency case). Only integer Shapiro steps are visible. (B): Back gate voltage = 5.0 V (high transparency case). Integer and half-integer Shapiro steps are visible.

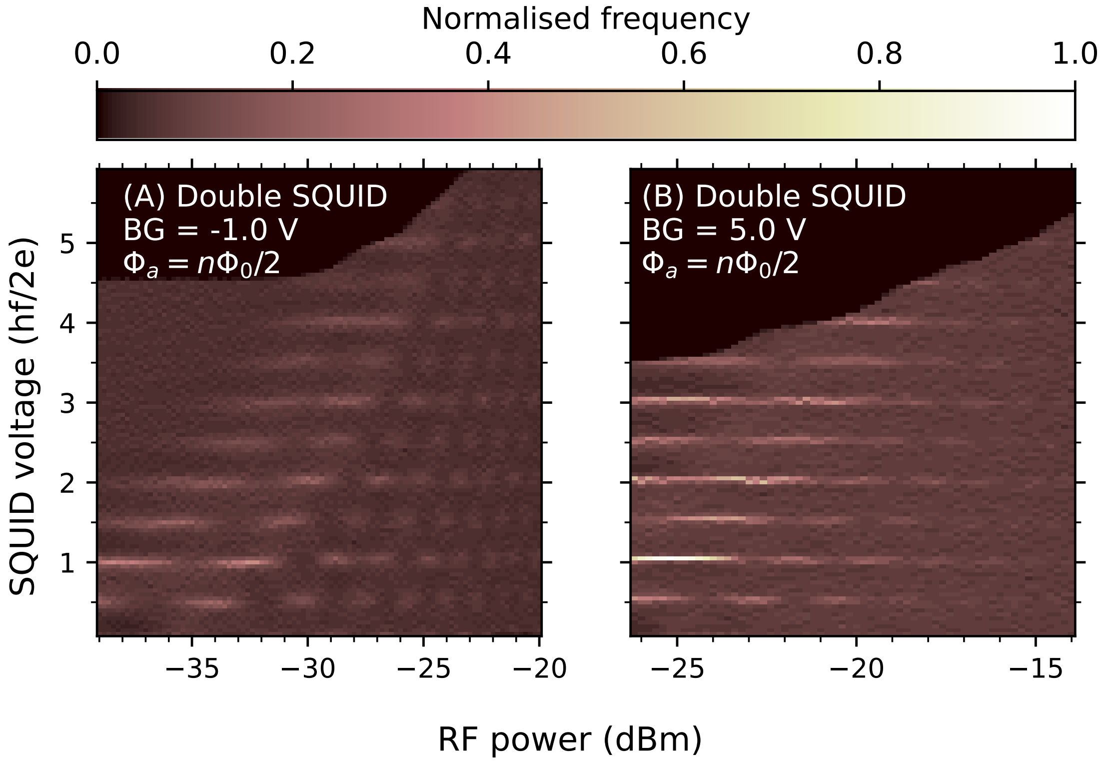


Figure 5.30: 3D histograms of the Shapiro step voltage against power, for half-integer flux, in the Double SQUID. Corresponds to data in figure 5.28. RF frequency = 16.6 GHz. (A): Back gate voltage = -1.0 V (low transparency case). (B): Back gate voltage = 5.0 V (high transparency case). Integer and half-integer Shapiro steps are visible in both cases, but with greater intensity in the high transparency case.

Figure 5.29 shows the integer flux histograms. In both plots, integer flux peaks are clearly visible. Weaker half-integer peaks are also visible in the 5.0 V plot (5.29B). The histogram plots for half-integer flux are in figure 5.30. In both plots, integer and half-integer plots are clearly visible. This is consistent with expectations for SQUIDs with half-integer flux. Between the two plots at half-integer flux, the peaks are more prominent for 5.0 V. This is consistent with the idea that both mechanisms contributing to half-integer Shapiro steps are present in the skewed SQUID, based on the simulations shown in figure 3.7 where the half-integer flux steps are wider for high-transparency junctions than low-transparency junctions.

To emphasise the information contained in the colourplots, figure 5.31 shows slices from each of the plots in figure 5.29. This is to illustrate the colourbar axis from the 3D histograms (before normalisation), but slices have been chosen to further show the observations associated with half-integer Shapiro steps. For a full picture of the parameter space, it is still necessary to use the histograms, but these slices show what the bright lines in the colourplots mean.

The main limitation revealed by the histogram slices is that to get clear peaks it is important to have as high-resolution current steps as possible. While it is quite obvious that having a smaller step size allows more detail in a measurement, in the histograms it can make a significant difference to the prominence of the observed peaks, and therefore the confidence in the effects shown. It is also a quantity which can reach a limit due to the experimental apparatus, showing the importance of the choice of parameters like power when making these measurements.

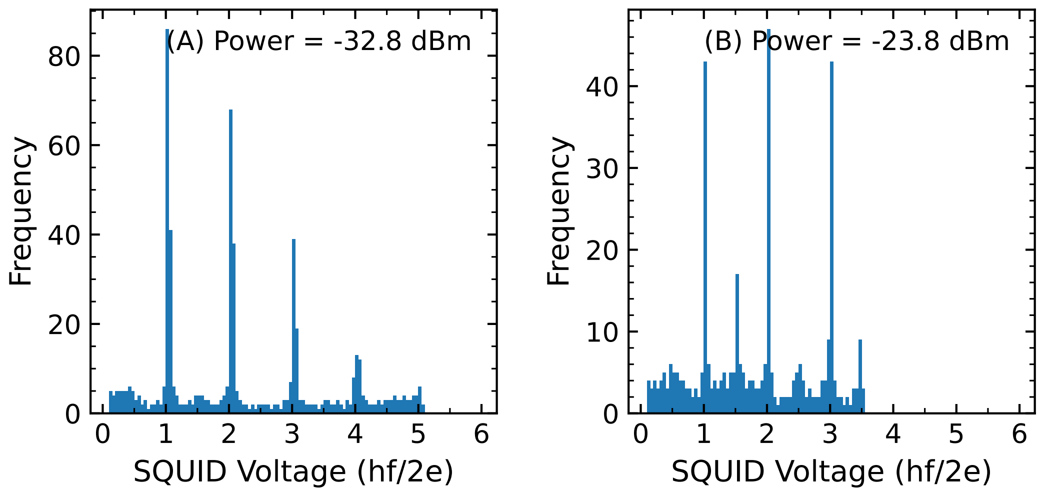


Figure 5.31: (A): The histogram slice corresponding to a power of -32.8 dBm with integer flux and low skewness (figure 5.29A). Peaks are only seen at integer Shapiro step voltages. (B): The histogram slice corresponding to a power of -23.8 dBm with integer flux and high skewness (figure 5.29B). More prominent peaks are seen at integer Shapiro step voltages, but notable peaks are also seen at half-integer step voltages.

Overall, the P-IV measurements give evidence that the graphene SQUIDs possess a non-sinusoidal current-phase relation. By plotting the histograms, the power is accounted for in the most practical way to allow for straightforward visualisation of the Shapiro steps. Tuning the transparency of the junctions and the magnetic flux in the SQUID loop causes the appearance of half-integer Shapiro steps in a manner which is consistent with both the simulated work and that expected based on measurements of similar devices in the literature. At integer flux, half-integer steps are only seen when the transparency of the GJJs is increased. But at half-integer flux, half-integer steps are visible at both high and low transparency, but the half-integer steps are more prominent in the high transparency case. Using a graphene SQUID rather than a single GJJ has allowed for an investigation of both mechanisms for half-integer Shapiro steps in the same device.

## 5.3 Conclusions and future work

This is the end of the experimental section, and the thesis. Here, the results of the experimental and simulations sections will be summarised first, and then finally there will be discussion of future directions for these measurements.

### 5.3.1 Summary of experiment and results

Graphene SQUIDs were characterised using dc and differential four-terminal voltage measurements in a current-biased configuration. The devices were subject to a number of different measurement conditions. The environmental parameters that could be adjusted were applied in different combinations to study several different effects.

The parameter most specific to the graphene SQUIDs was the gate voltage which could be applied to the devices. This was shown to give control over the critical current of the device, increasing $I_c$ with stronger gating. Adjusting the gate parameter alongside the other experimental conditions gave expanded insight into the behaviour of hBN encapsulated ballistic graphene SQUIDs, particularly with the application of an RF signal to probe Shapiro step phenomena.

Applying a magnetic field perpendicular to the plane of the SQUIDs' loops allowed the periodicity of the critical current oscillations to be observed. In combination with increasing the doping in the graphene, the modulation depth of the oscillations of the Big SQUID was seen to reduce, indicating a change in the critical current-dependent $\beta_L$ screening parameter (equation (5.6)). This gave insight into the inductance contributions in SQUIDs because it was possible to extract an inductance value from simulated results and compare them with the expected inductance. This suggested that the Big SQUID did not have a sinusoidal CPR, and may have had properties like other similar devices where the CPR is skewed with a dependence on the transparency of the junction contacts.

Hysteresis measurements were performed on the Double SQUID at different gate voltages. These were used to obtain an experimental estimate of the junction capacitance. The calculated value was similar to an estimate of the capacitance between the back gate and the SQUID loop. However, this hysteresis has been observed by others in similar devices and was attributed to overheating of the electrons. As it is not completely clear which capacitance contributions should be considered part of the junction capacitance, there is no conclusive result.

An antenna was used to create a high-frequency electric field and therefore study the effects of an induced ac current on the SQUIDs. The core phenomena being investigated were integer and half-integer Shapiro steps which should have been present if the graphene SQUIDs had skewed CPRs. Half-integer steps should also be visible in SQUIDs generally when there is half-integer flux circulating in the loop. In the Double SQUID, half-integer steps appear when a half-integer flux quantum is present in the loop as expected. Gating the graphene to high transparency also caused half-integer Shapiro steps to appear. This gave evidence that the Double SQUID has a skewed CPR like similar graphene devices. Shapiro steps were also investigated to a lesser extent with temperature. It was difficult to discern whether steps were being suppressed by a changing CPR or thermal noise, though flux oscillation measurements without the high-frequency signal at 4 K implied that the critical current of the device had been reduced to a similar value as at charge neutrality at base temperature.

A dimensionless numerical simulation of a SQUID using the RCSJ model was extended to include ac signals, and similar scenarios to those performed experimentally were also produced with the simulation. These showed qualitatively that the behaviour of the physical SQUIDs was possible and expected within the RCSJ model of a SQUID with a skewed CPR. The simulations showed the presence of further fractional Shapiro steps beyond half-integer.

### 5.3.2 Limitations and future work

The measurement taken were part of the first time Shapiro steps were studied in our measurement setup. This meant that this work came with a lot of learning about how best to take and analyse the measurements, and in the end the results were quite promising. The way that half-integer steps will appear due to half-integer flux in SQUIDs adds a complication which makes this work distinct from prior work on graphene JJs. This also means that there is plenty of work which can be done to improve the measurements and better understand the mechanisms at work.

One of the most difficult parts of the experimental section was time management. Thoroughly measuring a graphene SQUID means covering a huge parameter space if every variable is to be considered. Taking the measurements over an adequate range and resolution can then take multiple days per configuration. Combining the length of the measurements with the demand on the apparatus for other experiments meant that sometimes there were constraints on what was possible to do in any given experimental run. In addition to that the initial delays in training and experimental work because of the national coronavirus lockdowns in the United Kingdom in 2020 cannot be ignored, causing a backlog of experimental work to be done impacting our group and also our collaborators at the National Graphene Institute (University of Manchester).

The compromises that had to be made to produce the results in this thesis are initially what need to be returned to in future work. Particularly with regard to the fractional Shapiro step measurements, higher resolution measurements are necessary so that smaller steps can be resolved, or it can be confirmed that the features are lost in the noise floor. More direct measurements of the current-phase relation would help to support some of the arguments made regarding the change in Shapiro step behaviour at different gate voltages and temperatures, though this needs the SQUID to be highly asymmetric which is not possible with the devices shown here as they cannot be independently gated. Therefore, it is necessary to be as thorough as possible with the measurements that can be performed. Detailed measurements should allow for better, more quantitative analysis than what was shown here.

#### Temperature dependence

As there are only two values of flux which are of most interest, it may be more efficient to repeat these measurements using power-dependent Shapiro maps as in section 5.2.3. This accounts for power as a confounding variable and the histograms are a good visualisation method for the Shapiro steps. This is as well as ensuring that more low temperature data is taken and repeating for low transparency doping.

If time available for measurements was a concern, it may be possible just to take a small bias-power measurement around a few plateaus of interest in the P-IV map. Taking the temperature dependent data in this way would also effectively include the back gate dependent data, so it would have been sensible to combine these two investigations at the time.

In general, expanding these measurements to cover more intermediate temperature and back gate values would be valuable in the long term. Another limitation due to time is that mostly measurements were only taken with positive current bias. Measuring both positive and negative current biases, and sweeping the current in both directions, would allow any asymmetry effects in the SQUIDs to be observed.

### The Big SQUID

The Big SQUID was initially designed to act as a Josephson transmission line[15]. Many of the intended measurements were not made with this device, as the equipment needed was not in place, and the device itself was quite unstable because of the large loop. The focus then switched to using the Double SQUID to measure half-integer Shapiro steps. The ideal device design was not used as at the time it could not be made with a coplanar waveguide geometry. This project could be returned to, ideally with a new device constructed to more ideal parameters.

### Experiment setup

The puck sample holder is already good for securely holding an appropriately designed circuit board. This means it is straightforward to position devices within the sample environment consistently. For the Shapiro step measurements there was a complication relating to the positioning of the antenna. The antenna can be connected to the same wiring port each time, but the exact nature of the produced electric field would vary depending on variables such as the bend in the antenna and its orientation. Both of these change the antenna's positioning relative to the device, and thus could affect the coupling between it and the antenna. One option would be a more robust antenna, something that is more purpose built for the task, rather than one improvised from some flexible coaxial wire.

The Triton 400 used for these measurements has a low base temperature of 15 mK, but this performance been surpassed by improved dry dilution refrigerators. A lower base temperature could potentially allow fractional steps smaller than half-integer to be observed, as in experimental systems they will easily be suppressed by thermal noise. However, this also relies on having a very high resolution current supply.

### Simulations

There is one primary drawback to the choice of simulation methodology. In normalising all the parameters to produce a dimensionless simulation, there is great flexibility as it is possible to model completely arbitrary SQUID systems. However, it can be difficult to then compare those models directly to experiment. It requires that a real device is well characterised, and then the parameters need to be transformed back into the physical equivalents. Although, it may be possible to perform statistical fitting between a set of simulation data and a set of experimental data and extract the physical parameters that way.

As with the experimental measurements, there are many more combinations of parameters that could be tested using the simulations. Notably, an in depth look at the effect of the $\beta_C$ parameter could be useful, considering the results of the capacitance investigation and hysteresis experimentally.

Extending the simulation model to account for temperature would also be an interesting area to explore. This could just come as a modification for the skewed CPR equation, or implementing a threshold value which will switch the CPR model used back to sinusoidal in line with the discussed limitations in section 2.2.3.

# Appendix A

# Supplementary plots

These plots are not needed to fully illustrate the findings in the thesis, but may add additional context. Figure A.1 shows an instance when the simulation broke down for certain values.

Figures A.2, A.3, A.4, and A.5 were part of an investigation into the effects of the signal frequency on a voltage offset in the simulation results.

Figure A.6 shows a test simulation with a mixture of features that might be worth further exploration.

## A.1 Simulation

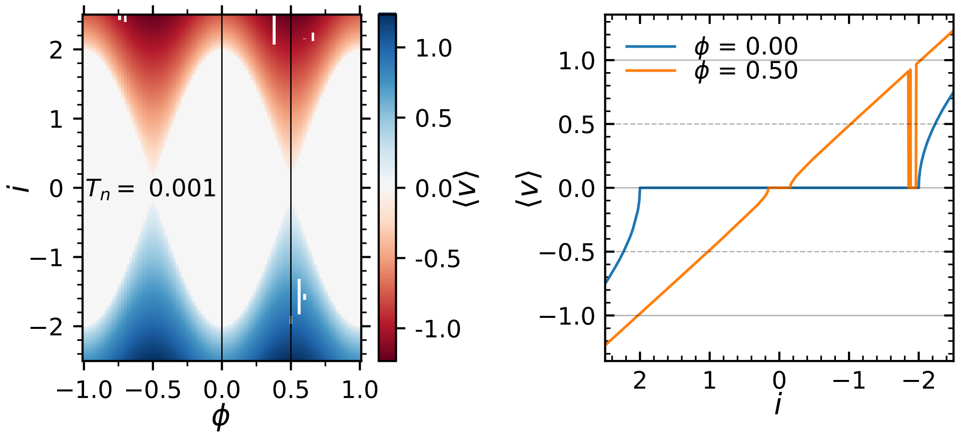


Figure A.1: Plot as in figure 3.6 but sliced at positive $0.5$ flux quanta instead of negative $0.5$ flux quanta. In this version the slice coincides with artifacts from the simulation which make the line plot more difficult to interpret. The artifacts are parts where the simulation has failed to solve the integration successfully, likely due to the use of a very small $\beta_c$.

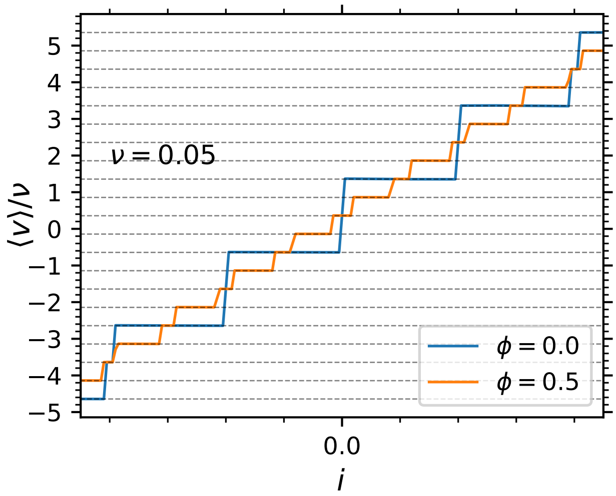


Figure A.2: Simulated Shapiro steps at integer and half-integer flux for drive frequency of 0.05. Notable here is the offset in voltage and that odd-integer Shapiro steps are missed in the integer flux case.

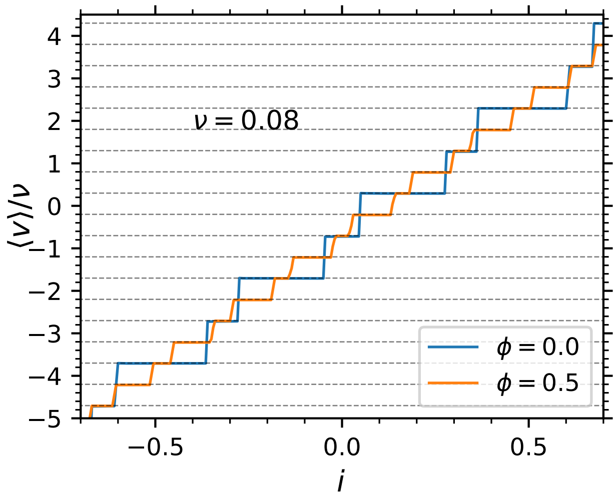


Figure A.3: Simulated Shapiro steps at integer and half-integer flux for drive frequency of $0.08$. A voltage offset is visible.

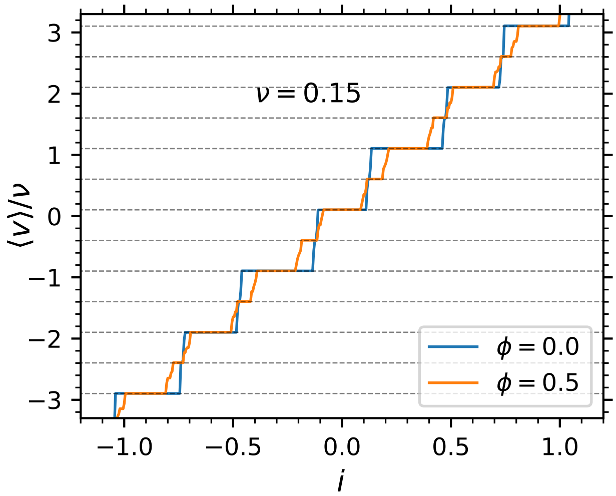


Figure A.4: Simulated Shapiro steps at integer and half-integer flux for drive frequency of $0.15$. A voltage offset is visible.

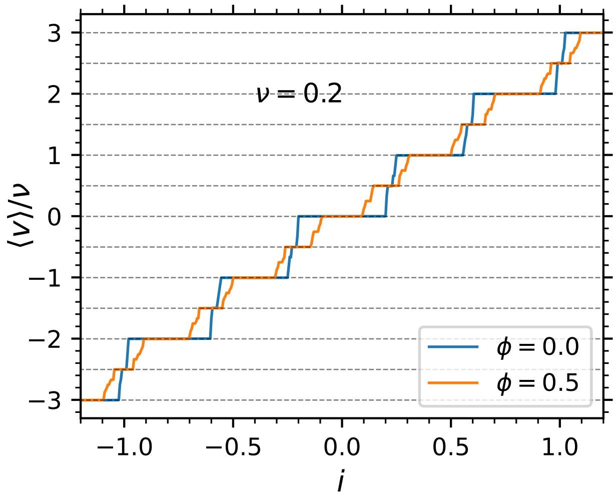


Figure A.5: Simulated Shapiro steps at integer and half-integer flux for drive frequency of $0.2$.

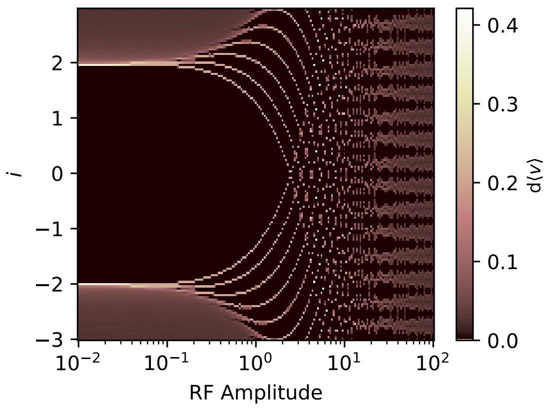


Figure A.6: Simulation plotting the differential of the average voltage against RF amplitude and current. The CPR is sinusoidal. $\beta_L = 13$, $\beta_C = 0.86$, $\nu = 0.21$. Notable in this plot is the change in appearance above an RF amplitude of 10, which may need further investigation.

## A.2 Double SQUID flux oscillations

An additional flux oscillation plot showing the flux offset discussed in section 5.1.3.

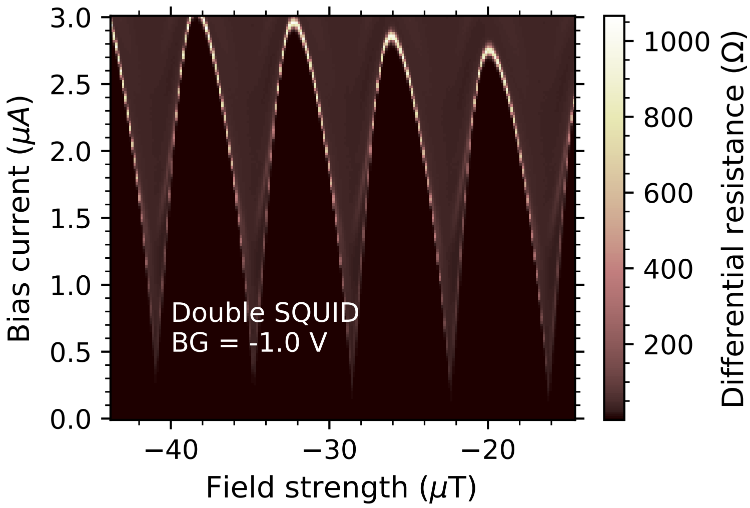


Figure A.7: Flux oscillations showing varying critical current maxima, which increase as the field strength is made more negative. The back gate is $-1.0$ V. Measured in the Double SQUID.

## A.3 Big SQUID flux oscillations

The flux oscillation plots taken from the Big SQUID and used to estimate its inductance in section 5.1.4. The results are presented in order of increasing back gate voltage from $-2.0$ to $5.0$ V. Most of the plots here show a significant amount of instability in the SQUID, due to flux jumps because of the large loop area (see figure 4.2.

However, the maximum and minimum critical currents of the SQUID remain stable in each plot, so even though the period of the SQUID cannot be reliably determined, the critical current parameters and associated oscillation depth can still be measured.

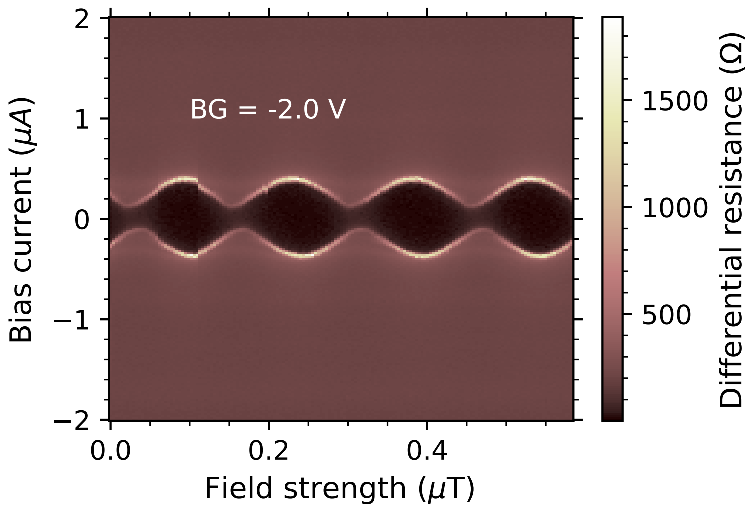


Figure A.8: Flux oscillations of the Big SQUID with back gate $= -2.0$ V.

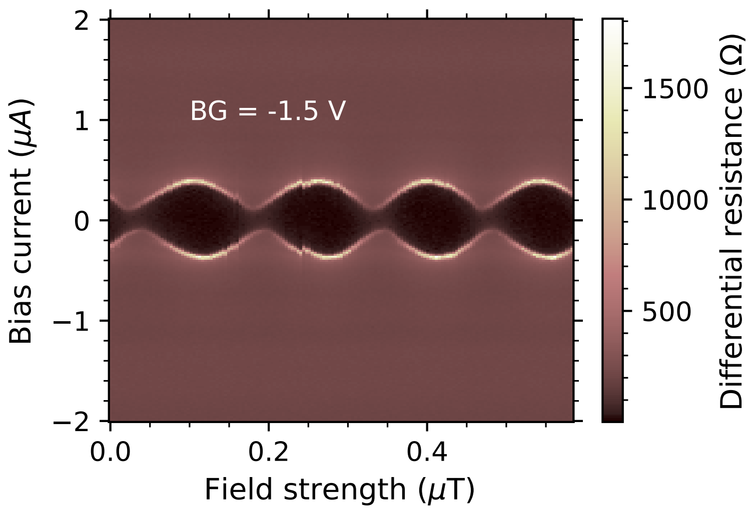


Figure A.9: Flux oscillations of the Big SQUID with back gate $= -1.5$ V.

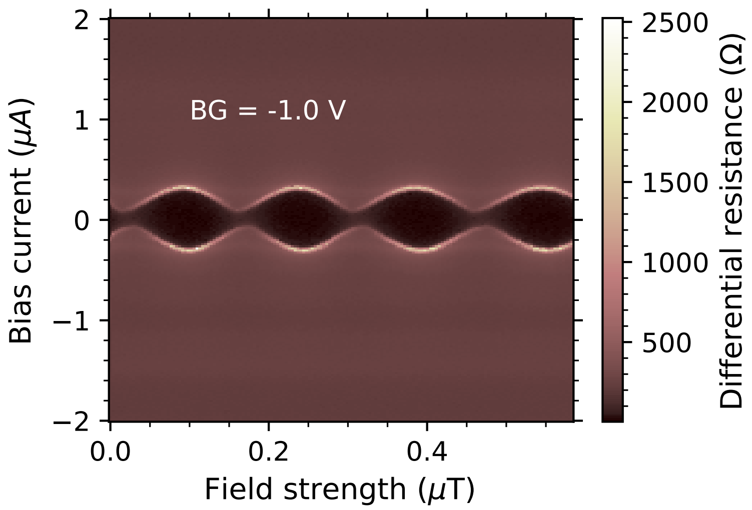


Figure A.10: Flux oscillations of the Big SQUID with back gate $= -1.0$ V.

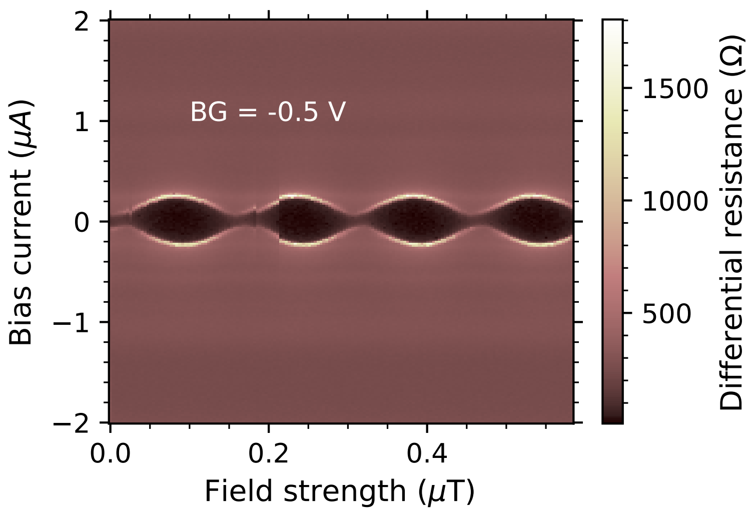


Figure A.11: Flux oscillations of the Big SQUID with back gate $= -0.5$ V.

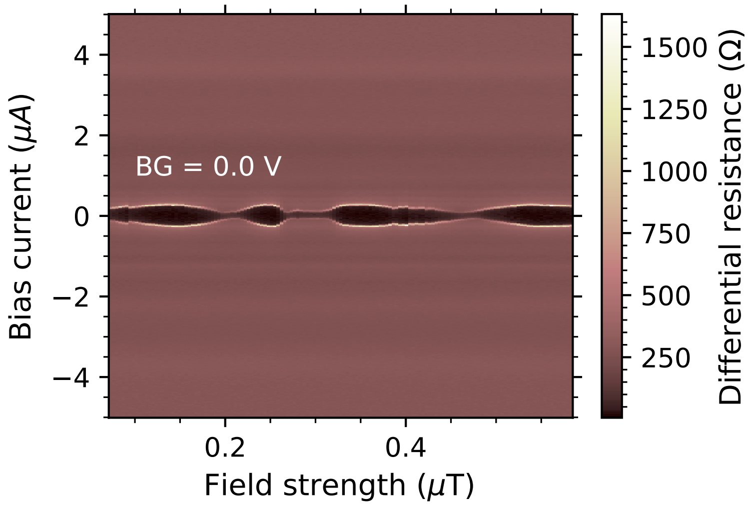


Figure A.12: Flux oscillations of the Big SQUID with back gate $= 0.0$ V.

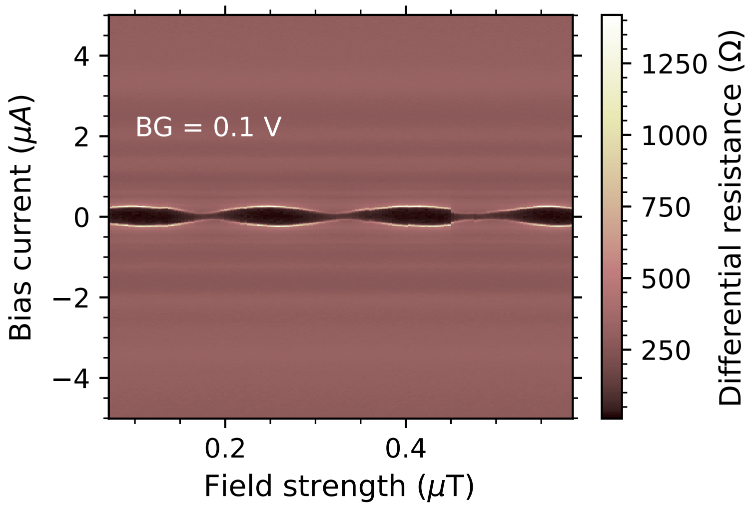


Figure A.13: Flux oscillations of the Big SQUID with back gate $= 0.1$ V.

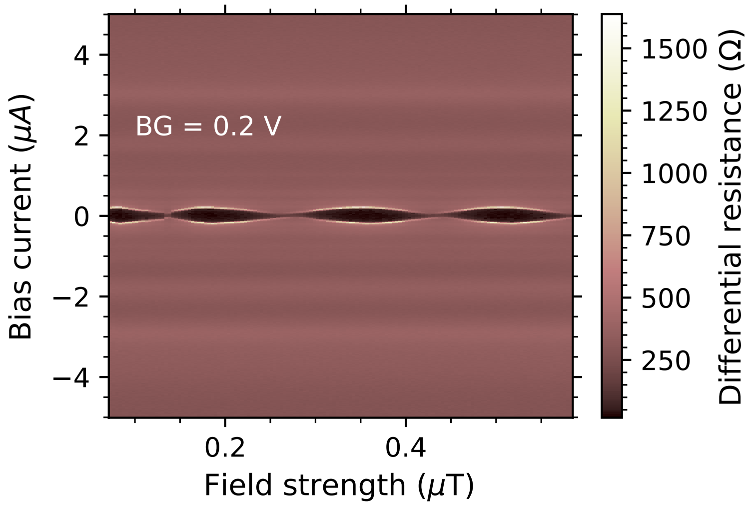


Figure A.14: Flux oscillations of the Big SQUID with back gate $= 0.2$ V.

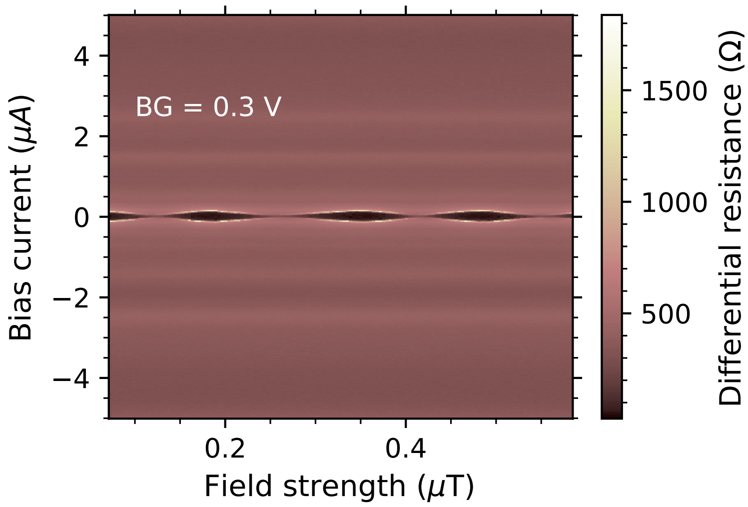


Figure A.15: Flux oscillations of the Big SQUID with back gate $= 0.3$ V.

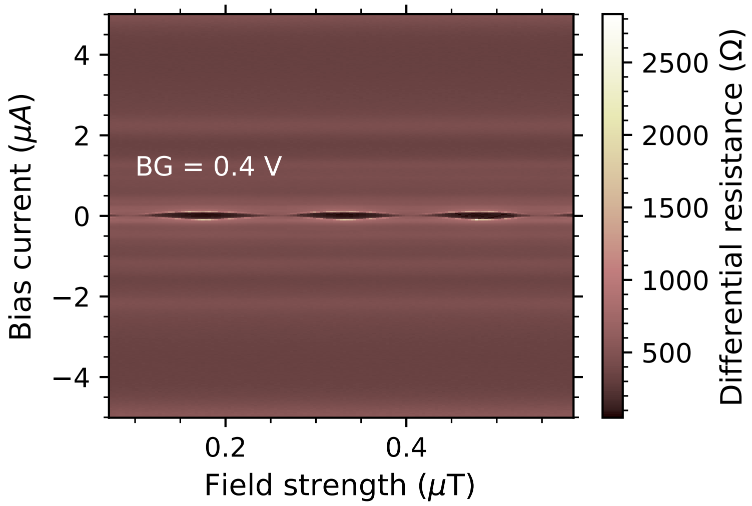


Figure A.16: Flux oscillations of the Big SQUID with back gate $= 0.4$ V.

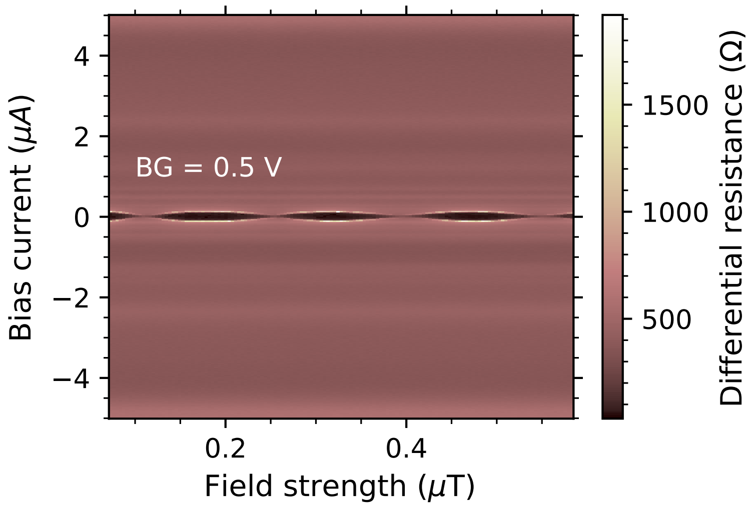


Figure A.17: Flux oscillations of the Big SQUID with back gate $= 0.5$ V.

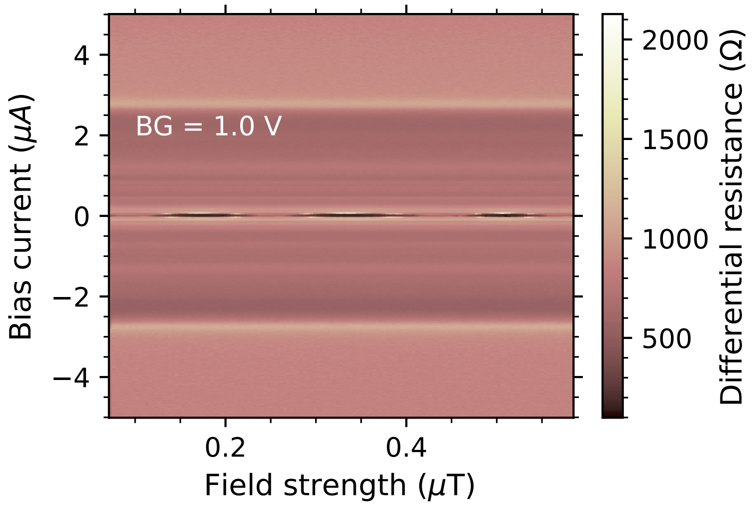


Figure A.18: Flux oscillations of the Big SQUID with back gate $= 1.0$ V.

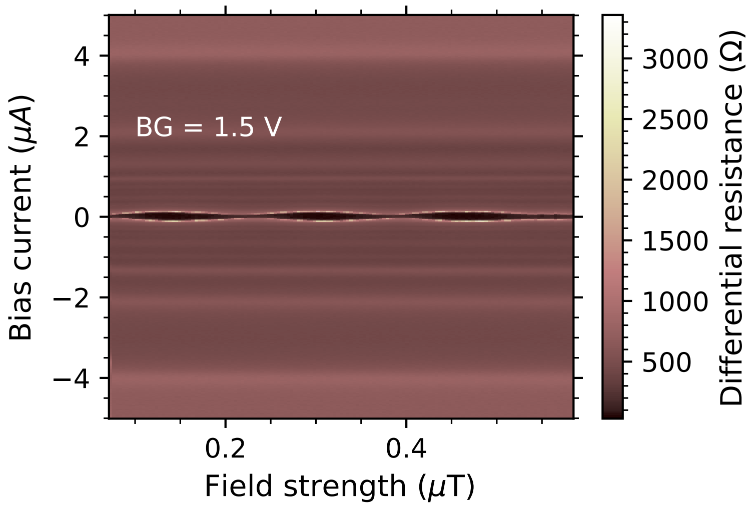


Figure A.19: Flux oscillations of the Big SQUID with back gate $= 1.5$ V.

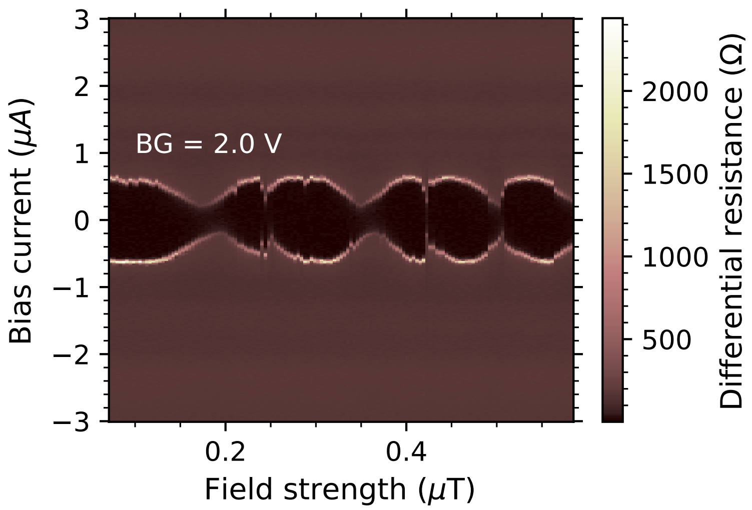


Figure A.20: Flux oscillations of the Big SQUID with back gate $= 2.0$ V.

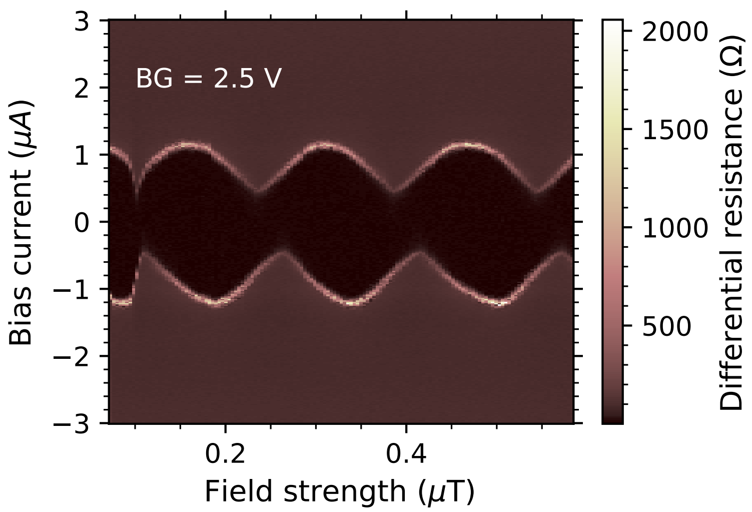


Figure A.21: Flux oscillations of the Big SQUID with back gate $= 2.5$ V.

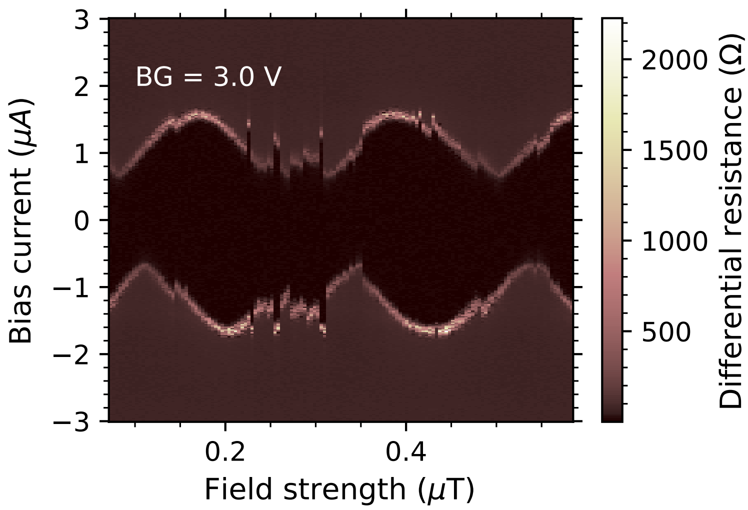


Figure A.22: Flux oscillations of the Big SQUID with back gate $= 3.0$ V.

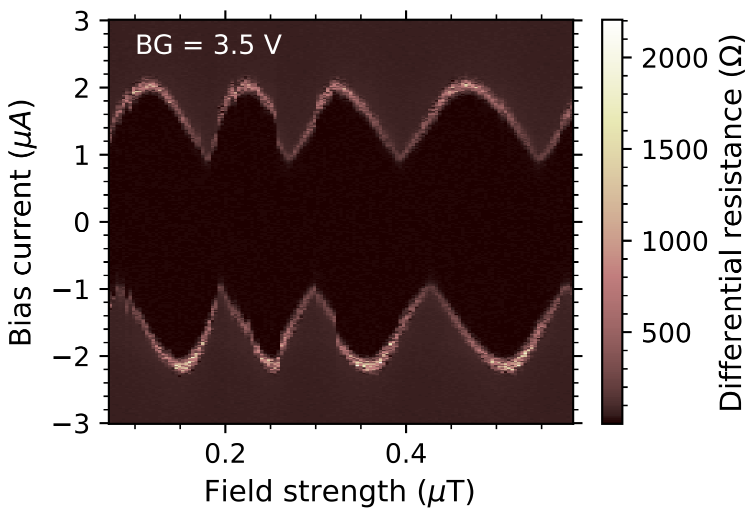


Figure A.23: Flux oscillations of the Big SQUID with back gate $= 3.5$ V.

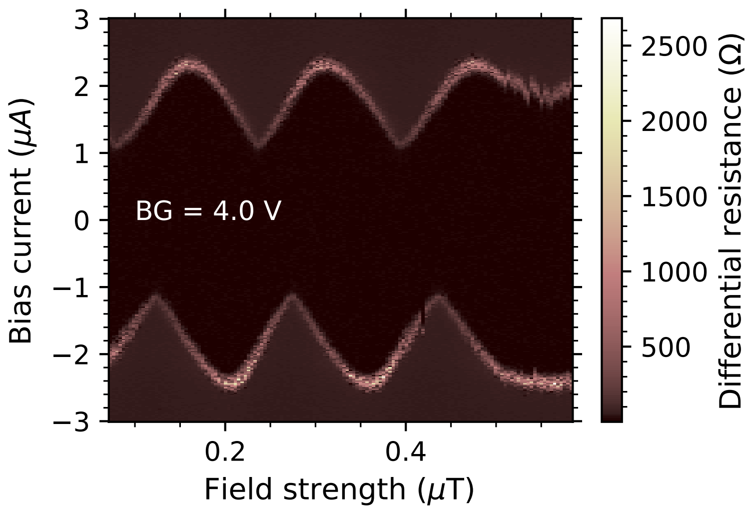


Figure A.24: Flux oscillations of the Big SQUID with back gate $= 4.0$ V.

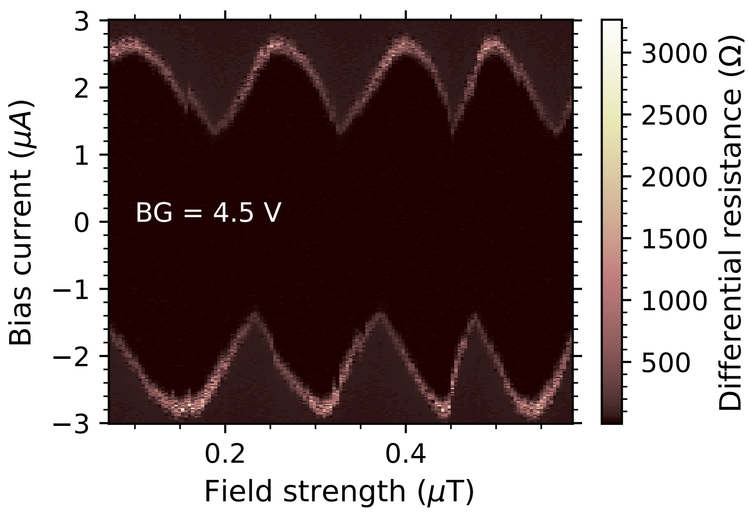


Figure A.25: Flux oscillations of the Big SQUID with back gate $= 4.5$ V.

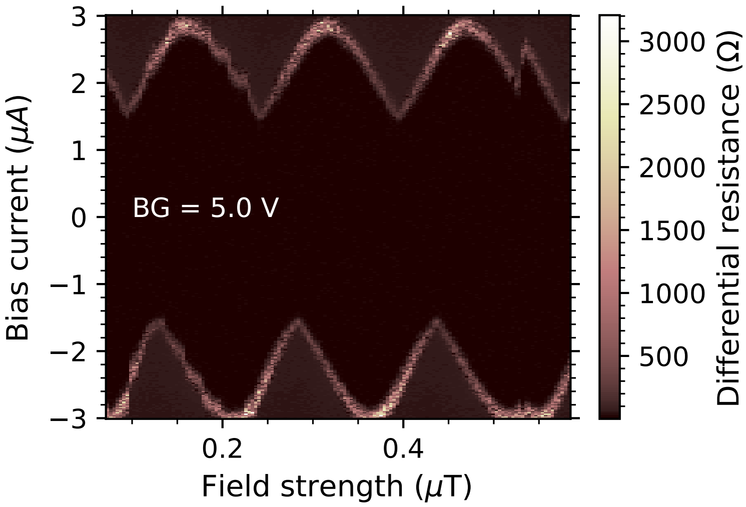


Figure A.26: Flux oscillations of the Big SQUID with back gate $= 5.0$ V.

## A.4 Hysteresis of the Double SQUID

Plot of hysteresis in the Double SQUID. These are the individual plots of the data used to determine the return current values used in figure 5.7. Some gate voltages were measured multiple times, this was mostly to change the size of the current step to get a better resolution transition, which is reflected in the size of the error bars in the cross-referenced plot.

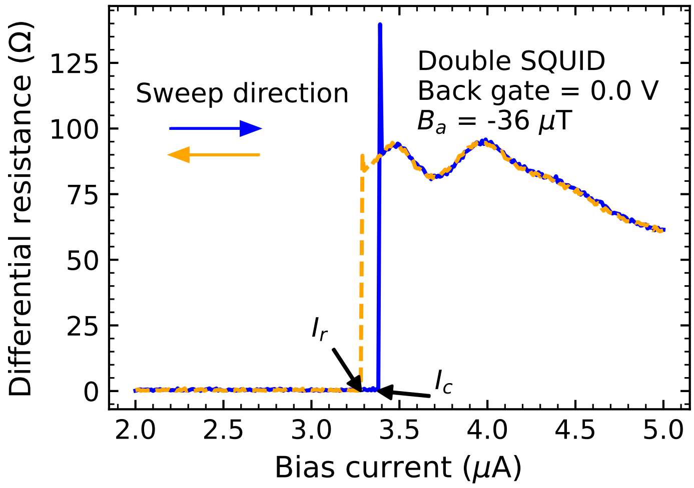


Figure A.27: Hysteresis measurement of the Double SQUID at 0 V back gate.

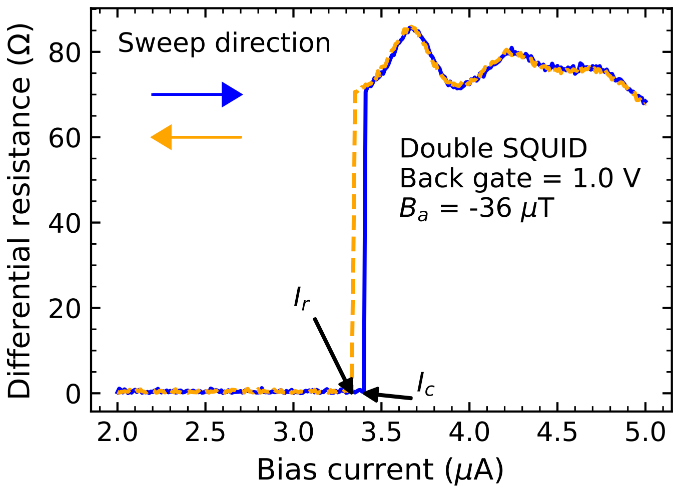


Figure A.28: Hysteresis measurement of the Double SQUID at 1 V back gate.

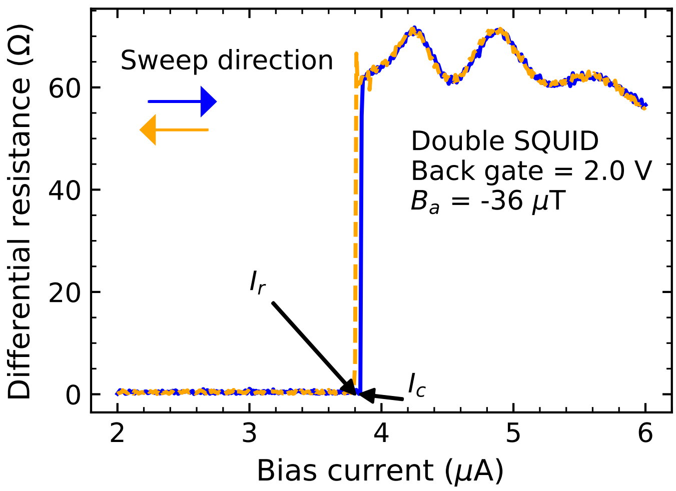


Figure A.29: Hysteresis measurement of the Double SQUID at 2 V back gate.

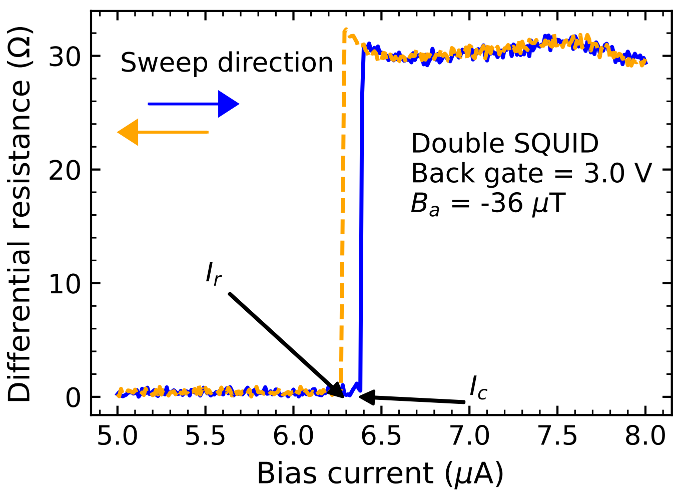


Figure A.30: Hysteresis measurement of the Double SQUID at 3 V back gate.

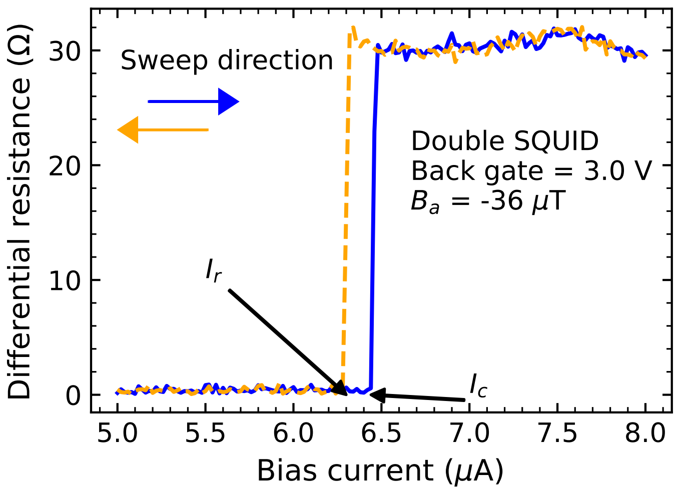


Figure A.31: Additional Hysteresis measurement of the Double SQUID at 3 V back gate.

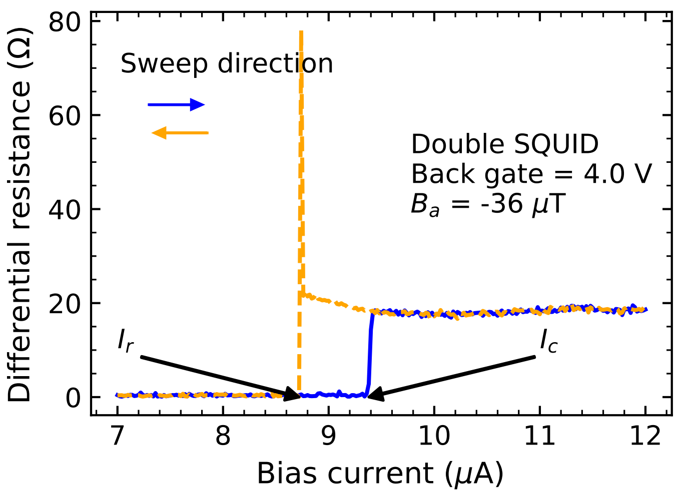


Figure A.32: Hysteresis measurement of the Double SQUID at 4 V back gate.

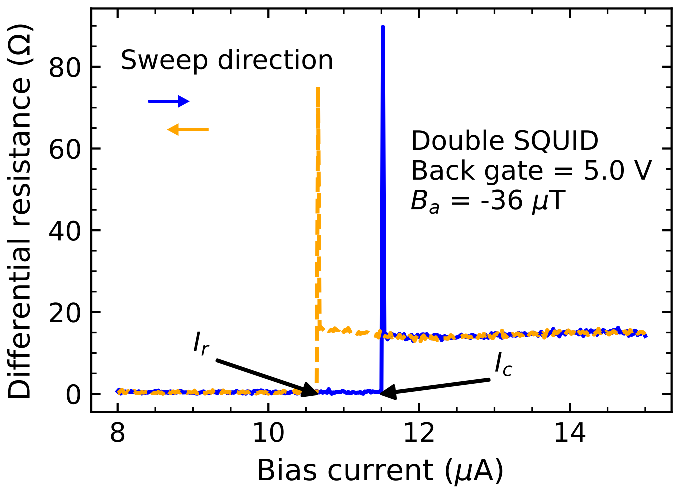


Figure A.33: Hysteresis measurement of the Double SQUID at 5 V back gate.

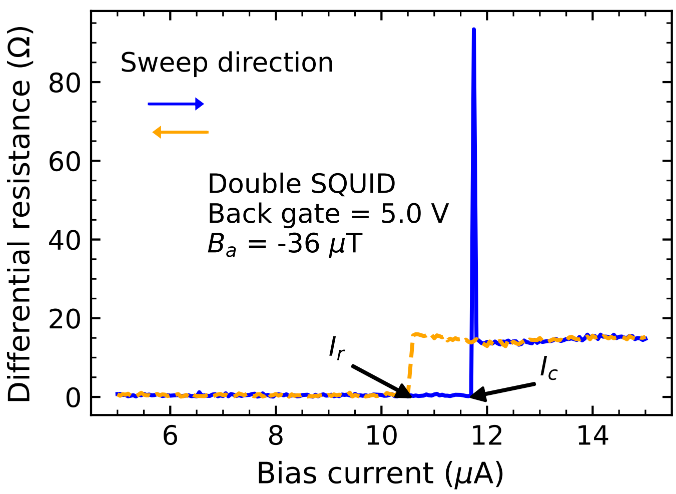


Figure A.34: Additional Hysteresis measurement of the Double SQUID at 5 V back gate.

## A.5 Heating from the RF signal

This is from a measurement where the signal generator was kept at decreasing power values for fixed intervals while the temperature of the mixing chamber was recorded. The sharp dip at the end corresponds to when the signal generator was switched off.

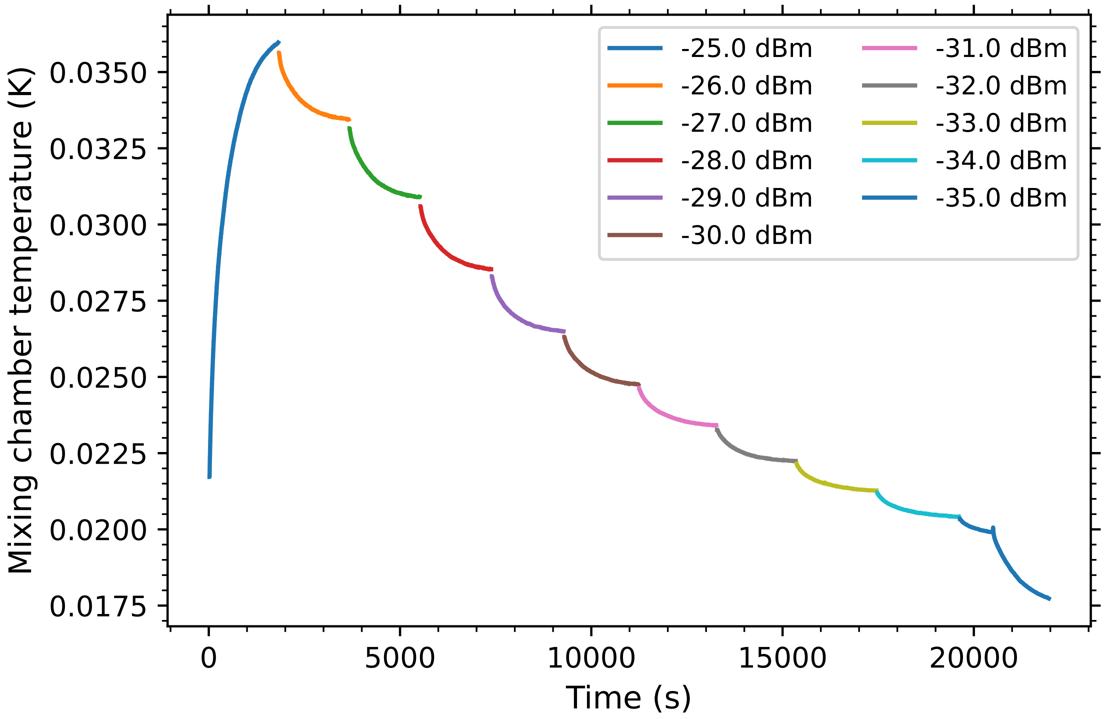


Figure A.35: Plot showing the temperature of the Triton mixing chamber over time for different amounts of power deposited by the RF signal. This shows that generally the temperature of the mixing chamber stays below 35 mK for powers below -26 dBm, though it can take over 30 minutes for the temperature to fully stabilise.

# Appendix B

# Device images

Device images in the main text of the thesis were edited to highlight certain features of interest. Here, the full original images are shown for additional context.

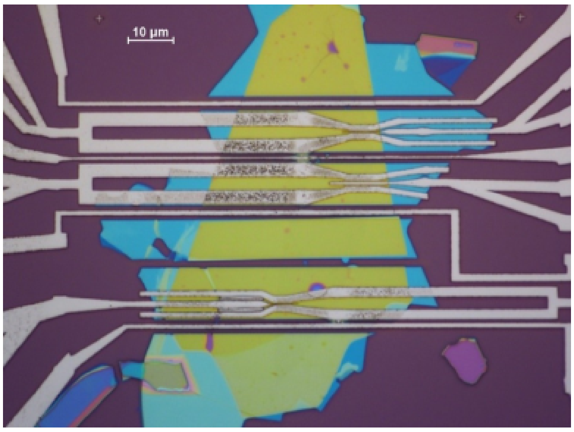


Figure B.1: Original photograph of the full Double SQUID device by M Ben Shalom, showing the two nominally identical devices in the top half of the image, with flux bias lines either side and between the SQUID loops. There is also a third SQUID in the lower part of the image. Only the topmost SQUID was used in the measurements in this thesis, as shown in figure 4.1.

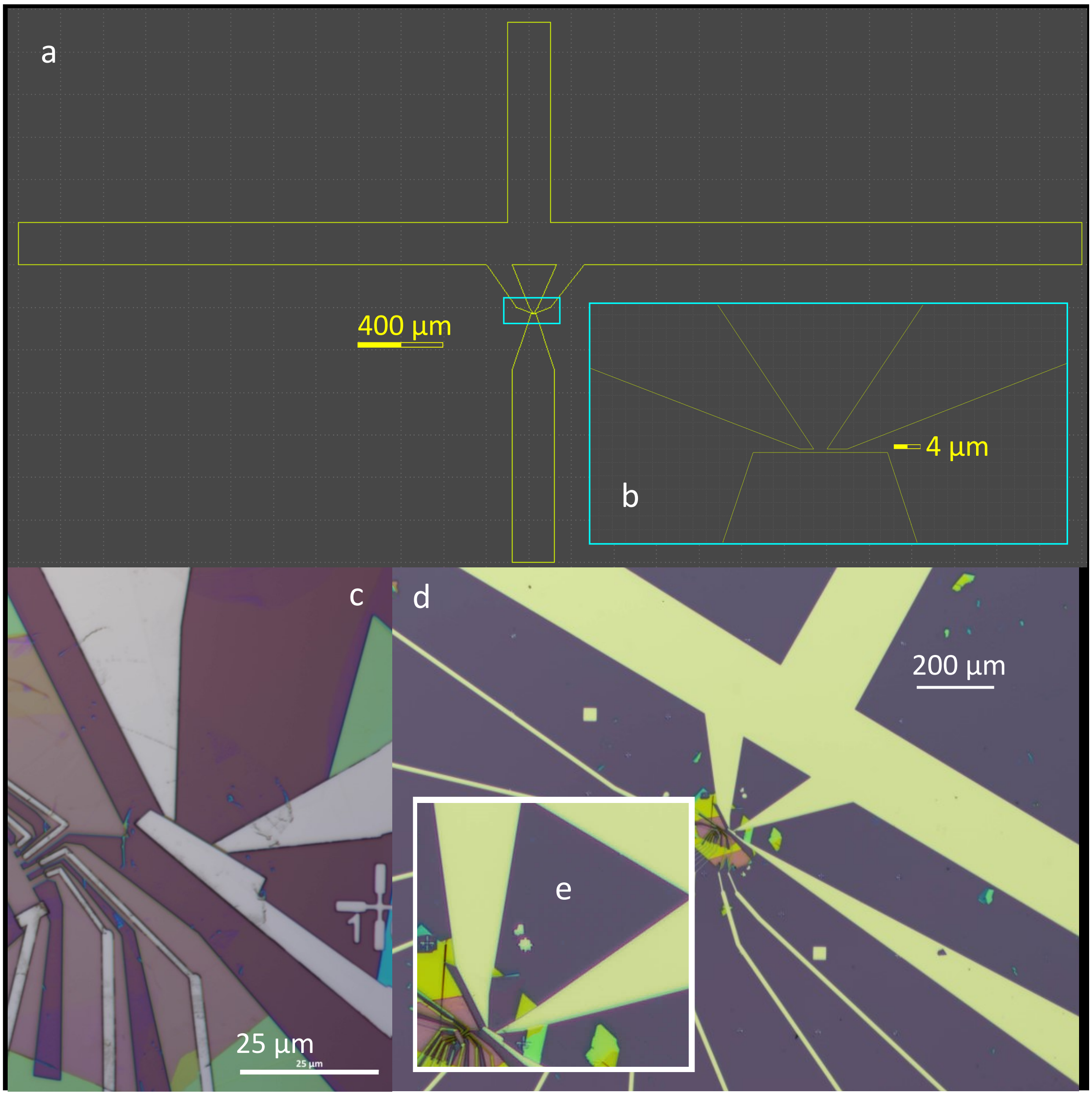


Figure B.2: As figure 4.2 but the areas that were masked have been revealed. They show thin wires on the left of the image (c) which are connected to another device that shared the graphene with the Big SQUID. These are also seen in (d) and (e).

# Appendix C

# Simulation information

## C.1 Python library versions

The simulation was run using Lancaster University's high end computing (HEC) cluster. Bash scripts were used to submit batch jobs to the HEC, but the calculations were performed in Python. To do this, the Anaconda 2018.12 distribution was used. Below, the libraries which were imported for use in the simulation and their versions are given. The Python version was 3.7.1.

Python 3.7.1

- os
- pickle
- sys
- time

Anaconda 2018.12

- numba 0.41.0
- numpy 1.15.4
- psutil 5.4.8
- scipy 1.1.0

# Appendix D

# Background theory

## D.1 Tilted-washboard potential

This theory is relevant to the RCSJ model, kept here for additional information.

The tilted-washboard potential is presented as an analogue of a mechanical system in which a particle moves in a periodic potential. In this case the equation of motion applies to a particle of mass $(\hbar/2e)^2 C$ in a gauge-invariant phase $\gamma$ dependent potential

$$U(\gamma) = -E_J \cos\gamma - \frac{\hbar I}{2e}\gamma \tag{D.1}$$

where $E_J$ is the Josephson coupling energy, and $I$ is the total current in an RCSJ model Josephson junction. This potential is constructed from a periodic term with amplitude equal to the Josephson coupling energy, but the y-coordinate of each point of increasing phase is reduced proportionally to the energy of the system. There is a transitional point when the current reaches the critical current of the junction: rather than encountering local minima as phase is increased, the corresponding points are now inflections on the downward curve, and there are no longer any regions of positive gradient. This is shown in figure D.1.

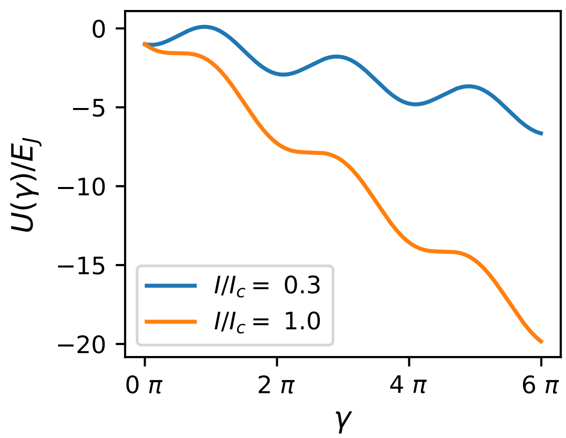


Figure D.1: Plot of the washboard potential of the RCSJ model for different ratios of the applied current to the critical current.

# Bibliography


[1] M. Tinkham, *Introduction to superconductivity*, 2nd. New York: Dover, 2004.

[2] C. Enss and S. Hunklinger, *Low-temperature physics*. Springer-Verlag, 2005.

[3] H. K. Onnes, "Further experiments with liquid helium," *Leiden Communications*, vol. 120b, 122b, 124c, 1911.

[4] D. Van Delft and P. Kes, "The discovery of superconductivity," *Physics Today*, pp. 38–43, 2010.

[5] A. M. Forrest, "Meissner and Ochsenfeld revisited," *European Journal of Physics*, vol. 4, pp. 117–120, 1983.

[6] C. Montagud-Montalvá, E. Navarro-Peris, T. Gómez-Navarro, X. Masip-Sanchis, and C. Prades-Gil, "Recovery of waste heat from data centres for decarbonisation of university campuses in a Mediterranean climate," *Energy Conversion and Management*, vol. 290, Aug. 2023. DOI: 10.1016/j.enconman.2023.117212.

[7] N. Satchell *et al.*, "Spin-valve Josephson junctions with perpendicular magnetic anisotropy for cryogenic memory," *Applied Physics Letters*, vol. 116, no. 2, Jan. 2020. DOI: 10.1063/1.5140095.

[8] X. Xue *et al.*, "CMOS-based cryogenic control of silicon quantum circuits," *Nature*, vol. 593, no. 7858, pp. 205–210, May 2021. DOI: 10.1038/s41586-021-03469-4.

[9] G. R. Pickett, "Cooling metals to the microkelvin regime, then and now," *Physica B*, vol. 280, pp. 467–473, 2000.

[10] A. T. Jones, C. P. Scheller, J. R. Prance, Y. B. Kalyoncu, D. M. Zumbühl, and R. P. Haley, "Progress in cooling nanoelectronic devices to ultra-low temperatures," *Journal of Low Temperature Physics*, vol. 201, no. 5-6, pp. 772–802, Dec. 2020. DOI: 10.1007/s10909-020-02472-9.

[11] S. Autti *et al.*, "Thermal transport in nanoelectronic devices cooled by on-chip magnetic refrigeration," *Physical Review Letters*, vol. 131, no. 7, Aug. 2023. DOI: 10.1103/PhysRevLett.131.077001.

[12] B. D. Josephson, "Possible new effects in superconductive tunnelling," *Physics Letters*, vol. 1, no. 7, pp. 251–253, 1962.

[13] F. Arute *et al.*, "Quantum supremacy using a programmable superconducting processor," *Nature*, vol. 574, no. 7779, pp. 505–510, Oct. 2019. DOI: 10.1038/s41586-019-1666-5.

[14] I. Bailey *et al.*, "Searching for wave-like dark matter with QSHS," *SciPost Phys. Proc*, vol. 12, pp. 18–22, 2023. DOI: 10.21468/SciPostPhysProc.12. [Online]. Available: https://www.oxinst.com/.

[15] K. K. Likharev and V. K. Semenov, "RSFQ logic/memory family: A new Josephson-junction technology for sub-terahertz-clock-frequency digital systems," *IEEE Transactions on Applied Superconductivity*, vol. 1, no. 1, 1991.

[16] H. Terai, T. Yamashita, S. Miki, K. Makise, and Z. Wang, "Low-jitter single flux quantum signal readout from superconducting single photon detector," *Optics Express*, vol. 1, no. 6, pp. 78–82, 2012. DOI: 10.1364/OE.20.020115.

[17] R. Fujimoto *et al.*, "Entangled photon pair detection by superconducting nanowire single-photon detectors with a single-flux-quantum coincidence circuit," *Applied Physics Express*, vol. 14, no. 10, Oct. 2021. DOI: 10.35848/1882-0786/ac211e.

[18] R. McDermott and M. G. Vavilov, "Accurate qubit control with single flux quantum pulses," *Phys. Rev. Appl.*, vol. 2, p. 014 007, 1 Jul. 2014. DOI: 10.1103/PhysRevApplied.2.014007. [Online]. Available: https://link.aps.org/doi/10.1103/PhysRevApplied.2.014007.

[19] K. Li, R. McDermott, and M. G. Vavilov, "Hardware-efficient qubit control with single-flux-quantum pulse sequences," *Physical Review Applied*, vol. 12, no. 1, Jul. 2019. DOI: 10.1103/PhysRevApplied.12.014044.

[20] Y. F. Wang, W. P. Gao, K. Liu, B. Ji, Z. Wang, and Z. R. Lin, "Single-flux-quantum-activated controlled- Z Gate for transmon qubits," *Physical Review Applied*, vol. 19, no. 4, Apr. 2023. DOI: 10.1103/PhysRevApplied.19.044031.

[21] C. H. Liu *et al.*, "Single flux quantum-based digital control of superconducting qubits in a multichip module," *PRX Quantum*, vol. 4, no. 3, Jul. 2023. DOI: 10.1103/PRXQuantum.4.030310.

[22] E. Leonard *et al.*, "Digital coherent control of a superconducting qubit," *Physical Review Applied*, vol. 11, no. 1, Jan. 2019. DOI: 10.1103/PhysRevApplied.11.014009.

[23] W. Zhao *et al.*, "Evolution of electronic structure in atomically thin sheets of $WS_2$ and $WSe_2$," *ACS Nano*, vol. 7, no. 1, pp. 791–797, Jan. 2013. DOI: 10.1021/nn305275h.

[24] J. D. Bernal, "The structure of graphite," in *Proceedings of the Royal Society London*, 1924, pp. 749–773. DOI: https://doi.org/10.1098/rspa.1924.0101.

[25] K. S. Novoselov *et al.*, "Electric field effect in atomically thin carbon films," *Science*, vol. 306, no. 5696, pp. 666–669, 2004. DOI: https://doi.org/10.1126/science.1102896.

[26] E. Shamsaei, F. B. de Souza, X. Yao, E. Benhelal, A. Akbari, and W. Duan, "Graphene-based nanosheets for stronger and more durable concrete: a review," *Construction and Building Materials*, vol. 183, pp. 642–660, Sep. 2018. DOI: 10.1016/j.conbuildmat.2018.06.201.

[27] Y. Leong, H. Lim, and I. Ibrahim, "Graphene in rubber formulations: a comprehensive review and performance optimization insights," *Molecular systems design and engineering*, 2023. DOI: 10.1039/D3ME00082F.

[28] P. Bhol, S. Yadav, A. Altaee, M. Saxena, P. K. Misra, and A. K. Samal, "Graphene-based membranes for water and wastewater treatment: A review," *ACS Applied Nano Materials*, vol. 4, no. 4, pp. 3274–3293, Apr. 2021. DOI: 10.1021/acsanm.0c03439.

[29] Z. Zhao *et al.*, "Polycrystalline few-layer graphene as a durable anticorrosion film for copper," *Nano Letters*, vol. 21, no. 2, pp. 1161–1168, Jan. 2021. DOI: 10.1021/acs.nanolett.0c04724.

[30] M. S. A. Bhuyan, M. N. Uddin, M. M. Islam, F. A. Bipasha, and S. S. Hossain, "Synthesis of graphene," *International Nano Letters*, vol. 6, no. 2, pp. 65–83, Jun. 2016. DOI: 10.1007/s40089-015-0176-1.

[31] A. K. Geim and I. V. Grigorieva, "Van der Waals heterostructures," *Nature*, vol. 499, no. 7459, pp. 419–425, 2013. DOI: 10.1038/nature12385.

[32] K. S. Novoselov, A. Mishchenko, A. Carvalho, and A. H. Castro Neto, "2D materials and van der Waals heterostructures," *Science*, vol. 353, no. 6298, Jul. 2016. DOI: 10.1126/science.aac9439.

[33] X. Xi *et al.*, "Ising pairing in superconducting NbSe2 atomic layers," *Nature Physics*, vol. 12, no. 2, pp. 139–143, Feb. 2016. DOI: 10.1038/nphys3538.

[34] J. Amontree *et al.*, "Reproducible graphene synthesis by oxygen-free chemical vapour deposition," *Nature*, May 2024. DOI: 10.1038/s41586-024-07454-5. [Online]. Available: https://www.nature.com/articles/s41586-024-07454-5.

[35] H. B. Heersche, P. Jarillo-Herrero, J. B. Oostinga, L. M. Vandersypen, and A. F. Morpurgo, "Bipolar supercurrent in graphene," *Nature*, vol. 446, no. 7131, pp. 56–59, Mar. 2007. DOI: 10.1038/nature05555.

[36] K. Ueda *et al.*, "Evidence of half-integer Shapiro steps originated from nonsinusoidal current phase relation in a short ballistic InAs nanowire Josephson junction," *Physical Review Research*, vol. 2, no. 3, Sep. 2020. DOI: 10.1103/PhysRevResearch.2.033435.

[37] G. Nanda *et al.*, "Current-phase relation of ballistic graphene Josephson junctions," *Nano Letters*, vol. 17, no. 6, pp. 3396–3401, Jun. 2017. DOI: 10.1021/acs.nanolett.7b00097.

[38] V. G. Mokerov, G. B. Galiev, J. Pozela, K. Pozela, and V. Juciene, "Electron mobility in a AlGaAs/GaAs/AlGaAs quantum well," *Semiconductors*, vol. 36, no. 6, pp. 674–678, Nov. 2001.

[39] C. Thelander, M. T. Björk, M. W. Larsson, A. E. Hansen, L. R. Wallenberg, and L. Samuelson, "Electron transport in InAs nanowires and heterostructure nanowire devices," *Solid State Communications*, vol. 131, no. 9-10 SPEC. ISS. Pp. 573–579, Sep. 2004. DOI: 10.1016/j.ssc.2004.05.033.

[40] M. A. Reed, J. N. Randall, R. J. Aggarwal, R. J. Matyi, T. M. Moore, and A. E. Wetsel, "Observation of discrete electronic states in a zero-dimensional semiconductor nanostructure," *Physical Review Letters*, vol. 60, no. 6, pp. 535–539, 1988.

[41] Y. Zhang, Y. Liu, C. Li, X. Chen, and Q. Wang, "Controlled synthesis of $Ag_2S$ quantum dots and experimental determination of the exciton bohr radius," *Journal of Physical Chemistry C*, vol. 118, no. 9, pp. 4918–4923, Mar. 2014. DOI: 10.1021/jp501266d.

[42] M. W. Doherty, N. B. Manson, P. Delaney, F. Jelezko, J. Wrachtrup, and L. C. Hollenberg, "The nitrogen-vacancy colour centre in diamond," *Physics Reports*, vol. 528, no. 1, pp. 1–45, Jul. 2013. DOI: 10.1016/j.physrep.2013.02.001.

[43] C. Pesado-Gómez *et al.*, "Fullerenes: Historical background, novel biological activities versus possible health risks," *Coordination Chemistry Reviews*, vol. 501, Feb. 2024. DOI: 10.1016/j.ccr.2023.215550.

[44] R. T. Harding *et al.*, "Spin resonance clock transition of the endohedral fullerene $^{15}N@C_{60}$," *Physical Review Letters*, vol. 119, no. 14, Oct. 2017. DOI: 10.1103/PhysRevLett.119.140801.

[45] A. H. Castro Neto, F. Guinea, N. M. Peres, K. S. Novoselov, and A. K. Geim, "The electronic properties of graphene," *Reviews of Modern Physics*, vol. 81, no. 1, pp. 109–162, Jan. 2009. DOI: 10.1103/RevModPhys.81.109.

[46] Y. Zhang, Y. W. Tan, H. L. Stormer, and P. Kim, "Experimental observation of the quantum Hall effect and Berry's phase in graphene," *Nature*, vol. 438, no. 7065, pp. 201–204, Nov. 2005. DOI: 10.1038/nature04235.

[47] P. E. Allain and J. N. Fuchs, "Klein tunneling in graphene: Optics with massless electrons," *European Physical Journal B*, vol. 83, no. 3, pp. 301–317, Oct. 2011. DOI: 10.1140/epjb/e2011-20351-3.

[48] H. Jiang *et al.*, "Synergistic-potential engineering enables high-efficiency graphene photodetectors for near- to mid-infrared light," *Nature Communications*, vol. 15, no. 1, Dec. 2024. DOI: 10.1038/s41467-024-45498-3.

[49] G. H. Lee *et al.*, "Graphene-based Josephson junction microwave bolometer," *Nature*, vol. 586, no. 7827, pp. 42–46, Oct. 2020. DOI: 10.1038/s41586-020-2752-4.

[50] F. E. Schmidt, M. D. Jenkins, K. Watanabe, T. Taniguchi, and G. A. Steele, "A ballistic graphene superconducting microwave circuit," *Nature Communications*, vol. 9, no. 1, Dec. 2018. DOI: 10.1038/s41467-018-06595-2.

[51] J. I.-J. Wang *et al.*, "Coherent control of a hybrid superconducting circuit made with graphene-based Van der Waals heterostructures," *Nature Nanotechnology*, vol. 14, no. 2, pp. 120–125, Feb. 2019. DOI: 10.1038/s41565-018-0329-2.

[52] Q. Cai *et al.*, "Comprehensive study and design of graphene transistor," *Micromachines*, vol. 15, no. 3, Mar. 2024. DOI: 10.3390/mi15030406.

[53] L. N. Cooper, "Bound electron pairs in a degenerate Fermi gas," *Physical Review*, vol. 104, no. 4, pp. 1189–1190, 1956.

[54] J. Bardeen, L. N. Cooper, and J. Schrieffer, "Microscopic theory of superconductivity," *Physical Review*, vol. 106, no. 1, pp. 162–164, 1957.

[55] J. Bardeen, L. N. Cooper, and J. R. Schrieffer, "Theory of superconductivity," *Physical Review*, vol. 108, no. 5, pp. 1175–1204, 1957.

[56] B. D. Josephson, "Supercurrents through barriers," *Advances in Physics*, vol. 14, no. 56, pp. 419–451, 1965. DOI: 10.1080/00018736500101091.

[57] P. W. Anderson and J. M. Rowell, "Probable observation of the Josephson superconducting tunneling effect," *Physical Review Letters*, vol. 10, no. 6, pp. 230–232, 1963.

[58] Y. L. Wu *et al.*, "Fabrication of Al/AlOx/Al Josephson junctions and superconducting quantum circuits by shadow evaporation and a dynamic oxidation process," *Chinese Physics B*, vol. 22, no. 6, Jun. 2013. DOI: 10.1088/1674-1056/22/6/060309.

[59] Y. Hai-Feng *et al.*, "Fabrication of high-quality submicron Nb/Al-AlOx/Nb tunnel junctions," *Chinese Physics B*, vol. 17, no. 8, 2008. DOI: 10.1088/1674-1056/17/8/052.

[60] M. J. Cyster, J. S. Smith, N. Vogt, G. Opletal, S. P. Russo, and J. H. Cole, "Simulating the fabrication of aluminium oxide tunnel junctions," *npj Quantum Information*, vol. 7, no. 1, Dec. 2021. DOI: 10.1038/s41534-020-00360-4.

[61] H. Paik *et al.*, "Observation of high coherence in Josephson junction qubits measured in a three-dimensional circuit QED architecture," *Physical Review Letters*, vol. 107, no. 24, Dec. 2011. DOI: 10.1103/PhysRevLett.107.240501.

[62] G. H. Lee, S. Kim, S. H. Jhi, and H. J. Lee, "Ultimately short ballistic vertical graphene Josephson junctions," *Nature Communications*, vol. 6, Jan. 2015. DOI: 10.1038/ncomms7181.

[63] C. T. Ke *et al.*, "Critical current scaling in long diffusive graphene-based Josephson junctions," *Nano Letters*, vol. 16, no. 8, pp. 4788–4791, Aug. 2016. DOI: 10.1021/acs.nanolett.6b00738.

[64] A. S. Mayorov *et al.*, "Micrometer-scale ballistic transport in encapsulated graphene at room temperature," *Nano Letters*, vol. 11, no. 6, pp. 2396–2399, Jun. 2011. DOI: 10.1021/nl200758b.

[65] P. Dubos, H. Courtois, B. Pannetier, F. K. Wilhelm, A. D. Zaikin, and G. Schön, "Josephson critical current in a long mesoscopic S-N-S junction," *Physical Review B - Condensed Matter and Materials Physics*, vol. 63, no. 6, Jan. 2001. DOI: 10.1103/PhysRevB.63.064502.

[66] P. Pandey, R. Kraft, R. Krupke, D. Beckmann, and R. Danneau, "Andreev reflection in ballistic normal metal/graphene/superconductor junctions," *Physical Review B*, vol. 100, no. 16, Oct. 2019. DOI: 10.1103/PhysRevB.100.165416.

[67] M. Zhu, M. B. Shalom, A. Mishchsenko, V. Fal'Ko, K. Novoselov, and A. Geim, "Supercurrent and multiple Andreev reflections in micrometer-long ballistic graphene Josephson junctions," *Nanoscale*, vol. 10, no. 6, pp. 3020–3025, Feb. 2018. DOI: 10.1039/c7nr05904c.

[68] R. Taboryski, J. Kutchinsky, and J. Bindslev Hansen, "Multiple Andreev reflections in diffusive SNS structures," *Superlattices and Microstructures*, vol. 25, no. 5, 1999. DOI: https://doi.org/10.1006/spmi.1999.0712.

[69] C. W. Beenakker, "Specular andreev reflection in graphene," *Physical Review Letters*, vol. 97, no. 6, 2006. DOI: 10.1103/PhysRevLett.97.067007.

[70] S. G. Cheng, Y. Xing, J. Wang, and Q. F. Sun, "Controllable Andreev retroreflection and specular Andreev reflection in a four-terminal graphene-superconductor hybrid system," *Physical Review Letters*, vol. 103, no. 16, Oct. 2009. DOI: 10.1103/PhysRevLett.103.167003.

[71] D. K. Efetov *et al.*, "Specular interband Andreev reflections at Van der Waals interfaces between graphene and NbSe2," *Nature Physics*, vol. 12, no. 4, pp. 328–332, Apr. 2016. DOI: 10.1038/nphys3583.

[72] J. K. Freericks, A. N. Tahvildar-Zadeh, and B. K. Nikolić, "Use of a generalized Thouless energy in describing transport properties of Josephson junctions," in *IEEE Transactions on Applied Superconductivity*, vol. 15, Jun. 2005, pp. 896–899. DOI: 10.1109/TASC.2005.850107.

[73] L. Wang *et al.*, "One-dimensional electrical contact to a two-dimensional material," *Science*, vol. 342, no. 6158, pp. 614–617, 2013. DOI: 10.1126/science.1244358.

[74] M. Ben Shalom *et al.*, "Quantum oscillations of the critical current and high-field superconducting proximity in ballistic graphene," *Nature Physics*, vol. 12, no. 4, pp. 318–322, Apr. 2016. DOI: 10.1038/nphys3592.

[75] M. D. Thompson *et al.*, "Graphene-based tunable SQUIDs," *Applied Physics Letters*, vol. 110, no. 16, Apr. 2017. DOI: 10.1063/1.4981904.

[76] I. V. Borzenets *et al.*, "Ballistic graphene Josephson junctions from the short to the long junction regimes," *Physical Review Letters*, vol. 117, no. 23, Dec. 2016. DOI: 10.1103/PhysRevLett.117.237002.

[77] T. Li, J. Gallop, L. Hao, and E. Romans, "Ballistic Josephson junctions based on CVD graphene," *Superconductor Science and Technology*, vol. 31, no. 4, 2018. DOI: 10.1088/1361-6668/aaab81.

[78] C. Beenakker, "Three "universal" mesoscopic Josephson effects," in *Transport Phenomena in Mesoscopic Systems*, H. Fukuyama and T. Ando, Eds., Berlin: Springer-Verlag, 1991, pp. 235–253.

[79] D. Giuliano and I. Affleck, "The Josephson current through a long quantum wire," *Journal of Statistical Mechanics: Theory and Experiment*, vol. 2013, no. 2, Feb. 2013. DOI: 10.1088/1742-5468/2013/02/P02034.

[80] F. Chiodi *et al.*, "Probing the dynamics of Andreev states in a coherent normal/superconducting ring," *Scientific Reports*, vol. 1, 2011. DOI: 10.1038/srep00003.

[81] A. A. Golubov, M. Y. Kupriyanov, and E. Il'ichev, "The current-phase relation in Josephson junctions," *Reviews of Modern Physics*, vol. 76, no. 2, pp. 411–469, Apr. 2004. DOI: 10.1103/RevModPhys.76.411.

[82] P. Rakyta, A. Kormányos, and J. Cserti, "Magnetic field oscillations of the critical current in long ballistic graphene Josephson junctions," *Physical Review B*, vol. 93, no. 22, Jun. 2016. DOI: 10.1103/PhysRevB.93.224510.

[83] Z. Huang, B. H. Elfeky, T. Taniguchi, K. Watanabe, J. Shabani, and D. Shahrjerdi, "Observation of half-integer Shapiro steps in graphene Josephson junctions," *Applied Physics Letters*, vol. 122, no. 26, Jun. 2023. DOI: 10.1063/5.0153646.

[84] D. Drung and H. Koch, "An electronic second-order gradiometer for biomagnetic applications in clinical shielded rooms," *IEEE Transactions on applied superconductivity*, vol. 3, no. 1, pp. 2594–2597, 1993.

[85] Y. V. Maslennikov, V. Y. Slobodchikov, V. A. Krymov, and Gulyaev Yu V, "Magnetometric SQUID systems and magnetic measurement methods for biomedical research," *Pattern Recognition and Image Analysis*, vol. 33, no. 4, pp. 1402–1428, Dec. 2023. DOI: 10.1134/S1054661823040296.

[86] E. Persky, I. Sochnikov, and B. Kalisky, "Annual review of condensed matter physics studying quantum materials with scanning SQUID microscopy," *The Annual Review of Condensed Matter Physics is*, vol. 13, pp. 385–405, 2021. DOI: https://doi.org/10.1146/annurev-conmatphys-031620-104226.

[87] R. Jaklevic, J. Lambe, A. Silver, and J. Mercereau, "Quantum interference effects in Josephson tunneling," *Physical Review Letters*, vol. 12, no. 7, pp. 159–160, 1964.

[88] A. H. Silver and J. E. Zimmerman, "Quantum states and transitions in weakly connected superconducting rings," *Physical Review*, vol. 157, no. 2, pp. 317–341, 1967.

[89] J. Clarke, "The use of superconducting junctions in magnetometry," *Revue de Physique Appliquée*, vol. 5, no. 1, p. 1, 1970. DOI: 10.1051/rphysap:019700050103200.

[90] R. D. Luca, "Quantum interference in Josephson junctions," *Journal of Modern Physics*, vol. 06, no. 05, pp. 526–535, 2015. DOI: 10.4236/jmp.2015.65057.

[91] A. A. Abrikosov, "The magnetic properties of superconducting alloys," *Journal of Physics and Chemistry of Solids*, vol. 2, pp. 199–208, 1957.

[92] J. Clarke and A. I. Braginski, *The SQUID handbook. Vol. 1, fundamentals and technology of SQUIDs and SQUID systems*. Wiley-VCH, 2004.

[93] J. R. Prance and M. D. Thompson, "Sensitivity of a DC SQUID with a non-sinusoidal current-phase relation in its junctions," *Applied Physics Letters*, vol. 122, no. 22, May 2023. DOI: 10.1063/5.0151607.

[94] A. Paghi *et al.*, "Josephson field effect transistors with InAs on insulator and high permittivity gate dielectrics," *arXiv*, 2024. DOI: https://doi.org/10.48550/arXiv.2412.16221.

[95] T. W. Larsen *et al.*, "Semiconductor-Nanowire-Based Superconducting Qubit," *Physical Review Letters*, vol. 115, no. 12, Sep. 2015. DOI: 10.1103/PhysRevLett.115.127001.

[96] Y.-J. Doh, J. A. Van Dam, A. L. Roest, E. P. A. M. Bakkers, L. P. Kouwenhoven, and S. De Franceschi, "Tunable supercurrent through semiconductor nanowires," *Science*, vol. 309, pp. 272–275, 2005. DOI: 10.1126/science.1113523.

[97] C. Ciaccia *et al.*, "Charge-4e supercurrent in a two-dimensional InAs-Al superconductor-semiconductor heterostructure," *Communications Physics*, vol. 7, no. 1, Dec. 2024. DOI: 10.1038/s42005-024-01531-x.

[98] J. O. Island, G. A. Steele, H. S. Van Der Zant, and A. Castellanos-Gomez, "Thickness dependent interlayer transport in vertical MoS2 Josephson junctions," *2D Materials*, vol. 3, no. 3, Jul. 2016. DOI: 10.1088/2053-1583/3/3/031002.

[99] K. H. Lee *et al.*, "Two-dimensional material tunnel barrier for Josephson junctions and superconducting qubits," *Nano Letters*, vol. 19, no. 11, pp. 8287–8293, Nov. 2019. DOI: 10.1021/acs.nanolett.9b03886.

[100] N. Huo, Y. Yang, Y. N. Wu, X. G. Zhang, S. T. Pantelides, and G. Konstantatos, "High carrier mobility in monolayer CVD-grown MoS2 through phonon suppression," *Nanoscale*, vol. 10, no. 31, pp. 15 071–15 077, Aug. 2018. DOI: 10.1039/c8nr04416c.

[101] S. M. Frolov, "Current-phase relations of Josephson junctions with ferromagnetic barriers," Ph.D. dissertation, University of Illinois, 2005.

[102] Y. Yao *et al.*, "Half-integer Shapiro steps in strong ferromagnetic Josephson junctions," *Physical Review B*, vol. 104, no. 10, Sep. 2021. DOI: 10.1103/PhysRevB.104.104414.

[103] N. O. Birge and N. Satchell, "Ferromagnetic materials for Josephson $\pi$ junctions," *APL Materials*, vol. 12, no. 4, Apr. 2024. DOI: 10.1063/5.0195229.

[104] Y. Cao *et al.*, "Unconventional superconductivity in magic-angle graphene superlattices," *Nature*, vol. 556, no. 7699, pp. 43–50, Apr. 2018. DOI: 10.1038/nature26160.

[105] F. K. de Vries *et al.*, "Gate-defined Josephson junctions in magic-angle twisted bilayer graphene," *Nature Nanotechnology*, vol. 16, no. 7, pp. 760–763, Jul. 2021. DOI: 10.1038/s41565-021-00896-2.

[106] E. Portolés *et al.*, "A tunable monolithic SQUID in twisted bilayer graphene," *Nature Nanotechnology*, vol. 17, no. 11, pp. 1159–1164, Nov. 2022. DOI: 10.1038/s41565-022-01222-0.

[107] C. Eichler and A. Wallraff, "Controlling the dynamic range of a Josephson parametric amplifier," *EPJ Quantum Technology*, vol. 1, no. 2, 2014. DOI: 10.1140/epjqt2.

[108] T. G. Zhou *et al.*, "Nonlinear inductance of intrinsic Josephson junction arrays and its application to tunable filters," in *IEEE Transactions on Applied Superconductivity*, vol. 17, Jun. 2007, pp. 586–589. DOI: 10.1109/TASC.2007.898176.

[109] C. Macklin *et al.*, "A near-quantum-limited Josephson traveling-wave parametric amplifier," *Science*, vol. 350, no. 6258, pp. 307–310, 2015. DOI: 10.1126/science.aaa8525.

[110] G. Butseraen *et al.*, "A gate-tunable graphene Josephson parametric amplifier," *Nature Nanotechnology*, vol. 17, no. 11, pp. 1153–1158, Nov. 2022. DOI: 10.1038/s41565-022-01235-9.

[111] J. Sarkar *et al.*, "Quantum-noise-limited microwave amplification using a graphene Josephson junction," *Nature Nanotechnology*, vol. 17, no. 11, pp. 1147–1152, Nov. 2022. DOI: 10.1038/s41565-022-01223-z.

[112] M. Kjaergaard *et al.*, "Superconducting qubits: Current state of play," *Annual Review of Condensed Matter Physics*, vol. 11, pp. 369–395, 2020. DOI: 10.1146/annurev-conmatphys.

[113] F. Stella *et al.*, "Integrating superconductive and optical circuits," *Applied Physics Letters*, vol. 92, no. 20, p. 202 505, May 2008. DOI: 10.1063/1.2931700.

[114] E. D. Walsh *et al.*, "Josephson junction infrared single-photon detector," *Science*, vol. 372, p. 2024, 2021. DOI: 10.1126/science.abf5539.

[115] S. Shapiro, "Josephson currents in superconducting tunneling: the effect of microwaves and other observations," *Physical Review Letters*, vol. 11, no. 2, pp. 80–82, 1963.

[116] B. Raes *et al.*, "Fractional Shapiro steps in resistively shunted Josephson junctions as a fingerprint of a skewed current-phase relationship," *Physical Review B*, vol. 102, no. 5, Aug. 2020. DOI: 10.1103/PhysRevB.102.054507.

[117] C. Vanneste, C. C. Chi, W. J. Gallagher, A. W. Kleinsasser, S. I. Raider, and R. L. Sandstrom, "Shapiro steps on current-voltage curves of dc SQUIDs," *Journal of Applied Physics*, vol. 64, no. 1, pp. 242–245, 1988. DOI: 10.1063/1.341471.

[118] Y. V. Kislinkskii *et al.*, "Superconducting current in hybrid heterojunctions," *Journal of Experimental and Theoretical Physics*, vol. 101, no. 3, pp. 494–503, 2005.

[119] G. H. Lee and H. J. Lee, "Josephson coupling realized in graphite-based vertical junction," *Applied Physics Express*, vol. 6, no. 2, Feb. 2013. DOI: 10.7567/APEX.6.025102.

[120] G.-H. Lee, S. Kim, S.-H. Jhi, and H.-J. Lee, "Ultimately short ballistic vertical graphene Josephson junctions (Supplementary figures)," *Nature Communications*, vol. 6, 2015.

[121] T. F. Larson *et al.*, "Zero crossing steps and anomalous Shapiro maps in graphene Josephson junctions," *Nano Letters*, vol. 20, no. 10, pp. 6998–7003, Oct. 2020. DOI: 10.1021/acs.nanolett.0c01598.

[122] P. Virtanen *et al.*, "SciPy 1.0: fundamental algorithms for scientific computing in Python," *Nature Methods*, vol. 17, no. 3, pp. 261–272, Mar. 2020. DOI: 10.1038/s41592-019-0686-2.

[123] J. R. Dormand and P. J. Prince, "A family of embedded Runge-Kutta formulae," *Journal of Computational and Applied Mathematics*, vol. 6, no. 1, pp. 19–26, 1980.

[124] C. R. Harris *et al.*, "Array programming with NumPy," *Nature*, vol. 585, no. 7825, pp. 357–362, Sep. 2020. DOI: 10.1038/s41586-020-2649-2.

[125] H. Nyquist, "Thermal agitation of electric charge in conductors," *Physical Review*, vol. 32, pp. 110–113, 1928.

[126] P. D. Welch, "The use of fast Fourier transform for the estimation of power spectra: a method based on time averaging over short, modified periodograms," *IEEE Transactions on Audio and Electroacoustics*, vol. 15, no. 2, pp. 70–73, 1967.

[127] A. Valizadeh, M. R. Kolahchi, and J. P. Straley, "On the origin of fractional Shapiro steps in systems of Josephson junctions with few degrees of freedom," *Journal of Nonlinear Mathematical Physics*, vol. 15, pp. 407–416, 2008.

[128] M. H. Bae, R. C. Dinsmore, M. Sahu, H. J. Lee, and A. Bezryadin, "Zero-crossing Shapiro steps in high- Tc superconducting microstructures tailored by a focused ion beam," *Physical Review B - Condensed Matter and Materials Physics*, vol. 77, no. 14, Apr. 2008. DOI: 10.1103/PhysRevB.77.144501.

[129] F. M. Pellegrino, G. Falci, and E. Paladino, "1/f critical current noise in short ballistic graphene Josephson junctions," *Communications Physics*, vol. 3, no. 1, Dec. 2020. DOI: 10.1038/s42005-019-0275-9.

[130] D. A. Rower *et al.*, "Evolution of 1/f flux noise in superconducting qubits with weak magnetic fields," *Physical Review Letters*, vol. 130, no. 22, Jun. 2023. DOI: 10.1103/PhysRevLett.130.220602.

[131] X. Du, I. Skachko, and E. Y. Andrei, "Josephson current and multiple Andreev reflections in graphene SNS junctions," *Physical Review B - Condensed Matter and Materials Physics*, vol. 77, no. 18, May 2008. DOI: 10.1103/PhysRevB.77.184507.

[132] V. E. Calado *et al.*, "Ballistic Josephson junctions in edge-contacted graphene," *Nature Nanotechnology*, vol. 10, no. 9, pp. 761–764, Sep. 2015. DOI: 10.1038/nnano.2015.156.

[133] A. Ranjan *et al.*, "Dielectric breakdown in single-crystal hexagonal boron nitride," *ACS Applied Electronic Materials*, vol. 3, no. 8, pp. 3547–3554, Aug. 2021. DOI: 10.1021/acsaelm.1c00469.

[134] A. Laturia, M. L. Van de Put, and W. G. Vandenberghe, "Dielectric properties of hexagonal boron nitride and transition metal dichalcogenides: from monolayer to bulk," *npj 2D Materials and Applications*, vol. 2, no. 1, Dec. 2018. DOI: 10.1038/s41699-018-0050-x.

[135] K. C. Fong and K. C. Schwab, "Ultrasensitive and wide-bandwidth thermal measurements of graphene at low temperatures," *Physical Review X*, vol. 2, no. 3, 2012. DOI: 10.1103/PhysRevX.2.031006.

[136] I. V. Borzenets, U. C. Coskun, H. T. Mebrahtu, Y. V. Bomze, A. I. Smirnov, and G. Finkelstein, "Phonon bottleneck in graphene-based Josephson junctions at millikelvin temperatures," *Physical Review Letters*, vol. 111, no. 2, Jul. 2013. DOI: 10.1103/PhysRevLett.111.027001.

[137] J. Luomahaara, V. Vesterinen, L. Grönberg, and J. Hassel, "Kinetic inductance magnetometer," *Nature Communications*, vol. 5, 2014. DOI: 10.1038/ncomms5872.

[138] Y. Lee, J. Yun, C. Lee, M. Sirena, J. Kim, and N. Haberkorn, "Penetration depth and critical fields in superconducting NbTi thin films grown by co-sputtering at room temperature," *Physica Scripta*, vol. 99, no. 6, Jun. 2024. DOI: 10.1088/1402-4896/ad4690.

[139] FastFieldSolvers S.R.L., *FastHenry*, 2019. [Online]. Available: https://www.fastfieldsolvers.com/default.asp.